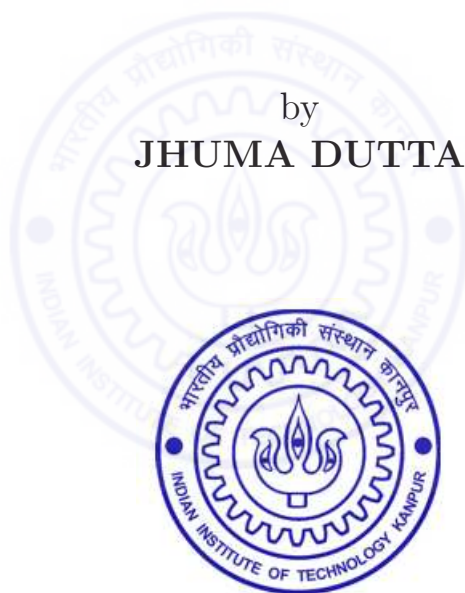

Photonic and Plasmonic Properties of Periodically Patterned Columnar Thin Films

*A Thesis Submitted
in Partial Fulfilment of the Requirements
for the Degree of
Doctor of Philosophy*

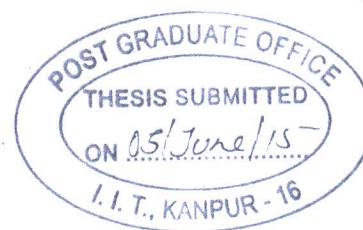
by
JHUMA DUTTA



to the
**DEPARTMENT OF PHYSICS
INDIAN INSTITUTE OF TECHNOLOGY
KANPUR**

June, 2015

CERTIFICATE

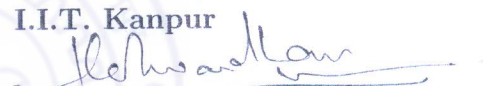


It is certified that the work contained in the thesis entitled "*Photonic and Plasmonic Properties of Periodically Patterned Columnar Thin Films*" by *Jhuma Dutta*, has been carried out under my supervision and that this work has not been submitted elsewhere for a degree.



Prof. S. Anantha Ramakrishna
Department of Physics

I.I.T. Kanpur



Prof. Harshawardhan Wanare
Department of Physics
I.I.T. Kanpur

05, June, 2015

STATEMENT

I hereby declare that the matter manifested in this thesis entitled: “Photonic and Plasmonic Properties of Periodically Patterned Columnar Thin Films”, is the result of research carried out by me in the Department of Physics, Indian Institute of Technology Kanpur, India under the supervision of Prof. S. Anantha Ramakrishna and Prof. Harshawardhan Wanare

In keeping with the general practice of reporting scientific observations, due acknowledgement has been made wherever the work described is based on the findings of other investigators.

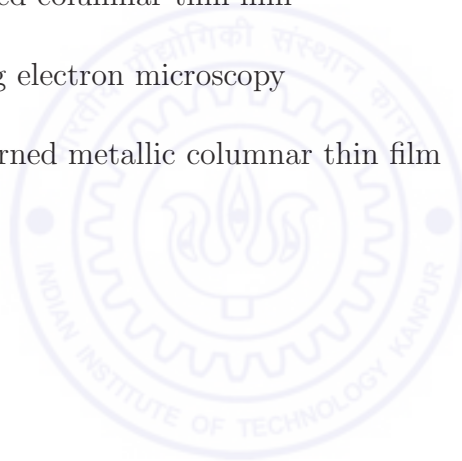
IIT Kanpur
June, 2015



JHUMA DUTTA
Ph.D. Student
Roll No : Y9109069

List of Acronyms

OAD	oblique angle deposition
LIL	laser interference lithography
CTFs	Columnar thin films
STFs	Sculptured thin films
SPP	surface plasmon polariton
AFM	atomic force microscopy
FEM	finite element method
PPCTF	periodically patterned columnar thin film
FESEM	Field effect scanning electron microscopy
PPMCTF	periodically patterned metallic columnar thin film



Synopsis

Name	: Jhuma Dutta
Roll No.	: Y9109069
Degree for which submitted	: Doctor of Philosophy
Department	: Physics
Thesis Title	: Photonic and Plasmonic Properties of Periodically Patterned Columnar Thin Films
Thesis Supervisor	: Prof. S. Anantha Ramakrishna Prof. Harshawardhan Wanare
Month and year of submission	: June, 2015

Exploring new optical properties of nanostructured thin films is a major focus of nanotechnology research, motivated by the enhanced properties that the nanostructure makes possible. Modern techniques have given us the unprecedented ability to control and fabricate accurately these structures at nanoscale. Yet miniaturization of optical device components from sub-micron to nano-scale remains one of the major outstanding challenges in order to fulfill the rapidly growing technological requirements. The requirement for the ability to form ordered arrays of well defined and periodic nanostructures in accurate, fast and inexpensive manners is the central issue for the miniaturization, multifunctionality and speed required in such systems. The enhanced properties are of great interest not only from an applied perspective but also from a fundamental point of view.

Oblique angle deposition (OAD) technique and laser interference lithography (LIL) provide advantages of fabrication of nanostructures over large areas, as required in many advanced technological and industrial applications. Columnar thin films (CTFs) are random porous nanostructures fabricated by OAD and have properties that are not intrinsically present in the materials they are composed of. LIL is a flexible nanostructuring method to inexpensively create large scale array of periodic submicrometer structures (wavelength scale) based on recording interference pattern. New developments such as surface plasmon LIL and multiphoton processes have advanced the resolution of this method to subwavelength scales. The ideal morphology

of CTFs consists of almost identical, straight and parallel nanowires of elliptical cross-section with extremely anisotropic properties. The diameters of the nanowire range from about 10 to 100 nm, and different morphologies are realizable through instantaneous variation in the growth direction of nanowires during physical vapor deposition. In OAD, a collimated vapor flux arrives on the substrate at large oblique angles relative to the substrate normal and the evaporant atoms nucleate on the substrate. The region behind the formed nucleus does not receive any further ad-atoms from the collimated vapor flux because of the shadowing by the nucleus. This preferential growth dynamics gives rise to the formation of randomly arranged isolated columnar structures. The incident vapor flux angle controls the slant angle of the columns and affects the degree of shadowing and thus the porosity of the film. If the substrate is rotated around the substrate normal while keeping the incident angle fixed, the morphology of the growth film is dramatically changed. An exceptional ability to form different shapes (such as helices, vertical columns, n-fold spirals, chevron shapes, ball-like structures etc.) with controlled substrate rotation during vapor deposition, makes OAD a versatile technique to fabricate desired nanostructures. Due to the complex structures of various shapes attainable by OAD, these are often known as Sculptured thin films (STFs). For the synthesis of well defined columnar arrays having appropriate separation and clear surface morphologies, pre-patterned seed layer is required. The knowledge of the mechanisms involved in the growth process is essential to fabricate periodically patterned structures. The macroscopic optical properties and the porosity of the CTF can be precisely tailored by controlling the vapour deposition parameters such as incident vapor flux angle, deposition rate etc. Due to the biaxial orthorhombic nature of CTFs, these structures show different optical properties such as anomalous optical dispersion, extreme birefringence and strong dichroism etc at visible and infrared wavelengths. CTFs are highly porous materials and are promising candidates for optical sensing applications such as chemical and biological sensors. Due to its nano-structural porosity, the refractive index of CTFs are found to be very low (refractive index close to air) and hence can be used as antireflective coating.

The objective of this thesis is to fabricate periodically patterned columnar thin films (PP-CTFs) and to study various optical properties to investigate opportunities for novel applications. Most of the OAD research related to optical studies was concentrated on unpatterned columnar or sculptured thin film structures. Very few studies have focussed on patterned columnar thin film structures. As periodic structures have several advantages over random structure, our idea is to combine the two structures.

One is nanoscale of the CTFs that is subwavelength and the other is sub-micro to micro- scale of the periodic gratings (wavelength scale). The extremely anisotropic optical properties offered by the nanocolumnar structure combined with the larger scale structures for photonic bandgap or diffractive effects provide for new physical phenomena. Potential applications of PP-CTFs are investigated in this thesis as blazed diffraction gratings, unidirectional surface plasmon couplers and tuning of diffraction efficiency as a function of slant angle of the grating.

In the first chapter, an introduction to CTFs and PP-CTFs are given. Various possible optical, electrical, and magnetic properties of such kind of structures have also been explained. The isotropic and anisotropic media, diffraction from periodic objects and blazed gratings, effective media and homogenization, metamaterials, hyperbolic materials, photonic band gap structures and surface electromagnetic wave are discussed broadly. This general overview has been used later in the thesis to understand the various photonic and plasmonic properties of PP-CTFs. In the last section, the motivation and scope of our study has also been described.

The second chapter, provides a description of the experimental methods and materials used in the thesis for fabricating periodically patterned columnar thin film (PP-CTF). The design consideration of OAD chamber and the various deposition parameters used are discussed. The detailed growth mechanisms of columnar structure with various complex morphologies of sculptured thin film structures are also explained. PP-CTFs are fabricated by depositing columnar thin film on pre-patterned substrates by combining two experimental techniques such as LIL and OAD. The substrate pre-patterning by laser interference lithography and laser micromachining have been discussed. Details of the growth mechanism of periodically patterned structures are discussed in terms of simple geometrical phenomenon of the self-shadowing process. Surface morphology of the growth structure are characterized by Field effect scanning electron microscopy (FESEM) and atomic force microscopy (AFM). Optical set-up for measuring the angle resolved transmittance spectra are presented. Diffraction efficiencies are measured using various wavelength of lasers with different optical components such as Glan- Thomson polarizers, beam splitters and neutral density filters. The finite element method (FEM) based COMSOL Multiphysics ® simulation tool is used to model the periodic silver nanocolumnar arrays fabricated to understand their electromagnetic properties.

In the third chapter, we have discussed how a periodically patterned columnar

thin film made of dielectric material behave as a blazed diffraction grating. Blazed gratings are special class of diffraction gratings, which have an ability to enhance diffraction intensity at the non-specular transmission or reflection diffraction orders and it has enormous applications in spectroscopy and optical modulators. The conventional blazed grating available in the market are fabricated using very expensive methods such as reactive ion etching. Here we made blazed gratings of dielectric materials using very inexpensive method by combining LIL and OAD techniques. Triangular prismatic air cavities were periodically formed by merging the growth of diverging columnar structures of CaF_2 within the fabricated structure by controlling the various deposition parameters of vapour flux. We present here a system of PP-CTF, a class of which are shown to behave as blazed diffraction gratings. The diffraction efficiencies of these gratings have been measured and the scalar Kirchhoff-Fresnel diffraction theory shows that an asymmetric diffraction arises due to the presence of triangular air prismatic cavities within the PP-CTF. The intensities of the diffracted order depends quite sensitively on the effective permittivity tensor of the CTFs, which in turn depends on the porosity of the film. Because of different refractive indices for two polarizations, the calculated and measured diffraction efficiencies of PP-CTFs for s - and p - polarized light are different. The principal refractive indices of the deposited CTFs are estimated from the diffraction efficiencies. These structures were designer built using a very unconventional approach and represent a new class of gratings.

*These results have also been published in Jhuma Dutta, S. Anantha Ramakrishna and Akhlesh Lakhtakia; Applied Physics Letters **102**, 161116 (2013)*

In the fourth chapter, plasmonic properties of periodically patterned metallic columnar thin films (PPMCTFs) have been investigated. FESEM images of anisotropic plasmonic structures on 1-D gratings, reveal that deposition of silver columnar arrays took place only on the ridges of the gratings and form an asymmetric structure in the morphologically significant plane. Morphologically significant plane is defined as the plane in which the slanted silver nano-columns lie. The anisotropic plasmonic grating structure, which breaks the symmetry of the grating structure shows strong asymmetric diffraction and provides for an asymmetric coupling to SPP waves propagating along one direction. Asymmetric coupling has been shown earlier in slanted sinusoidal gratings and binary blazed plasmonic gratings, but efficient asymmetric SPP coupling on periodically patterned anisotropic metal films have been measured for the first time in this thesis. Such asymmetric coupling to unidirectional SPP waves is very important for efficiently coupling radiation to the SPP waves in plasmonic devices and circuits.

When the plane of incidence is orthogonal to the morphologically significant plane, then asymmetry is lost and coupling to SPP become symmetric. In other words, when the structure is rotated by an angle of 90° , then the light can not experience the slant angle of the grating and give rise to symmetric coupling to SPP waves with respect to the positive and negative angle of incidence. Coupling to SPP occurs for both p - and s - polarizations in case of asymmetric structure in contrast to excitation of SPP only through p - polarization in case of corrugated structure. The s - polarized incident light could couple to the SPP waves due to scattering arising from either the columnar structure of the CTF or from the surface roughness that is visible in the FESEM images. To verify whether the columnar structure itself is responsible for this effect, numerical simulations have been performed considering only the columnar structure with no surface roughness. In case of anisotropic plasmonic structure on 2-D grating, different kinds of coupling to SPP occurs by varying the azimuthal angle between the morphologically significant plane and plane of incidence. In 2D grating, there are different crystal symmetry directions, and by changing the azimuthal orientation of the plane of the structure with respect to the plane of incidence, it is possible to tune the SPP dispersion. These systems are extremely interesting from the perspectives of new physical insights into anisotropic metallic or hyperbolic systems as well as novel applications in plasmonic devices and circuits. The Bruggeman homogenization formalism was used to homogenize the silver CTFs into homogeneous hyperbolic biaxial materials. The wavenumber of the SPP wave guided by the planar interface of the homogenized metallic CTF and an isotropic dielectric material, was derived using Maxwell's equations. The predicted dispersions of the SPP waves matched the measured dispersions very well.

*A part of these results have been published in Jhuma Dutta, S. Anantha Ramakrishna and Akhlesh Lakhtakia; Journal of Applied Physics **117**, 013102 (2015)*

In the fifth chapter, we have discussed the experimental investigation of the re-orientation by ion beam irradiation of slanted plasmonic nanocolumns of silver grown on small period photoresist gratings. The slant angle of the nanocolumns in the PP-CTFs arises during the deposition process due to a self shadowing effect and is a quantity fixed during the fabrication. This is a very critical parameter that determines the photonic properties like the diffraction and surface plasmon coupling efficiencies. The slant angle of silver nanocolumns can be changed to any angle from as-grown to upright nanocolumns uniformly over large areas by irradiating the grating with a focused Ga ion beam source. The plastic deformation of the nanocolumns causes large change in the

measured diffraction efficiencies and coupling with the incidence light. Electromagnetic numerical simulations reveal tuning of the photonic and plasmonic properties such as diffraction efficiencies and surface plasmon coupling for two different orientation of silver nanocolumns. Video clips for the bending of metallic nanocolumnar rods in real time were obtained from the FESEM, which reveal more details showing the gradual bending of nanocolumns that rise up to an angle that is almost directly proportional to the time of irradiation until they are oriented in a direction parallel to the ion beam direction. The investigated large area reconfiguration of the silver nanocolumns on gratings by ion beam irradiation is very possibly the first demonstration of the method over large scale areas for optical applications.

These results have been published in Jhuma Dutta, S. Anantha Ramakrishna; Nanotechnology **26**, 205301 (2015).

In the sixth chapter, a novel application using superstructures of CTFs to fingerprint visualization was discussed. Visualization of latent fingerprints is enhanced by deposition of CTFs at large oblique angle of CaF_2 and silica SiO_2 on fingerprint marks on two nonporous surfaces such as smooth glass slides and highly reflecting rough aluminium sheets. The vapour flux gets shadowed by the physical residues left behind in the fingerprint and preferentially gets deposited on these residues. The deposited CTFs are highly scattering and results in an enhanced visibility of fingerprint. The fingerprints typically become visible even upon visual inspection when the CTF was deposited on the prints. Microscopic techniques such as dark-field imaging lead to enhanced visibility of the CTF treated fingerprints on the smooth surfaces of glass. For a rough aluminum surface, the dark-field images and bright field images yield almost comparable visibility of the CTF ridges on the substrate due to large scattering from the roughness. The visualization can be further enhanced by treating the deposited CTFs with a fluorescent dye and fluorescence imaging. A specific fluorescent amino-acid reagent (1,2-indanedione+alanine) and non-specific laser dye (Rhodamine 6G) are shown to help to enhance the visualization of the deposited CTFs due to the localization and entrenchment of the dye within the CTF regions.

These results have been published in Jhuma Dutta, S. Anantha Ramakrishna, I. Mekkaoui Alaoui; Forensic Science International **228**, 3237 (2013)

List of Publications

I. Journal Articles

1. *Periodically patterned columnar thin films as blazed diffraction gratings*; **Jhuma Dutta**, S. Anantha Ramakrishna, and Akhlesh Lakhtakia; Applied Physics Letters **102**, 161116 (2013)
2. *Fingerprint visualization enhancement by deposition of columnar thin films and fluorescent dye treatment*; **Jhuma Dutta**, S. Anantha Ramakrishna, and I. Mekkaoui Alaoui; Forensic Science International **228**, 3237 (2013)
3. *Asymmetric coupling and dispersion of surface-plasmon-polariton waves on a periodically patterned anisotropic metal film*; **Jhuma Dutta**, S. Anantha Ramakrishna and Akhlesh Lakhtakia; Journal of Applied Physics **117**, 013102 (2015)
4. *Reconfiguring gratings of slanted plasmonic nanocolumns by ion beam irradiation*; **Jhuma Dutta**, S. Anantha Ramakrishna; Nanotechnology **26**, 205301 (2015)
5. *Characteristics of surface plasmon polariton waves excited on 2D periodically patterned columnar thin film of silver*; **Jhuma Dutta**, S. Anantha Ramakrishna, and Akhlesh Lakhtakia; (submitted)

II. Conference Proceedings

6. *Surface-plasmon-polariton dispersions from metallic columnar thin film deposited on 2D dielectric grating*; **Jhuma Dutta**, S. Anantha Ramakrishna, and Akhlesh Lakhtakia; Photonics 2014: 12th International Conference on Fiber Optics and Photonics © OSA 2014
7. *Asymmetric and symmetric coupling of surface-plasmon-polariton waves to planar interfaces with periodically patterned slanted columnar thin films of silver*; **Jhuma Dutta**, S. Anantha Ramakrishna, and Akhlesh Lakhtakia; Proc. of SPIE Vol. **9502**, 95020R-1 (2015)

To my Parents



Acknowledgments

First of all I would like to express my sincere gratitude to my thesis supervisor, Prof. S. Anantha Ramakrishna for constant guidance, suggestions and encouragement throughout the period of my research work. I believe his constant mentorship made me a better researcher and better scientific writer. Without his continuous support, this thesis would not be the same as presented here.

I would like to give my special thanks to our collaborator Prof. Akhlesh Lakhtakia from Department of Engineering Science and Mechanics, Penn State University, USA who became my informal supervisor. His wide knowledge and logical way of thinking have been of great value for me. His helpful suggestions, valuable advice and personal guidance have provided a good basis for the present thesis.

I would also like to thank my co-supervisor Prof. H. Wanare, for his comments, suggestions and discussions during this research and even writing the thesis.

I would also like to thank Prof. Mekkaoui Alaoui, who helped in doing many experiments of fingerprint visualization.

I sincerely acknowledge our peer review committee member, Prof. R. Vijaya for her valuable suggestions. I must also acknowledge Prof. V. Subrahmanyam, Prof. Sutapa Mukherji and Prof. Avinash Singh for teaching various interesting subjects during my course work.

I am grateful to the members of my research group for their kind help and stimulating interactions. In particular, I would like to thank Dr. Jeyadheepan for helping to build up Oblique Angle Deposition (OAD) chamber and Dr. Prashanta for setting up Laser Interference Lithography and angle resolved transmittance measurement. I would also like to express my sincere thanks to my labmates, in particular, Govind who helped in many experiments, simulations and lot of valuable discussions, Gangadhar for Laser Interference Lithography, Dheeraj, Prince, Raghawendra, Rajesh, Jitendra, Rameshwari, Sriram and other lab mates for their constant support.

I want to thank our Y9 batch, specially Vandana and Pranati who made my stay enjoyable at IITK. I am thankful to Nitul for his help during ion beam irradiation experiments.

I would also like to extend my appreciation to Nanoscience center and Ion beam complex for providing the facility to access Field effect scanning electron microscopy

and Focussed ion beam.

But above all, I am eternally grateful to my parents for their love and continuous support during all these years. Finally love to my brother who had always stood by my side.

Very special thanks to my husband for his patient love and support during my good days and encouragement through my bad ones. I ran all my ideas and results through him and anxiously waited for his criticism as well as appreciation, everything got better after that.

June, 2015

Jhuma Dutta



Contents

List of Publications	xi
1 Introduction	1
1.1 Overview of Columnar thin films	4
1.2 Theoretical Background/General Overview	6
1.2.1 Isotropic and Anisotropic media	6
1.2.2 Diffraction from periodic objects and Blazed gratings	10
1.2.3 Effective media and Homogenization	15
1.2.4 Metamaterials	17
1.2.5 Hyperbolic Media	20
1.2.6 Photonic Bandgap Structures	21
1.2.7 Surface electromagnetic waves	23
1.3 Motivation and scope of thesis	30
2 Fabrication, Characterization and Simulation techniques	33
2.1 Introduction	33
2.2 Nano and Micro fabrication set up	35
2.2.1 Oblique Angle Deposition (OAD)	35
2.2.2 Laser Interference Lithography	43
2.3 Structural characterization	45
2.4 Fabrication of periodically patterned CTFs	46

2.4.1	Substrate pre-patterning	48
2.4.2	Fabrication of periodically patterned dielectric CTFs (PPDCTFs)	49
2.4.3	Fabrication of periodically patterned metallic CTFs (PPMCTFs)	51
2.5	Optical Measurements	54
2.5.1	Measurement of Surface Plasmon Resonances and dispersion	54
2.5.2	Diffraction efficiency measurement	55
2.6	Techniques for Numerical Simulations	56
2.6.1	Limitations of Finite Element Methods	58
3	Periodically patterned dielectric CTFs as blazed diffraction gratings	59
3.1	Introduction	59
3.2	Behaviour of PPCTFs as blazed diffraction gratings	61
3.2.1	Deposition and Structural morphology of the PPCTFs	61
3.2.2	Theory of PPCTF as an anisotropic blazed grating	63
3.2.3	Measurements of Diffraction efficiency of PPCTFs	69
3.3	Discussion and Conclusions	71
4	Asymmetric Coupling and dispersion of SPP Waves on PPMCTFs	73
4.1	Introduction	73
4.2	Asymmetric diffraction of periodically patterned metallic CTFs	76
4.3	SPP Waves on 1D PPMCTFs: incidence in the morphologically significant plane	78
4.3.1	Theory of SPP wave propagation	80
4.3.2	Coupling of p -polarized light to SPP waves	84
4.3.3	Coupling of s -polarized light to SPP waves	87
4.4	Symmetric Coupling and dispersion of SPP Waves for 1D PPMCTFs: incidence in the plane orthogonal to the morphologically significant plane	90
4.5	SPP dispersion on two dimensional (2-D) PPMCTFs	93

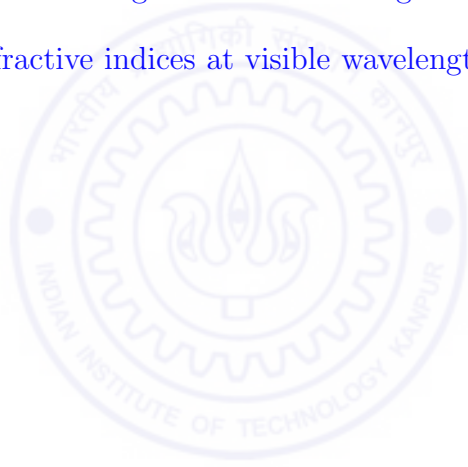
4.6	Analysis of the SPP dispersion on 2-D PPMCTFs	96
4.6.1	Square grating, $\psi = 0^\circ$ (Γ -X)	100
4.6.2	Square grating, $\psi = 45^\circ$ (Γ -M)	102
4.6.3	Square grating, $\psi = 90^\circ$ (Γ -Y)	102
4.6.4	Hexagonal grating, $\psi = 0^\circ$ (Γ -M)	103
4.6.5	Hexagonal grating, $\psi = 30^\circ$ (Γ -K)	105
4.6.6	Hexagonal grating, $\psi = 90^\circ$ (Γ -Y)	105
4.7	Conclusions	105
5	Reconfiguring PPCTFs by Ion Beam Irradiation	109
5.1	Introduction	109
5.2	Bending of slanted Ag nanocolumnar arrays	111
5.2.1	Mechanism of bending	115
5.3	Photonic Properties of the Ag CTF for different Slant Angles	116
5.4	Electromagnetic simulations of slanted nanocolumn gratings	119
5.5	Potential applications	123
5.6	Conclusions	125
6	Fingerprint Visualization Enhancement	127
6.1	Introduction	127
6.2	CTFs deposition on Fingerprint and Fluorescent dye treatment	130
6.2.1	Sample preparation	130
6.2.2	Post-treatment by Fluorescent dyes	131
6.3	Optical Imaging Techniques	132
6.3.1	Observations under white light	132
6.3.2	Bright-field and Dark-field Microscopic Imaging	135
6.4	Fluorescence Spectra and Fluorescence Imaging of Fingerprints	136

6.5	Conclusions	140
7	Conclusions and Future Work	141
7.1	Conclusions	141
7.2	Suggestions for Future Work	143
	Bibliography	155



List of Tables

3.1	Measured and predicted (in parenthesis) diffraction efficiencies ($ T(n2\pi/d)/T_0 ^2$) for unpolarized light diffracted through a PP-CTF with $d = 1125$ nm and $d = 600$ nm.	69
3.2	Measured and predicted (in parenthesis) diffraction efficiencies ($ T(n2\pi/d)/T_0 ^2$) for s and p polarized light diffracted through a PP-CTF with $d = 1125$ nm.	70
3.3	Principal refractive indices at visible wavelengths	70





List of Figures

1.1	Schematic of CTFs growing, with column inclination angle χ with respect to the plane of the substrate. The vapour incidence angle is χ_v . The columns grow along the direction of the unit vector \hat{u}_τ	5
1.2	FESEM image of CTFs made of (a) silicon dioxide (SiO_2) (b) silver (Ag) and (c) indium tin oxide (ITO) on silicon substrates.	6
1.3	The Index ellipsoid for an anisotropic medium; red dotted circle is isotropic sphere, whose refractive index along all directions is n_0 , black tilted ellipsoid signify the anisotropic media, where the refractive index along shorter axis is n_0 and along longer axis is $n_{\text{eff}}(\theta)$; k is the direction of propagation.	7
1.4	Propagation of electromagnetic wave in a uniaxial crystal [28]	9
1.5	Structure of rectangular phase grating	10
1.6	Regular blazed grating (RBG)	12
1.7	Binary blazed grating (BBG)	13
1.8	Schematic picture showing infinitely long wire-array metamaterial of radius r and lattice of periodicity a , that behaves as a low frequency plasma when the electric field of the electromagnetic wave is oriented along the wires.	18
1.9	Isofrequency curves in hyperbolic metamaterials when (a) $\epsilon_{\parallel} = \epsilon_{\perp}$ (b) $\epsilon_{\parallel} < 0$ and $\epsilon_{\perp} > 0$ (c) $\epsilon_{\parallel} > 0$ and $\epsilon_{\perp} < 0$	21

1.10	(a) A chart for operating speed vs critical device dimension (nm) in case of semiconductors (electronics), dielectrics (photonics) and metals (plasmonics) is adapted from M.L.Brongersma and V.M.Shalaev [67]. (b) Schematic picture of the charge oscillations that propagates along the surface of a metal-dielectric interface showing the exponential decay of the electromagnetic fields normal to the surface.	23
1.11	Black and red solid lines are dispersion curves of SPPs at the silver–air and silver–dielectric interfaces respectively. The two light lines, one for air ($\epsilon_1 = 1$) and other for dielectric ($\epsilon_2 = 2.25$) are represented by black and red dashed lines. Black and red dotted lines are asymptotic lines for silver–air and silver–dielectric interfaces respectively.	25
1.12	Prism coupling to SPPs using attenuated total internal reflection in the (a) Kretschmann geometry and (b) Otto geometry.	26
1.13	(a) Phase matching of incident light with SPPs using grating coupled configuration. (b) SPP dispersion curve and coupling by a grating. . . .	27
1.14	Plasmonic band structure, where SPPs are propagating in both positive and negative directions along x - axis. Red solid line in both positive and negative regions, represent the initial SPP dispersion curves at silver-air interface. SPP dispersion curves are translated by $m(2\pi/\Lambda)$ with integer values of m and $\Lambda = 1000$ nm, result in a manifold of SPP dispersions.	28
2.1	(a) Photograph of OAD chamber (b) inside view of the OAD chamber, where source to substrate distance=27 cm, quartz crystal thickness monitor and electron beam evaporator are shown. (c) movable substrate and two steppers motors are shown, where one is for θ rotation and other one is for ϕ rotation.	35
2.2	Schematic representation of the geometry of the OAD system showing the relative placement of the vapor source and the orientation of the substrate. (b) The growth of columns along the direction of incident vapour source, forming an angle β with the substrate normal, less than the incident angle α	38

2.3	Structure zone model, where the transition temperatures between zones I and II and between zones II and III are 0.3 and 0.5 respectively. Figure is reproduced from (Ref. [78])	39
2.4	Plot of two different analytic curves relating the column tilt angle β and the deposition angle α . Solid red line represents tangent rule and black dotted line is according to Tait's rule.	41
2.5	FESEM image of (a) SiO ₂ , CTFs (b) MgF ₂ , zig-zag (chevron) structure (c) MgF ₂ , square spiral structure (d) MgF ₂ , chiral structure (d) SiO ₂ , straight rods.	42
2.6	Transmission through CTFs of CaF ₂ placed between two crossed polarizers as a function of rotation angle of the sample. Red line represents the transmission through plane glass film and black line represent the transmission through CTFs.	43
2.7	(a) Experimental set up of two beam LIL (b) Schematic diagram of LIL with beam splitter BS spatial filter containing lense L and pin hole P arrangement.	44
2.8	Schematic representation of the geometry of shadowing: where a_g is the exposure height, h_g is the seed height, w_g is the seed width and d_s is the inter-seed distance.	46
2.9	Laser interference lithographically patterned photo-resist on a glass substrate, (a) AFM image of one dimensional grating with periodicity 700 nm, (b) FESEM image of two dimensional hexagonal grating with periodicity 800 nm.	48
2.10	Cross-sectional FESEM images comparing aperiodic and periodic OAD SiO ₂ CTFs growth on silicon substrates at a deposition angle of $\chi_v = 10^\circ$ (a) CTFs on planar unpatterned substrate; periodically patterned CTFs deposited on 1D grating (b) with periodicity 600nm and seed width is 300nm, (c) with periodicity 600nm and seed width is 200nm and (d) with periodicity 500nm and seed width is 300nm.	49

2.11 (a), (b) Top view FESEM images of periodically patterned structures on laser machined glass substrate consisting of helical columns of MgF_2 grown by OAD. Width of the hollow region is $\sim 1.5 \mu\text{m}$ with total periodicity $\sim 3 \mu\text{m}$	50
2.12 (a) Top view FESEM image of silver columnar structure by thermal evaporator deposited at a vapor incidence angle of 85° when deposition rate is $3 \pm 0.5 \text{ \AA s}^{-1}$ and (b) cross-sectional FESEM image of silver columnar structure when deposition rate is $11 \pm 0.5 \text{ \AA s}^{-1}$	51
2.13 Cross-sectional FESEM images comparing aperiodic and periodic OAD silver CTFs growth on silicon substrates at a deposition angle of $\chi_v = 4^\circ$ (a) CTFs on planar unpatterned substrate; periodically patterned CTFs deposited on 1D grating (b) with periodicity 500nm and ridge width is 250nm, (c) with periodicity $1 \mu\text{m}$ and ridge width is 500nm, (d) with periodicity 800nm and seed width is 200nm.	52
2.14 Cross-sectional FESEM image of Ag CTFs deposited on a 2-D square grating (a) with periodicity 700nm and seed width is 350nm, (b) with periodicity 500nm and seed width is 250nm.	53
2.15 Schematic of the optical set-up to measure the angle-resolved transmittance spectra for light transmitted through the plasmonic thin films/CTF samples.	55
2.16 The structure of FEM simulation used to model periodic silver nanocolumnar arrays.	57
3.1 (a),(b) Cross-sectional FESEM image of a 1100-nm-thick PP-CTF of CaF_2 deposited on a 1-D photoresist grating of 600-nm period. The prismatic (triangular) air cavities are clearly visible. (c) Asymmetric diffraction through the structure is shown at $\lambda = 532 \text{ nm}$. (d) Top view of the FESEM image showing flaring of nanocolumns. (e) and (f) Asymmetric diffraction through PP-CTF on a 2-D photoresist grating at $\lambda = 473 \text{ nm}$ and $\lambda = 532 \text{ nm}$ respectively.	62

- 3.2 (a) Schematic of the PP-CTF as a blazed grating containing prismatic air cavities with base b , height h , and cavity angle θ_b . The photoresist grating is made of strips of height W and the period is denoted by d . The refractive indices of the different materials are indicated. n_1 , n_2 , n_3 are the principal refractive indices of the columnar structure. (b) A single blazed element convoluted with periodic arrangement of periodic comb function (periodically placed δ -functions). 64
- 3.3 (a), (b), (c), (d) and (e) are calculated diffraction efficiency $|T(k_0 \sin \psi)/T_0|^2$ in transmission vs. diffraction angle ψ for a blazed grating with period $d = 1125$ nm for $\lambda \in [248, 442, 473, 532, 633]$ nm respectively. Diffraction angles (ψ) due to the periodic arrangement are identified by red lines, while the diffraction envelope is a green curve and the diffraction efficiency of each order is represented in black. 68
- 4.1 Top view of FESEM images of PP-CTFs of silver with (a) $d = 500$ nm, (b) $d = 580$ nm, (c) $d = 770$ nm and (d) cross-sectional FESEM image of PP-CTFs of silver with $d = 500$ nm 76
- 4.2 Top row: From left to right, the first three bar diagrams present the measured diffraction efficiencies in the transmission mode for $d = 770$ nm and $\lambda \in \{442, 532, 633\}$ nm for incident p -polarized (black) and incident s -polarized (red) light, and the fourth diagram is for $d = 580$ nm and $\lambda = 532$ nm. Bottom row: Measured diffraction efficiencies in the reflection mode for $d \in \{770, 580\}$ nm and $\lambda \in \{442, 532\}$ nm for incident p -polarized and incident s -polarized light. The inset is a photograph showing asymmetric diffraction for $\lambda = 442$ nm. 77
- 4.3 Schematic showing the (a) corrugated Ag film with normally incident vapor flux and (b) columnar morphology along with the principal axes ($\hat{\tau}, \hat{b}, \hat{n}$) of the CTF while (x, y, z) are the Cartesian coordinates with obliquely incidence vapor flux. Angle of incidence θ with respect to the substrate normal and polarizations p - and s - are shown. 79

- 4.4 (a) Angle-resolved transmittance spectra for corrugated Ag film when the incident light is p - polarized and the period of the grating is 770 nm and thickness of the Ag film is 30 nm, (b) symmetric diffraction through corrugated silver film for $\lambda = 442$ nm, (c) asymmetric diffraction through PPMCTFs for $\lambda = 442$ nm, (d) angle-resolved transmittance spectra for PPMCTFs when the incident light is p - polarized and period of the grating is 770 nm. (e) angle-resolved transmittance spectra for PPMCTFs when the incident light is s - polarized and period of the grating is 770 nm. Different types of SPP coupling in two cases are clearly shown. 79
- 4.5 (a) Real and (b) imaginary parts of $\varepsilon_{a,b,c}$ predicted as functions of the wavelength by the Bruggeman model with ellipsoidal voids ($f_v = 0.88$, $\gamma_\tau^{(m)} = 7$, $\gamma_b^{(m)} = 1.2$, $\gamma_\tau^{(v)} = 10$, and $\gamma_b^{(v)} = 1$); (c) real and (b) imaginary parts of $\varepsilon_{a,b,c}$ predicted as functions of the wavelength by the Bruggeman model with spherical voids ($f_v = 0.91$, $\gamma_\tau^{(m)} = 15$, $\gamma_b^{(m)} = 1.5$, $\gamma_\tau^{(v)} = 1$, and $\gamma_b^{(v)} = 1$); 82
- 4.6 Angle-resolved transmittance spectra when the incident light is p polarized and the period $d =$ (a) 770 nm, (e) 680 nm, (i) 580 nm, and (m) 500 nm; angle-resolved transmittance spectra when the incident light is s polarized and the period $d =$ (b) 770 nm, (f) 680 nm, (j) 580 nm, and (n) 500 nm; theoretical plots for the dispersion of SPP waves obtained using $\tilde{\varepsilon}$ predicted by the Bruggeman model with ellipsoidal voids ($f_v = 0.88$, $\gamma_\tau^{(m)} = 7$, $\gamma_b^{(m)} = 1.2$, $\gamma_\tau^{(v)} = 10$, and $\gamma_b^{(v)} = 1$) when the period $d =$ (c) 770 nm, (g) 680 nm, (k) 580 nm, and (o) 500 nm; and theoretical plots for the dispersion of SPP waves obtained using $\tilde{\varepsilon}$ predicted by the Bruggeman model with spherical voids ($f_v = 0.91$, $\gamma_\tau^{(m)} = 15$, $\gamma_b^{(m)} = 1.5$, $\gamma_\tau^{(v)} = 1$, and $\gamma_b^{(v)} = 1$) when the period $d =$ (d) 770 nm, (h) 680 nm, (l) 580 nm, and (p) 500 nm. The theoretical predictions for the CTF/photoresist interface are solid lines, while those for the CTF/air interface are dashed lines. The orders $n = \pm 1$ and ± 2 for Bragg scattering are indicated. 85
- 4.7 Propagation length for SPP waves with spherical voids. 86

- 4.8 Simulated transmittance spectra for the structure with period $d \in \{770, 680, 580, 500\}$ nm when s -polarized light is incident at $\theta = 5^\circ$. Red and blue solid-line arrows correspond to SPP waves guided by the CTF/air interface with $n = -1$ and $n = +1$ orders, respectively; black and green solid-line arrows correspond to SPP waves guided by the CTF/photoresist interface with $n = -1$ and $n = +1$ orders, respectively; and black and green dotted-line arrows correspond to SPP waves guided by CTF/photoresist interface with $n = -2$ and $n = +2$ orders, respectively. 87
- 4.9 Simulated distributions of (a) E_x , (b) E_y , and (c) E_z in the structure with period $d = 580$ nm illuminated by s -polarized light of free-space wavelength 650 nm incident at $\theta = 5^\circ$. The incident plane wave of the form $\exp(-i\omega t)$ was assumed and the shown fields are in phase with the incident wave. Lengths of the major and two minor axes of the ellipsoids are 520 nm and 90 nm, respectively with a 100-nm-thick photoresist film on a glass substrate. 88
- 4.10 (a) Schematic of a PP-CTF, when the plane of incidence coincides with the morphologically significant plane i.e the xz plane. (b) Schematic of a PP-CTF illuminated obliquely either a p -polarized or an s -polarized plane wave. The morphologically significant plane of the PP-CTF is designated as the xz plane and the plane of incidence as the yz plane (i.e., $\psi = 90^\circ$). Both positive and negative values of the angle of incidence θ are indicated. 91
- 4.11 SPP dispersion plots when incident plane wave is orthogonal to the morphologically significant plane; when the incident light is p polarized and the period $d =$ (a) 770 nm, (d) 580 nm, and (g) 500 nm; angle-resolved transmittance spectra when the incident light is s polarized and the period $d =$ (b) 770 nm, (e) 580 nm, and (h) 500 nm; theoretical plots for the dispersion of SPP waves obtained using $\tilde{\epsilon}$ predicted by the Bruggeman model with ellipsoidal voids ($f_v = 0.88$, $\gamma_\tau^{(m)} = 7$, $\gamma_b^{(m)} = 1.2$, $\gamma_\tau^{(v)} = 10$, and $\gamma_b^{(v)} = 1$) when the period $d =$ (c) 770 nm, (g) 680 nm, (k) 580 nm, and (o) 500 nm; The theoretical predictions for the CTF/photoresist interface are black solid lines, while those for the CTF/air interface are red solid lines. The orders $n = \pm 1$ and ± 2 for Bragg scattering are indicated as 1^{st} and 2^{nd} order. 92

- 4.12 Schematics of (a) symmetry directions for 2D square and (b) hexagonal lattices in reciprocal space, which is important for the understanding of the in-plane momentum-matching condition for coupling of the incident light to an SPP wave. (c) Schematic of a periodically patterned CTF of silver with the xz plane as its morphologically significant plane [1, 136]. Also shown is the component $k_0 \sin \theta$ of the wave vector of the incident light in the xy plane, where θ is the angle of incidence with respect to the z axis. This in-plane component is split into components $k_0 \sin \theta \cos \psi$ along the x axis and $k_0 \sin \theta \sin \psi$ along the y axis. 93
- 4.13 FESEM images of a PP-CTFs of silver on a square grating ($d = 580$ nm). The morphologically significant plane is the xz plane. Light is incident either (a) in the xz plane, i.e., $\psi = 0^\circ$, or (b) in the yz plane, i.e., $\psi = 90^\circ$. The positive and negative values of θ shown are needed to understand the asymmetry of the data in Figs. 4.15 and 4.16. 94
- 4.14 Photographs of asymmetric diffraction of normally incident p -polarized light by a CTF deposited on either (a,b) the square grating or (c,d) the hexagonal grating for either (a,c) $\lambda = 442$ nm or (b,d) $\lambda = 532$ nm. 94
- 4.15 Measured specular transmittance of the silver CTF deposited on the square grating for (a) $\psi = 0^\circ$ (Γ -X), (b) $\psi = 45^\circ$ (Γ -M), and (c) $\psi = 90^\circ$ (Γ -Y), when the incident light is p polarized. Corresponding solutions of Eq. (4.18) for (d) $\psi = 0^\circ$ (Γ -X), (e) $\psi = 45^\circ$ (Γ -M), and (f) $\psi = 90^\circ$ (Γ -Y), with dotted curves representing the SPP waves bound tightly to the CTF/air interface and solid curves representing the SPP waves bound tightly to the CTF/photoresist interface. 101
- 4.16 Measured specular transmittance of the silver CTF deposited on the hexagonal grating for (a) $\psi = 0^\circ$ (Γ -M), (b) $\psi = 30^\circ$ (Γ -K), and (c) $\psi = 90^\circ$ (Γ -Y), when the incident light is p polarized. Corresponding solutions of Eq. (4.19) for (d) $\psi = 0^\circ$ (Γ -M), (e) $\psi = 30^\circ$ (Γ -K), and (f) $\psi = 90^\circ$ (Γ -Y), with dotted curves representing the SPP waves bound tightly to the CTF/air interface and solid curves representing the SPP waves bound tightly to the CTF/photoresist interface. 104

- 5.1 Schematic diagram showing (a) the direction of the ion beam at an angle of 52° and the bending direction of nanocolumns with respect to the substrate normal. (b) incident plane wave direction : $+\theta$ is the angle when the incident wave vector is mostly along the nanocolumnar axis and $-\theta$ is the angle when the incident wave vector has large perpendicular component to the columnar axis, α is the slant angle/orientation angle that Ag nanocolumn makes with z axis (substrate normal) and polarization of the incident plane wave is shown when direction E field is in the morphologically significant (xz) plane. 112
- 5.2 (a) Top view and (b) cross-sectional view of FESEM images showing periodically patterned array (periodicity = 500 nm) of Ag nanocolumns, nanocolumn dimensions are 520nm (length) \times 80nm (diameter) with orientation angle of 80° with respect to the substrate normal. (c) ion beam irradiation on an area of $5\ \mu\text{m} \times 5\ \mu\text{m}$ for exposure time of 10 s (d) for 20 s by 30 keV Ga ion beam and 0.3 nA beam current. 113
- 5.3 FESEM images showing (a) the same structure as mentioned above imaged with higher magnification. (b) ion beam irradiation on an area of $3\ \mu\text{m} \times 3\ \mu\text{m}$ for exposure time of 10 s (c) for 20 s by 30 keV Ga ion beam and 0.3 nA beam current. Dotted thin lines delineate the irradiated area. 114
- 5.4 Schematic representation of the temperature gradient and thermal stress developed in the nanocolumn leading to its bending. 115
- 5.5 (a) FESEM image of periodically patterned array (periodicity = 600 nm) of Ag nanocolumns, nanocolumn dimensions are 520 nm (length) \times 80 nm (diameter) with orientation angle of (a) 80° with respect to the substrate normal, (b) and (c) are optical images of transmitted diffraction spots showing asymmetric diffraction at $\lambda = 442\ \text{nm}$ and at $\lambda = 532\ \text{nm}$ respectively, 0, +1 and -1 diffraction orders are mentioned below. The table shows the measured diffraction efficiencies in the transmission mode for the sample on fused silica substrate (a) at $\lambda \in \{442, 532\}\ \text{nm}$ for incident p -polarized light. 117

5.6	(a) Scanning ion microscopy images of periodically patterned array (periodicity = 500 nm) of Ag nanocolumns, nanocolumn dimensions are 520 nm (length) \times 80 nm (diameter) with orientation angle of (a) 80° and (b) 0° with respect to the substrate normal, (c) optical images of diffraction spots showing asymmetric diffraction at $\lambda = 442$ nm before irradiation, (d) symmetric diffraction after irradiation for the region shown in (b), 0, +1 and -1 diffraction orders with measured diffraction efficiencies in the reflection mode for the sample for incident p -polarized light.	118
5.7	Calculated transmission and reflection from gratings of slanted nanocolumns: (a), (b) Angle dependent transmittance for 0, T_{-1} and T_{+1} diffraction order for the nanocolumn orientation angle of 80° and 40° and (c), (d) Angle dependent reflectance for 0, T_{-1} and T_{+1} diffraction order for the nanocolumn orientation angle of 80° and 40°. Wavelength of the incidence light is 442 nm	120
5.8	Transmittance spectra as a function of angle of incidence with slant angle of 40° and periodicity 600 nm with three different intercolumn separation such as (a) 5 nm, (b) 10 nm and (c) 15 nm along y direction.	120
5.9	FEM simulations of electric fields $ E_x $, $ E_y $, $ E_z $ distributions of standing waves pattern modes or Fabry perot modes in Ag nanocolumns array illuminated by p-polarized light of free-space wavelength 442 nm incident at $\theta = 0^\circ$ with period $d = 600$ nm when the nanocolumns makes an angle of (a), (b), (c) 80° (d), (e), (f) 40° with the substrate normal. Lengths of major and two minor axes of the ellipsoid are 520 nm and 80 nm respectively.	122
6.1	Schematic of CTF deposition on different regions of fingerprint ridges by oblique incident vapor flux.	129

- 6.2 (a) Fingerprint on a highly reflecting aluminum sheet with (left side) and without (right side) CTF deposition, whitish marks on the substrate in the left side is clearly visible under room light conditions. (b) Fingerprint with deposited CTF (left side) and plain fingerprint (right side) on microscopic glass slide, observed under the white light, incident obliquely on the surfaces. (c) Fingerprint with deposited CTF (left side) and plain fingerprint (right side) on rough aluminum sheet, observed under the white light, incident obliquely on the surfaces. 133
- 6.3 Fingerprint marks (a) with and (b) without the deposited CTF (evaporant material, SiO_2) on glass slide were viewed using optical microscope in reflection mode under bright field conditions with $5\times$ magnification. Fingerprint marks (c) with and (d) without the deposited CTF (evaporant material, SiO_2) on microscopic glass slide were viewed using optical microscope in reflection mode under dark field conditions with $5\times$ magnification. 134
- 6.4 Fingerprint marks (a) with and (b) without the deposited CTF (evaporant material, SiO_2) on reflecting aluminum sheet were viewed using optical microscope in reflection mode under bright field conditions with $5\times$ magnification. Fingerprint marks (c) with and (d) without the deposited CTF (evaporant material, SiO_2) on reflecting aluminum sheet were viewed using optical microscope in reflection mode under dark field conditions with $5\times$ magnification. 135
- 6.5 (a) Fluorescence spectra obtained from neat solutions of Rhodamine 6G and 1,2-indanedione + alanine when excited with 442 nm blue laser and a long pass filter with a cut off of 480 nm. (b) Spectra of fluorescence obtained from fingermarks on various surfaces and treated with 1,2-indanedione: paper (solid line), CaF_2 CTF deposited on aluminum sheet (... line) and glass slide (line). The blue excitation light had a peak wavelength of $\lambda = 488$ nm and green excitation had a peak wavelength of $\lambda = 542$ nm. 137

6.6	Fluorescence microscope images dye treated fingerprints and CTF deposited on fingerprint marks viewed under blue light excitation in a fluorescence microscope. Top row panels are for Rhodamine 6G treated fingerprint marks, while the bottom row panels are for alanine + 1,2-indanedione treated substrates. From left to right, the four panels in each row respectively correspond to CTF deposited fingerprint marks on aluminum substrate, plain fingerprint on rough aluminium substrate, CTF deposited finger mark on glass substrate and plain fingermark on smooth glass substrate.	137
6.7	Fluorescence images of fingermarks detected by illuminating with a 532 nm laser and detecting the fluorescence through a 532 nm notch filter. Panels (a) and (b) are the fluorescence images fingerprint marks with SiO ₂ CTF and Rhodamine 6G treatment on a rough aluminum sheet and a glass slide respectively. Panels (c) and (d) are the fluorescence images fingerprint marks with SiO ₂ CTF and alanine + 1,2-indanedione treatment on a rough aluminium sheet and a glass slide respectively. The green background in panel (c) is due to the strong reflected laser light from the rough aluminium surface leaking through the notch filter, which is almost as bright as the fluorescence.	138
7.1	SPP Coupler	144
7.2	(a) Cross-sectional FESEM image of ITO columnar structure, (b) ITO columnar structure interpenetrated with P3HT : PCBM active layer and (c) J-V plot of OPVDs of ITO columnar structure and planar ITO substrate	145

Chapter 1

Introduction

Thin film technologies have attracted tremendous attention due to their applications in various fields such as microelectronics, optics, magnetic, hard and corrosion resistant coatings, energy generation and micro-mechanics. Exploring new optical properties of nanostructured thin films is a major focus of nanotechnology research for future applications. This is motivated by the enhanced properties of the nanostructured materials in various fields as optical, electrical, magnetic, catalytic applications etc. The enhanced properties are of great interest not only from an applied perspective but also from a fundamental point of view. Modern techniques have given us the unprecedented ability to control and fabricate accurately these structures at the nanometer length scales. The capability to obtain large ordered arrays of well defined and periodic nanostructures in accurate, reproducible, fast and inexpensive manner is a central issue for the miniaturization, multifunctionality, manufacturability and operational speed required in such systems.

The invention of the oblique angle deposition (OAD) technique enabled the fabrication of nanostructured thin films with highly tailorable anisotropic optical, electrical, and magnetic properties [1]. Based on the growth conditions and deposition parameters, a precise control of the nanostructure in terms of the morphology, the porosity and the crystal structure is controlled to improve the properties of engineered nanostructured materials. Over the years, the OAD technique is the method of choice, because it is inexpensive and scalable method for the growth of nanostructured columnar thin

films (CTFs).

In the OAD technique, essentially, a substrate is held at a large oblique angle with respect to the incoming collimated vapor flux. As the vapor atoms condense and nucleate on the substrate, the subsequent vapor atoms can not reach in the shadowed regions behind the nucleated sites and land on the previously nucleated adatoms/islands, resulting in the evolution of a columnar morphology. The ideal morphology of CTFs consists of almost identical, straight and parallel nanowires of elliptical cross-section with extremely anisotropic properties. When light is incident on the anisotropic CTFs media, it experiences linear birefringence, and hence the CTFs can be used as linear polarizers, filters, quarter wave plates and other polarizing components etc. [2]. By rotating the substrate about an axis normal to the surface, three dimensional sculpturing of the columnar morphology can be achieved during deposition. Under suitable conditions such as fixed values of angles of the deposition rates, combined with substrate rotation, chiral structures with fixed pitch comparable or smaller than the wavelength of light can be flexibly grown [3]. When linearly polarized light interacts with a helical or chiral sculptured thin films (CSTFs) while propagating along the helical axis, the transmitted light exhibits a rotation of the plane of polarization analogous to that in cholesteric liquid crystals and the phenomenon is called optical rotatory dispersion [4]. CSTFs also exhibit circular Bragg phenomenon in a narrow wavelength regime, where incident right circularly polarized (RCP) light is preferentially transmitted and incident left circularly polarized (LCP) light is preferentially reflected, by a structurally left handed chiral structure in the Bragg regime [5]. The structural anisotropy and chirality attainable with STFs can be very large compared to that obtainable with liquid crystals of similar molecular media. The optical property of a helical thin film like chiral sculptured thin film or thin birefringent films arranged in a helix predominantly depends on the pitch of the helix with respect to the wavelength of light propagating along the helical axis. For example, for high pitch value, the medium is a retarder (Mauguin limit), for low pitch it is a rotator (de Vries limit) and for comparable value Bragg reflector. In other words, the optical properties of helical structure depends on

two parameters β and γ . Where, β = the twist per unit length of the helix and γ = half of the local phase retardation per unit length, i.e. $\gamma = \pi \Delta n / \lambda$, where Δn is the layer birefringence of the medium. (i) In case $\beta \gg \gamma$, the medium behaves as a rotator or known as de-Vries limit, (ii) In case $\beta \ll \gamma$, the medium acts as a guided linear retarder or Mauguin limit, and (iii) $\beta \approx \gamma$, the medium behaves as a Bragg reflector.

CTFs fabricated by OAD are random porous nanostructures that have properties due to the columnar morphology that are not normally present in the materials they are composed of. The new properties principally are consequences of the structure. Periodic structures in photonics facilitate a far-reaching control of light propagation and light-matter interaction compared to homogeneous media. The columnar structure fabricated by OAD has column diameters much smaller than the wavelength of interest, and hence quasi-static effective medium theory can be used to model and understand the optical properties [6]. Periodicity gives yet another control parameter: in integrated optical devices, periodic structures make possible many applications such as bandstop filters, input-output couplers, modulators, distributed feedback lasers and directional couplers etc. [7]. The primary focus of this thesis is on the basic physical principles and potential applications associated with the existence of Bragg diffraction from periodic structures, plasmonic effects in metallic nanostructures and engineered effective medium properties in periodic dielectric and metallo-dielectric columnar nanostructured systems. The nanostructure with OAD gives novel effective medium properties, while the periodicity at wavelength scale will involve Bragg scattering and generation and interaction of specific optical modes. The extremely anisotropic optical properties offered by the nanocolumnar structure with larger scale structures for photonic bandgap or diffractive effects provide for new physical phenomena.

Periodically patterned columnar thin films (PP-CTFs) are fabricated by combining two experimental techniques. First LIL was used for creating one and two dimensional gratings which were used as a seed layer; second e-beam evaporation for depositing dielectric and metals on the gratings by the OAD method. LIL is a flexible nanostructuring method to inexpensively create large scale array of periodic submi-

chrometer structures (wavelength scale) based on recording interference pattern. When the collimated vapour flux arrives at highly oblique angles to the pre-seeded surface, due to self-shadowing, only the ridges of the gratings are exposed to the collimated flux, which leads to almost no deposition in the shadowed regions (valleys) and hence PP-CTFs are formed. In the next Sections, we have given an overview of the CTFs and the theoretical background, which will help in understanding the motivation and scope of this thesis.

1.1 Overview of Columnar thin films

The growth of CTFs by OAD was actually first reported by Kundt in 1885 [1]. CTFs are nanostructured thin films with extremely anisotropic properties fabricated by using physical vapor deposition (PVD) [1]. They consist of parallel arrays of columnar nanowires, which can be grown on a substrate by directing the vapor flux at a small angle of χ_v with respect to the plane of the substrate. The almost parallel columns are oriented at an angle of $\chi \geq \chi_v$ as shown in the schematic 1.1. \hat{u}_n and \hat{u}_b are the unit vectors along the two short axes and \hat{u}_τ is the unit vector along the longer axis of the columns. The vapour incidence angle (χ_v) is related to the column inclination angle (χ) by an empirical tangent rule of Nieuwenhuizen and Haanstra [8], $\tan \chi = 2 \tan \chi_v$. Due to the nanostructured nature and the anisotropic structure, CTFs can be treated as effectively biaxial anisotropic media, when illuminated by light of wavelength much larger than the columnar diameters and the intercolumnar distance. Such a homogenized medium can be characterized by three principal refractive indices and the orientations of the two optical axes. During fabrication of columnar arrays using the OAD method, these five variables can be changed throughout the time of deposition, even continuously. Details of the deposition method, and the columnar growth mechanism are explained in Chapter 2. The macroscopic optical properties and the nanostructural porosity of the CTF can be tailored by controlling the vapour deposition parameters.

Due to their biaxial ortho-rhombic nature, CTFs show novel optical proper-

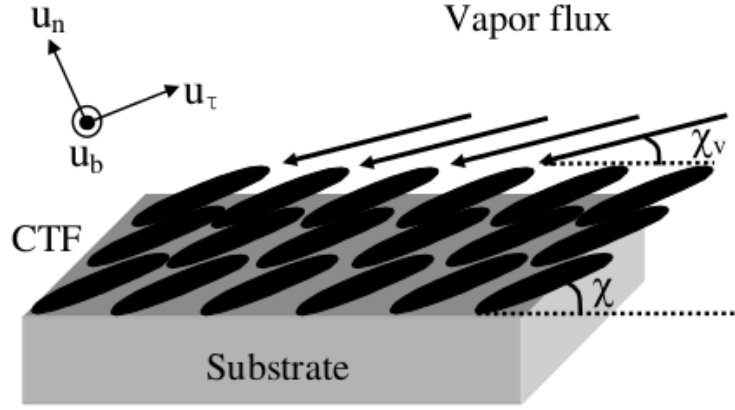


Figure 1.1: Schematic of CTFs growing, with column inclination angle χ with respect to the plane of the substrate. The vapour incidence angle is χ_v . The columns grow along the direction of the unit vector \hat{u}_τ .

ties such as anomalous optical dispersion, extreme birefringence, and strong dichroism [9–11] at visible and infrared wavelengths. CTFs are highly porous material and are promising candidates for sensing applications such as chemical and biological sensors [12] with optical interrogation. Different types of surface modes such as surface plasmon polariton (SPP) waves [13], Tamm waves [14], Dyakonov waves [15] and Dyakonov-Tamm waves [16] are possible at the interfaces between CTF anisotropic media and isotropic media. For a CTF whose porous spaces are infiltrated by a fluid, the phase speed and the propagation length of SPP are very sensitive to the refractive index ‘ n ’ of the fluid infiltrated the CTF’s void regions and so anisotropic CTF media can be used as SPP based sensors [17]. Due to the structural porosity, the refractive index of CTFs are typically found to be very low (refractive index close to air), and hence attractive for use as anti-reflective coatings [18]. As other examples, the optical dielectric tensor of obliquely evaporated nickel film have been measured using the excitation of surface plasmons [19]. The anisotropic optical dielectric functions of cobalt slanted columnar thin film were determined in the THz frequency range using generalized spectroscopic ellipsometry [20]. Anisotropic V_2O_5 CTFs transformed into VO_2 CTFs after annealing at $550^\circ\text{C}/3$ min and exhibit superior thermochromic properties [21].

Growth as slanted CTFs are possible for different kinds of materials involving

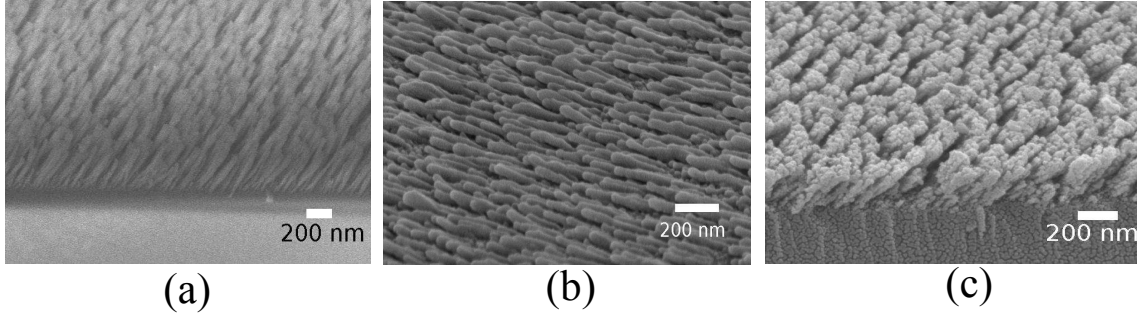


Figure 1.2: FESEM image of CTFs made of (a) silicon dioxide (SiO_2) (b) silver (Ag) and (c) indium tin oxide (ITO) on silicon substrates.

metallic, dielectric and semiconducting materials. Field effect scanning electron microscopy (FESEM) images of some CTFs of a few materials are shown in Fig. 1.2. Fig 1.2 (a) shows the FESEM image of a CTF of silica (SiO_2), which can be used for broadband antireflection coating application [18]. Fig. 1.2(b) shows CTFs of silver, which can be used as SPP biosensors [17], Surface enhanced raman spectroscopy (SERS) substrates [22] and fluorescence enhancement structure [23]. Fig. 1.2(c) shows CTFs made of indium tin oxide (ITO) (post annealing in oxygen), which can be used for many applications as birefringent and transparent conducting electrode. The structural ITO electrode due to its high surface area it shows an increased current density and hence increase the efficiency of solar cells [24, 25] for which it is used as an electrode. The optical scattering properties of such a structured electrode also pose no impediments [26]

1.2 Theoretical Background/General Overview

1.2.1 Isotropic and Anisotropic media

Here we consider light in homogeneous isotropic and anisotropic media. By homogeneous we imply that the dielectric permittivity and other material properties are position independent inside the medium. By anisotropy, it is implied that the dielectric permittivity and other material properties are direction dependent. In anisotropic

optical media, the polarization of the medium becomes direction dependent in contrast to isotropic media. Anisotropic media can be described in terms of dielectric tensor and in the principal co-ordinate frame (x, y, z) , the dielectric tensor can be written as [27],

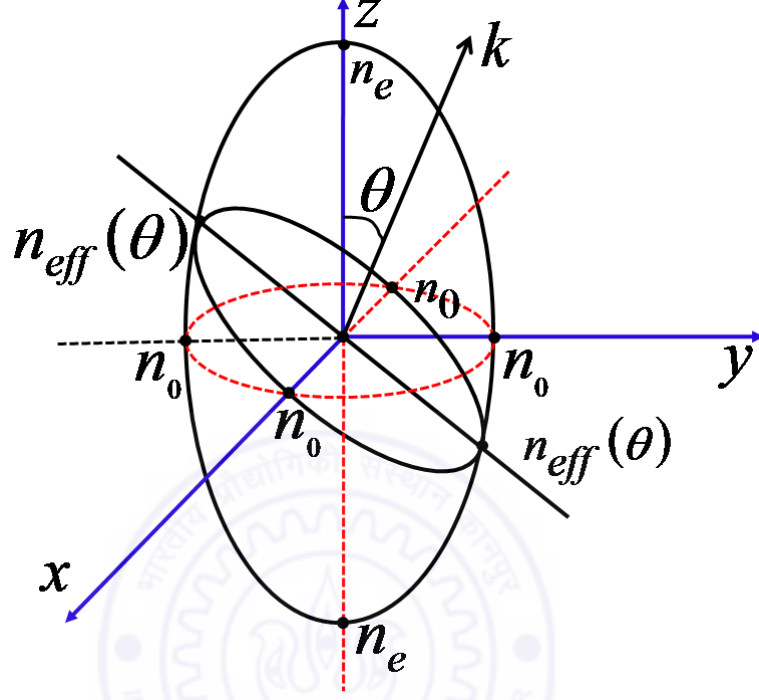


Figure 1.3: The Index ellipsoid for an anisotropic medium; red dotted circle is isotropic sphere, whose refractive index along all directions is n_0 , black tilted ellipsoid signify the anisotropic media, where the refractive index along shorter axis is n_0 and along longer axis is $n_{\text{eff}}(\theta)$; k is the direction of propagation.

$$\hat{\epsilon} \equiv \begin{pmatrix} \epsilon_x & 0 & 0 \\ 0 & \epsilon_y & 0 \\ 0 & 0 & \epsilon_z \end{pmatrix}, \quad (1.1)$$

where ϵ_x , ϵ_y , ϵ_z are relative permittivities of the medium. Here $\epsilon_{x,y,z}$ can be position dependent in an inhomogenous medium. Relative permittivities and principal indices of refraction are related by the relation $\mu\epsilon_i = n_i^2$, $i=x, y, z$, where the principal indices of refraction along three axes are n_x , n_y and n_z and $\mu = 1$ for a non-magnetic medium. Anisotropic media can be uniaxially or biaxially anisotropic. In uniaxially anisotropic media, any two of the principal indices of refraction are equal, whereas for biaxially anisotropic media, $n_x \neq n_y \neq n_z$. If all three principal indices of refraction are equal, the medium is optically isotropic. The optical properties of anisotropic

materials depend on the direction of propagation and the polarization of the incident electromagnetic wave.

Few examples of naturally occurring anisotropic materials are crystals such as calcite, quartz, Potassium Dihydrogen Phosphate (KDP) and many kinds of liquid crystals. Columnar thin film structures also behave as anisotropic media, but these are artificially made. Since the column diameter of the CTFs range from 10-100nm due to OAD, therefore these films are considered as effectively homogeneous orthorhombic biaxial media at visible and infrared regimes [1]. All These materials exhibit many peculiar optical phenomenon including double refraction, optical rotation, electro-optical and acusto-optical effects etc. In double refraction, an unpolarized incident beam of light gets refracted at the surface of a birefringent material and splits into two beams of light with different polarizations [28]. One of the beam is labelled as ordinary ray (n_o) which obey Snell's law and the other is labelled as extraordinary ray (n_e) obey Snell's law under the condition that the component of k (wave vector) parallel to the interface is unchanged. However, the power flow will be deflected in a non-Snell direction due to the non-collinearity of the phase vector and the power flow. Many optical devices are made of anisotropic materials such as birefringent filters and sheet polarizers etc.

Propagation of electromagnetic wave in an anisotropic media is different from that in an isotropic media. In isotropic media, the polarization \vec{P} of the media and the electric displacement vector \vec{D} are parallel to the applied electric field \vec{E} direction. In anisotropic media, \vec{P} and \vec{D} are no longer parallel to \vec{E} [28], instead two distinct linear polarizations, specified by the direction of \vec{D} , can exist for the wave. The orientation of \vec{D} and the relative magnitudes of refractive indices in a crystal can be understood in terms of the index ellipsoid, also called *optical indicatrix*. The index ellipsoid is shown in Fig. 1.3. The effective refractive index n_{eff} for a wave travelling along the direction \vec{k} at an angle θ to the z axis (principal axis) is given by [28],

$$n_{\text{eff}}^2(\theta) = n_o^2, \\ n_{\text{eff}}^2(\theta) = \frac{n_o^2 n_e^2}{\sqrt{(n_o^2 \cos^2 \theta + n_e^2 \sin^2 \theta)}}, \quad (1.2)$$

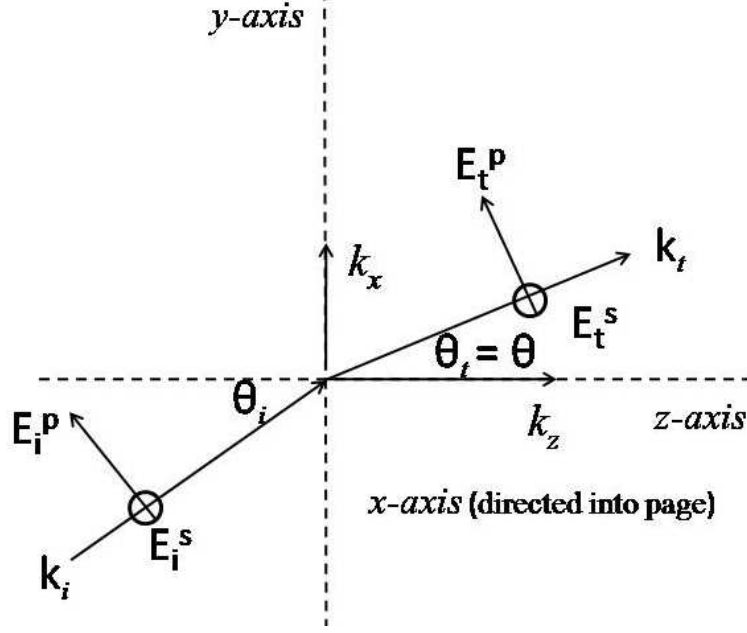


Figure 1.4: Propagation of electromagnetic wave in a uniaxial crystal [28]

where n_0 and n_e are the ordinary and extraordinary refractive indices; θ is the angle between the direction of propagation k and the optical axis. The index in the first equation corresponds to the electric field component which points in the x -direction, never notices the index n_e associated with excitation of the crystal lattice in the z -dimension, regardless of θ . The x field component is associated with the ordinary wave as that of an isotropic medium, the index is independent of θ . The second index corresponds to the electric field component contained in the $y - z$ plane, which vary with θ . Since in the second case, the component of the electric field is directed partly along the optic axis, hence it is called the extraordinary wave.

Consider an electromagnetic wave that propagates in the $y - z$ plane, making an angle θ with the z axis as shown in Fig. 1.4. Let us assume that the index outside the crystal is $n = 1$, Snell's law may be represented as,

$$\sin \theta_i = n \sin \theta_t \quad (1.3)$$

where θ_i is the angle of incidence, n is the refractive index inside the crystal and θ_t is the transmitted angle. For s polarization which corresponds to ordinary wave, the θ_t

can be calculated as

$$\sin \theta_t = \frac{\sin \theta_i}{n}. \quad (1.4)$$

For p polarization where n is a function of θ_t , the transmitted angle can be calculated as,

$$\tan \theta_t = \frac{n_e \sin \theta_i}{n_0 \sqrt{n_e^2 - \sin^2 \theta_i}}. \quad (1.5)$$

Thus s and p polarized light (i) refract into the crystal at two different angles, (ii) they travel at two different velocities and (iii) they have two different wavelengths in the crystal.

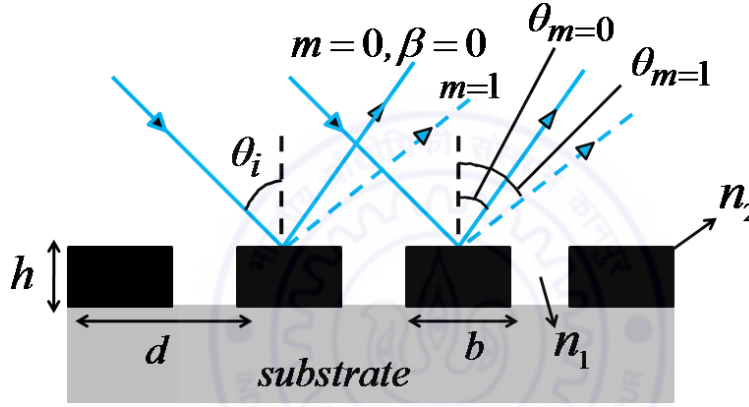


Figure 1.5: Structure of rectangular phase grating

1.2.2 Diffraction from periodic objects and Blazed gratings

A diffraction grating is typically a periodic dielectric structure which imposes a periodic variation in amplitude and/or phase on an incident light front. One of the traditional applications arise in grating spectrometers. A schematic picture of the structure of a rectangular one dimensional grating is shown in the Fig. 1.5, where d is the periodicity of the grating, b is the width of the rectangle, h is the height of each rectangle, n_1 is the refractive index of air and n_2 is the refractive index of the dielectric material. The diffraction from gratings can be characterized by the transmission function of the grating, and the diffracted intensity for such gratings is estimated in the Fraunhofer limit by taking the Fourier transform of the corresponding transmission function [27].

The diffraction efficiency of a grating is typically defined as the ratio of the intensity of the diffracted order to that of the intensity of the incident light. The grating equation relates the direction of the diffracted modes to the period and is given by [27–29],

$$d(\sin \theta_i + \sin \theta_m) = m\lambda; \quad m = 0, \pm 1, \pm 2, \dots, \quad (1.6)$$

where θ_i is the angle of incidence, θ_m is the angle of diffraction and m is the order of diffraction. For a particular incident angle θ_i , the direction θ_m of each principal maximum varies with the wavelength. Periodic objects can only transfer integral bragg momenta to the incident waves to obtain the scattered waves that interfere constructively along specific directions. For normal incidence and a fixed value of d , the maximum order of diffraction is given by $m = \lfloor \frac{d \sin \theta_m}{\lambda} \rfloor$. The resolving power of a grating for a given order is defined as $R = mN$. Thus, for a given order of diffraction, the resolving power increases with the total number of grating lines N involved in the diffraction. Increase in the number of grating lines increases the light energy throughput into a specific order [29]. The rectangular grating made of transparent medium as shown in Fig. 1.6 can be treated as phase grating if the height of the grating $h < \frac{\lambda}{2}$ and scattering from the grating due to incident wave should not be too strong and resonant. The transfer function of the rectangular grating is given by the phase shift in transmission across the grating

$$T(x) = \begin{cases} \exp(ik_0 h n_1), & 0 < x < b, \\ \exp(ik_0 h n_2), & b < x < d. \end{cases}$$

where k_0 is the wave vector in free-space.

Blazed gratings

As there is no dispersion in the zeroth order diffraction principal maximum, this represents a waste of light energy and results in reduced grating efficiency. The technique of

shaping individual grating elements, so that the diffraction envelope maximum shifts into another order is called *blazing* the grating. A blazed grating can diffract much of the incident energy to a specified non-specular reflected and/or transmitted order on one side of the zeroth (specular) order. The zeroth order usually contains most intense interference intensity ($m = 0$) as it coincides with the maximum of the single slit diffraction envelope ($\beta = 0$) [27] as shown in Fig. 1.5. $\beta = 0$ implies the condition where the far field path difference between the rays from the center and from any edge of the grating element is zero. By introducing prismatic elements, the corresponding zero path difference is shifted to the direction of refracted beam or the reflected beam which now correspond to the case of $\beta = 0$, whereas the interference maxima remain fixed in position and their positions are determined by the grating equation given in Eq. 1.6 itself. Thus diffraction by a blazed grating combines refraction and diffraction. Prismatic elements in a periodic grating as shown in Fig. 1.6 introduce a phase shift

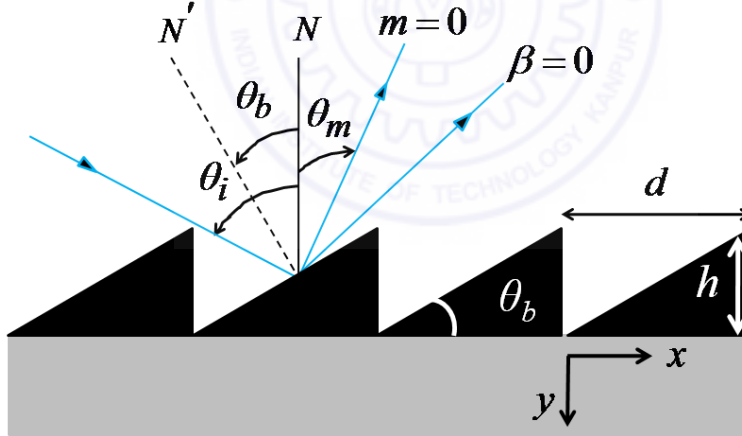


Figure 1.6: Regular blazed grating (RBG)

into the transmitted light. Let us consider the transmission function of the grating is $T(x)$ and has a periodic linear phase shift. The far field diffraction pattern is the fourier transform of the transmission function $T(x)$ and can be expressed as,

$$F(k) = \int_{-\infty}^{\infty} T(x) e^{ikx} dx. \quad (1.7)$$

A periodic shift in the real space is a shift of origin in the Fourier space, which can be expressed as,

$$\int_{-\infty}^{\infty} T(x) e^{-ik_0 x} e^{ikx} dx = F(k - k_0). \quad (1.8)$$

Two kinds of blazed gratings are popular, one is regular blazed grating (RBG) with triangular or prismatically shaped elements and the other one is a binary blazed grating (BBG). RBG has typically periodic sawtooth shaped modulation on the surface and a schematic of RBG is shown in Fig. 1.6. Here d is the periodicity of the grating, h is the height of each sawtooth, n is the refractive index of the material and θ_b is the blaze angle. A beam is incident at an angle of θ_i and diffracted at an angle of θ_m measured from the normal, where N is the normal to the grating surface and N' is the normal to the grating element facets. According to the law of reflection, angle of incidence is equal to the angle of reflection w.r.t N' and hence $\theta_i - \theta_b = \theta_m + \theta_b$. Putting this relation into Eq. 1.6, we get

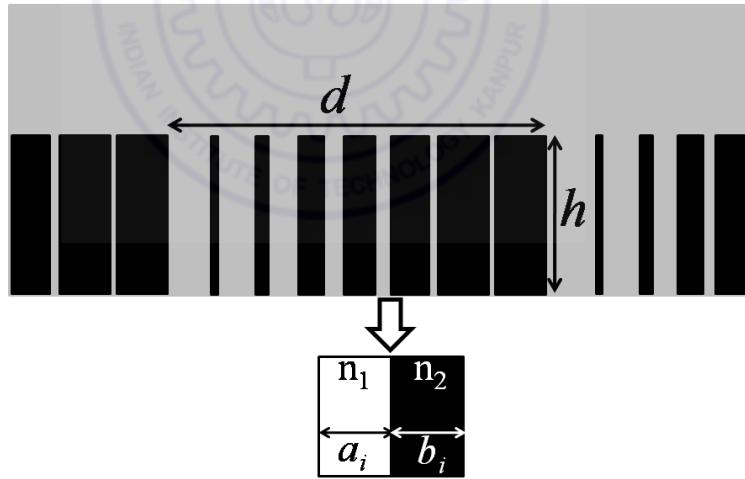


Figure 1.7: Binary blazed grating (BBG)

$$d[\sin \theta_i + \sin(2\theta_b - \theta_i)] = m\lambda. \quad (1.9)$$

Two special cases can be considered depending on Eq. 4.19. First case is the Littrow configuration, where light is incident along the normal N' , so that $\theta_b = \theta_i$ and

$\theta_m = -\theta_i$ and then the Eq. 4.19 becomes $m\lambda = 2d \sin \theta_b$

$$\theta_b = \sin^{-1} \left(\frac{m\lambda}{2d} \right). \quad (1.10)$$

Here $d \sin \theta_b$ = height of the prismatic element. A grating that is blazed for wavelength λ and order m in a Littrow configuration, must have a step height an integral number m of half wavelengths. In the second case, light is incident along the normal N to the grating surface itself, then $\theta_i = 0$ and $\theta_b = -\theta_m/2$. Now Eq. 4.19 gives,

$$\theta_b = \frac{1}{2} \sin^{-1} \left(\frac{m\lambda}{d} \right). \quad (1.11)$$

One of the chief difficulties with RBG is the fabrication of this structure with ideal size and profile. BBG is an alternative approach to RBG with binary profiles that can achieve high diffraction efficiency into a specified order. BBG is composed of surface-relief diffractive elements with subwavelength binary features and is schematically shown in Fig. 1.7. Here the width of the empty space (white space) is a_i and the width of the ridge (black space) is b_i , where $i=1,2,\dots,N$. The refractive index of white space is n_1 and the refractive index of black space is n_2 . The height of the grating is h . According to *form-birefringence* [30] theory the effective refractive indices (n_{eff}) of a single localized substructure for TE and TM polarized light is given by

$$\begin{aligned} n_{\text{eff}}(TE) &= \sqrt{n_1^2(1-f) + n_2^2 f}, \\ n_{\text{eff}}(TM) &= \frac{1}{\sqrt{\frac{1-f}{n_1^2} + \frac{f}{n_2^2}}}, \end{aligned} \quad (1.12)$$

where the fill factor $f = \frac{b_i}{a_i+b_i}$. Diffraction Efficiencies of both kinds of gratings are calculated using the form-birefringence theory and discussed in [30].

1.2.3 Effective media and Homogenization

Homogenized composite materials (HCM) are mixtures of different materials (components), where the particle sizes of the component materials are much smaller than the wavelength of light. Suppose identical spherical or ellipsoidal particles made of a linear material are randomly dispersed in a linear host material, and the particle sizes are electrically small, then the composite material can be considered as an effectively homogeneous material. The effective material parameters of this composite material are estimated using Homogenization theories. Two of the most common homogenization theories are the Maxwell Garnett (MG) formalism and the Bruggemann formalism.

Maxwell Garnett formalism

Maxwell Garnett (MG) formalism is used for dilute composite materials whereas Bruggemann formalism is a more general technique for estimating the effective constitutive parameters of homogenized composite materials (HCMs). The effective medium properties of composite materials are expressed in terms of their component's fraction and the particle aspect ratio. Effective medium parameters can be derived from the spatial averaging of the properties of the individual constitutive structures under the assumption that the size of the inclusion (d) is much smaller than the wavelength (λ), i.e. $\lambda \gg d$. Hence, one is able to experience only average quantities such as the dipolar and quadropolar fields etc. Thus, the average responses can be expressed as ,

$$\langle D \rangle = \epsilon_0 \epsilon_{\text{eff}} \langle E \rangle, \quad \langle B \rangle = \mu_0 \mu_{\text{eff}} \langle H \rangle, \quad (1.13)$$

where E and H are the total electric and magnetic fields. MG formalism is useful when the filling fraction, f , is small and the particles effectively do not feel the effect of the scattered fields arising due to the other neighbouring particles. According to the MG formalism, in the small particle limit, the effective dielectric permittivity satisfies an equation which is determined self-consistently [31]. A self consistent solution is derived

from the solution of local fields around the element and insisting that the fluctuation of the local field around its effective value should average to zero, and can be expressed as,

$$\frac{\epsilon_B - \epsilon_{\text{eff}}}{\epsilon_{\text{eff}} + L(\epsilon_B - \epsilon_{\text{eff}})} + f \frac{\epsilon_A - \epsilon_B}{\epsilon_B + L(\epsilon_A - \epsilon_B)} = 0, \quad (1.14)$$

where medium A is considered to be an ellipsoidal particle coated with a shell of medium B and surrounded by a uniform medium ϵ_{eff} . f is the fraction of material A in the mixture and L is the depolarization factor that depends on the particle's aspect ratio. The self consistent conditions are that this theory neglects the role of the distorted near-fields and the reduced polarization of the particles.

Bruggemann formalism

The Bruggemann formalism considers a spatial distribution of materials, which are characterized by the volume fractions and the electromagnetic response of an inclusion embedded in the composite medium, usually described by a depolarization dyadic. The Bruggemann formalism is applicable for isotropic, anisotropic and bi-anisotropic materials HCMs [32,33]. Let us consider a binary mixture that is considered to consist of two different ellipsoid shaped particles of the component materials such as a and b . In M-G, it was assumed that the dilute phase is dispersed in the host medium. The Bruggemann formalism treats both the components a and b on equal footing and hence it is not limited to a dilute mixture. Recently Mackay and Lakhtakia compared Bruggemann Homogenization formalism with two different depolarization dyadic as, (i) when the component particles a are embeded in a background of isotropic component b and vice versa, (ii) when both the component particles a and b are embeded in a homogenized anisotropic background [32]. They confirmed that the derivation of depolarization dyadics in the second case is more accurate when the following conditions are met, (i) when the component particles become more aspherical, (ii) when the volume fractions of the component materials are in the mid-range values, (iii) when the homogenized component material is dissipative. Let the relative permittivities of

the two components be ϵ_a and ϵ_b , and their corresponding volume fractions be denoted by f_a and $f_b = 1 - f_a$ respectively. The effective permittivity parameters $\epsilon_{x,y,z}^{Br}$ are given implicitly by the three coupled equations [32], whose detailed explanation is given in Appendix A.

$$\frac{\epsilon_a - \epsilon_j^{Br}}{1 + D_j, L_j(\epsilon_a - \epsilon_j^{Br})} f_a + \frac{\epsilon_b - \epsilon_j^{Br}}{1 + D_j, L_j(\epsilon_b - \epsilon_j^{Br})} f_b = 0; \quad j \in \{x, y, z\}, \quad (1.15)$$

with the depolarization dyadic components L_j (in the first case), is given by

$$L_j = \frac{U_x U_y U_z}{2} \int_0^\infty \frac{1}{(s + U_j^2) \sqrt{(s + U_x^2)(s + U_y^2)(s + U_z^2)}} ds; \quad j \in \{x, y, z\}, \quad (1.16)$$

where U_x , U_y and U_z are the shape parameters. The depolarization dyadic components D_j (in the second case), specified by double integrals [32],

$$D_x = \frac{1}{4\pi} \int_0^{2\pi} \int_0^\pi \frac{\sin^3 \theta \cos^2 \phi}{U_x^2 \rho} d\phi d\theta, \quad (1.17)$$

$$D_y = \frac{1}{4\pi} \int_0^{2\pi} \int_0^\pi \frac{\sin^3 \theta \sin^2 \phi}{U_y^2 \rho} d\phi d\theta, \quad (1.18)$$

$$D_z = \frac{1}{4\pi} \int_0^{2\pi} \int_0^\pi \frac{\sin \theta \cos^2 \phi}{U_z^2 \rho} d\phi d\theta. \quad (1.19)$$

These involve the scalar parameter, ρ , defined as

$$\rho = \frac{\sin^2 \theta \cos^2 \phi}{U_x^2} \epsilon_x^{Br} + \frac{\sin^2 \theta \sin^2 \phi}{U_y^2} \epsilon_y^{Br} + \frac{\cos^2 \theta}{U_z^2} \epsilon_z^{Br}. \quad (1.20)$$

Note that due to the coupled nature of the three equations, numerical methods are generally needed to extract the homogenized relative permittivity parameters $\epsilon_{x,y,z}^{Br}$.

1.2.4 Metamaterials

A metamaterial (MTM) is an artificially structured material which obtains its properties from the geometrical resonances of the inclusions in the structure rather than the constituent materials [34]. A metamaterial has an inhomogeneity scale (d) that

is much smaller than the wavelength of incident electromagnetic wave (λ) i.e. $d \leq \lambda/4$ to $\lambda/6$. Due to subwavelength size of the unit cell, the electromagnetic wave can not sense the individual unit cells of the structure and hence responds to an average polarization (\vec{P}) and magnetization (\vec{M}) of the structures. Hence, the electromagnetic response of the effective medium is expressed in terms of homogenized material parameters [34]. The structural elements of a MTM can be engineered to attain both electric and magnetic resonances at pre-defined frequencies [34, 35]. The unique properties of MTMs arise from the resonances supported by the size and shape of the unit cells (meta-atoms) embedded in the medium. Smith et al. showed in 2000 at microwave frequencies that a structured material could simultaneously have negative permeability and permittivity [36], which is termed a negative refractive index material. MTMs can be nanostructured media of dielectric, semiconductors and metals and can function over almost the entire electromagnetic spectrum from microwave to terahertz to visible frequencies. MTMs are able to show strong magnetic response at higher frequencies, where natural materials do not show any magnetic response [37].

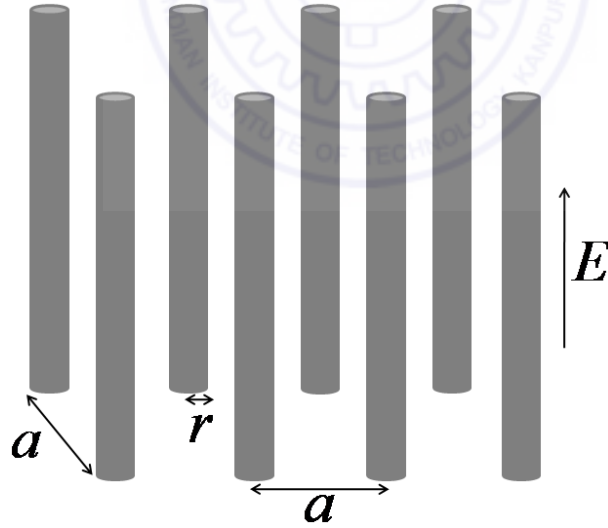


Figure 1.8: Schematic picture showing infinitely long wire-array metamaterial of radius r and lattice of periodicity a , that behaves as a low frequency plasma when the electric field of the electromagnetic wave is oriented along the wires.

Metals have negative permittivity below their plasma frequencies due to their free electrons, and typically the plasma frequency for metal is in the UV or visible frequency range. Pendry et al [38, 39] showed that microwave metamaterials that consist of a very

low density of thin aligned metallic wires display plasma-like behaviour. The plasma frequency of this dilute medium could be tuned with the geometrical parameters of the array and could be reduced down to microwave frequencies. Fig. 1.8 schematically shows an array of infinitely long thin metallic wires of radius (r) on a square lattice of periodicity (a) that behaves as a low frequency plasma when the electric field of the light is oriented along the wires. Since electrons are confined only inside the wires and due to low density of wires, the effective electron density, N_{eff} , decreases. N_{eff} can be expressed as, $N_{\text{eff}} = N \frac{\pi r^2}{a^2}$, where N is the density of electrons in the wire itself. It also appears as if electrons have acquired large effective mass m_{eff} due to the large self inductance of the thin wires (Inductance and mass are both inertial effects). These two effects reduce the plasma frequency of the effective medium which is given by

$$\omega_p = \sqrt{\frac{N_{\text{eff}} e^2}{m_{\text{eff}} \epsilon_0}}. \quad (1.21)$$

This medium has negative permittivity only for incident waves with electric field parallel to the axis of the wire, and hence behaves as an anisotropic medium. Such metallic wires oriented along all the three directions can reasonably form an isotropic plasma. Sangeeta et al have shown that at optical frequencies, it is the filling fraction that predominantly defines the effective medium response for light polarized such that the electric field is along the aligned nanowires, and the effective medium parameter is given by

$$\epsilon_{\text{eff}} = f \epsilon_m + (1 - f) \epsilon_b, \quad (1.22)$$

where ϵ_m and ϵ_b are the dielectric permittivities of the metal and background medium respectively [40]. They also demonstrated the possibility of transmission band below the plasma frequency of the metallic wire array by modifying the background medium by coherent optical processes such as electromagnetically induced transparency for a resonant atomic background medium [40]. MTMs have various applications such as subwavelength imaging [41], negative refractive index [42], cloaking [43] and perfect absorbers [44] etc. that are possible by careful design of the inclusion in the unit cell.

1.2.5 Hyperbolic Media

Hyperbolic materials (HM) are artificial materials that have an indefinite permittivity tensor describing their response, i.e., the eigenvalues of the permittivity tensor are not of any definite sign (positive or negative) [45]. Alternatively one can see that one of the principal components of dielectric permittivity or magnetic permeability is opposite in sign to the other two principal components [46]. Such type of materials can be represented for an uniaxial anisotropic crystal as

$$\hat{\epsilon} \equiv \begin{pmatrix} \epsilon_{\perp} & 0 & 0 \\ 0 & \epsilon_{\perp} & 0 \\ 0 & 0 & \epsilon_{\parallel} \end{pmatrix}, \hat{\mu} \equiv \begin{pmatrix} \mu_{\perp} & 0 & 0 \\ 0 & \mu_{\perp} & 0 \\ 0 & 0 & \mu_{\parallel} \end{pmatrix}, \quad (1.23)$$

where \perp and \parallel indicate components parallel and perpendicular to the anisotropy axis. Representations in other rotated systems are discussed in Chapter 4. The dispersion relation of light in anisotropic medium is given by,

$$\frac{k_x^2 + k_y^2}{\epsilon_{\parallel}} + \frac{k_z^2}{\epsilon_{\perp}} = \frac{\omega^2}{c^2}, \quad (1.24)$$

where k_x , k_y and k_z are the x , y and z components of the wave vector respectively, ω is the frequency of incident light and c is the speed of light. The equi-frequency surfaces using this dispersion relation are shown in Fig. 1.9. where (a) is an isotropic dielectric with $\epsilon_{\parallel} = \epsilon_{\perp}$, which is a sphere, (b) extraordinary waves in an uniaxial anisotropic media with $\epsilon_{\parallel} < 0$; $\epsilon_{\perp} > 0$ which is a hyperboloid of first kind and (c) $\epsilon_{\parallel} > 0$; $\epsilon_{\perp} < 0$ which is a hyperboloid of second kind. Hence such media are considered as hyperbolic media.

Examples of HM are layered metal–dielectric structures [47], hyperlens [48], multilayer fishnet structures [49], nanorod arrays [50], graphene metamaterials [46]. One of the important application of HM is the potential for subwavelength imaging and focussing. Negative refractive index (NRI) media are useful for perfect lensing [51] with

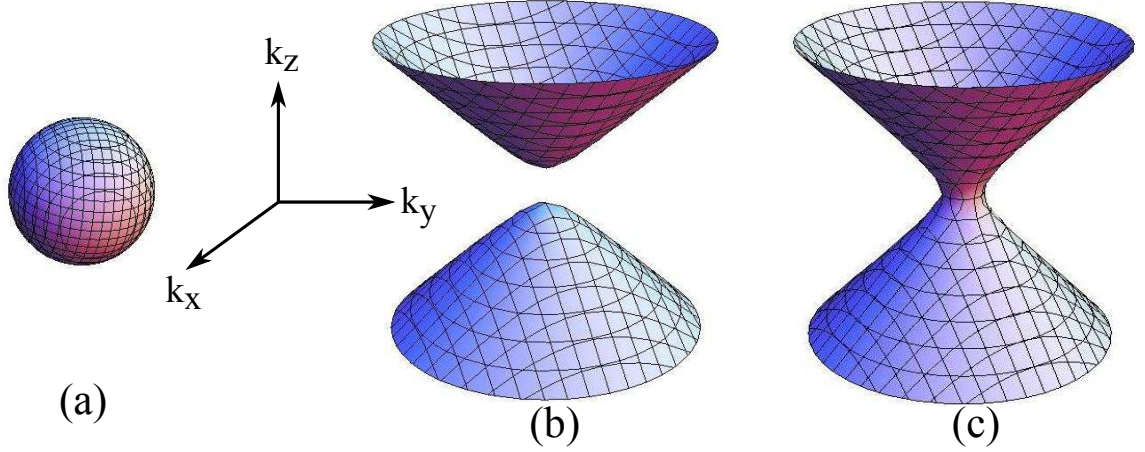


Figure 1.9: Isofrequency curves in hyperbolic metamaterials when (a) $\epsilon_{\parallel} = \epsilon_{\perp}$ (b) $\epsilon_{\parallel} < 0$ and $\epsilon_{\perp} > 0$ (c) $\epsilon_{\parallel} > 0$ and $\epsilon_{\perp} < 0$

subwavelength image information, and one of the alternative for NRI media are hyperbolic media [47]. Negative refraction at optical wavelengths have been reported for an array of metallic nanorods [52] and one of the important application of such kind of HM are subwavelength imaging and focussing [53–55]. Fabrication of anisotropic HM is easier compared to the isotropic NRI media as the only criterion for the HM is to constrain the motion of free electrons in one or two spatial directions. There are various possible techniques to make a hyperbolic material. One of the standard techniques is to fabricate a nanostructured wire metamaterial using electrochemical deposition of a metal (gold or silver) into a porous alumina membrane created by anodization [56]. Another useful method is to use alternating thin films of a plasmonic metal and a dielectric medium [53].

1.2.6 Photonic Bandgap Structures

Photonic band gap (PBG) structures are periodic dielectric structures which control the propagation of electromagnetic wave inside the structure by virtue of the periodic variation. Considering the analogy between Schrödinger equation and Helmholtz's equation for propagation, Eli Yablonovitch, in 1987, built an artificial periodic structure to control the propagation of the light [57]. By using the analogy in solid state physics where a crystal lattice corresponds to a periodic arrangement of the atomic potential

for electrons, in this structure he used a periodic arrangement of permittivity [58]. Electrons in a periodic potential exhibit electronic band gaps where no allowed states are possible in a range of energies. The electronic wave function in such a periodic potential can be described by a Bloch wave, a plane wave multiplied by a periodic function $u_{i\vec{k}}(\vec{r})$ with the periodicity of the lattice,

$$\psi_{i\vec{k}}(\vec{r}) = e^{i\vec{k} \cdot \vec{r}} u_{i\vec{k}}(\vec{r}), \quad (1.25)$$

where the index ‘ i ’ labels the different solutions to the Schrödinger equation and k is the wavevector of this particular state. Similarly photons in a periodically inhomogeneous material, exhibit photonic band gap where the permittivity (ϵ) is a periodic function of position [59]

$$\begin{aligned} \epsilon &= \epsilon(\vec{r}), \\ \epsilon(\vec{r} + \vec{R}) &= \epsilon(\vec{r}), \end{aligned}$$

where \vec{R} is a direct lattice vector. $\vec{R} = n_1 \vec{a}_1 + n_2 \vec{a}_2 + n_3 \vec{a}_3$. The lattice constant of the periodic structure should be of the order of half a wavelength of the electromagnetic radiation to exhibit a photonic bandgap. Structures obeying such kind of behaviour are also termed as photonic crystals (PCs) or photonic band gap materials. Photonic crystals are periodic dielectric structure and they can be periodic in one, two and three dimensions. One of the main difference of PCs with MTMs is that the size of the unit cells by which MTMs are composed are small compared to the operating wavelength and the MTMs can be characterized by effective medium properties, whereas for PCs the unit cell is of the order of the operating wavelength which gives rise to Bragg scattering due to the periodicity of the PCs. Three dimensional structures with sufficient dielectric contrast are required for complete photonic bandgap [60], which are more challenging to fabricate. John and Toader suggested tetragonal lattice of square spiral posts fabricated by OAD which exhibit a complete 3D PBG [61]. This structure consists of square spiral posts grown on a 2D substrate that is initially pre-seeded with

a square lattice. By introducing point and line defects inside the periodic crystal linear waveguides and point-like cavities are formed resulting in localized electromagnetic states [62].

1.2.7 Surface electromagnetic waves

Surface Plasmon Polariton waves

Surface plasmons (SPs) are collective excitations of free electrons existing at the planar interface between a metal and a dielectric material. When SPs are coupled with electromagnetic excitations or photons, the excitation is commonly known as SPP. SPPs exhibit important roles and applications in near field imaging and superlensing [51], extraordinary optical transmission [63], local field enhancement, sensing and waveguiding [64], plasmonic solar cells [65] and nonlinear optical effects [66] etc. Fig. 1.10

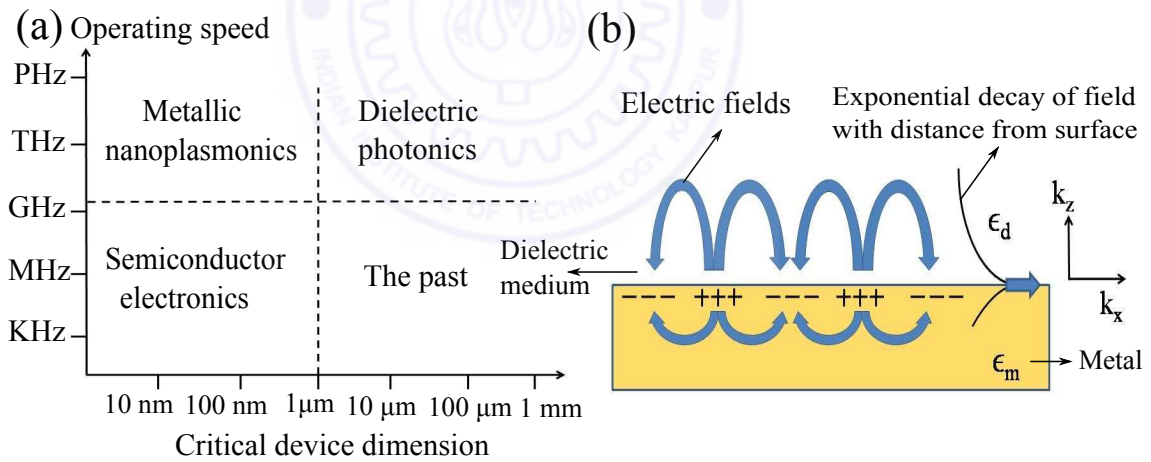


Figure 1.10: (a) A chart for operating speed vs critical device dimension (nm) in case of semiconductors (electronics), dielectrics (photonics) and metals (plasmonics) is adapted from M.L.Brongersma and V.M.Shalaev [67]. (b) Schematic picture of the charge oscillations that propagates along the surface of a metal-dielectric interface showing the exponential decay of the electromagnetic fields normal to the surface.

(a) shows a chart for the operating speed vs critical device dimensions for nanofabrication of devices: past, present and projected for the future. Although high speed data transmission rates can be achieved with dielectric photonic circuits, the main problem with dielectric photonic devices is that the component sizes can not be reduced to

the nanometer scale because of the diffraction limit of light. This diffraction limit of dielectric photonics can be overcome by excitation of surface plasmons on metal surfaces while still operating at optical frequencies [68]. The subwavelength control and manipulation of optical energy is possible with such metallic nanostructures. Various experimental techniques are available for fabricating plasmonic structures such as interference lithography, electron beam lithography, focused ion beam nanofabrication, stencil lithography [69] etc. Usually metals suffer from high resistive losses. Noble metals like silver and gold (with s-shell electrons) are good plasmonic materials because they exhibit low dissipation at visible and infrared wavelengths.

Two kinds of surface plasmons can be categorised. When SPs are propagating at the interface of planar metal surface, they are termed as propagating surface plasmon (SPPs) and when localized to metal nanoparticles, then they are known as localized surface plasmons (LSPs). Localized surface plasmons exist on bound metal surfaces and these are non-propagating electromagnetic excitations. These two characteristics are the main ingredients for making good use of surface plasmon in plasmonic based devices. The expression for the electric field of a SPP propagating along x direction as shown in the Fig. 1.10 (b) is given by,

$$E_{\text{SPP}}(x, z) \approx e^{i\beta x - k_z |z|}. \quad (1.26)$$

This corresponds to a surface mode with propagating wave vector $k_x = \beta$ and exponentially decaying normal to the surface with decaying constant k_z as shown in Fig. 1.10 (b). Expressions for k_z in dielectric and metallic media respectively are given by,

$$\left. \begin{aligned} k_{zd} &= \sqrt{\beta^2 - \left(\frac{\omega}{c}\right)^2 \cdot \epsilon_d} \\ k_{zm} &= \sqrt{\beta^2 - \left(\frac{\omega}{c}\right)^2 \cdot \epsilon_m} \end{aligned} \right\}, \quad (1.27)$$

where ϵ_m and ϵ_d are dielectric permittivities of metal and dielectric medium respectively and $\epsilon_m = 1 - \frac{\omega_p^2}{\omega^2}$. Solving Maxwell's equations at the interfaces of isotropic, homogeneous dielectric and metallic media for an homogeneous solution, the wave vector for

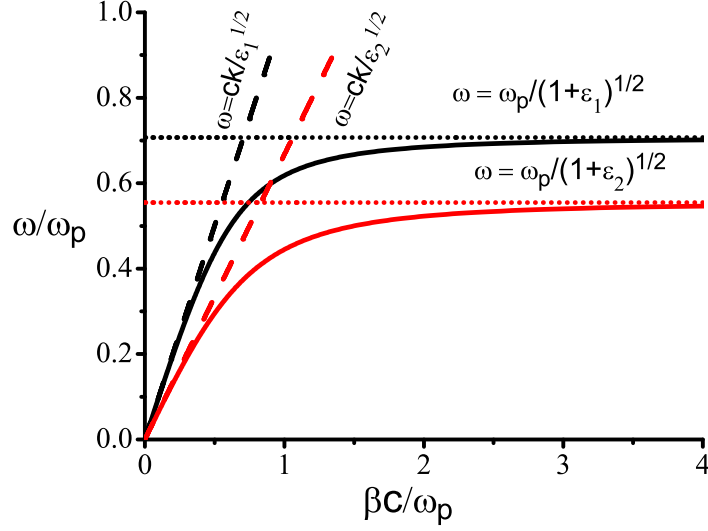


Figure 1.11: Black and red solid lines are dispersion curves of SPPs at the silver–air and silver–dielectric interfaces respectively. The two light lines, one for air ($\epsilon_1 = 1$) and other for dielectric ($\epsilon_2 = 2.25$) are represented by black and red dashed lines. Black and red dotted lines are asymptotic lines for silver–air and silver–dielectric interfaces respectively.

the SPP wave is found to be $\beta = k_0 \sqrt{\frac{\epsilon_d \epsilon_m}{\epsilon_d + \epsilon_m}}$ [13].

Fig. 1.11 shows the SPP dispersion curves for silver–air and silver–dielectric interfaces, where both the curves start at $\omega = 0$ and $\beta = 0$. At large value of β , the two dispersion curves coincide with two asymptotic horizontal lines at $\omega = \omega_{sp}$, where ω_{sp} is a frequency satisfying $\epsilon(\omega_{sp}) = -\epsilon_1$ for silver–air interface and $\epsilon(\omega_{sp}) = -\epsilon_2$ for silver–dielectric interface. For small values of β , dispersion curves approach their corresponding light lines, where $k_x = (\omega/c)\sqrt{\epsilon_1}$ (for air) and $k_x = (\omega/c)\sqrt{\epsilon_2}$ (for dielectric). Due to ohmic losses in metals, the SPP field decays exponentially with the propagation distance and the propagation length is related to the imaginary part of dielectric constant of metal which is given by,

$$L_{SPP} = (2\text{Im}\beta)^{-1}. \quad (1.28)$$

Typically, the propagation length in the visible to NIR range is 10 to 100 μm on a Ag or Au surface. Since $\beta > \frac{\omega}{c}$, the wave vector k_z is imaginary. The SPs field amplitude decreases exponentially (as $\exp(-|k_z|z)$) normal to the surface. The values

of skin depths in dielectric and metallic media respectively are given by,

$$d_1 = \frac{\lambda}{2\pi} \left(\frac{\text{Re}[\epsilon_m] + \epsilon_d}{\epsilon_d^2} \right), \quad (1.29)$$

$$d_2 = \frac{\lambda}{2\pi} \left(\frac{\text{Re}[\epsilon_m] + \epsilon_d}{\text{Re}[\epsilon_m]^2} \right). \quad (1.30)$$

For example, in case of silver, at $\lambda = 600$ nm, the decay lengths are $d_1 = 300$ nm and $d_2 = 24$ nm. The dispersion curve located at the left side of the light line is called

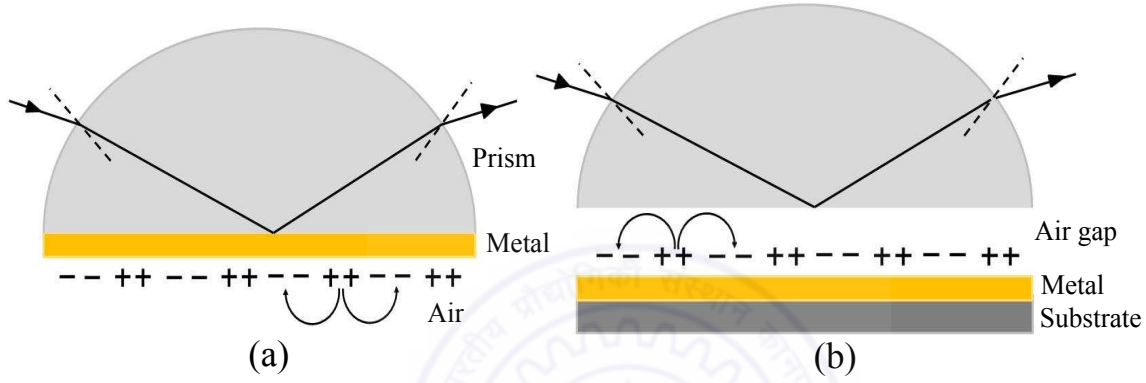


Figure 1.12: Prism coupling to SPPs using attenuated total internal reflection in the (a) Kretschmann geometry and (b) Otto geometry.

as the *radiative* region and the region located at the right side is called nonradiative region. SPPs are classified as *nonradiative* modes, because direct coupling to SPPs with the incident light from free space is not possible. The SPP dispersion plot reveals that there is a momentum mismatch between the incident light (air light line) and SPPs at any incident frequency ' ω_0 '. Hence one needs momentum matching devices or techniques to couple light in free space to the SPP.

A prism coupled configuration for exciting SPPs known as attenuated total reflection (ATR) method, was demonstrated by Otto [70] and also by Kretschmann and Raether [70] in 1968. In the Kretschmann configuration, a thin metal film is deposited on the prism and is illuminated through a dielectric prism at an angle of incidence greater than the critical angle as shown in Fig. 1.12 (a), which increases the wavevector for incident light because of the dielectric permittivity of the prism. The dispersion relation of the evanescent wave generated by the prism is given by, $k_{xd} = (\omega/c)\sqrt{\epsilon_p} \sin \theta_i$, where ϵ_p is the dielectric permittivity of the prism. The in-plane momentum of the inci-

dent light wavevector coincides with the SPP wavevector on an air-metal interface and hence coupling to SPPs occurs. In the Otto configuration, the prism is separated from the metal film by a small air gap and total internal reflection occurs at the prism–air interface as shown in Fig. 1.12 (b), which is used to excite the SPPs at the metal–air interface.

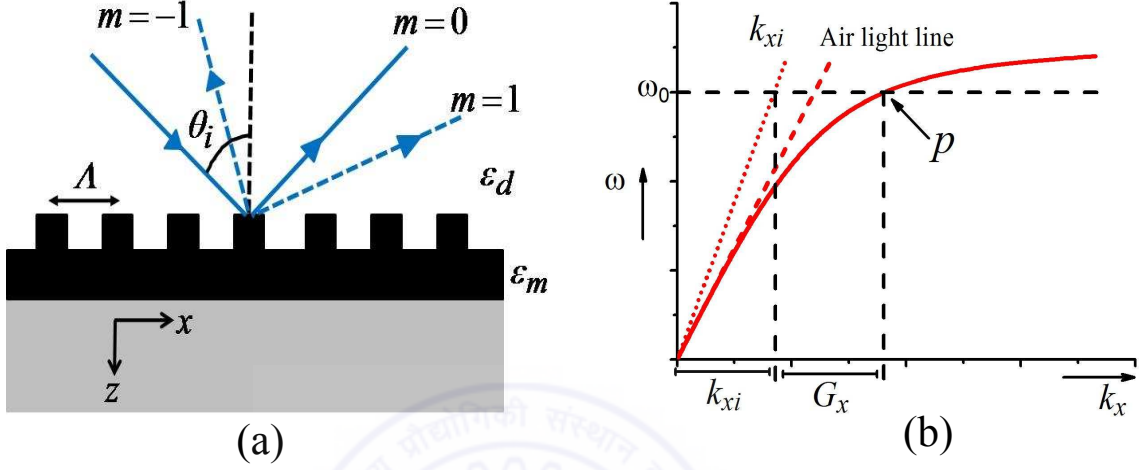


Figure 1.13: (a) Phase matching of incident light with SPPs using grating coupled configuration. (b) SPP dispersion curve and coupling by a grating.

As the prisms are bulky, for miniaturization of the devices grating couplers are used for SPP coupling [70]. Periodic structures are introduced on the metal surfaces to diffract incident light into SPPs as shown in Fig. (c). In 1902, Wood reported an anomalous decrease in the intensity of reflected light at certain angles of incidence by a metallic grating [70]. Although the concept of SPPs was not understood at that time, the phenomenon observed by Wood can be attributed to the excitation of SPPs by the periodic structure of the grating. Let us consider a one-dimensional (1-D) corrugated metallic surface with period Λ shown in Fig. 1.13 (a) and light is incident at an angle of θ_i . The grating generates various diffracted orders in addition to the specularly reflected and transmitted light. The dips in the specularly reflected and transmitted spectra by varying θ_i can be attributed to the excitation of SPPs and the energy of the incident light is transferred to SPPs at that specific angle due to phase matching. The condition for the excitation of SPPs by the grating is expressed as,

$$\beta = k_{xi} + G_x, \quad (1.31)$$

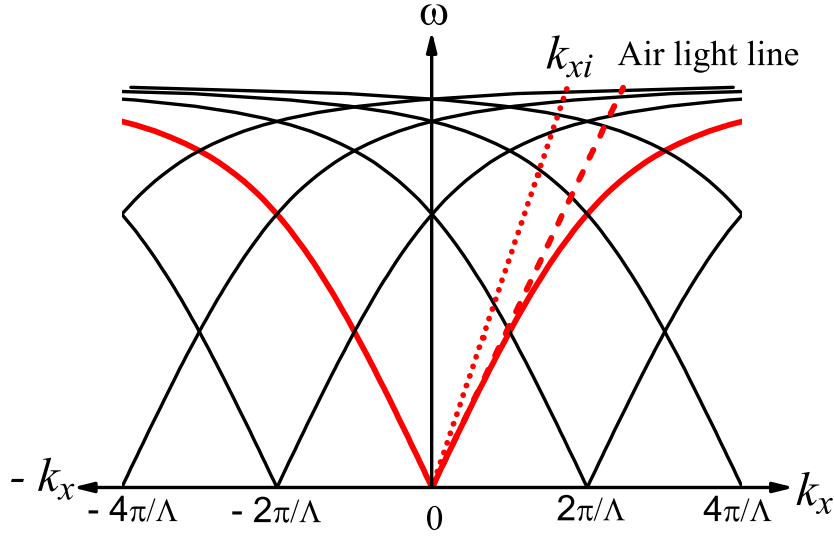


Figure 1.14: Plasmonic band structure, where SPPs are propagating in both positive and negative directions along x -axis. Red solid line in both positive and negative regions, represent the initial SPP dispersion curves at silver-air interface. SPP dispersion curves are translated by $m(2\pi/\Lambda)$ with integer values of m and $\Lambda = 1000$ nm, result in a manifold of SPP dispersions.

where β is the SPP wavevector, k_{xi} is the x component of incident light and is given by, $k_{xi} = k_0 \sin \theta_i$, $G_x = m(2\pi/\Lambda)$ is the reciprocal lattice vector. As we see in Fig. 1.13 (b), that k_{xi} alone cannot be as large as β , so the role of the grating is to provide a quasi-wavevector of $m(2\pi/\Lambda)$ to k_{xi} and allow it to become as large as β . Excitation of SPPs is possible only for p - polarized light in case of 1D grating and not for s - polarized light, as the boundary conditions are not satisfied for s - polarized case [13]. In page 112, Fig. 4.2 of ref. [71], it can be seen that for surface wave propagating along the x axis, the electric field has two components along the x and z axes. The z components of the electric field is complex, hence the electric field has elliptical polarization in the xz plane. The existence of z component of the electric field demands the presence of surface charge $P_{z2} - P_{z1}$ along the interface. Hence the surface wave can be viewed as surface charge density wave as shown in the Fig. 4.3 of ref. [71]. For surface wave to exist, it must have some finite extension along the z axis. For p polarization, both x and z components of the electric field is present. Hence it can excite the surface Plasmon. Whereas for s polarization, electric field has only y component but no z

component. Therefore it can not excite surface Plasmon.

SPPs are propagating in both positive and negative directions along x axis as shown in Fig. 1.14. Hence SPP dispersion curves are plotted for both positive and negative values of k_x . Red solid lines are initial SPP dispersion curve similar to that in Fig. 1.13. All black solid lines appear by the translation of the initial SPP dispersion curve by a factor of $m(2\pi/\Lambda)$ for various diffracted orders. Analogous to photonic band structure of photonic crystals, Fig. 1.14 represents the plasmonic band structure of the plasmonic structure. Many branches are folded within the line of k_{xi} into the radiative region and SPPs are excited by the incident light at the crossing points of these branches.

Other surface waves

Apart from the surface plasmon wave, there are several other kinds of surface waves that can exist at the various kinds of interfaces such as Dyakonov waves, Tamm waves, and Dyakonov–Tamm waves, that are known since the last 25 years [72]. Dyakonov surface wave was predicted theoretically in the year 1988 [73]. For existence of such kind of surface wave, one of the partnering medium should be a transparent anisotropic medium, where anisotropic medium is either uniaxial or biaxial and the other medium is isotropic. It is localized at an interface because of the difference between the symmetry of the two media in contact. Let us consider an isotropic medium with permittivity ϵ and an uniaxial crystal with permittivities ϵ_{\parallel} and ϵ_{\perp} , when the optic axis is parallel to the interface. The condition for Dyakonov wave is quite stringent and the wave exists if $\epsilon_{\parallel} > \epsilon > \epsilon_{\perp}$, only in a very narrow angular range (of nearly 1 deg) relative to the crystal optical axis. Recently in 2009, experimental observation of Dyakonov waves [15] was reported at the interface of Potassium titanyl phosphate (KTP), which is a biaxial crystal and an index-matched liquid fulfilling the conditions for such waves.

The Tamm surface wave, predicted in the year 1977, exists at an interface (at $z = 0$), when one of the half space is occupied by a nonhomogeneous material whose

constitutive properties vary along z axis [74]. Experimental observation for Tamm waves was found in AlGaAs/GaAs superlattices with a terminating layer of AlAs in 1990 [14].

Dyakonov–Tamm (DT) waves exist at the interface of two dielectric materials, where one of the dielectric materials is both anisotropic and periodically non-homogeneous. Experimental realization of such kind of surface waves have been observed in the year 2013 [75] and in a grating-coupled configuration in the year 2014 [16]. The angular range of DT wave is much larger compared to that of Dyakonov wave and often covers the entire 360° angular range.

1.3 Motivation and scope of thesis

The goal of this PhD work was to study the photonic and plasmonic properties of PP-CTFs and to investigate opportunities for novel applications in various areas. The following aspects of periodically patterned CTFs were studied: (i) As blazed diffraction gratings (ii) For asymmetric coupling of incident light to SPP waves using periodically patterned silver nano-columnar arrays, (iii) As gratings with tunable diffraction efficiencies as a function of slant angle of the silver nanocolumnar array. A thorough understanding of the radiative interactions of these systems nanoscale level as well as the micro-scale (wavelength scale) was attempted.

CTFs are known to be deposited by making incident a collimated vapor flux at large oblique angles to a substrate. Using a substrate that is periodically patterned at micro/nanoscales, new kinds of PP-CTFs have been fabricated and the fabrication details are discussed in Chapter 2.

Dielectric PP-CTFs are shown to function as blazed diffraction gratings with large asymmetric diffraction efficiencies. Blazed gratings have enormous applications in spectroscopy. But the conventional blazed gratings available in the market are fabricated using very expensive method such as reactive ion etching. Here we made

blazed gratings of dielectric materials using very inexpensive methods known as OAD. The PP-CTF of various dielectrics such as CaF_2 / MgF_2 / SiO_2 and metals such as silver are shown to be conveniently fabricated by this method. The complete morphology of the PP-CTF is shown to be determined by controlling the angle and flux rate of depositions. PP-CTFs are shown to have enhanced photonic and plasmonic properties. The gratings presented here possibly represent the first transmission blazed gratings at deep ultraviolet frequencies.

Dielectric gratings can be considered as transmission phase gratings, but in case of gratings made of plasmonic metals, both the amplitude and phase of the incident light get modified after interacting with the structure. Analytical vectorial solutions for this kind of structure are difficult and numerical techniques are required to calculate and understand the interaction of electromagnetic waves with the structure. The blazing effect of the gratings of periodically patterned dielectric CTFs as a result of the spatially linear phase shifts caused by prismatic air cavities in the significant plane of incidence was understood using scalar Kirchhoff-Fresnel diffraction theory and discussed in Chapter 3.

A CTF made of plasmonic metals like silver makes for an effectively biaxially anisotropic continuum. PP-CTFs of silver showed strong blazing action and asymmetrically coupled optical radiation to SPP waves for both p- and s- polarizations propagating only along one direction supported by the CTF/dielectric interfaces. The excitation of SPP waves guided by the planar interfaces of air (or some isotropic dielectric material) of nano-engineered CTFs made of a metal has been investigated quite well, the same phenomenon when the metallic CTF is periodically patterned is studied in detail here. For development of high performance optical components and circuits, tailoring SPs by control of the nanostructures is expected, which offer challenges for the new generation of nanophotonic devices. Homogenization of the metallic CTFs using the Bruggeman formalism revealed them to display hyperbolic dispersion, and the dispersion of SPP waves on both 1-D and 2-D gratings of such anisotropic hyperbolic media was found to be adequately described thereby. The PP-CTFs of slanted

silver nanocolumns show large amounts of asymmetric coupling to surface plasmons propagating only in one direction and can be used as unidirectional couplers. Detailed discussions are given in Chapter 4.

Electromagnetic simulations of the grating structures reveal large changes in the photonic properties with the slant angle such as diffraction efficiencies and the electromagnetic near fields. Furthermore, these slanted nanocolumnar structures can be uniformly reconfigured by an ion beam irradiation method and give rise to reconfigurable blazed gratings. Thereby the diffraction efficiencies for different wavelength bands as well as the unidirectional coupling to surface plasmons can be optimized by changing the blazing (angle) condition. These structures were found to be extremely reconfigurable giving rise to enormous flexibility in applications and are discussed in Chapter 5.

A novel application using superstructures of CTFs to fingerprint visualization was developed. Visualization of latent fingerprints is enhanced by deposition of CTFs at large oblique angle of CaF_2 and SiO_2 on fingerprint marks on two nonporous surfaces such as smooth glass slides and highly reflecting rough aluminium sheets. The visualization becomes enhanced due to the scattering of light caused by the superstructures of the CTFs deposited on the fingermarks. Further enhanced visualization is obtained by treating the deposited CTFs with a fluorescent dye and fluorescence imaging. Detailed discussions are given in Chapter 6.

Finally, some recommendations for future works are given in Chapter 7.

Chapter 2

Fabrication, Characterization and Simulation techniques

2.1 Introduction

Miniaturization of optical device components down to sub-micrometer and nano-meter lengthscales is one of the major outstanding challenges during last few decades in order to fulfill the rapidly growing technological requirements. A wide variety of methods and tools have been developed to fabricate micro and nano structures in a dependable and reproducible manner over this time. Optical lithography is widely used in the semiconductor industry, including 22 nm and 40 nm channels/ gates for transistors/ MOSFETs etc where deep ultraviolet light is used. For fabrication of high quality nanostructures, e-beam lithography (EBL) [76] and focused ion beam (FIB) milling are most commonly used [77]. However, these processes depend on very costly instrumentation, and the main drawback of these systems for optical application is low throughput for large area patterning. Therefore, cost effective and simple techniques for nanostructuring such as OAD and LIL are attractive as patterning over large areas by these techniques is easily possible. High porosity (increased surface to volume ratio) and an exceptional ability to form different shapes (such as helices, vertical columns, n-fold spirals, chevron shapes, ball-like structures etc.) with the deposition angle and

controlled substrate rotation during vapor deposition, makes OAD a versatile technique to fabricate desired nanostructures. Due to the complex structures attainable and the large controllability of OAD, these films are often known as ‘Sculptured thin films’ (STFs) [1].

Using OAD on non-planar substrates results in the deposition of randomly arranged isolated nano-structures with non-specific diameters [78]. For many important applications as well as precise control of properties, periodic patterning of the growth structures are needed rather than random structures. For example, square spiral structures fabricated on tetragonal lattices behave as a 3-D photonic crystals with a complete bandgap [61,79] and narrow band pass optical filters [80,81]. Control over the morphology of the random nanostructures can be attained by introducing artificial seed patterns onto the substrate surface prior to the oblique angle deposition. These arranged patterns act as the seeds by shadowing out the rest of the substrate for the nucleation of the columns which would otherwise be random. Several micro- and nano-patterning methods such as photo-lithography, EBL, FIB, nanoimprint lithography (NIL), laser machining and direct laser writing (DLW) etc. can be used for pre-patterning the substrate. Method like LIL is especially suitable for making large areas of such patterns in an inexpensive and quick manner.

We combined the OAD and LIL techniques for fabricating PP-CTFs. In this chapter, we set out the details of the experimental apparatus and techniques used by us. In the first part of the next section, we explain the design considerations for an OAD chamber, the growth mechanisms for columnar structures, different possible morphological structures using this technique and some of their applications. In the later parts of the section, we explain the principle of LIL to fabricate large area patterns on photo-resist layers with submicrometer features and their structural characterization. In the third section, we explain the mechanisms of the geometry for shadowing the incident flux to fabricate periodically patterned CTFs, and give some experimental details of the 1-D and the 2-D pre-patterned substrates with their AFM and FESEM images. In the fourth section, we explain fabrication of dielectric and metallic CTFs

on 1-D and 2-D patterned substrates. As we are interested mainly in photonic and plasmonic properties of the PP-CTFs, so the fifth section outlines the experimental set-up for measuring the dispersion of the surface plasmons in the PP-CTFs and the optical diffraction efficiencies. The last section, the simulation techniques for studying electromagnetic properties and fields in the structured composite media are discussed.

2.2 Nano and Micro fabrication set up

2.2.1 Oblique Angle Deposition (OAD)

OAD method is a bottom-up self organization based method that can be used to grow high aspect ratio nanostructures with greatly reduced fabrication cost and time. An advantage of OAD over other nanostructuring methods is that the technique is suitable for mass production of large area samples.

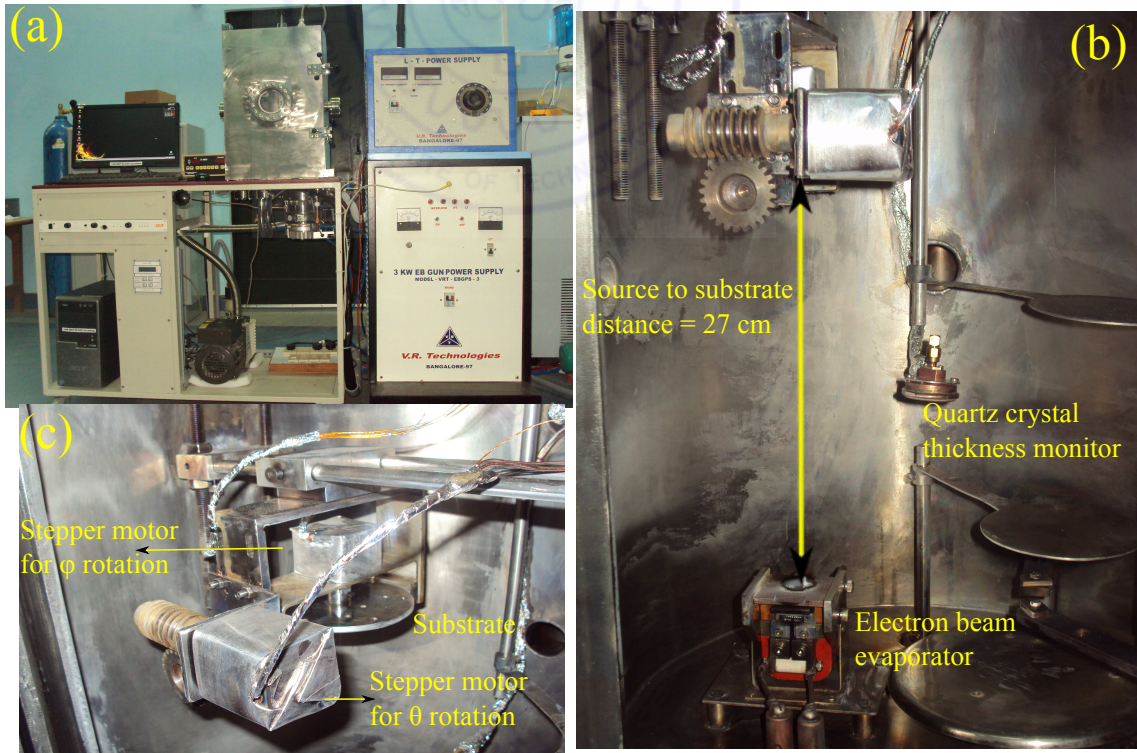


Figure 2.1: (a) Photograph of OAD chamber (b) inside view of the OAD chamber, where source to substrate distance=27 cm, quartz crystal thickness monitor and electron beam evaporator are shown. (c) movable substrate and two steppers motors are shown, where one is for θ rotation and other one is for ϕ rotation.

Design considerations for OAD chamber

Fig. 2.1 (a) shows the photograph of the OAD chamber which was used for the growth of nanostructures. Fig. 2.1 (b) shows the inside view of the OAD chamber where source (target material) to substrate distance was kept as 27 cm. A 3 kW electron beam gun power supply was used for electron beam evaporator. The accelerating voltage used was 6 kV and the current through the tungsten filament was 25 mA. To fabricate high quality structures, a collimated vapour flux is required, one way of realizing which is by simply increasing the source to substrate distance. However the number of collisions will increase if the vapour species has to travel a larger distance before reaching the substrate. The Number of collisions can be suppressed if the vapour mean free path is larger than the source–substrate distance, which can be attained by decreasing the residual pressure in the vacuum chamber or increasing the vacuum. High vacuum or lower pressure is required for larger mean free path, which depends on the pressure in the chamber as

$$l = \frac{k_B T}{\sqrt{2} \pi d^2 P}, \quad (2.1)$$

where k_B is the Boltzmann constant in J/K, T is the temperature in K, P is the pressure in pascals and d is the diameter of gas particles in meters. For example, at room temperature, with a number density of $10^{19} - 10^{15}$ molecules/m³ and as the vacuum changes from 10^{-3} mbar to 10^{-7} mbar, the mean free path varies from 10 cm to 1 km. A Rotary pump is used for getting rough vacuum down to about 0.1 mbar whereas a turbo-molecular pump is used for getting the high vacuum of about 10^{-6} mbar inside the chamber. Two gauges are connected to the OAD chamber to measure the pressure inside. One is a pirani vacuum gauge which measures the rough vacuum, pressure down to 10^{-3} mbar and the other one is cold cathod vacuum gauge which measures high vacuum. In our chamber, residual vacuum in the range of 2 to 5×10^{-6} mbar pressure is used for all the depositions.

Deposition rates are defined as the increase in film thickness per unit time and were measured with a water cooled quartz crystal thickness monitor (QCM) placed

close to the movable substrate. Fig. 2.1 (c) shows two vacuum compatible stepper motors (Dual Stepper Motor Drive Model SMD2, Arun Motors, UK), which are controlled through a controller and interfacing with a program written in LABVIEW instrumentation. The entire assembly is placed above the vapour source to adjust the angle of incidence of the vapour flux in situ during the deposition. The substrate motion is mainly described by two parameters as shown in Fig. 2.1(c). The schematic design of the OAD chamber is presented in Fig. 2.2(a), where the two rotation angles are clearly defined. One is vapour incidence angle α , the angle between substrate normal and incident vapour flux mean direction and the other one is ϕ , the angle of rotation about the substrate normal. We have used worm- gear arrangement to control the α rotation to fix the angle at any particular angle without slipping, because the worm will rotate the gear and allow higher torque to be transmitted but the gear can not rotate the worm. This allows the motor control unit to be used to control both the stepper motors by switching between them. An incident flux angle $\alpha = 0^\circ$ means the position of the substrate normal is directly pointing towards the source, whereas $\alpha = 90^\circ$ means substrate normal is perpendicular to the line joining between center of the vapor source to the center of the substrate. For the calibration of $\alpha = 0^\circ$, the position was adjusted for zero position using an intiation switch which was provided in the OAD arrangement itself. The resolution of stepper motor is 0.9° but the associated worm gear arrangement has a ratio of number of turns 1:40, hence the nominal angular resolution of α is 0.0225° and for ϕ is 0.9° .

Growth Mechanics

Self shadowing and ad-atom diffusion are the dominant growth mechanisms to control the growth of the columnar structures [82]. Under the high vacuum of the OAD chamber, initially the vapour flux arrives and randomly diffuse across the substrate surface. The adsorbed atoms or adatoms, (i) can join together and form a nucleus, (ii) can attach to existing nuclei or the adatom can re-evaporate from the surface. Each of the individual processes depends on its respective kinetics and energetics.

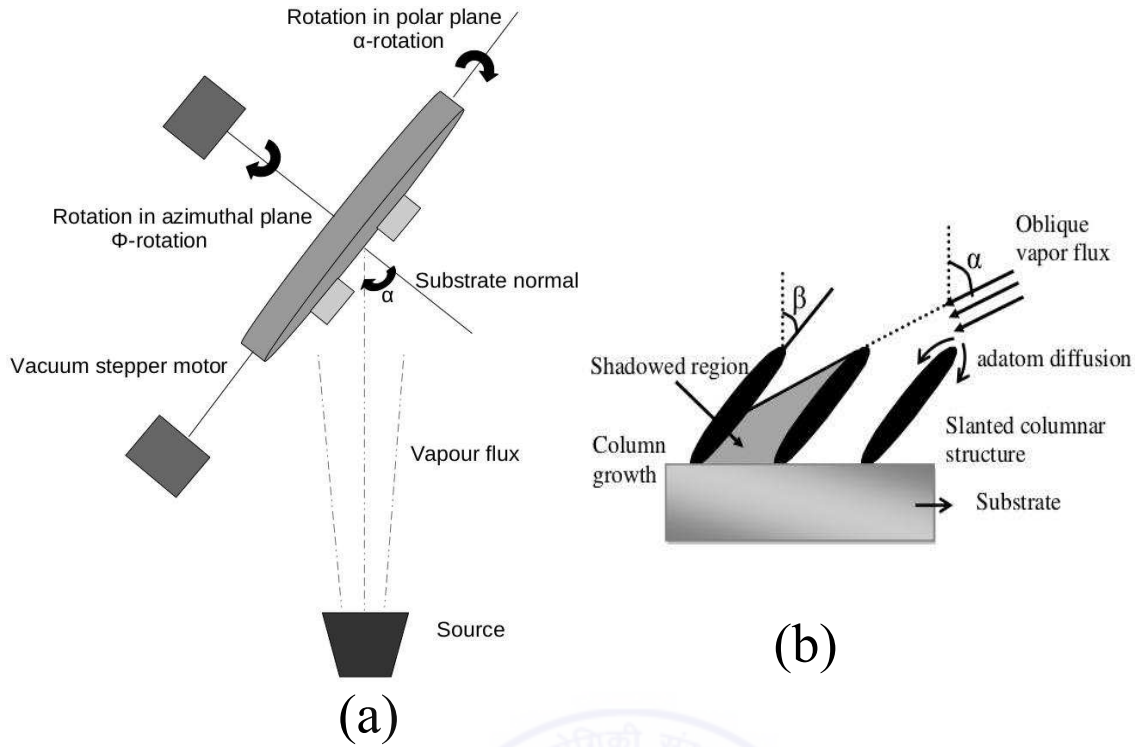


Figure 2.2: Schematic representation of the geometry of the OAD system showing the relative placement of the vapor source and the orientation of the substrate. (b) The growth of columns along the direction of incident vapour source, forming an angle β with the substrate normal, less than the incident angle α .

Depending on the surface and interfacial energetics of the substrate and condensing atoms, three growth regimes are followed by the continued deposition. The first growth mode is called layer or Frank Van der Merwe growth, where the growth will occur by monolayer formation. The atoms are strongly bound to the substrate than bound to each other and the nuclei in this regimes are two dimensional and single atom in height. The second growth mode is island or Volmer-Weber growth. Here the atoms interact with each other more strongly than the interaction with the substrate and the nuclei formation in this regime is three dimensional. The third growth regime is called layer plus island or Stranski-Krastanov growth. This third type of growth is a combination of the previous two modes. First the surfaces in monolayer are covered by the atoms due to the strong interaction with the substrate, and after the deposition of one or several layers island formation occur. Among all these growth regime, the second growth mode i.e Volmer-Weber growth mode is the most important case for OAD.

It is assumed that the atoms from the vapour flux come in with very low energy

such that they immediately get quenched on the substrate as soon as they reach the substrate, which would be effective at low temperatures (as explained below). The first arrivals will assemble into small clusters of atoms or molecules that act as nucleation centers for further growth. Material, thus, tends to get deposited on the already deposited nuclei rather than in the shadowed region, due to which the columns grow preferentially along the direction of incident vapour flux. This growth of columns further shadows out the other regions of the substrate. The angle of incidence controls the slant angle of the columns and affects the degree of shadowing, and thus, the nanoscale porosity of the film.

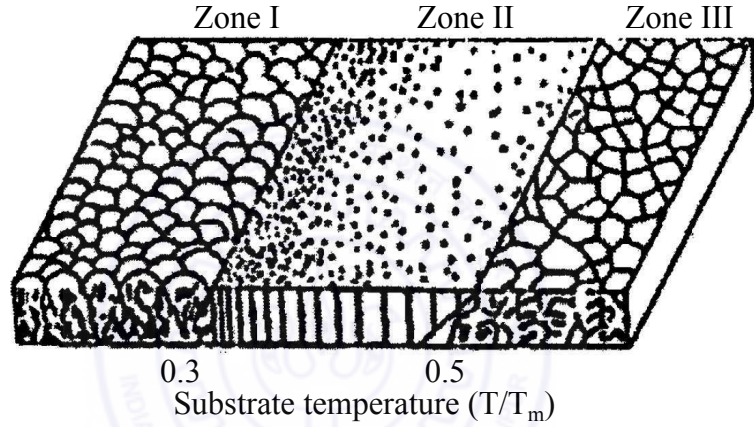


Figure 2.3: Structure zone model, where the transition temperatures between zones I and II and between zones II and III are 0.3 and 0.5 respectively. Figure is reproduced from (Ref. [78])

The formation of CTFs is well described by a *structure zone model* [78] as shown in Fig. 2.3. Movchan and Demchishin introduced three zones in phase space to describe the top surfaces and cross sections of the morphology of the grown structures. All the zones are categorized according to the effect of the substrate temperature (T_s) on the growing film. The Three zones (named as I,II,III), are sparated from each other by two transition temperatures T_1 and T_2 , where $T_1/T_m \simeq 0.3$ and $T_2/T_m \simeq 0.5$. T_m represents the melting point of the material being deposited. In zone I, $T_s < T_1$ and as a result diffusion is very slow because of the low temperature. Diffusion and substrate temperature are related by the equation [78],

$$D \propto \exp(-E_a/k_b T_s), \quad (2.2)$$

where k_b is Boltzmann's constant and E_a is the energy barrier of the diffusion process. Adatoms either have enough kinetic energy during deposition or receive thermal energy from the surface to overcome this energy barrier. In a physical vapour deposition process, the adatoms come with negligible kinetic energy. The limited adatom mobility due to lower substrate temperature results in quickly quenching the adatoms, and hence in a very porous columnar structure with tapered columns and domed tops. In zone II, the substrate temperature lies between T_1 and T_2 . Therefore due to slightly increased temperature, the column diameters increase and the tapering reduces, due to which dense CTFs are produced. In zone III, substrate temperature is larger than T_2 , due to which bulk diffusion along with surface diffusion occurs because of sufficient energy being available. The high ad-atom mobility makes the self-shadowing ineffective and results in the formation of clusters. The separation of the columns is more in the direction of the plane parallel to the incident plane of the vapour because of enhanced shadowing. On the other hand bundling occurs in the transverse direction due to unaffected shadowing, which leads to anisotropy in the columnar structure [1]. By rotating the substrate about a fixed axis this anisotropy can be reduced.

The slant angle of the columns (α) are found to be different from the incidence angle (β) of the vapour as shown in Fig. 2.2 (b). This observation is based on experiments under a variety of deposition conditions such as shadowing between the columns, deposition rate, deposition pressure, deposition temperature, vacuum composition, substrate type and crystallinity of the deposited material. In oblique incidence, atoms are shadowed by neighbouring atoms, due to which the average pair orientation depending on the distance between the atoms and relative vertical position of the atoms shifts from the vapour incidence direction towards the substrate normal. After reaching the substrate surface, the adatoms sustain a part of their parallel momentum.

According to Hara's model [83], this conservation of parallel momentum plays a major role in the formation of the column and the columnar axis deviates from the vapour incidence direction to the film normal. Different models have given different empirical relations between α and β in literature. From several experimental observations,

it was concluded that the column tilt angle β is less than the vapour incident angle α and the geometric relation is given by an empirical *tangent rule* of Nieuwenhuizen and Haanstra [8],

$$\tan\alpha = 2\tan\beta. \quad (2.3)$$

But with increase in oblique deposition angle, the tangent rule does not make satisfactory predictions. Hence, in that case, Tait's rule has been developed [84] alternatively to give

$$\beta = \alpha - \arcsin((1 - \cos\alpha)/2). \quad (2.4)$$

Fig. 2.4 shows the plot of column tilt angle β vs the deposition angle α , where the

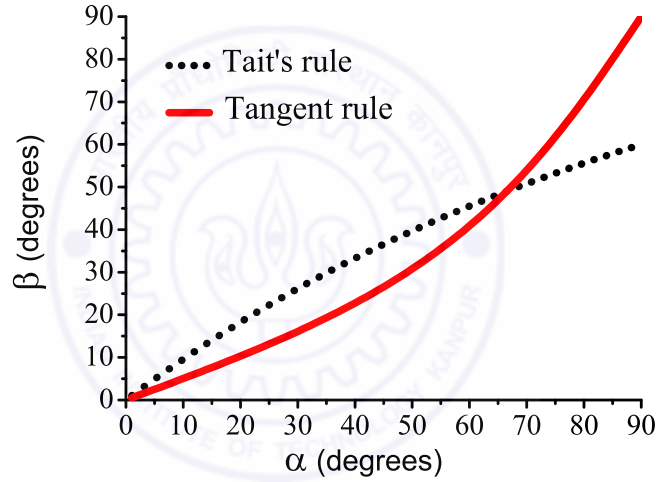


Figure 2.4: Plot of two different analytic curves relating the column tilt angle β and the deposition angle α . Solid red line represents tangent rule and black dotted line is according to Tait's rule.

solid red line and the black dotted line represent the two analytical curves according to the tangent rule and Tait's rule respectively.

Different Morphological Structures and their Applications

To grow CTFs, the substrate normal is kept fixed at an angle α with respect to the direction of incident vapor flux. Fig. 2.5 (a) shows CTFs made of SiO_2 , when $\alpha = 85^\circ$. The columnar morphology can be changed into different shapes by controlling

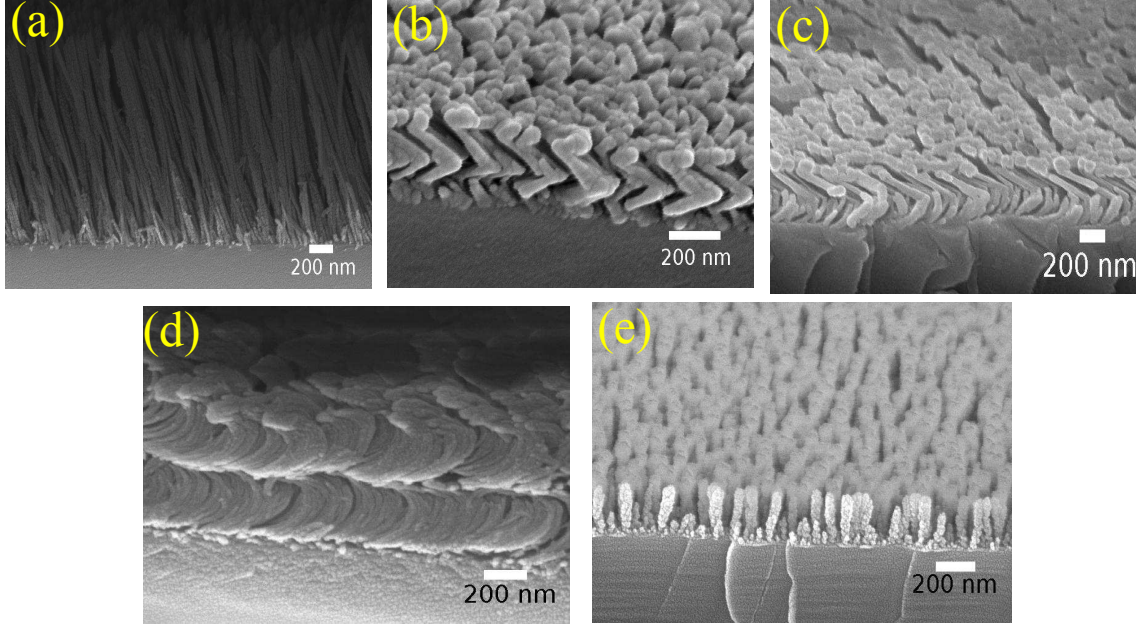


Figure 2.5: FESEM image of (a) SiO₂, CTFs (b) MgF₂, zig-zag (chevron) structure (c) MgF₂, square spiral structure (d) MgF₂, chiral structure (e) SiO₂, straight rods.

the substrate angular frequency (ϕ) and substrate position relative to the evaporation source. There are two different types of substrate rotation are used, one is a stepwise substrate rotation and the other one is continuous substrate rotation. Fig. 2.5 (b) and (c) show zig-zag and square spiral structures made of MgF₂, when $\alpha = 85^\circ$ with deposition rate of $5-6 \text{ \AA s}^{-1}$ and the substrate is rotated by an angle of $\phi=180^\circ$ and 90° respectively at stepwise regular intervals of 10 minutes. Fig. 2.5 (d) shows a chiral structure made of MgF₂ with the pitch of helix of about 300nm, when $\alpha = 85^\circ$ and the substrate is rotated continuously with a very slow rotation speed of 0.15 r.p.m. at a nominal deposition rate of $5-6 \text{ \AA s}^{-1}$. Fig. 2.5 (e) shows rods structure made of SiO₂, when deposited at a rate of $5-6 \text{ \AA s}^{-1}$ at an angle of $\alpha = 85^\circ$ and the substrate is rotated continuously with a very fast rotation speed. The angle of inclination of the nanocolumn and film porosity are controlled by changing the vapor incidence angle α .

Due to the multiscale porous nature of the structures grown by OAD, large surface areas becomes available and these have been suggested and used for various sensor applications [85,86]. The morphological anisotropy and chirality are expected to give rise to large optical birefringence [11]. Fig. 2.6 shows the transmitted intensity af-

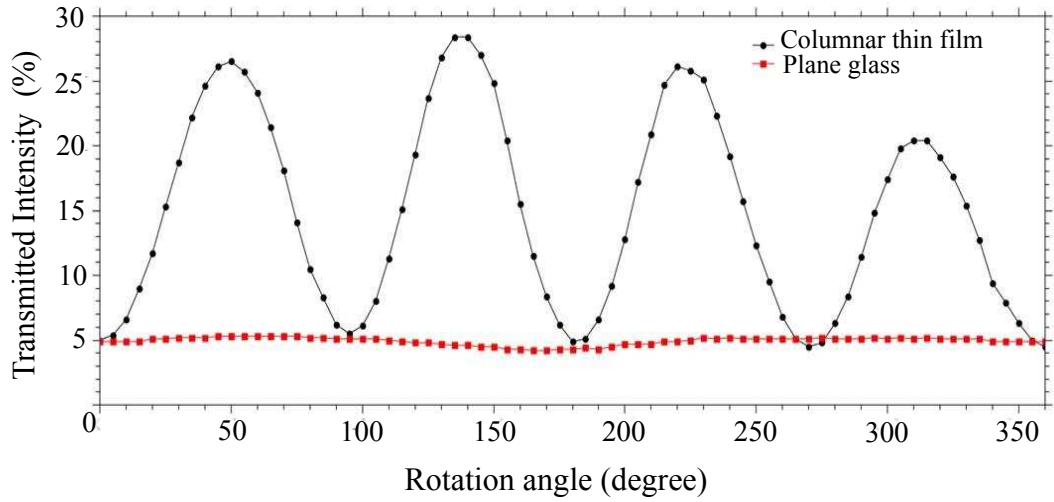


Figure 2.6: Transmission through CTFs of CaF_2 placed between two crossed polarizers as a function of rotation angle of the sample. Red line represents the transmission through plane glass film and black line represent the transmission through CTFs.

ter passing through the CTFs of CaF_2 placed in between two crossed polarizers as a function of rotation angle of the sample. Red line represents the transmission through plane glass substrate whereas black line represent the transmission through CTFs. In case of plane glass, the percentage of transmission is almost constant (5%) due to the isotropic nature of the glass. But for CTFs, the percentage of transmission varies from maximum value (28%) to minimum value (5%) which represent the optical birefringence of CTFs sample. Other important applications of these structures have been for linear polarization filters [87], circular polarization filters [5], narrow band pass optical filters [81], surface enhanced fluorescence [23] etc. STFs made of noble metals such as Ag and Au show highly sensitive surface enhanced raman spectroscopy (SERS) that is relevant for potential biosensing applications [22].

2.2.2 Laser Interference Lithography

LIL is a maskless nanolithography technique for patterning one- (1-D) and two- (2-D) dimensional periodic structures [88–90]. Even 3-D structures are possible with multi-beam techniques. In this technique, the interference pattern of two or more coherent beams of light are recorded in a light sensitive medium, such as a photoresist that re-

sponds to the periodic intensity distribution. By a single exposure of a photoresist for few seconds to a two beam interference pattern of sufficient intensity, one can produce 1-D sub-micron gratings, whereas by double exposures with a rotation of the substrate in between, different types of 2-D periodic structures such as square, hexagonal gratings are possible. The experimental set up for LIL is shown in Fig. 2.7 (a). The electric field vector of two coherent optical beams as shown in the schematic 2.7 (b) can be expressed as

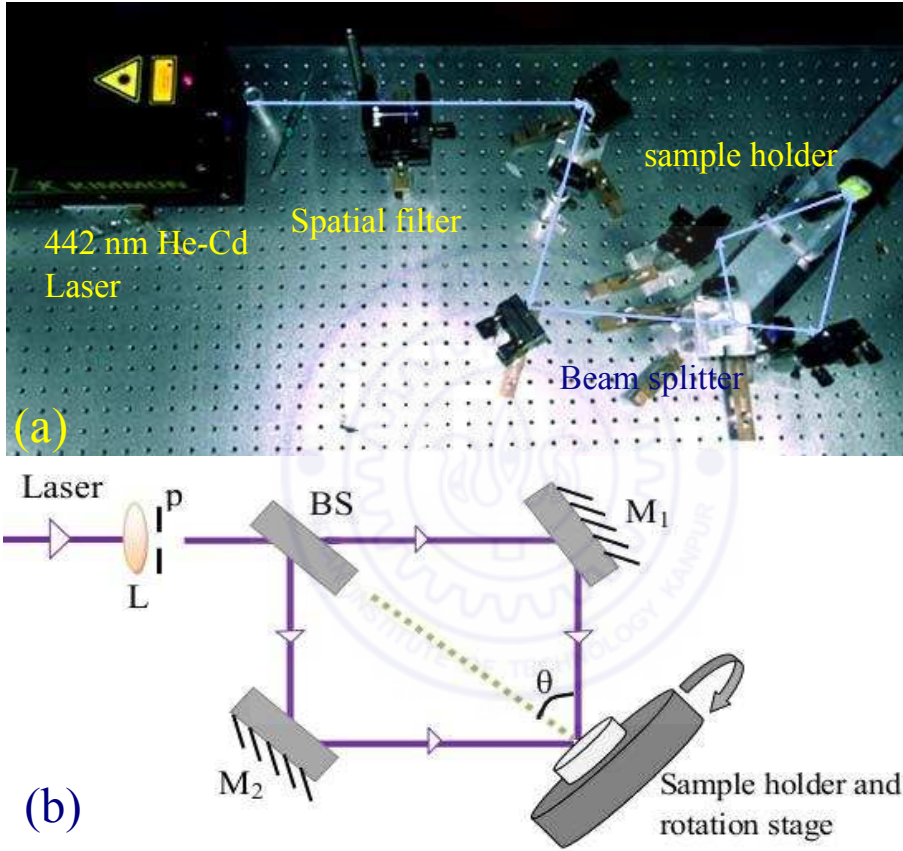


Figure 2.7: (a) Experimental set up of two beam LIL (b) Schematic diagram of LIL with beam splitter BS spatial filter containing lens L and pin hole P arrangement.

$$E_1(x, z) = E_{01} \exp[i(k_{x1}x + k_{z1}z - \omega t + \phi_1)]\hat{e}_1, \quad (2.5)$$

$$E_2(x, z) = E_{02} \exp[i(k_{x2}x + k_{z2}z - \omega t + \phi_2)]\hat{e}_2, \quad (2.6)$$

where E_{01} , $k_{x1,z1}$, ϕ_1 and \hat{e}_1 are amplitude, wave vector components, phase and unit polarization vector for the first coherent beam respectively, whereas E_{02} , $k_{x2,z2}$, ϕ_2 and \hat{e}_2 denote the same for the second coherent beam. The resultant intensity at a

given point of two coherent optical beams with the same polarization, generating 1-D periodic intensity modulation is given by

$$I(x, z) = |E_{01}|^2 + |E_{02}|^2 + 2E_{01}E_{02} \cos[(k_{x1} - k_{x2})x + (k_{z1} - k_{z2})z + \phi_{12}], \quad (2.7)$$

where $\phi_{12} = \phi_1 - \phi_2$, is phase difference between the two beams at a given point in space. The spatial periodicity of the interference pattern is determined by the difference between the wave vectors while the contrast of the interference pattern is controlled by the electric field amplitude, phase and polarization of each beam [88]. The periodicity d , of the resultant interference pattern is given by,

$$d = \frac{\lambda}{2n \sin \theta}, \quad (2.8)$$

where λ = wavelength of the laser used, n = index of refraction of the photoresist, θ = angle between the two beams that interfere. Minimum value of the period $d = \lambda/2$. By translating the position of the sample holder, the periodicity of the 1-D grating structure can be changed. For patterning of 2-D grating structures, the sample holder has to be rotated by an angle of 90° for square gratings with 4-fold symmetry and 60° for hexagonal grating structures with 6-fold symmetry. Several factors such as beam polarization, phase and fluence of the incident beam control the shape of the desired structure [88]. After patterning on the photoresist, the same structure can be transformed to a metallic structure by depositing metals on these fabricated gratings, and the subsequent use of lift off and etching techniques [91].

2.3 Structural characterization

For structural characterization of the nanocolumnar structures, a field effect scanning electron microscope (FESEM) (BP 40 SUPRA Carl Zeiss instruments) and to image the topography of the submicron dielectric gratings, atomic force microscope (XE70, Park Systems, South Korea) are used. For all the fabricated structures highly polished

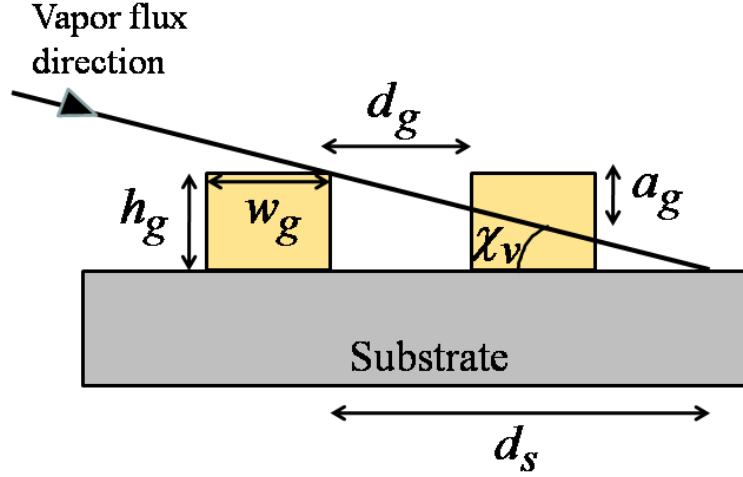


Figure 2.8: Schematic representation of the geometry of shadowing: where a_g is the exposure height, h_g is the seed height, w_g is the seed width and d_s is the inter-seed distance.

silicon wafer, and fused silica glass were used as substrates. For the FESEM imaging, a 5 nm layer of gold was deposited at normal incidence to reduce charging effect during the imaging. For cross sectional FESEM images, Si samples were cleaved usually along (001, the cleaving direction of Si) and for glass samples, the samples were broken by introducing cracks with a diamond tip on the other side and applying some pressure at the edges of the sample. All the geometrical parameters such as the tilt angle, lengths of the slanted columns along shorter and longer axes were estimated by averaging over 25 nanocolumns from the cross-sectional FESEM images of each sample.

2.4 Fabrication of periodically patterned CTFs

In order to grow periodically patterned structures, the substrates must be pre-patterned with 1-D or 2-D lattices of height variations which serve to nucleate the growth of the columns on the ridges while shadowing out the valleys. The regularity of the nanostructure can be controlled by optimizing the seed parameters such as height of the seed structure on the substrate which avoids random nucleation and the deposition rates. The size and shape of the seeds are critical parameters, whereas the composition of the seed material is less important and somewhat independent of the GLAD film material being deposited. The effect of lattice period, height and width of the seed

on grown structure is well explained in Ref. [92]. As the vapor flux is incident very obliquely, the ridges of the photoresist grating shadow the valleys of the grating from the collimated flux, resulting in almost no columnar growth in the shadowed regions. By controlling the size, shape and spacing between the seeds and the deposition rates, single or multiple columns will grow at each seed on the lattice.

Growth of periodically patterned structures can be understood in terms of a simple geometrical phenomenon of the self-shadowing process [93]. A simplistic model of the shadowing behaviour and its dependence on the depth modulation of the seed layer is presented schematically in Fig. 2.8. Here d_g , h_g and w_g are the distance between the two grating lines, height and width of the grating. χ_v is the angle between the average vapour flux direction and the substrate plane. d_s is the geometrical shadowing distance. Using proper photoresist pattern geometries, the shadowing distance of the collimated vapour flux can be controlled. A long range shadowing helps to grow CTF selectively on the top surface of both 1D and 2D pattern. The selectivity of the growth of CTFs on the sidewalls of the photoresist feature and on the bare bottom surfaces is directly related to the distance between the two seeds which in turn related to geometrical shadowing distances. The shadowing distance d_s as shown in Fig. 2.8 due to an oblique angle flux of sidewall height h_g is given by $d_s = h_g / \tan(\chi_v)$. If $d_g < d_s$, then the growth on the side walls of the seeds is expected [93]. A fraction $a_g \approx d_g / d_s$ describes the exposure height of the adjacent seed as shown in Fig. 2.8. Periodically patterned structures such as fabrication of submicrometer regular arrays of pillars and helices have also been reported [94–96].

Glass slides or fused silica pieces and silicon wafers were chosen as substrates for the fabrication of PP-CTFs. The samples fabricated on glass slides were used for the optical experiments relevant to diffraction in transmission or the excitation of SPP waves particularly when transmission needs to be measured. The samples fabricated on silicon substrates were mostly used for cross-sectional imaging on a field-emission scanning electron microscope (FESEM), principally due to the ease of cleaving the silicon pieces.

2.4.1 Substrate pre-patterning

LIL was used to pre-pattern the positive photoresist films that act as periodic seed layers for subsequent deposition of a CTF. A 500-nm-thick film of positive photoresist (ma-P 1205, Micro-resist Technology) was spin coated on pre-cleaned smooth glass and silicon substrates baked at 80°C and then exposed to an interference pattern generated by superposing two laser beams split out from a He-Cd laser (442 nm, 30 mW, Kimmon, Japan). The photoresist film was then developed to form uniform gratings over areas of about 10 mm². By single exposure of 1 minute, one-dimensional gratings were patterned, whereas by double exposures for 30 sec-30 sec, after rotating the the photo-resist film by 90° and 60° angles resulted in the formation of square and hexagonal patterns. Atomic force microscopy (AFM) was used to determine the periodicity d for different gratings. All gratings had an approximately 50–50 duty cycle and a depth modulation of 100 nm. Fig. 2.9 (a) shows AFM image of one dimensional grating with periodicity 700 nm. Fig. 2.9 (b) shows FESEM image of two dimensional hexagonal grating with periodicity 800 nm.

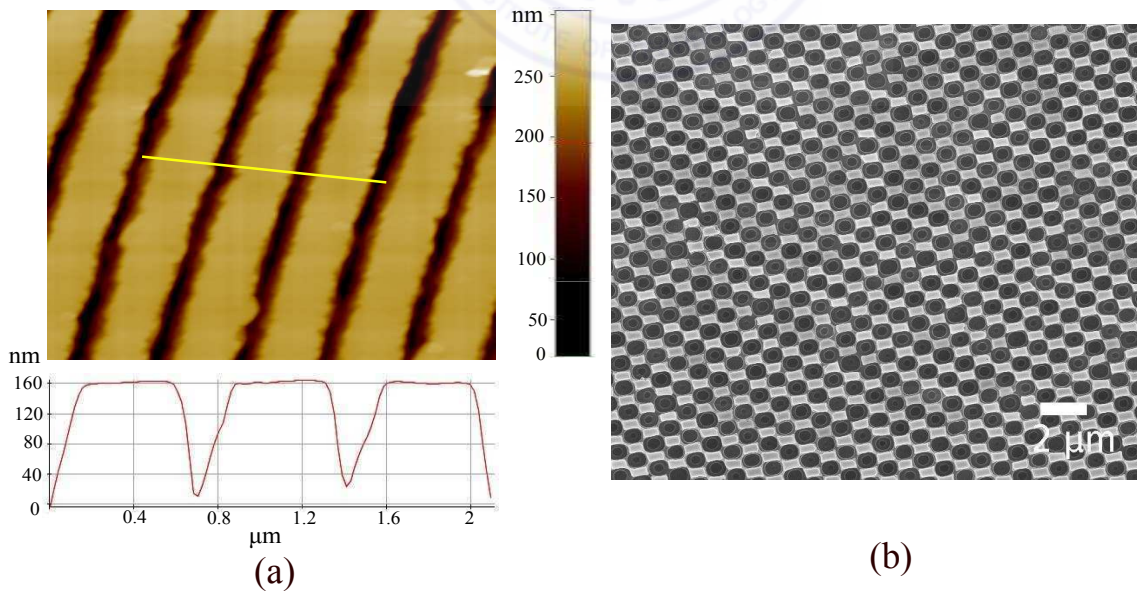


Figure 2.9: Laser interference lithographically patterned photo-resist on a glass substrate, (a) AFM image of one dimensional grating with periodicity 700 nm, (b) FESEM image of two dimensional hexagonal grating with periodicity 800 nm.

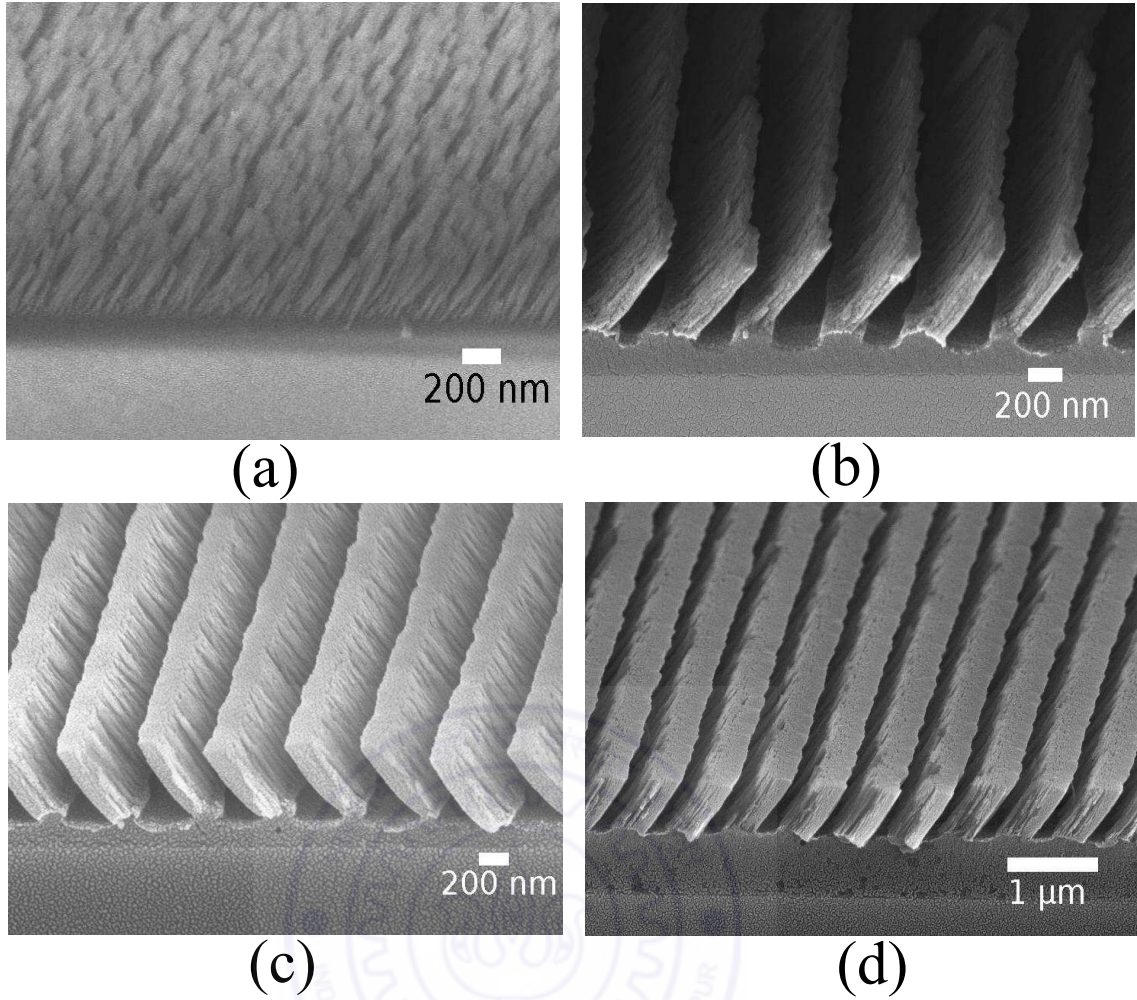


Figure 2.10: Cross-sectional FESEM images comparing aperiodic and periodic OAD SiO_2 CTFs growth on silicon substrates at a deposition angle of $\chi_v = 10^\circ$ (a) CTFs on planar unpatterned substrate; periodically patterned CTFs deposited on 1D grating (b) with periodicity 600nm and seed width is 300nm, (c) with periodicity 600nm and seed width is 200nm and (d) with periodicity 500nm and seed width is 300nm.

2.4.2 Fabrication of periodically patterned dielectric CTFs (PPDCTFs)

Periodically patterned dielectric CTFs were made by depositing SiO_2 , MgF_2 or CaF_2 and directing the vapour flux at an oblique angle of $\chi_v = 10^\circ$ towards lithographically fabricated micrometer /sub- micrometer gratings and laser micromachined glass substrates. The patterned substrates were loaded on a stepper motor controlled substrate holder, which is 27 cm above the electron beam crucible. Both patterned and unpatterned substrates were kept inside the chamber to observe the differences, and

compare the aperiodic and periodic structures under identical deposition conditions. Deposition was carried out on gratings with various periods and ridge widths simultaneously to ensure identical deposition conditions. The deposition rate was maintained at $15-20 \text{ \AA s}^{-1}$ with the help of a quartz crystal monitor. The base pressure within the chamber was 5×10^{-6} mbar, which rose to about 1.2×10^{-5} mbar during the deposition. CTFs of about 600-nm nominal thickness (nominal thickness because we used density and acoustic impedance for solid films for the QCM detector while we were actually depositing porous films) were grown in this manner. After completing the deposition, the samples were first cleaved and imaged by FESEM.

Fig. 2.10 (a) shows the cross-sectional FESEM image of CTFs on a planar unpatterned substrate. Fig. 2.10 (b) shows the cross-sectional FESEM image of CTFs deposited on a 1-D grating with periodicity of 600nm and a ridge width of 300nm. Fig. 2.10 (c) shows the cross-sectional FESEM image of CTFs deposited on a 1-D grating with periodicity of 600nm and ridge width of 200nm. Fig. 2.10 (d) shows cross-sectional FESEM image of CTFs deposited on a 1-D grating with periodicity of 500nm and the ridge width of 300nm. It was observed from all the FESEM images that, no film growth took place in the shadow regions behind the seeds and thickness of the slanted structure increases with the increase in the ridge width under identical deposition conditions.

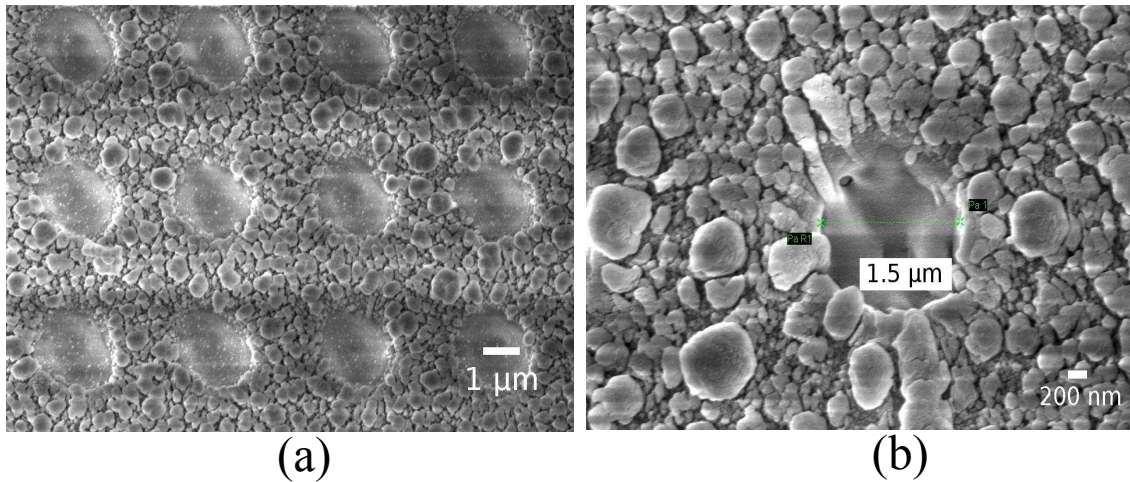


Figure 2.11: (a), (b) Top view FESEM images of periodically patterned structures on laser machined glass substrate consisting of helical columns of MgF_2 grown by OAD. Width of the hollow resion is $\sim 1.5 \mu\text{m}$ with total periodicity $\sim 3 \mu\text{m}$.

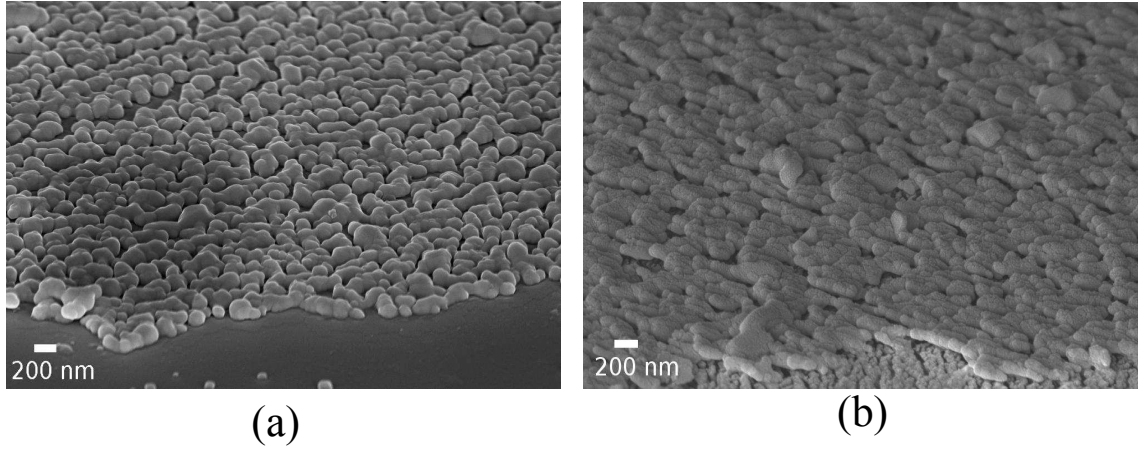


Figure 2.12: (a) Top view FESEM image of silver columnar structure by thermal evaporator deposited at a vapor incidence angle of 85° when deposition rate is $3 \pm 0.5 \text{ \AA s}^{-1}$ and (b) cross-sectional FESEM image of silver columnar structure when deposition rate is $11 \pm 0.5 \text{ \AA s}^{-1}$.

Laser micromachining on a glass substrate was carried out by using a 248 nm KrF excimer laser at 323 mJ pulse energy. Fig. 2.11 (a) and (b) show top view FESEM images periodically patterned structures on laser micromachined glass substrates consisting of helical columns of MgF_2 grown by OAD. In these cases, the size of the hollow regions ($\sim 2 \mu\text{m}$) and the period ($\sim 4 \mu\text{m}$) are much larger. There is no deposition in the holes and an architecture of a chiral medium with air holes is realised.

2.4.3 Fabrication of periodically patterned metallic CTFs (PPM-CTFs)

CTFs of silver were fabricated by thermal evaporator using a primary current of 11 A. Fig. 2.12 (a) shows top view FESEM image when deposition rate of silver vapor flux is $3 \pm 0.5 \text{ \AA s}^{-1}$ and Fig. 2.12 (b) shows cross-sectional FESEM image when deposition rate is increased up to $11 \pm 0.5 \text{ \AA s}^{-1}$. It can be seen that due to poor collimation, silver vapor flux diffuse all over the substrate even after increasing the deposition rate and hence column formation did not happen in both the cases. Further, the thermal source probably contributed to a radiant heating of the substrate as well. The electron beam evaporator provides a better collimation of the vapor flux than the thermal evaporator

as observed in the case of dielectrics. The radiant heating is also much lesser. Hence we used the electron beam evaporator for the fabrication of periodically patterned silver columnar structures.

Periodically patterned silver CTFs were fabricated by electron beam evaporator with 6 KV accelerating voltage and 20 mA current. A collimated flux of silver (Ag) vapour was directed obliquely towards 1-D and 2-D gratings of photoresist in a vacuum chamber. Silver vapor was directed at an angle $\chi_v = 4^\circ$ with respect to the mean

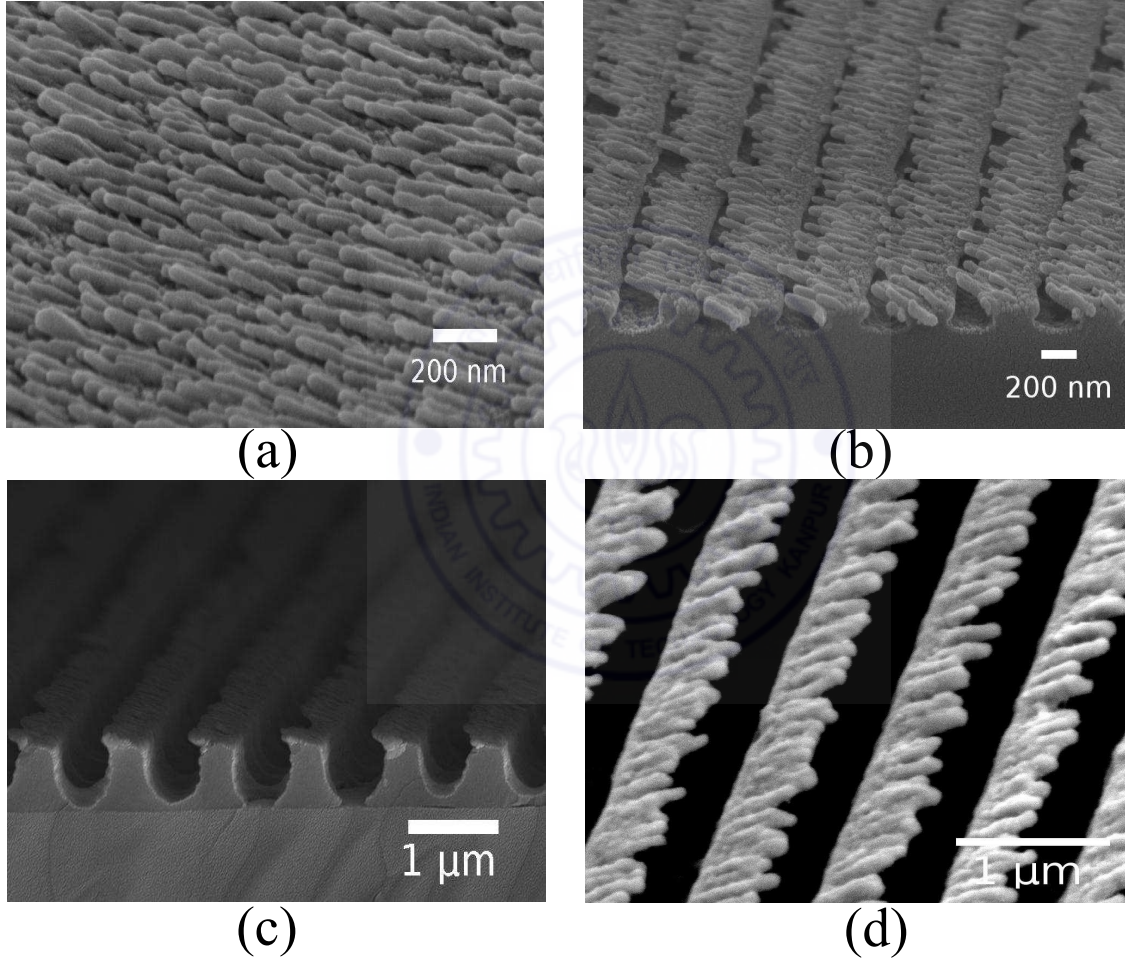


Figure 2.13: Cross-sectional FESEM images comparing aperiodic and periodic OAD silver CTFs growth on silicon substrates at a deposition angle of $\chi_v = 4^\circ$ (a) CTFs on planar unpatterned substrate; periodically patterned CTFs deposited on 1D grating (b) with periodicity 500nm and ridge width is 250nm, (c) with periodicity 1μm and ridge width is 500nm, (d) with periodicity 800nm and seed width is 200nm.

plane of the grating. The deposition rate was maintained at $5 - 7 \text{ \AA s}^{-1}$ with the help of a quartz crystal monitor. Base pressure within the chamber was 4×10^{-6} mbar, which rose to about 1×10^{-5} mbar during deposition. CTFs of about 500 nm nominal

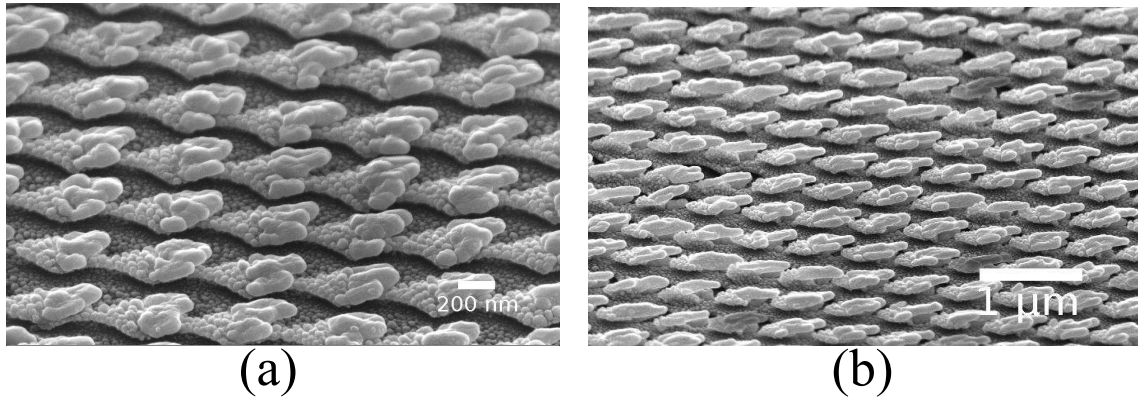


Figure 2.14: Cross-sectional FESEM image of Ag CTFs deposited on a 2-D square grating (a) with periodicity 700nm and seed width is 350nm, (b) with periodicity 500nm and seed width is 250nm.

thickness were grown in this manner.

Fig. 2.13 (a) shows top view of FESEM image of Ag CTFs on planar unpatterned substrates. Randomly arranged silver nanocolumns are clearly observed from the image. Fig. 2.13 (b) shows the cross-sectional FESEM image of Ag CTFs deposited on a 1-D grating with periodicity of 500nm and ridge width of 250nm. In this case silver nanocolumns appear only on the ridges. Fig. 2.13 (c) shows the cross-sectional FESEM image of Ag CTFs deposited on a 1-D grating with periodicity of $1\mu\text{m}$ and ridge width of 500nm. The width of the ridge is almost covered by the silver nanocolumns as the projection of the length of the silver column is almost equal with the ridge width. Fig. 2.13 (d) shows top view of FESEM image of Ag CTFs deposited on a 1-D grating with periodicity 800nm and ridge width is 200nm. In this figure due to the smaller ridge width, the larger separation between the silver nanocolumnar arrays can be observed. From all the figures such as 2.13 (b), (c) and (d) it can be clearly observed that the density of the silver nanocolumns reduces when the ridge width is almost equal to the diameter of the single silver column.

Fig. 2.14 (a) shows the cross-sectional FESEM image of Ag CTFs deposited on a 2-D square grating with periodicity 700nm and ridge width 350nm. In this case, a bunch of just two or three nanocolumns are appear on a single seed and the separation between the bunches are equal on both sides of 2-D gratings. Fig. 2.14 (b) shows the cross-sectional FESEM image of Ag CTFs deposited on a 2-D square grating with

periodicity 500nm and ridge width is 250nm. Here, in this case, due to the smaller width almost a single nanocolumn appears on a single seed.

From all the FESEM images as shown in Fig. 2.10, 2.13 and 2.14, We can clearly see the differences in the morphology of periodically patterned structures and their dependence on pattern seed geometry. The seed enforced structural periodicity is maintained throughout the film, even as the OAD columns continue to grow. The seed pattern shadows extend all the way from the back of one seed to the front of the nearest neighboring seed in the direction of the incoming flux.

2.5 Optical Measurements

2.5.1 Measurement of Surface Plasmon Resonances and dispersion

Angle-resolved transmittance spectra of the periodically patterned CTFs were determined using a collimated beam of beam size 1mm×1mm from a 100-W tungsten-halogen lamp and a fiber spectrometer (USB4000+, Ocean Optics) with a resolution of 0.5 nm in the 500-1000 nm wavelength range. A Glan–Thompson polarizer was used to linearly polarize (either *p* or *s*) the incident light. The optical set-up is shown in Fig. 2.15. The sample was placed on a motorized rotation stage, a micro-stepping motor, which is computer controlled by interfacing with a program written in LABVIEW instrumentation and synchronized with the NIR-Visible spectrometer. An Ocean Optics spectrometer (model HR 2000+) was used to record the spectrally analyzed transmission beam. The transmission spectra were obtained at an angular rotation of the grating in steps of 0.1°. Dispersion plots are presented in a 2-D contour plot with transmission dips and peaks represented by colour bar. The locus of transmission minima as a function of angle of incidence (θ) and wavelength (λ) give the dispersion of the surface plasmon.

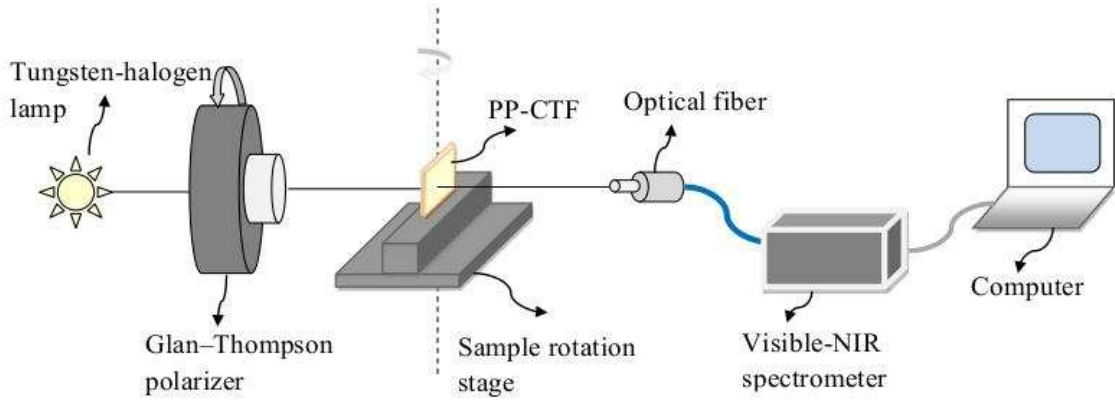


Figure 2.15: Schematic of the optical set-up to measure the angle-resolved transmittance spectra for light transmitted through the plasmonic thin films/CTF samples.

2.5.2 Diffraction efficiency measurement

Diffraction efficiencies of the periodically patterned CTFs were measured using lasers of wavelengths 442, 473, 532 and 633 nm. A beam splitter is used in front of the laser, which divides the original beam into two parts. One beam is used to measure the intensities of incident, 0th, +1 and -1 diffracted orders and the other beam is used as a reference to monitor the fluctuation of the input laser light at every instant. A Glan-Thompson polarizer was used to linearly polarize the incident light (usually either p or s polarization state). A silicon photodiode placed on a goniometric stage was used to measure the laser intensity at different angles for the zeroth and higher diffraction orders after passing through the samples. Neutral density filters were used to attenuate the beam to avoid saturation of the photodiode. An excimer laser of wavelength 248 nm was also used to measure the diffraction efficiency of periodically patterned dielectric structures. Laser power meters were used to measure the various powers for unpolarized light.

2.6 Techniques for Numerical Simulations

In this thesis, full wave numerical simulations were carried out in three-dimensions to study the electromagnetic properties of periodically patterned metallic structure. A FEM based software (COMSOL Multiphysics, Version 4.4, 3-dimensional harmonic propagation mode in RF module) with a 32 node computer cluster and 64 GB RAM is used for these studies.

FEM is a spectral technique [97] for finding approximate solutions to boundary value problems involving partial differential equations. This method is used to solve a large variety of problems encountered in practice such as steady or transient problems in linear or nonlinear regimes for one, two and three dimensional domains. The term finite element emanates from the procedure in which a continuous physical structure is divided into small, but finite sized elements and variational methods are used from the calculus of variations to solve the problem by minimizing an associated error function.

The elementary modelling steps in COMSOL Multiphysics are given by,

1. Selection of proper application mode such as RF module (used in this work), Wave Optics module, Heat Transfer module etc.
2. Draw the geometry of the structure from elementary bodies like rectangle, cylinder or ellipsoid (used in our case) or otherwise the geometry can also be extruded from the 2D drawing or can directly be loaded from the CAD.
3. Define the incident frequency or wavelength, boundary conditions and material parameters like refractive index or permittivity from material library or can be specified by the user etc.
4. Mesh the geometry, either choose it from the predefined (we chose extremely fine meshing for the volume occupied by the silver nanocolumn from predefined) or defined by the user.
5. Choose the solver parameters and solve the problem. We have used the para-

metric solver to determine the wavelength dependent reflectance and transmittance.

Since finite element based numerical techniques are more suitable for encapsulating geometrical feature [98], we employed the commercial software (COSMOL MULTIPHYSICS) based on FEM to study the electromagnetic properties.

Fig. 2.16 shows the simulation domain which is used to model the periodic silver nanocolumnar arrays. The simulation domain has one unit cell which contains one silver column that is tilted with respect to the substrate normal at a slant angle of α in the air domain. The silver column is placed on a photo-resist which is upon a glass substrate. The material properties of silver, photo-resist and glass like refractive indices and permittivities can be defined either from the model library or they can be user defined.

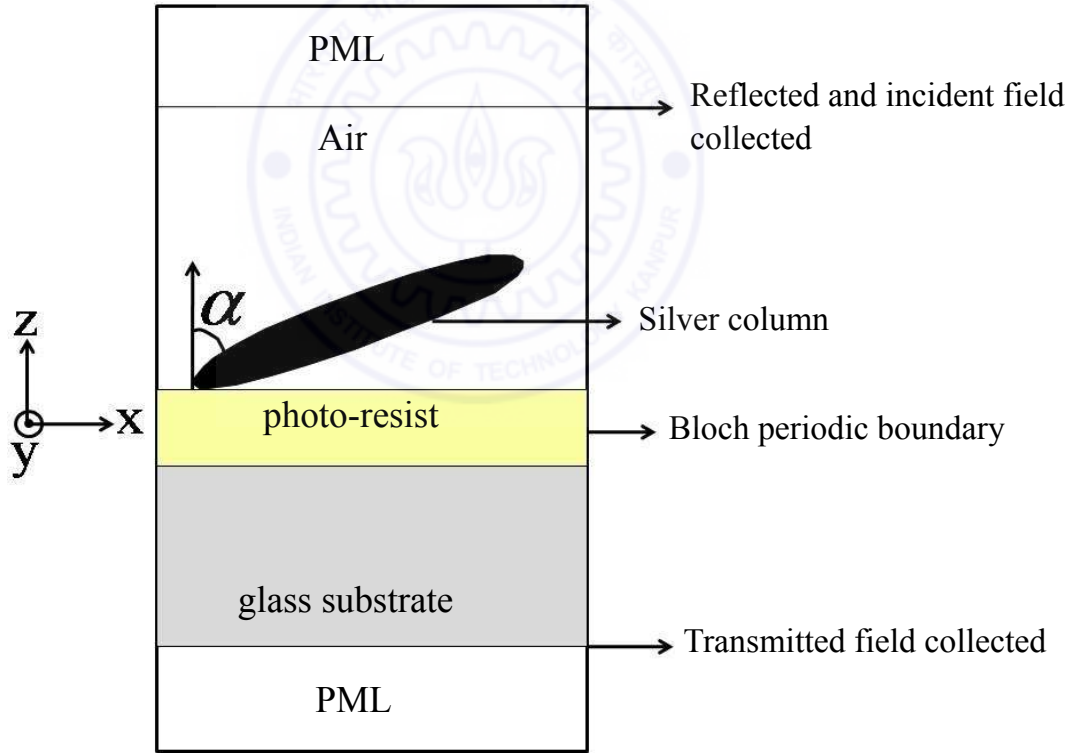


Figure 2.16: The structure of FEM simulation used to model periodic silver nanocolumnar arrays.

Six boundary areas are there within a computational domain and proper boundary conditions have to be defined. Along the z direction perfectly matched layer (PML) boundary conditions are applied above and below the periodic array to prevent multiple

reflections of the incident wave [97]. Periodic boundary conditions (PBC) consistent with the Floquet theory [59] were applied along both the x and y directions. PBC along x and y signifies multiple silver columns in reality, which allows us to calculate the diffracted modes, making a large saving of memory and computational time. Extremely fine meshing (4 nm) has been used for describing the Ag nanocolumns and regions close to them, which minimizes the numerical errors in the calculations. Periodic boundary conditions at the faces perpendicular to x and y directions must have identical meshes. Port conditions are applied for the incident wave in the top interior boundary of the PML, which collect the reflected and transmitted fields after interacting with the structure in the top and bottom boundary respectively. Periodic ports conditions are used to measure the reflected and transmitted diffraction orders.

Compared to other simulation methods, this COMSOL simulation method is well suited for the solutions of our problem, as this provides Floquet periodic boundary conditions with periodic port to compute the reflected and transmitted diffraction orders as a function of incident angles and wavelength.

2.6.1 Limitations of Finite Element Methods

Despite the several advantages of finite element methods,

1. the most significant limitation of finite element methods is that the accuracy of the expected solution is usually a function of the mesh resolution.
2. obtaining solutions with finite element methods often needs substantial amounts of computer memory and user time.
3. still an approximate technique and provides solution only at nodal points.

Chapter 3

Periodically patterned dielectric CTFs as blazed diffraction gratings

3.1 Introduction

Diffraction gratings with high efficiency are very important for a variety of applications, such as spectroscopy, lithography and optical telecommunications. Blazed diffraction gratings represent a special class of diffraction gratings, which have an ability to enhance diffraction intensity at the non-specular reflection/transmission diffraction order. When incident light falls on a grating with symmetric profile, the energy is distributed into different specular and non-specular diffraction order. But in case of the asymmetric surface profile, a grating can concentrate most of the energy from an incident wave into a specified non-specular diffraction order, and hence increases the diffraction efficiency of that particular order, which is known as blazing effect. Mostly blazed gratings have a sawtooth profile instead of the conventional rectangular profile.

In literature, people have usually reported fabrication of blazed grating using interference lithography and anisotropic etching, which is then replicated using nanoimprint lithography [99], which are very expensive methods. One of the difficulty with the sawtooth profile is the fabrication of the structure with ideal size and profile. Symmetric binary gratings furnished with an asymmetric high refractive index coating exhibit a

blazed grating effect and produce high diffraction efficiencies [100]. Symmetric gratings are fabricated by standard UV casting process with 440 nm period and subsequently 150 nm of ZnS is evaporated on top of that at an oblique angle. The structure shows 70% diffraction efficiency for unpolarized light and 90% diffraction efficiency for polarized light into the first order at a wavelength of 510 nm. It was also mentioned that, replacing ZnS material with metal, the presented structure is capable of enhancing one of the evanescent modes to launch surface plasmons into a specific direction for p -polarized light which is similar to the work investigated in [101].

An alternative approach of the conventional blazed grating structure is binary blazed grating (BBG, explained in Chapter 1), which is comparatively easier to fabricate. BBG is composed of surface-relief diffractive elements with subwavelength binary features which operate in the visible domain. Blazed binary subwavelength gratings were fabricated by etching of a TiO_2 layer coated upon a glass substrate [102]. The grating composed of square array of square pillars and designed to work for He-Ne operation. First order diffraction efficiencies were reported as 82.4% and 81.7% for TE and TM polarization, respectively. With the progress of nanofabrication technologies, it is possible to fabricate such kind of structures. Many researchers have reported the fabrication of BBG structures by several methods, for example by a combination of electron-beam lithography and reactive ion etching [103].

In this thesis, we made a blazed grating using very cost effective technique by combining LIL and OAD technique. A CTF fabricated by OAD is analogous to biaxial crystal and can be used for many different kinds of optical devices [2]. Periodic patterning of a substrate at micrometer and sub-micrometer length scales before the deposition of a CTF on it can result in a photonic structure with controllable anisotropy and optical response. Deposition on a patterned substrate may result in a patterned CTF, because the seed pattern of the substrate shadows out various areas in relation to the arriving collimated vapor flux, thereby preventing deposition in these areas [93, 104]. A periodically patterned CTF (PP-CTF) can be expected to have interesting optical properties due to the interplay of anisotropy and transverse periodicity. Thus, a CTF

deposited on a periodic array of rectangular grooves was envisioned to function as a narrowband linear-polarization rejection filter [81].

In this study, PP-CTFs were made by evaporating CaF_2 and directing the vapor flux obliquely towards lithographically fabricated micrometer/sub-micrometer gratings. The growth of the PP-CTFs was controlled by the deposition rate to form prismatic air cavities within them. These PP-CTFs function like blazed diffraction gratings with asymmetric diffraction patterns and diffraction efficiencies up to 80% in transmission at ultraviolet-visible wavelengths. Diffraction theory adequately establishes that the blazing action arises due to the prismatic cavities and explains the measured diffraction efficiencies.

3.2 Behaviour of PPCTFs as blazed diffraction gratings

3.2.1 Deposition and Structural morphology of the PPCTFs

The cross-sectional FESEM image of PP-CTFs with prismatic air inclusions is shown in Fig. 3.1 (a). The PP-CTFs studied here in this chapter are made by evaporating CaF_2 and directing the vapor flux obliquely towards lithographically fabricated micrometer/sub-micrometer gratings. CTFs were deposited by electron-beam evaporation of CaF_2 , the collimated vapor being directed at angles of 10° - 20° with respect to the mean substrate plane, with deposition rates of $15 - 20 \text{ \AA s}^{-1}$. The base pressure in the vacuum chamber was 5×10^{-6} mbar that dropped to about 1.2×10^{-5} mbar during deposition. By controlling the vapor flux, it was possible to grow merging columns of CaF_2 such that prismatic air columns were periodically formed in the structure. Typically each nanocolumn grows along the flux direction, but also expands in the lateral direction in a cauliflower-like growth pattern. This results in PP-CTF with typically flaring out nanocolumns with a gross nanocolumns directionality as shown in Fig. 3.1

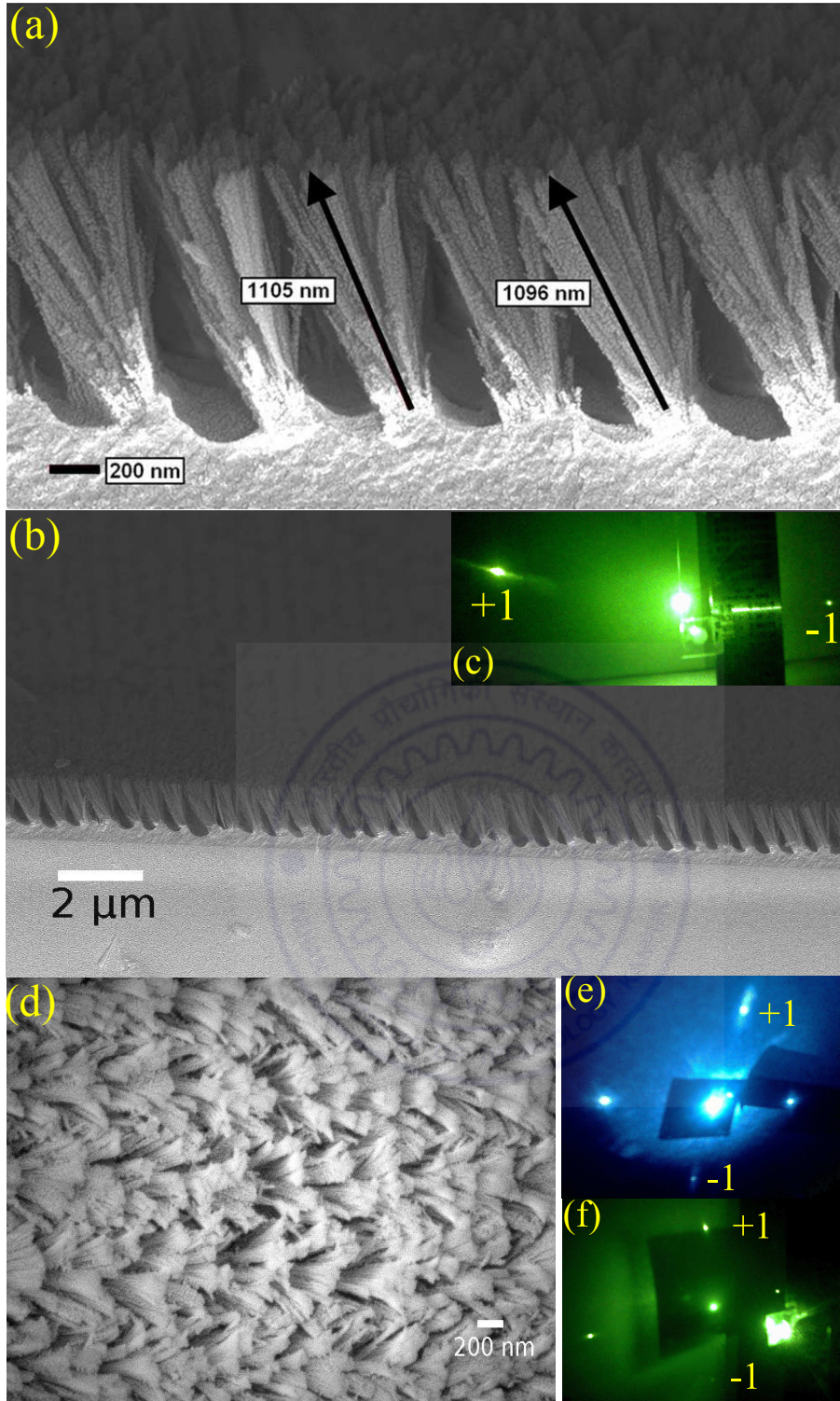


Figure 3.1: (a),(b) Cross-sectional FESEM image of a 1100-nm-thick PP-CTF of CaF_2 deposited on a 1-D photoresist grating of 600-nm period. The prismatic (triangular) air cavities are clearly visible. (c) Asymmetric diffraction through the structure is shown at $\lambda = 532$ nm. (d) Top view of the FESEM image showing flaring of nanocolumns. (e) and (f) Asymmetric diffraction through PP-CTF on a 2-D photoresist grating at $\lambda = 473$ nm and $\lambda = 532$ nm respectively.

(a), (b) and clearly observed from the Fig. 3.1 (d). Triangular prismatic air cavities are formed within the growing thin film due to the merging of the slightly diverging columnar structures, as revealed by the FESEM image shown in Fig. 3.1 (a) and (b). Fig. 3.1 (b) shows the pattern on large area which is required for free space optical measurements. Fig. 3.1 (c) shows the asymmetric diffraction of light with large differences of intensity between the +1 and -1 orders on transmission through the structure at $\lambda = 532$ nm. The vapor incidence direction and the rate of deposition can be effectively used to change the shape and angles of the prismatic inclusions and hence, the diffractive properties. The detailed fabrication process is given in Chapter 2. We confirmed that the deposited PP-CTFs are reasonably uniform over areas larger than 10 mm^2 .

Fig. 3.1 (e) and (f) show diffraction through PP-CTF of CaF_2 deposited on a 2-D photoresist grating with 600 nm period, at $\lambda = 473$ nm and $\lambda = 532$ nm respectively. It is clear from the two images that asymmetric diffraction appears only along one direction, where CTFs are oriented. But in the perpendicular direction, the diffraction between +1 and -1 orders remain symmetric. So, it can be understood that the direction of orientation of CTFs is more important rather than the nature of grating periodicity.

3.2.2 Theory of PPCTF as an anisotropic blazed grating

An analytical approach based on the scalar diffraction theory is used to calculate the diffractive properties of PP-CTFs made of dielectric materials. Fig. 3.2 (a) schematically represents the PP-CTF as a phase grating. Note that the $x - z$ plane is the morphologically significant plane for the CTF. For light incident and diffracted in this plane, the s - and p - polarized plane waves essentially decouple and a scalar treatment of the diffraction suffices [1]. For the principal axes of the CTF shown in Fig. 3.2 (a), let us take n_1, n_2, n_3 to be the principal refractive indices, where n_1 is along the long axis of the columns, and n_2 and n_3 are the indices along the directions perpendicular

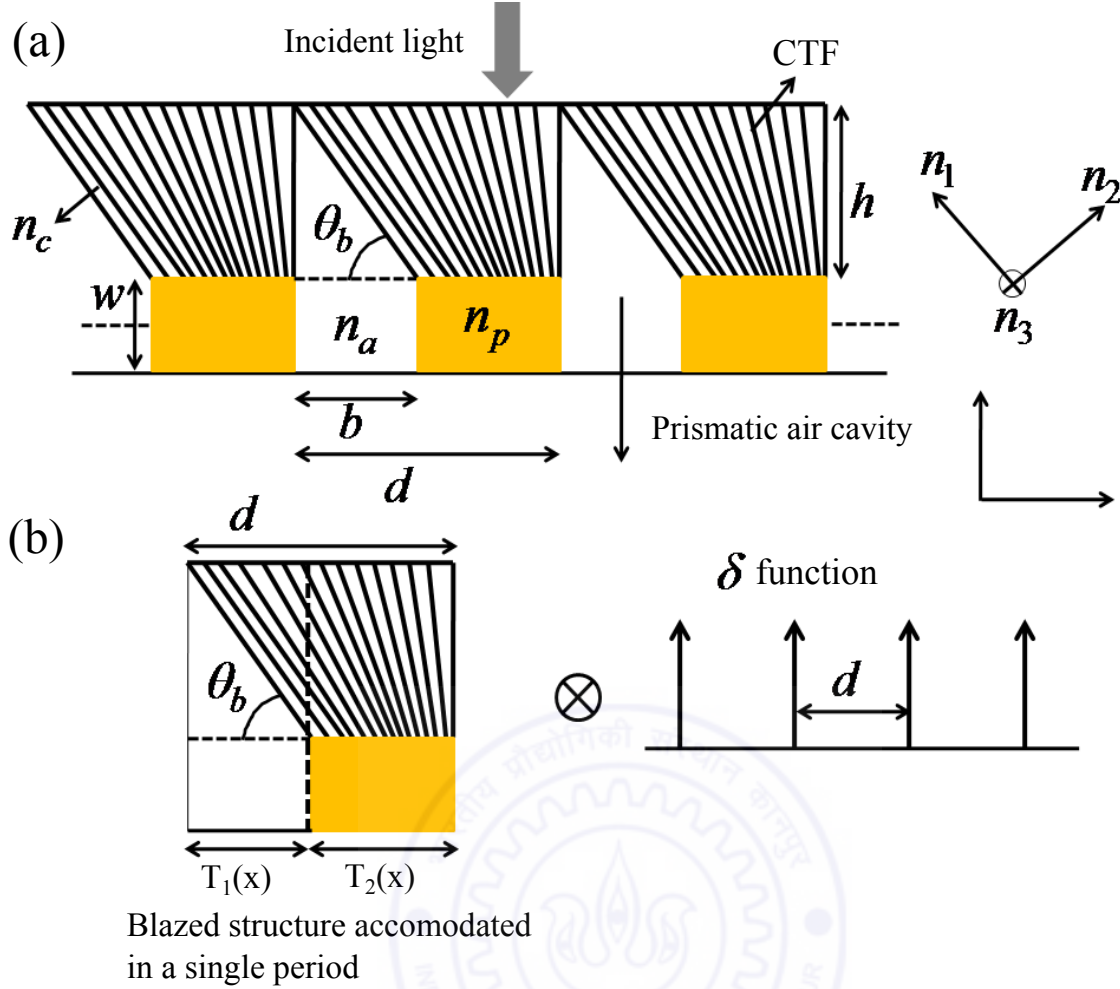


Figure 3.2: (a) Schematic of the PP-CTF as a blazed grating containing prismatic air cavities with base b , height h , and cavity angle θ_b . The photoresist grating is made of strips of height W and the period is denoted by d . The refractive indices of the different materials are indicated. n_1 , n_2 , n_3 are the principal refractive indices of the columnar structure. (b) A single blazed element convoluted with periodic arrangement of periodic comb function (periodically placed δ -functions).

to the columnar axis. There may be a linear birefringence at normal incidence, due to the ortho-rhombic biaxial nature of PP-CTF [2], because in a slanted columnar film one polarization interacts with a mixture of two of the principal indices. Light incident normally on PP-CTF experiences an effective refractive index n_c , which is a combination of n_1 and n_2 , when polarized parallel to the morphologically significant plane (p polarization). Therefore, the diffraction of s -polarized light (when polarized perpendicular to the morphologically significant plane) is primarily described by n_3 , while p polarized light is described by n_1 and n_2 . The dispersion relation in the principal frame of reference which depends on the direction of propagation in the biaxial

media is given by [27],

$$\frac{u_1^2}{n_c^2 - n_1^2} + \frac{u_2^2}{n_c^2 - n_2^2} + \frac{u_3^2}{n_c^2 - n_3^2} = \frac{1}{n_c^2}, \quad (3.1)$$

where u_1 , u_2 and u_3 are the unit vector along the propagation vector K along n_1 , n_2 and n_3 as shown in Fig. 3.2, respectively. Let a wave be incident normally in the morphologically significant plane containing the refractive indices n_1 and n_2 . Then for p -polarization,

$$u_1 = \cos \theta, \quad (3.2)$$

$$u_2 = \sin \theta, \quad (3.2)$$

$$u_3 = 0. \quad (3.3)$$

where θ is the angle that n_1 makes with the z axis. The PP-CTF was modeled as a blazed grating made of a material of refractive index n_c , where $n_c = n_3$ for the diffraction of s -polarized light, while

$$n_c = \frac{n_1 n_2}{\sqrt{(n_1^2 \cos^2 \theta + n_2^2 \sin^2 \theta)}}, \quad (3.4)$$

for p polarized light, with θ being the angle of the columns with the substrate normal. The prismatic air cavities give rise to a linear phase shift along the transverse direction in the manner of a blazed grating. Note that, in comparison, a conventional blazed grating has prismatic elements of a high-refractive-index material embedded in a material of low refractive index (air), whereas these PP-CTFs have those elements made of air embedded in a material of refractive index $n_c > 1$. For CTFs made of CaF_2 , n_c ranges from 1.44 (bulk CaF_2) to 1.1 for highly porous films [82, 105].

We first determine the transmission function for the periodic arrangement of blazed structures by assuming that the grating structure is weakly scattering and modulates only the phase of the transmitted light. The diffraction efficiencies in the far field are computed by applying a Fourier transform [106] on the transmitted fields. Our

analytical model provides a conceptual understanding of the physical concepts dictating the response of the blazed structures. We show that the results of the analytical approach agree well with the measured diffraction efficiencies. This model is valid for any periodic structures with arbitrary shapes as long as the period is larger than the wavelength of incident light.

Let us assume a plane wave normally incident on the blazed grating from the top as shown in Fig. 3.2 (a) and apply Fresnel–Kirchhoff boundary conditions for the periodic structure, where wavefront is modulated due to different refractive indices in different regions as shown in Fig. 3.2 (b). We consider a periodic arrangement of N prismatic air cavities with base b , height h , and cavity angle θ_b . The photoresist grating is made of strips of height W and the period is denoted by d . The total transmission function of the blazed grating $T(x)$ is expressed as the convolution of the transmission function $T_{\text{periodic}}(x)$ of a periodic arrangement with a period d and that of a single element of the prismatic air cavity $T_{\text{prismatic}}(x)$ as shown in Fig. 3.2 (b),

$$T(x) = T_{\text{prismatic}} \otimes T_{\text{periodic}}. \quad (3.5)$$

T_{periodic} is expressed as

$$T_{\text{periodic}} = \sum_m \delta(x - md). \quad (3.6)$$

Each single element of prismatic air cavity has an amplitude transmission of 1 over the width d , but introduces a position (x) dependent phase shift into the transmitted light. Thus the transmission function for single element is expressed as $T_{\text{prismatic}}(x) = T_1(x) + T_2(x)$ where,

$$\begin{aligned} T_1(x) &= \exp [ik_0 \{ (n_a - n_c)x \tan \theta + W n_a \}], & 0 < x < b, \\ T_2(x) &= \exp [ik_0 (W n_p + h n_c)], & b < x < d. \end{aligned} \quad (3.7)$$

Here the exponential term represents the phase function introduced by the prismatic cavity, $k_0 = 2\pi/\lambda$ is the free-space wavenumber; n_a and n_p are refractive indices of air

and the developed photoresist respectively.

The far-field diffraction pattern can now be evaluated using the Fourier transform of the total transmission function. The Fourier transform of the transmission function $T(x)$ in the far zone can be expressed as $T(k_0 \sin \psi)$ and is given by,

$$T(k_0 \sin \psi) = \left\{ \int_0^b e^{ik_0[(n_a - n_c)x \tan \theta + W n_a]} e^{ik_0 \sin \psi x} dx + \int_b^d e^{ik_0(W n_p + h n_c)} e^{ik_0 \sin \psi x} dx \right\} \times T_0 \frac{\sin[Nk_0(\sin \psi)d/2]}{\sin[k_0(\sin \psi)d/2]}, \quad (3.8)$$

where T_0 is the zeroth-order transmission coefficient. The terms within the braces represent the diffraction envelope that is due to diffraction from a single element (i.e., one period) while the last factor arises from interference between light scattered by the periodically placed elements. The linear phase-shift transmission with distance for the function of the prismatic cavity—the first term of the sum in Eq. 3.8—tends to shift the diffraction envelope to one side. The PP-CTF had a highly asymmetric diffraction pattern, which was understood to result from the spatially linear phase shifts caused by the prismatic air cavities. We demonstrate by diffraction theory that the asymmetric diffraction from these films is due to the blazing action of the prismatic air cavities. The optical anisotropy of the CTFs itself can not result in highly asymmetric transmission as shown in Ref. [107] (see the plot of transmittance vs angle of incidence for CTFs made of aluminium).

Fig. 3.3 shows the dependence of the diffraction efficiency $|T(k_0 \sin \psi)/T_0|^2$ on the diffraction angle ψ calculated for $\lambda \in [248, 442, 473, 532, 633]$ nm. For these calculations, the following values of the various parameters—obtained by taking averages over five locations on the SEM image of a PP-CTF—were used: $d = 1125$ nm, $h = 1050$ nm, $W = 200$ nm, and $\theta_b = 55^\circ$; furthermore, $n_a = 1$ (air) and $n_p = 1.68$ is the refractive index of the photoresist [108]. The diffraction envelope maximum is shifted from the zeroth-order direction (i.e., $\psi = 0^\circ$) towards the direction of the columnar orientation, indicating the shift of the transmitted intensity from the zeroth order to positive orders. It is seen that the shift is maximum for $\lambda = 248$ nm. Due to the shift of diffraction

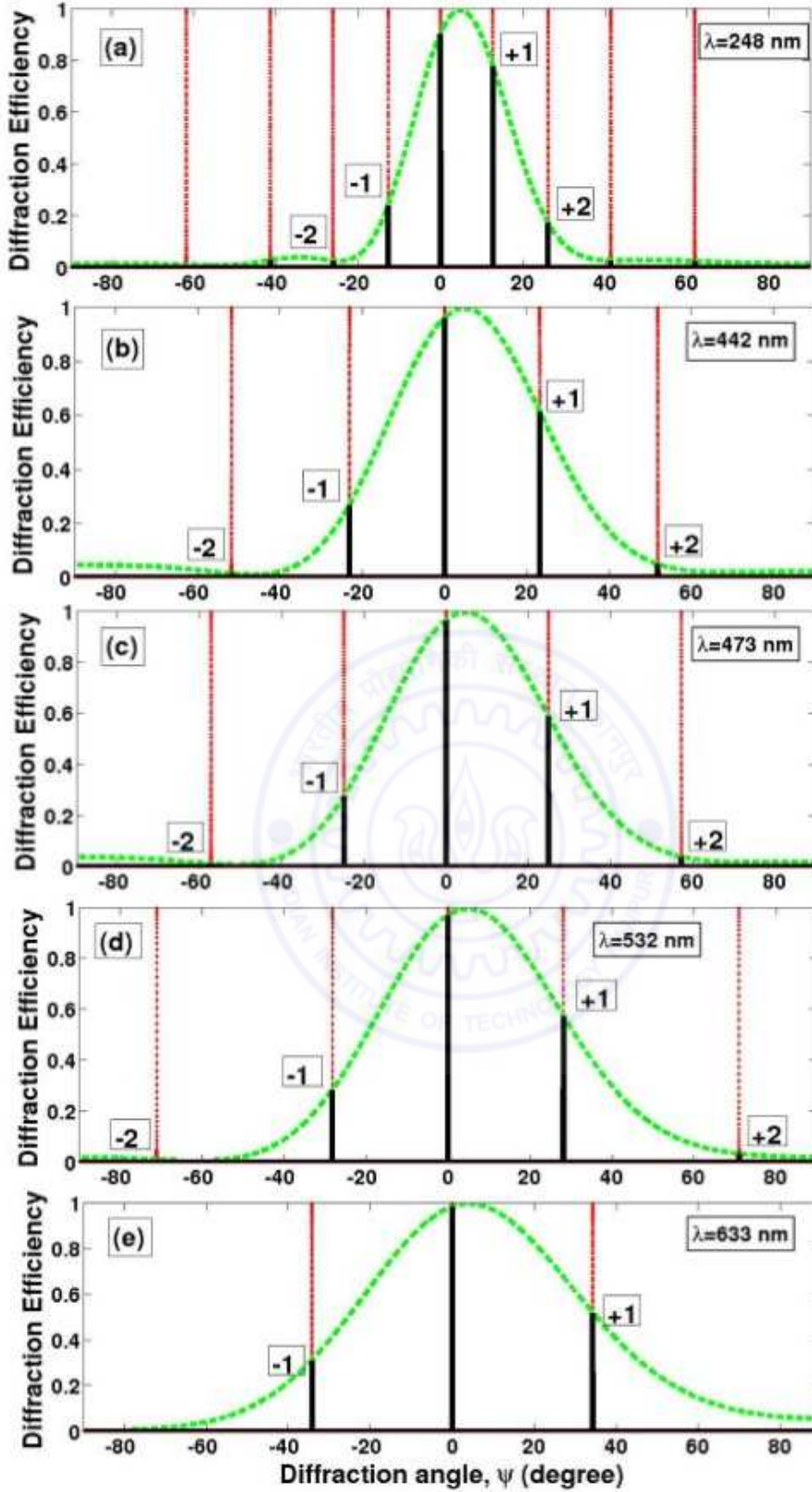


Figure 3.3: (a), (b), (c), (d) and (e) are calculated diffraction efficiency $|T(k_0 \sin \psi)/T_0|^2$ in transmission vs. diffraction angle ψ for a blazed grating with period $d = 1125$ nm for $\lambda \in [248, 442, 473, 532, 633]$ nm respectively. Diffraction angles (ψ) due to the periodic arrangement are identified by red lines, while the diffraction envelope is a green curve and the diffraction efficiency of each order is represented in black.

λ (nm)	Period	Diffraction efficiency (%)			
		$n = 1$	$n = -1$	$n = 2$	$n = -2$
248 nm	1125 nm	81(86)	32(27)	21(19)	4.1(3)
442 nm	1125 nm	62.4(64)	28.4(28)	11.4(5)	3.8(1.4)
	600 nm	36 (52)	8 (31)	-	-
473 nm	1125 nm	60.8(62)	31(28.3)	7.2(4.36)	2.9(1.56)
	600 nm	22 (51)	9 (32)	-	-
532 nm	1125 nm	57(59)	32(29.2)	6.1(4)	2.5 (1.03)
	600 nm	10 (50)	2 (33)	-	-
633 nm	1125 nm	36(55)	17(30)	-	-

Table 3.1: Measured and predicted (in parenthesis) diffraction efficiencies ($|T(n2\pi/d)/T_0|^2$) for unpolarized light diffracted through a PP-CTF with $d = 1125$ nm and $d = 600$ nm.

envelope to the right side, the diffraction efficiency of the +1 order is much higher than the -1 order for all the wavelengths and maximum at $\lambda=248$ nm.

3.2.3 Measurements of Diffraction efficiency of PPCTFs

These PP-CTFs typically exhibit an asymmetric diffraction pattern in both transmission and reflection, when illuminated normally by a laser, with the diffracted orders on either side having highly unequal intensities. For normally incident unpolarized laser beams, diffraction efficiencies in transmission were measured for $\lambda \in [248, 442, 473, 532, 633]$ nm. The measured diffraction efficiencies $|T(n2\pi/d)/T_0|^2$ of orders $n \in \{\pm 1, \pm 2\}$ are shown in Tables 3.1, for $d = 1125$ nm and $d = 600$ nm, along with the diffraction efficiencies predicted by the Eq. 3.8. For the predictions, the refractive index n_c of the PP-CTF was estimated to be 1.132, which is the volume-averaged refractive index of a 70% porous film of CaF_2 [82]. The experimental data and the theoretical predictions (explained in the previous section) for the 1125 nm period grating agree quite well in Table 3.1. The measured diffraction efficiencies are slightly lower than their predicted counterparts—most probably, due to the larger reflectivity of the substrate for the diffracted beams at large angles compared to the zeroth-order at normal incidence which is not accounted in Eq. 3.8. For the grating

λ (nm)	Polarization	Diffraction efficiency (%)			
		$n = 1$	$n = -1$	$n = 2$	$n = -2$
442 nm	p	75(81)	28(26)	12(15)	4.28(2.8)
	s	62(64)	26.7(28)	6.7(5)	2.7(1.5)
473 nm	p	73(76)	37(26.5)	12.3(11.2)	4.6 (2.4)
	s	60(61)	31(29)	6.4(4)	2.3(1.24)
532 nm	p	69(70)	33(26.8)	7.2(7.4)	3.4 (2)
	s	53(57)	33.6(30)	5(3)	2.3(1)
633 nm	p	41(57)	24(30)	-	-
	s	33(53)	19(32)	-	-

Table 3.2: Measured and predicted (in parenthesis) diffraction efficiencies ($|T(n2\pi/d)/T_0|^2$) for s and p polarized light diffracted through a PP-CTF with $d = 1125$ nm.

λ (nm)	Principal refractive indices	
	n_1	$n_2 = n_3$
442	1.35	1.13
473	1.331	1.127
532	1.31	1.12
633	1.27	1.11

Table 3.3: Principal refractive indices at visible wavelengths

with the shorter period, however, the data reveal that a lower level of agreement occurs, although the qualitative trends are maintained. The measured diffraction efficiencies for $\lambda = 532$ nm are somewhat smaller than the predicted values, as expected because the Kirchhoff-Fresnel boundary conditions become inaccurate for feature sizes that are comparable to the wavelength. The phase and amplitude changes due to scattering become very appreciable and the PP-CTF can no longer be treated as a phase grating. A full photonic bandstructure calculation would be required for quantitative predictions. In any case, Table 3.1 demonstrates that the asymmetric diffraction is the result of the blazing caused by the prismatic cavities.

The diffraction efficiencies measured for incident s - and p - polarized light at visible wavelengths are shown in Table 3.2. Since light is incident in the morphologically significant plane, so s - and p - polarizations can be treated independently and the values of n_c for each polarizations are related to the n_1 , n_2 and n_3 according to Eq. 3.4. This

allows an estimation of the principal indices (n_1, n_2, n_3) given in Table 3.3 using the diffraction efficiencies by fitting an appropriate n_c for each polarization (see Eq. 3.4) and using $\theta = 40^\circ$ from SEM data. An assumption of uniaxiality whereby $n_2 = n_3$ (perpendicular to the column axis) has been made by us for obtaining the values, although most CTFs are known to be slightly biaxial [109]. One advantage of this measurement is that, from the measured diffraction efficiencies we can calculate the principal refractive indices of the grating material which are otherwise estimated from ellipsometry measurements.

3.3 Discussion and Conclusions

Let us now point out some advantages of PP-CTF gratings. PP-CTFs are readily made with UV-compatible materials like CaF_2 and MgF_2 . The OAD technique is well suited for inexpensive mass manufacture and can work upto much smaller periods down to 150 nm [104]. Transmission blazed diffraction gratings for UV and x-ray applications with high groove densities and large areas have certain advantages, particularly when the zeroeth order beam is required to go straight through [110]. X-ray telescopes usually utilize grazing incidence mirrors to focus the incident light, but imperfections in the mirrors cause angular deviations and scattering from the ideal direction of specular reflection. Transmission gratings have the advantage of being insensitive to grating misalignments and non-flatness inside the spectrometers. These gratings can also be useful, for example, when angularly separating the harmonics generated by intense laser pulses at UV wavelengths down to 150 nm [99, 111]. Apart from their common use in spectroscopy, there has been recent interest in using blazed gratings for preferential coupling to surface plasmons on a metallic film [101, 112] (note that this is extensively discussed in Chapter 4), where the use of such PP-CTFs gratings with anisotropic materials can give rise to interesting phenomena. Another salient point is that the intensities of the diffracted orders depend quite sensitively on the effective permittivity tensor of the CTF which, in turn, depends on the porosity of the film. Measurement

of the diffraction efficiencies may provide a way to quantize the CTF porosity, which is otherwise accessible only from gravimetric analysis. From the discussion as explained above, it is clear that diffraction efficiency is a function of the refractive index n_c of CTF, which is estimated from volume average refractive index of porous film.

In this chapter, we have discussed how a PP-CTFs made of dielectric material behaves as a blazed diffraction grating. The conventional blazed gratings available in the market are fabricated using very expensive methods such as reactive ion etching. Here we made blazed gratings of dielectric materials using very inexpensive method by combining LIL and OAD techniques. We have presented a new kind of PP-CTFs made by evaporating CaF_2 and directing the resulting collimated vapor flux obliquely towards micrometer/sub-micrometer gratings fabricated by LIL. Triangular prismatic air cavities were periodically formed by merging the growth of diverging columnar structures of CaF_2 within the fabricated structure by controlling the various deposition parameters of the vapour flux. The formation of prismatic air cavities in the PP-CTF is responsible for highly asymmetric diffraction patterns. PP-CTFs function like blazed diffraction grating with asymmetric diffraction efficiency in transmission at ultraviolet-visible wavelengths. A simple model considering the prismatic air cavities within the PP-CTF as blazing elements of a phase diffraction grating and scalar diffraction theory was efficacious in capturing the essential features of the measured diffraction efficiencies. The intensity of the diffracted order depends quite sensitively on the effective permittivity tensor of the CTFs, which in turn depends on the porosity of the film. Because of different refractive indices for two polarizations, the calculated and measured diffraction efficiencies of PP-CTFs for s and p polarized light are different. The principal refractive indices of the deposited CTFs were estimated from the diffraction efficiencies.

Chapter 4

Asymmetric Coupling and dispersion of SPP Waves on PPMCTFs

4.1 Introduction

SPP waves guided by the interface of a metal and a dielectric medium have been projected to carry information in future miniaturized all-optical plasmonic chips [113]. Excitation of SPPs by a periodic modulation or diffraction grating opens the possibilities of miniaturization of plasmonics based devices [114, 115]. Control over the dispersion of SPP waves and their coupling to light are critical for this and other applications. In order to develop modern plasmonic technology, manipulation of SPP coupling efficiencies and propagation directions is an important requirement. While SPP waves supported by the interface of a metal and a dielectric medium, both isotropic and homogeneous, have been well known for several decades [13], interest has arisen in the case of the partnering dielectric medium being periodically nonhomogeneous normal to the interface [116], which allow the possibility of multiple SPP waves that will enable extremely sensitive multi-analyte sensors [117].

An important aspect is the excitation of SPP waves by incident light, which is

usually mediated by a dielectric or a grating coupler [13]. In symmetric grating structures, normally incidence light equally excites SPPs in two opposite directions, which leads to poor SPP coupling in both the directions and reduces the amplitudes of both SPP waves. This symmetric SPP coupling might be a limiting factor for developing efficient functionalized plasmonic circuits. One way to enhance the coupling to one of the two SPP waves is by creating asymmetry in the plasmonic grating structure. Coupling of light solely into SPP waves propagating along a single direction is an important requirement in many instances, which can be achieved by arrangements such as oblique incidence on a grating [118] or by interference effects made possible by appropriately placed nanoscatterers [119]. Slanted metal gratings were predicted to couple light preferentially into SPP waves propagating in a specific direction [120, 121] and slanted sinusoidal gratings and binary blazed plasmonic gratings have been similarly used [101]. A nanoslit coupler [122] and dislocated double layered gratings [123] have also been recently investigated for unidirectional coupling to SPP waves. Unidirectional coupling to SPP has recently been shown to be useful for outcoupling light from a light-emitting diode [124].

Control of propagation for applications such as subwavelength focusing of SPP waves [125] requires not only anisotropic dielectric materials, but anisotropic metals as well. The CTF of a metal, deposited by an obliquely incident collimated metal vapor flux on a substrate [1], is highly anisotropic, as has been demonstrated for CTFs of plasmonic metals such as silver and gold [126] as well as magnetic materials like cobalt [127]. The excitation of SPP waves guided by the planar interfaces of air (or some isotropic dielectric material) of nano-engineered CTFs made of a metal has been investigated quite well [126, 128], but the same phenomenon when the metallic CTF is periodically patterned has been given attention only recently [129]. We believe that the combination of the anisotropy offered by the nano-columnar morphology with the diffractive properties provided by the periodic patterning will provide access to new plasmonic phenomena. Periodically patterned CTFs of inorganic dielectric materials such as CaF_2 were recently shown to function well as blazed diffraction gratings [130].

Hence, it is attractive to investigate the plasmonic properties of periodically patterned CTFs made of plasmonic metals.

In this chapter, lithographically patterned submicron gratings of silver CTFs with slanted nanocolumns have been shown to provide for a strong unidirectional coupling to SPP waves. Experiments on the dispersion of SPP waves have revealed that the silver CTF is an effectively anisotropic metal with hyperbolic dispersion [45]. The nano-columnar orientation and the porosity of the CTF completely define the effective permittivity tensor, and thereby provide a route to generate any desired characteristics for the hyperbolic medium. Due to the columnar morphology, not only incident p -polarized light, but also incident s -polarized light indirectly couples to the SPP waves via internally scattered waves. Angle resolved transmittance measurements of silver CTFs deposited on square gratings as a function of polarization and azimuthal angle between the plane of incidence and the morphologically significant plane were reported. In 2D grating, there are different crystal symmetry directions, and by changing the polarization angle we can tune the band dispersion. Angle-resolved zeroth order transmission through a 2D perforated metallic slab atop of a dielectric wafer has been investigated earlier [131], but the same phenomenon for a metallic PP-CTFs deposited on a 2D dielectric grating has not been studied yet. A detailed study of control of the SPP dispersion by controlling the orientation ψ (angle between the plane of incidence and morphologically significant plane) on 2D grating will complete the deeper understanding of the potential of metallic CTF further. Recently Nefedov et al. shown total absorption in asymmetric hyperbolic media [132]. Due to left-right asymmetry in this structure, new kinds of coupling are observed in the SPP dispersion diagram, which is represented with a gray scale level map. Intensities for the positive and negative diffraction orders are also found to be asymmetric because of the anisotropy of the CTF. Here we focus on the dispersion plots which show interesting features of excitation of surface plasmons, when plane of incidence make different angles $\psi = 0^\circ$, $0^\circ < \psi < 90^\circ$ and $\psi = 90^\circ$ with respect to the morphologically significant plane (the plane where silver nanocolumns are oriented).

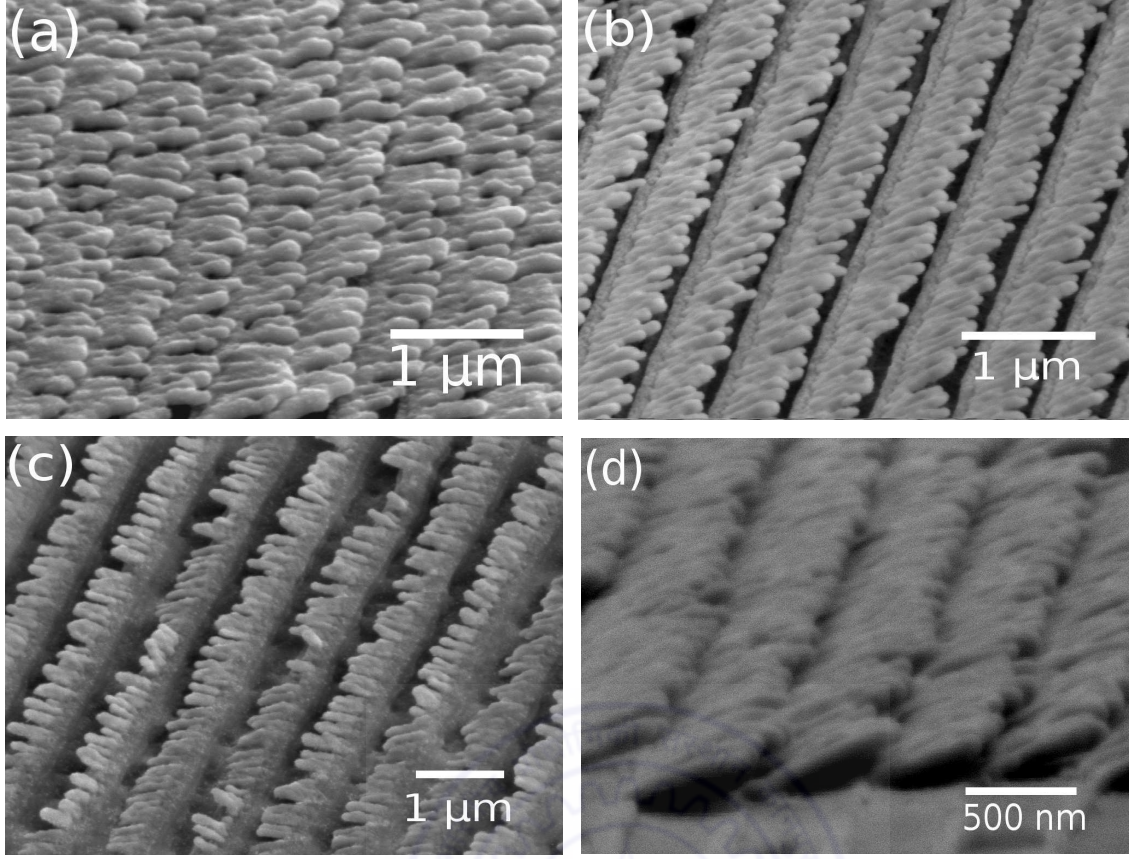


Figure 4.1: Top view of FESEM images of PP-CTFs of silver with (a) $d = 500$ nm, (b) $d = 580$ nm, (c) $d = 770$ nm and (d) cross-sectional FESEM image of PP-CTFs of silver with $d = 500$ nm

4.2 Asymmetric diffraction of periodically patterned metallic CTFs

FESEM images of periodically patterned silver CTFs with different periodicities are shown in Fig. 4.1. All the structures are fabricated at identical deposition conditions (detailed fabrication procedure is given in Chapter 2) such as vapor flux angle $\alpha = 86^\circ$ and deposition rate of $5-7 \text{ \AA s}^{-1}$. Fig. 4.1 (a), (b) and (c) show top view FESEM images of periodically patterned CTFs of silver with $d = 500$ nm, $d = 580$ nm and $d = 770$ nm respectively. Fig. 4.1 (d) shows cross-sectional FESEM image of periodically patterned CTFs of silver with $d = 500$ nm. Deposition of silver columnar arrays exist only on the top of the ridges of the grating and with increase in periodicity of the grating the separation between the lines containing the silver arrays also increases. Overall, the

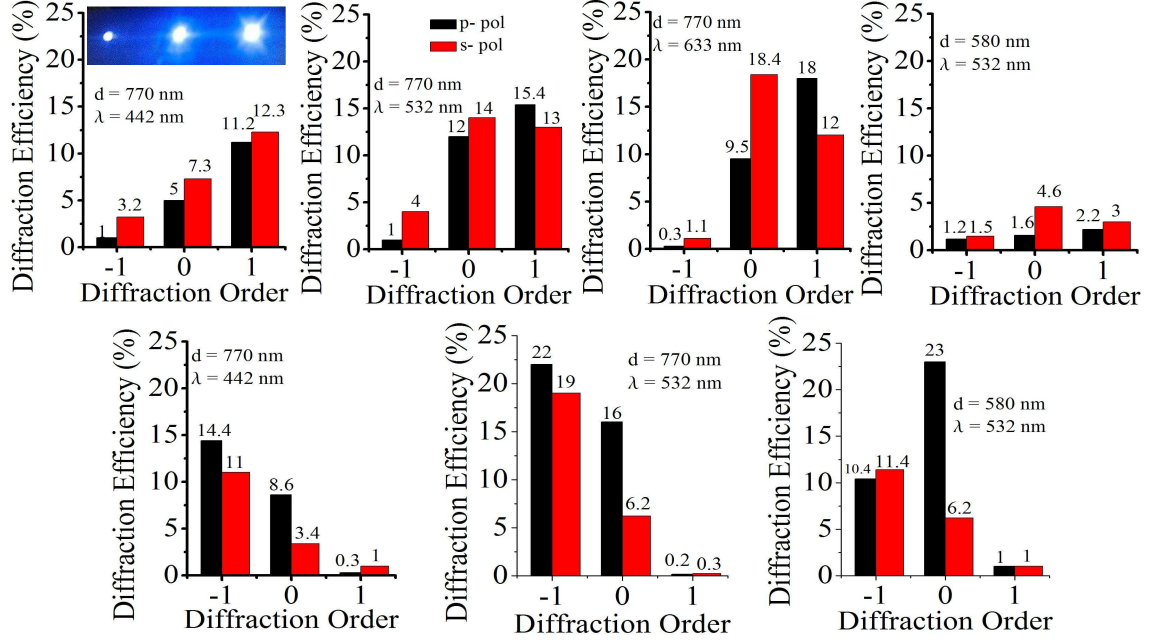


Figure 4.2: Top row: From left to right, the first three bar diagrams present the measured diffraction efficiencies in the transmission mode for $d = 770$ nm and $\lambda \in \{442, 532, 633\}$ nm for incident p -polarized (black) and incident s -polarized (red) light, and the fourth diagram is for $d = 580$ nm and $\lambda = 532$ nm. Bottom row: Measured diffraction efficiencies in the reflection mode for $d \in \{770, 580\}$ nm and $\lambda \in \{442, 532\}$ nm for incident p -polarized and incident s -polarized light. The inset is a photograph showing asymmetric diffraction for $\lambda = 442$ nm.

fabricated samples were fairly smooth and scattered very little light from the CTF regions outside the grating area (~ 20 mm²), while exhibiting strong diffraction orders in the reflection from the CTF-coated grating regions.

Diffraction efficiencies of all the samples were measured using lasers of wavelength 442, 532 and 633 nm. Highly asymmetric diffraction patterns were exhibited by the periodically patterned silver CTFs, similarly to blazed diffraction by periodically patterned dielectric CTFs [130]. The diffraction efficiencies (i.e., the ratio of the diffracted intensity to the incident intensity) measured for the various orders are tabulated in Fig. 4.2 for incident p and s -polarized light, when the period $d \in \{770, 580\}$ nm and the wavelength $\lambda \in \{442, 532, 633\}$ nm in the transmission mode (top row) and in the reflection mode (bottom row). The asymmetry between the $n = +1$ and $n = -1$ orders is more pronounced for incident p -polarized light than for incident s -polarized light. One photograph of the diffraction pattern taken using $\lambda = 442$ nm wavelength is shown in the inset of Fig. 4.2 which shows asymmetric diffraction. Low efficiencies

were observed for the case of $d=580\text{nm}$ and $\lambda=532\text{nm}$. Parenthetically, we remark on enhanced absorptance when the wavelength approaches the period of the grating.

Diffraction efficiencies are functions of the height, period, and duty cycle of a slanted grating [101, 120]. Although full-scale three-dimensional computations (see Chapter 5) will be required for optimization, the periodically patterned silver CTFs clearly show potential for uni-directional coupling of light to SPP waves.

4.3 SPP Waves on 1D PPMCTFs: incidence in the morphologically significant plane

Fig. 4.3 (a) shows schematic of symmetric structure of corrugated silver thin film where direction of polarization and angle of incidence with respect to grating normal are shown. Fig. 4.3 (b) shows schematic of asymmetric structure of silver patterned structure on one dimensional periodic substrate. Periodicity of the grating is along x axis and $x - z$ plane is the morphologically significant plane where silver columns are oriented. $\hat{\tau}$ and \hat{n} are the directions of unit vector along the longer axis and shorter axis of the silver columns in the morphologically significant plane, whereas \hat{b} is the unit vector along the direction perpendicular to both $\hat{\tau}$ and \hat{n} . Angle of incidence with respect to the direction of silver columns is shown in Fig. 4.3 (b).

Angle-resolved transmission spectra were measured for two different cases and their corresponding SPP dispersion plots are compared. Different dispersions and coupling of SPP can be observed for the two cases as shown in Fig. 4.4. Fig. 4.4 (a) shows SPP dispersion plot for corrugated Ag thin film of periodicity 770 nm and 30 nm film thickness of Ag as shown in the schematic 4.3 (a). Here the grating structure is symmetric, so excitation to SPPs by p - polarized incident light is equal in two opposite directions. Fig. 4.4 (b) shows the optical image of diffraction pattern through corrugated Ag film using a laser of wavelength 442 nm.

Fig. 4.4 (d) is the SPP dispersion plots for p - polarization of the structure as

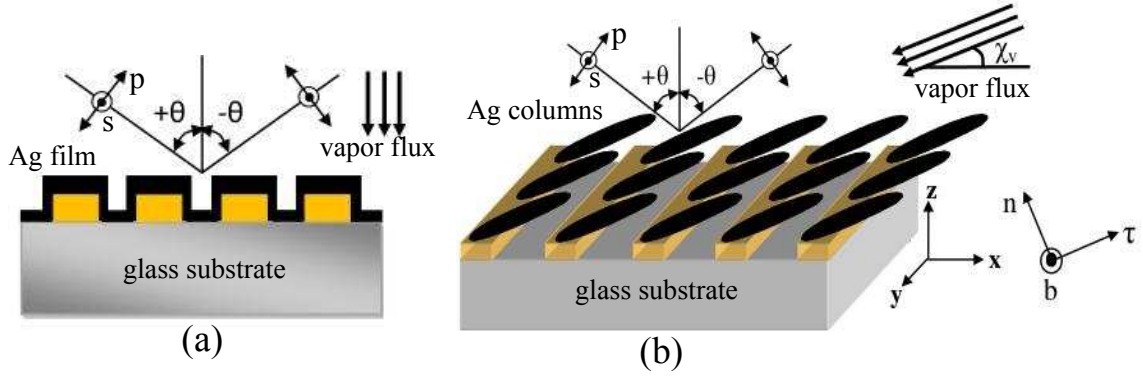


Figure 4.3: Schematic showing the (a) corrugated Ag film with normally incident vapor flux and (b) columnar morphology along with the principal axes ($\hat{\tau}$, \hat{b} , \hat{n}) of the CTF while (x, y, z) are the Cartesian coordinates with obliquely incidence vapor flux. Angle of incidence θ with respect to the substrate normal and polarizations p - and s - are shown.

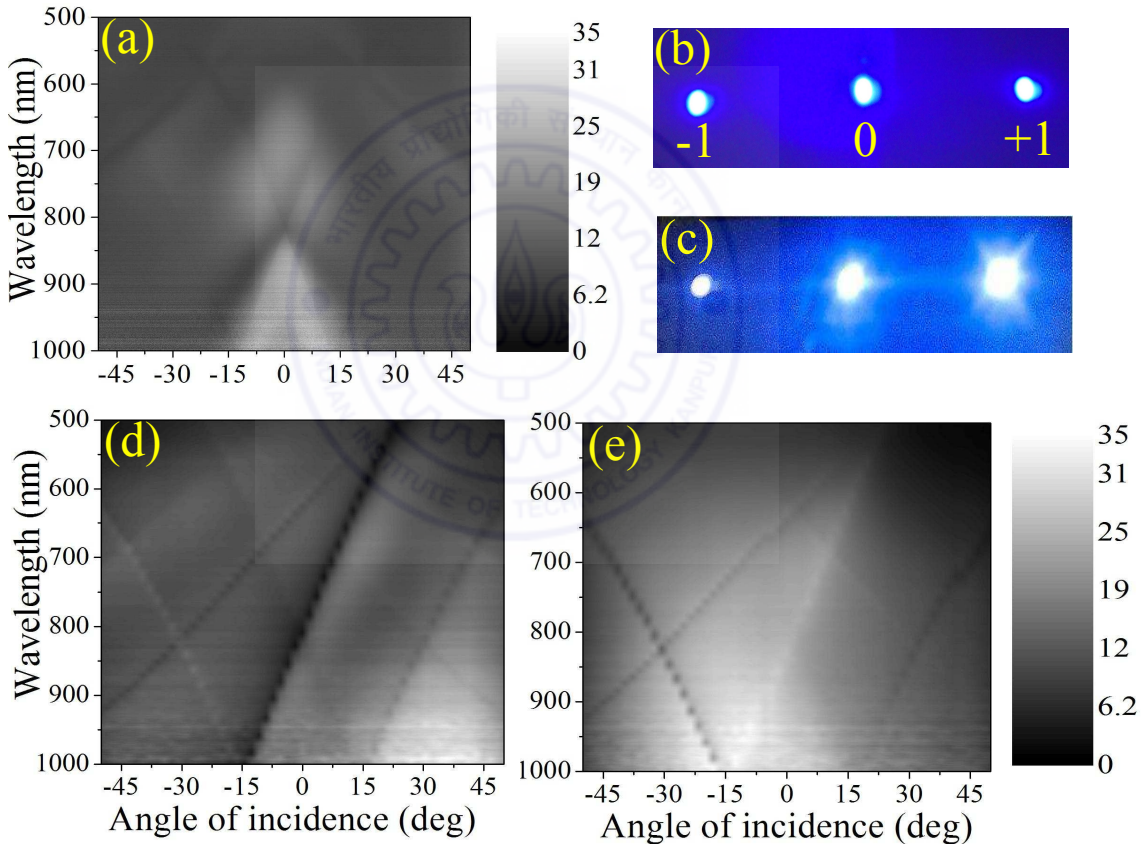


Figure 4.4: (a) Angle-resolved transmittance spectra for corrugated Ag film when the incident light is p - polarized and the period of the grating is 770 nm and thickness of the Ag film is 30 nm, (b) symmetric diffraction through corrugated silver film for $\lambda = 442$ nm, (c) asymmetric diffraction through PPMCTFs for $\lambda = 442$ nm, (d) angle-resolved transmittance spectra for PPMCTFs when the incident light is p - polarized and period of the grating is 770 nm. (e) angle-resolved transmittance spectra for PPMCTFs when the incident light is s - polarized and period of the grating is 770 nm. Different types of SPP coupling in two cases are clearly shown.

shown in FESEM image of Fig. 4.1 (c) and in the schematic of Fig. 4.3 (b). We can clearly see that the coupling is asymmetric for PPMCTFs as compared to the coupling for symmetric structure. This is because the structure as shown in schematic 4.3 (b) is asymmetric and anisotropic in nature. The diffraction pattern through this PPMCTFs is shown in Fig. 4.4 (c). Coupling of SPPs to s polarized light for PPMCTFs is shown in Fig. 4.4 (e) whereas there is no s- polarized coupling for the corrugated structure. One of the difference is that the relative permittivity for corrugated Ag structure is isotropic whereas for PPMCTFs, the relative permittivity is anisotropic. The relative permittivity parameters are calculated using the Bruggeman formalism and putting these permittivities into the Maxwell's equation, the theoretical dispersion plots are estimated for PPMCTFs with four different periodicities in the next section.

4.3.1 Theory of SPP wave propagation

Relative-permittivity model for the CTF

The effective relative permittivity tensor in the principle frame of reference for parallelly oriented ellipsoidal metallic inclusions can be expressed as $\text{Diag}[\varepsilon_b, \varepsilon_c, \varepsilon_a]$. Here ε_b is the effective relative permittivity along the longer axis of the silver columns (i.e., along the unit vector $\hat{\tau}$) whereas ε_c and ε_a are the same along two shorter axes of the silver columns in the unit vector directions \hat{b} and \hat{n} respectively. This effective relative permittivity tensor in a homogeneous dielectric host material is computed using Bruggemann homogenization formalism with exact depolarization dyadic. The effective relative permittivity tensor $\tilde{\varepsilon}$ of a CTF in the lab frame of reference can be written as [1]

$$\tilde{\varepsilon} \equiv \begin{pmatrix} \varepsilon_{xx} & \varepsilon_{xy} & \varepsilon_{xz} \\ \varepsilon_{yx} & \varepsilon_{yy} & \varepsilon_{yz} \\ \varepsilon_{zx} & \varepsilon_{zy} & \varepsilon_{zz} \end{pmatrix} = \mathcal{S}_y \cdot \begin{pmatrix} \varepsilon_b & 0 & 0 \\ 0 & \varepsilon_c & 0 \\ 0 & 0 & \varepsilon_a \end{pmatrix} \cdot \mathcal{S}_y^T, \quad (4.1)$$

where the matrix

$$\mathcal{S}_y = \begin{pmatrix} \cos \chi & 0 & -\sin \chi \\ 0 & 1 & 0 \\ \sin \chi & 0 & \cos \chi \end{pmatrix}, \quad (4.2)$$

indicates a rotation about the y axis and χ is the angle that the silver column makes with the x axis which is determined from the empirical formula [84]. ε_b , ε_c , and ε_a are the eigenvalues of $\tilde{\varepsilon}$, whereas the corresponding eigenvectors of $\tilde{\varepsilon}$ are given by

$$\hat{\tau} = \hat{x} \cos \chi + \hat{z} \sin \chi, \quad (4.3)$$

$$\hat{b} = -\hat{y}, \quad (4.4)$$

$$\hat{n} = -\hat{x} \sin \chi + \hat{z} \cos \chi. \quad (4.5)$$

The eigenvalues of $\tilde{\varepsilon}$ can be estimated using a Bruggeman formalism wherein the bulk metal and the voids are supposed to be distributed as prolate ellipsoids [1], so long as the porosity (i.e., the void volume fraction) f_v is sufficiently large [133]. That being true for all the CTFs investigated by us, the Bruggeman formalism requires the solution of the three coupled equations expressed compactly as

$$(1 - f_v) (\varepsilon_m \mathcal{I} - \tilde{\varepsilon}) \cdot \left[\mathcal{I} + i\omega \varepsilon_0 \underline{\underline{\mathcal{D}}}^{(m)} \cdot (\varepsilon_m \mathcal{I} - \tilde{\varepsilon}) \right]^{-1} + f_v (\varepsilon_v \mathcal{I} - \tilde{\varepsilon}) \cdot \left[\mathcal{I} + i\omega \varepsilon_0 \underline{\underline{\mathcal{D}}}^{(v)} \cdot (\varepsilon_v \mathcal{I} - \tilde{\varepsilon}) \right]^{-1} = 0. \quad (4.6)$$

Here, ε_0 is the permittivity of free space; ε_m and $\varepsilon_v = 1$ are the relative permittivity scalars of the bulk metal and the voids, respectively; \mathcal{I} is the idempotent; the depolarization tensors

$$\underline{\underline{\mathcal{D}}}^{(m,v)} = \frac{2}{i\pi\omega\varepsilon_0} \int_{\varphi=0}^{\frac{\pi}{2}} \int_{\vartheta=0}^{\frac{\pi}{2}} \frac{(\sin \vartheta \cos \varphi)^2 \hat{n}\hat{n} + (\sin \vartheta \sin \varphi / \gamma_b^{(m,v)})^2 \hat{b}\hat{b} + (\cos \vartheta / \gamma_\tau^{(m,v)})^2 \hat{\tau}\hat{\tau}}{(\sin \vartheta \cos \varphi)^2 \varepsilon_a + (\sin \vartheta \sin \varphi / \gamma_b^{(m,v)})^2 \varepsilon_c + (\cos \vartheta / \gamma_\tau^{(m,v)})^2 \varepsilon_b} \sin \vartheta d\vartheta d\varphi; \quad (4.7)$$

and $\gamma_{\tau,b}^{(m,v)}$ are the shape parameters of the ellipsoids [1]. The parameters $\gamma_{\tau,b}^{(m,v)}$ and f_v have to be chosen by comparing theoretical predictions of optical response character-

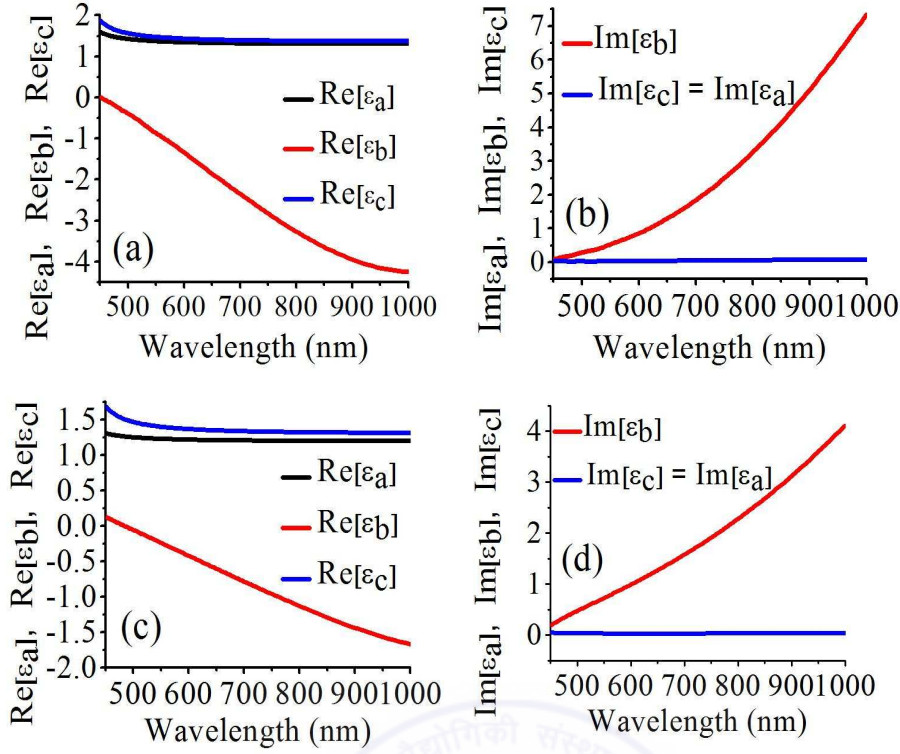


Figure 4.5: (a) Real and (b) imaginary parts of $\varepsilon_{a,b,c}$ predicted as functions of the wavelength by the Bruggeman model with ellipsoidal voids ($f_v = 0.88$, $\gamma_\tau^{(m)} = 7$, $\gamma_b^{(m)} = 1.2$, $\gamma_\tau^{(v)} = 10$, and $\gamma_b^{(v)} = 1$); (c) real and (b) imaginary parts of $\varepsilon_{a,b,c}$ predicted as functions of the wavelength by the Bruggeman model with spherical voids ($f_v = 0.91$, $\gamma_\tau^{(m)} = 15$, $\gamma_b^{(m)} = 1.5$, $\gamma_\tau^{(v)} = 1$, and $\gamma_b^{(v)} = 1$);

istics against their experimental counterparts [134].

In order to understand the experimental results using theory, the formulation presented in Sec. 4.3.1 was employed. The Drude model was used for the relative permittivity of silver as

$$\varepsilon_m(\omega) = 5.7 - \omega_p^2 / [\omega(\omega + i\gamma_p)], \quad (4.8)$$

where the angular frequency ω is in units of eV, $\omega_p = 9.2$ eV, and $\gamma_p = 0.021$ eV.

Fig. 4.5 shows the variations of $\varepsilon_{a,b,c}$ with wavelength. Two cases are considered here, first when the shape of both the silver inclusions and voids are ellipsoidal, and second when the silver inclusion is ellipsoidal whereas void is spherical. Fig. 4.5 (a), (b) are real and imaginary parts of $\varepsilon_{a,b,c}$ predicted as functions of the wavelength for the first case using the parameters $f_v = 0.88$, $\gamma_\tau^{(m)} = 7$, $\gamma_b^{(m)} = 1.2$, $\gamma_\tau^{(v)} = 10$, and $\gamma_b^{(v)} = 1$.

Fig. 4.5 (c), (d) are real and imaginary parts of $\varepsilon_{a,b,c}$ predicted as functions of the wavelength for the second case using the parameters $f_v = 0.91$, $\gamma_\tau^{(m)} = 15$, $\gamma_b^{(m)} = 1.5$, $\gamma_\tau^{(v)} = 1$, and $\gamma_b^{(v)} = 1$. Clearly, the real part of the projection ε_b of $\tilde{\varepsilon}$ on the columnar axis $\hat{\tau}$ is negative over the visible and near-infrared frequencies, while $\text{Re}[\varepsilon_{a,c}] > 0$ in both the cases. Hence, the metal CTF is a biaxial medium with an indefinite relative permittivity tensor. Also, the homogenization model predicts a large imaginary part of ε_b and there is a consistency in the plots for both sets of parameters.

SPP wavenumber

Suppose that the metallic CTF occupies the half space $z > 0$ and the isotropic dielectric material occupies the half space $z < 0$ as shown in the schematic 4.3 (b). Thus, SPP-wave propagation is guided by the plane $z = 0$. As the $x-z$ plane is the morphologically significant plane for the CTF, any SPP wave propagating along the x axis in the $x-y$ plane can be either s polarized (i.e., $E_x = E_z = 0$ and $H_y = 0$) or p polarized (i.e., $E_y = 0$ and $H_x = H_z = 0$).

The p -polarized electromagnetic fields in the homogenized metallic CTF ($z > 0$) are given by

$$\left. \begin{aligned} \vec{E}_m &= E_{xm} \left(\hat{x} + \frac{ik_x k_{zm} + k_0^2 \varepsilon_{zz}}{k_x^2 - k_0^2 \varepsilon_{zz}} \hat{z} \right) e^{i(k_x x + i k_{zm} z)} \\ \vec{H}_m &= -E_{xm} \left(\hat{y} \omega \varepsilon_0 \frac{\varepsilon_{zx} k_x + i k_{zm} \varepsilon_{zz}}{k_x^2 - k_0^2 \varepsilon_{zz}} \right) e^{i(k_x x + i k_{zm} z)} \end{aligned} \right\}, \quad (4.9)$$

and in the isotropic dielectric material ($z < 0$) by

$$\left. \begin{aligned} \vec{E}_d &= E_{xd} \left(\hat{x} - \frac{ik_x}{k_{zd}} \hat{z} \right) e^{i(k_x x - i k_{zd} z)} \\ \vec{H}_d &= E_{xd} \left(\hat{y} \omega \varepsilon_0 \frac{i \varepsilon_d}{k_{zd}} \right) e^{i(k_x x - i k_{zd} z)} \end{aligned} \right\}, \quad (4.10)$$

where k_0 is the free-space wavenumber. E_{xm} and E_{xd} are the amplitudes of the em wave in the metallic and dielectric medium respectively. k_x is the x component of the wave vector; k_{zm} and k_{zd} are the z components of the wave vector in the metallic and dielectric medium respectively.

Substitution of Eqs. (4.9) into the Maxwell curl equations for the CTF leads to

the relationship

$$k_x^2 \varepsilon_{xx} + 2ik_x k_{zm} \varepsilon_{xz} - k_{zm}^2 \varepsilon_{zz} - k_0^2 \varepsilon_a \varepsilon_b = 0, \quad (4.11)$$

between k_x and k_{zm} . Two values of k_{zm} exist for every k_x ; we must choose that value which satisfies the constraint $\text{Re}(k_{zm}) > 0$ in order to ensure decay of fields as $z \rightarrow \infty$. Likewise, the dispersion equation

$$k_x^2 - k_{zd}^2 - k_0^2 \varepsilon_d = 0, \quad (4.12)$$

follows from the substitution of Eqs. (4.10) into the Maxwell curl equations for the isotropic dielectric material. Two values of k_{zd} exist for every k_x ; we must choose that value which satisfies the constraint $\text{Re}(k_{zd}) > 0$ in order to ensure decay of fields as $z \rightarrow -\infty$. Enforcing the continuity of E_x and H_y across the interface $z = 0$ yields the dispersion equation

$$k_x^2 \varepsilon_d - ik_{zd} k_x \varepsilon_{zx} + (k_{zd} k_{zm} - k_0^2 \varepsilon_d) \varepsilon_{zz} = 0, \quad (4.13)$$

for SPP-wave propagation. The solution k_x of Eq. (4.13) is the wavenumber k_{SPP} of the p -polarized SPP wave propagating along the x axis. Newton Raphson method is used to solve for k_x using Mathematica Program.

4.3.2 Coupling of p -polarized light to SPP waves

Evidence of coupling to SPP waves is available in the measured angle-resolved transmission spectra presented in Fig. 4.6. Given the large thickness of the silver CTF, SPP waves localized at the CTF/photoresist interface will not be detuned due to scattering from the CTF/air interface and vice versa [13]. When θ satisfies the condition

$$\text{Re}(\vec{k}_{\text{SPP}}) = k_0 \sin \theta \hat{x} + n(2\pi/d) \hat{x}, \quad (4.14)$$

for resonant excitation of an SPP wave, where $\vec{k}_{\text{SPP}} = k_{\text{SPP}} \hat{x}$ and $n \neq 0$ is either a positive or a negative integer, the incident light couples to the SPP wave and there is a strong attenuation of the transmitted field. The transmittance minima trace out the dispersions of the SPP waves. Fig. 4.6 (a), (e), (i), and (m) show the angle-resolved

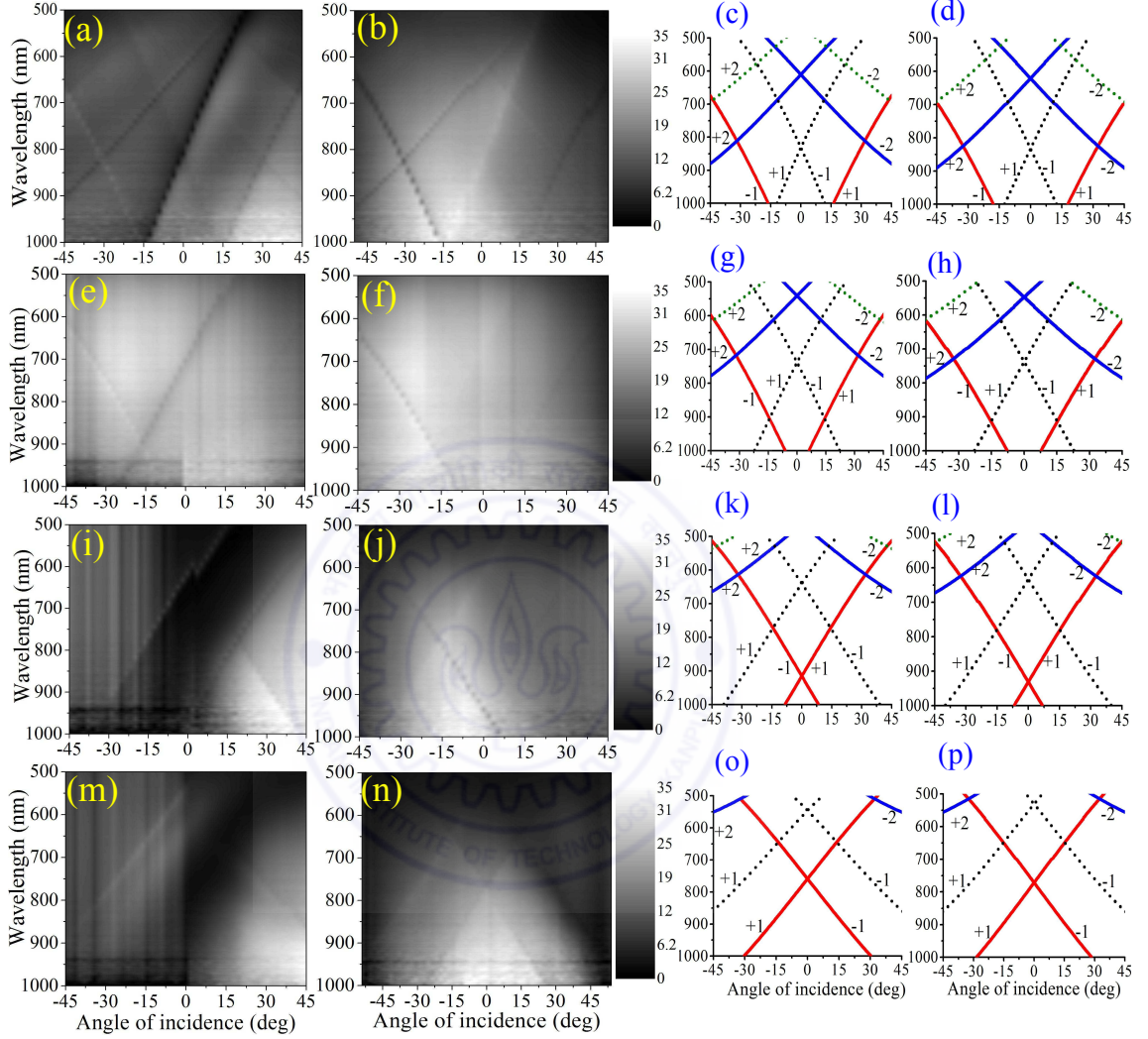


Figure 4.6: Angle-resolved transmittance spectra when the incident light is p polarized and the period $d =$ (a) 770 nm, (e) 680 nm, (i) 580 nm, and (m) 500 nm; angle-resolved transmittance spectra when the incident light is s polarized and the period $d =$ (b) 770 nm, (f) 680 nm, (j) 580 nm, and (n) 500 nm; theoretical plots for the dispersion of SPP waves obtained using $\tilde{\epsilon}$ predicted by the Bruggeman model with ellipsoidal voids ($f_v = 0.88$, $\gamma_\tau^{(m)} = 7$, $\gamma_b^{(m)} = 1.2$, $\gamma_\tau^{(v)} = 10$, and $\gamma_b^{(v)} = 1$) when the period $d =$ (c) 770 nm, (g) 680 nm, (k) 580 nm, and (o) 500 nm; and theoretical plots for the dispersion of SPP waves obtained using $\tilde{\epsilon}$ predicted by the Bruggeman model with spherical voids ($f_v = 0.91$, $\gamma_\tau^{(m)} = 15$, $\gamma_b^{(m)} = 1.5$, $\gamma_\tau^{(v)} = 1$, and $\gamma_b^{(v)} = 1$) when the period $d =$ (d) 770 nm, (h) 680 nm, (l) 580 nm, and (p) 500 nm. The theoretical predictions for the CTF/photoresist interface are solid lines, while those for the CTF/air interface are dashed lines. The orders $n = \pm 1$ and ± 2 for Bragg scattering are indicated.

transmittance spectra obtained with p -polarized light for four values of d . If the CTF

were to be replaced by a dense metal film, the coupling to the SPP waves would be symmetric with respect to the sign of θ . Instead, the four figures evince a strong asymmetry with respect to positive and negative θ , and only one of the two branches is present in most cases. Momentum transfer from the grating is possible in this case only for $n > 0$, as will become clear in the sequel. While a gross angularly asymmetric transmittance with respect to the normal by slanted metallic CTFs is well known [107] and is also evident from Fig. 4.6, it had not been hitherto realized that slanted metallic CTFs deposited on gratings can be useful for unidirectional coupling to SPP waves. One of the advantages is that in our structure the degree of transmission/reflection asymmetry at any given angle of incidence is tunable as a function of the nano-columnar tilt angle. Electromagnetic simulations (shown in Chapter 5) confirm that transmission asymmetry can be enhanced or suppressed as a function of the nano-columnar tilt angle. Thus the structures offer a flexibility in optimized uni-directional coupling for various angles of incidence. This flexibility is advantageous for asymmetric transmission even for normal incidence, which is favorable for minimizing the space occupied by the apparatus or device.

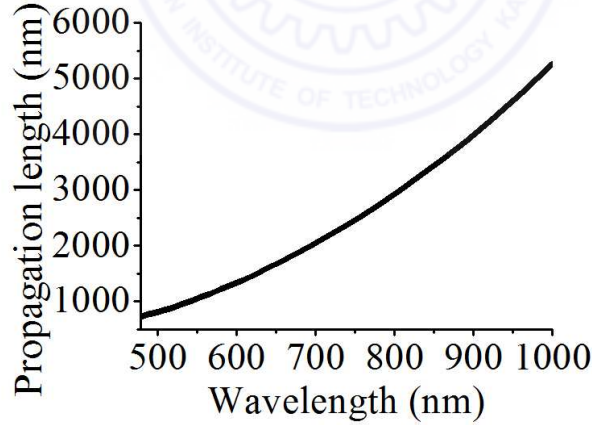


Figure 4.7: Propagation length for SPP waves with spherical voids.

Using the the effective relative permittivity tensor $\tilde{\epsilon}$, in Eq. (4.13), the SPP wave number k_{SPP} was determined. The predicted occurrences of SPP waves localized to the interface of this hyperbolic medium with the photoresist ($\epsilon_d = 2.6$) are shown in Fig. 4.6 (c), (g), (k), and (o) (for ellipsoidal voids) with $d = 770, 680, 580$, and 500 nm, respectively. Likewise, the predicted occurrences of SPP waves localized to the interface

of the same hyperbolic medium with air ($\varepsilon_d = 1$) are shown in Fig. 4.6 (d), (h), (l), and (p) (for spherical voids) with $d = 770, 680, 580$, and 500 nm, respectively. Just a single value of $f_v (= 0.88)$ sufficed to predict the dispersions accurately for all three values of the period d , when compared with the experimentally obtained Fig. 4.6 (a), (e), (i), and (m). The FESEM images also indicate $f_v \simeq 0.9$ for all four silver CTFs. The propagation length of an SPP wave calculated as the inverse of the imaginary part of k_{SPP} is shown in Fig. 4.7.

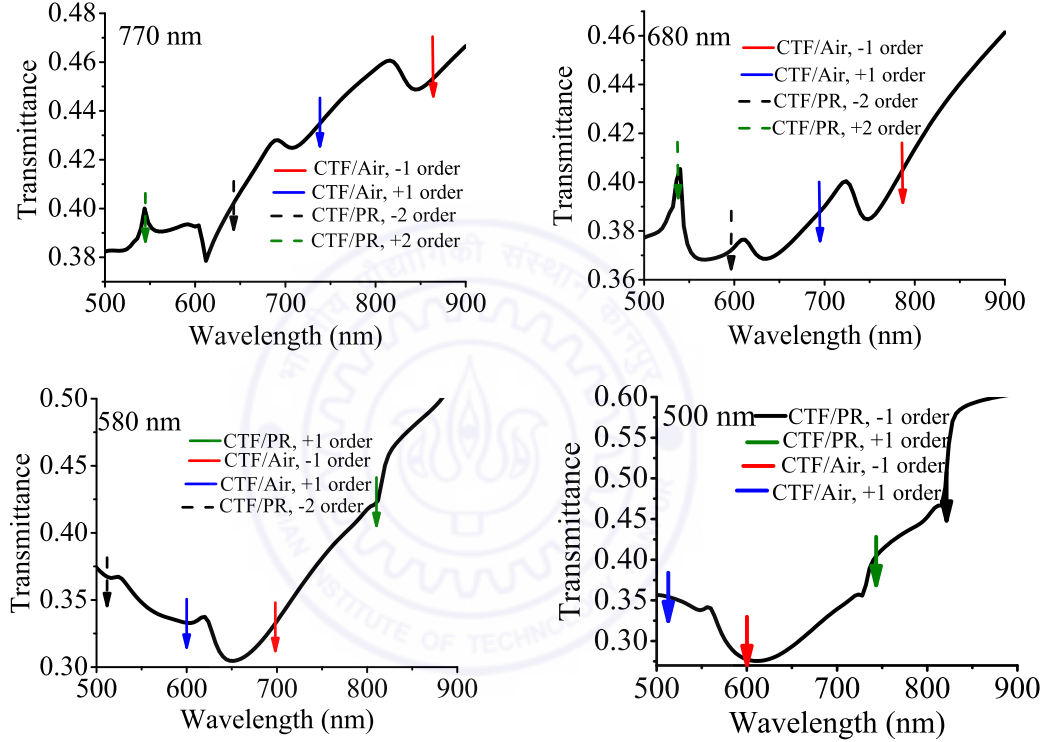


Figure 4.8: Simulated transmittance spectra for the structure with period $d \in \{770, 680, 580, 500\}$ nm when s -polarized light is incident at $\theta = 5^\circ$. Red and blue solid-line arrows correspond to SPP waves guided by the CTF/air interface with $n = -1$ and $n = +1$ orders, respectively; black and green solid-line arrows correspond to SPP waves guided by the CTF/photoresist interface with $n = -1$ and $n = +1$ orders, respectively; and black and green dotted-line arrows correspond to SPP waves guided by CTF/photoresist interface with $n = -2$ and $n = +2$ orders, respectively.

4.3.3 Coupling of s -polarized light to SPP waves

A theoretical treatment of the metallic CTF as a homogeneous continuum indicates that s -polarized incident light cannot couple to an SPP wave in the present situation.

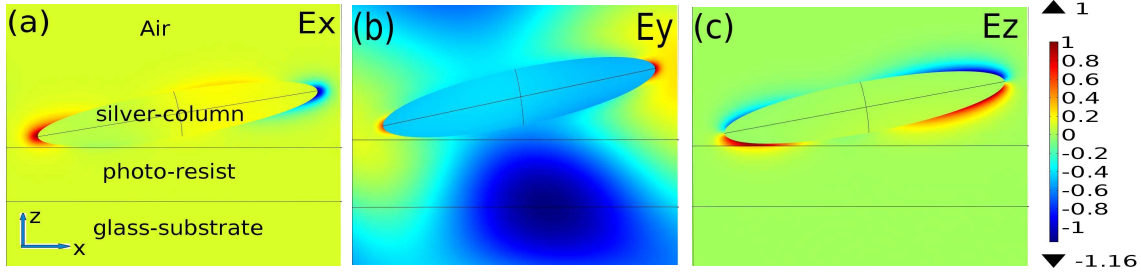


Figure 4.9: Simulated distributions of (a) E_x , (b) E_y , and (c) E_z in the structure with period $d = 580$ nm illuminated by s -polarized light of free-space wavelength 650 nm incident at $\theta = 5^\circ$. The incident plane wave of the form $\exp(-i\omega t)$ was assumed and the shown fields are in phase with the incident wave. Lengths of the major and two minor axes of the ellipsoids are 520 nm and 90 nm, respectively with a 100-nm-thick photoresist film on a glass substrate.

Yet, in Fig. 4.6 (b), (f), (j), and (n), dispersive features indicative of that coupling are evident in the angle-resolved transmittance spectra obtained with s -polarized light. The s -polarized incident light could couple to the SPP waves due to scattering arising from either the columnar structure of the CTF or from the surface roughness that is visible in the FESEM images. Note that the scattered fields from the three dimensional morphology of the slanted nano-columns would not preserve the polarization. It is the broken symmetry due to the 3-D morphology that lies at the heart of this coupling of s -polarized light to the SPP waves. To verify whether the columnar structure itself is responsible for this effect, we performed numerical simulations considering only the columnar structure with no roughness.

The simulations were performed using COMSOL Multiphysics software to validate the coupling of s -polarized light to SPP waves even in the absence of surface roughness. A periodic array of silver prolate ellipsoids with their major axes oriented along the nano-columnar axis (i.e., $\hat{\tau}$) was considered as the CTF. The ellipsoids were placed on a dielectric substrate of refractive index 1.65. Periodic boundary conditions consistent with the Floquet theory were applied along both the x and y directions. The unit cell size was $d(\hat{x}) \times 110 \text{ nm}(\hat{y}) \times 1300 \text{ nm}(\hat{z})$, where d is the periodicity of the array. Transmittance spectra were calculated by integrating the power flow on the planes immediately below and above the array of ellipsoids.

The transmission through a periodic array of appropriately oriented silver ellip-

soids revealed strong spectral minima that approximately coincide with the measured transmittance minima for all the grating periods d considered for this paper. We show plots of the simulated transmittance spectra for $d \in \{770, 680, 580, 500\}$ nm in Fig. 4.8. The transmittance dips in the plots should correspond to the resonant wavelengths/angles at which coupling with SPP waves occurs.

Fig. 4.9 shows the magnitudes of the Cartesian components of the electric field excited at resonance by the s -polarized incident light (which does not have x - and z -directed components). Very significantly, large localized E_x and E_z are excited of similar magnitudes as E_y . Thus, it becomes clear that the scattered fields, particularly the large near-zone fields associated with plasmonic nanocolumns, do not preserve the polarization state due to the ellipsoidal cross sections of the nanocolumns and couple to the SPP waves on the two interfaces. The locations of the measured transmittance minima arising due to coupling with SPP waves are marked by arrows in Fig. 4.8. The measured and simulated transmittance minima agree well and confirms that the coupling to SPP occurs due to the nanostructure.

The simulations clearly reveal that the coupling of the s -polarized light to the SPP waves can occur entirely due to the finite cross-sections of the nanocolumns and nanoscale roughness will play a minimal role. This validates the point that non-preservation of the polarization state in the scattered fields causes the coupling to SPP waves. The indirect coupling of the incident s -polarized light excites SPP waves more symmetrically for $\theta \gtrless 0$ (positive and negative θ) than the direct coupling of the incident p -polarized light.

However, we note that the overall transmittance is a little bit higher in the simulated results than the experimental measurements. This could arise due to various assumptions about the thickness of the metal layer (absent in the simulations) and the density of the nanocolumns along the grating lines. An additional mechanism for both the coupling of SPP waves to s -polarized light as well as the lowered transmittance can arise from imperfections in the fabricated structures which leads to slightly misaligned nanocolumns or bending of the nanocolumns along the grating direction. Such

nanocolumns can create cross-polarization in the plane of incidence for s -polarized light which can also couple to SPP waves.

4.4 Symmetric Coupling and dispersion of SPP Waves for 1D PPMCTFs: incidence in the plane orthogonal to the morphologically significant plane

In the previous section, we focused on the SPP dispersion when the plane of incidence coincides with the morphologically significant plane of the metallic PP-CTF. The Bruggemann homogenization formalism was used to estimate the relative permittivity tensor of the metallic CTF (which underlies the concept of the PP-CTF), thereby revealing hyperbolic dispersion. After solving the frequency-domain Maxwell equations while enforcing the standard boundary conditions across the planar interface of the homogenized metallic CTF and an isotropic dielectric material, a straightforward expression for the SPP wavenumber was derived. The resulting theoretical dispersion plots exactly matched with the SPP dispersion plots obtained experimentally with PP-CTFs of various periods. Experimental data revealed asymmetric transmission with respect to the thickness direction of the CTF, that asymmetry being concomitant with asymmetric coupling to SPP waves. A detailed study of the dependence of SPP dispersion on the angle ψ between the plane of incidence and the morphologically significant plane of the PP-CTF will yield a deeper understanding of the potential of metallic PP-CTFs for plasmonic applications. Whereas the previous section was devoted to theoretical and experimental investigation for $\psi = 0^\circ$ as shown in Fig. 4.10 (a), here we focus on $\psi = 90^\circ$ as shown in the schematic of Fig. 4.10 (b). Our objectives here are to determine theoretically and experimentally (a) what happens when the wave vector of the incident plane wave is orthogonal to the morphologically significant plane and (b) whether the asymmetry previously observed for $\psi = 0^\circ$ persists or not.

When light of free-space wavelength λ_0 and wavenumber $k_0 = 2\pi/\lambda_0$ is incident

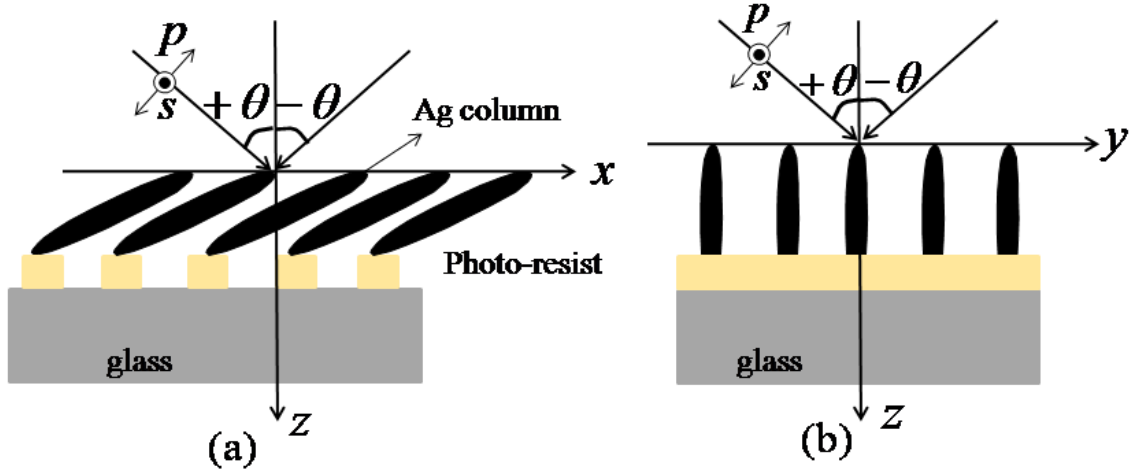


Figure 4.10: (a) Schematic of a PP-CTF, when the plane of incidence coincides with the morphologically significant plane i.e the xz plane. (b) Schematic of a PP-CTF illuminated obliquely either a p -polarized or an s -polarized plane wave. The morphologically significant plane of the PP-CTF is designated as the xz plane and the plane of incidence as the yz plane (i.e., $\psi = 90^\circ$). Both positive and negative values of the angle of incidence θ are indicated.

on a PP-CTF, the n^{th} diffracted order is expected to indicate the excitation of an SPP wave, provided that

$$\text{Re}(k_{\text{SPP}}) = \pm \sqrt{[k_0 \sin \theta \cos \psi + n(2\pi/d)]^2 + (k_0 \sin \theta \sin \psi)^2}, \quad (4.15)$$

where k_{SPP} is the SPP wavenumber, d is the period, and $n \in \{\pm 1, \pm 2, \dots\}$. For $\psi = 90^\circ$, the procedure to estimate k_{SPP} is available in Appendix A

When $\psi = 90^\circ$, the asymmetry of the PP-CTF should not be germane because the distinction between the negative and positive values of θ is expected to vanish; see Fig. 4.10 (b). Moreover, Eq. (4.15) simplifies to

$$\text{Re}(k_{\text{SPP}}) = \pm \sqrt{n^2 (2\pi/d)^2 + k_0^2 \sin^2 \theta}, \quad (4.16)$$

which is insensitive to the sign of θ . The solutions of Eq. (4.16) turn out to be organized in quasi-parabolic branches for the chosen range of θ .

Fig. 4.11 (a) presents the total specular transmittance measured over the ranges $\lambda_0 \in [500, 1000]$ nm and $\theta \in [-45^\circ, 45^\circ]$ when the incident light is p polarized, $\psi = 90^\circ$,

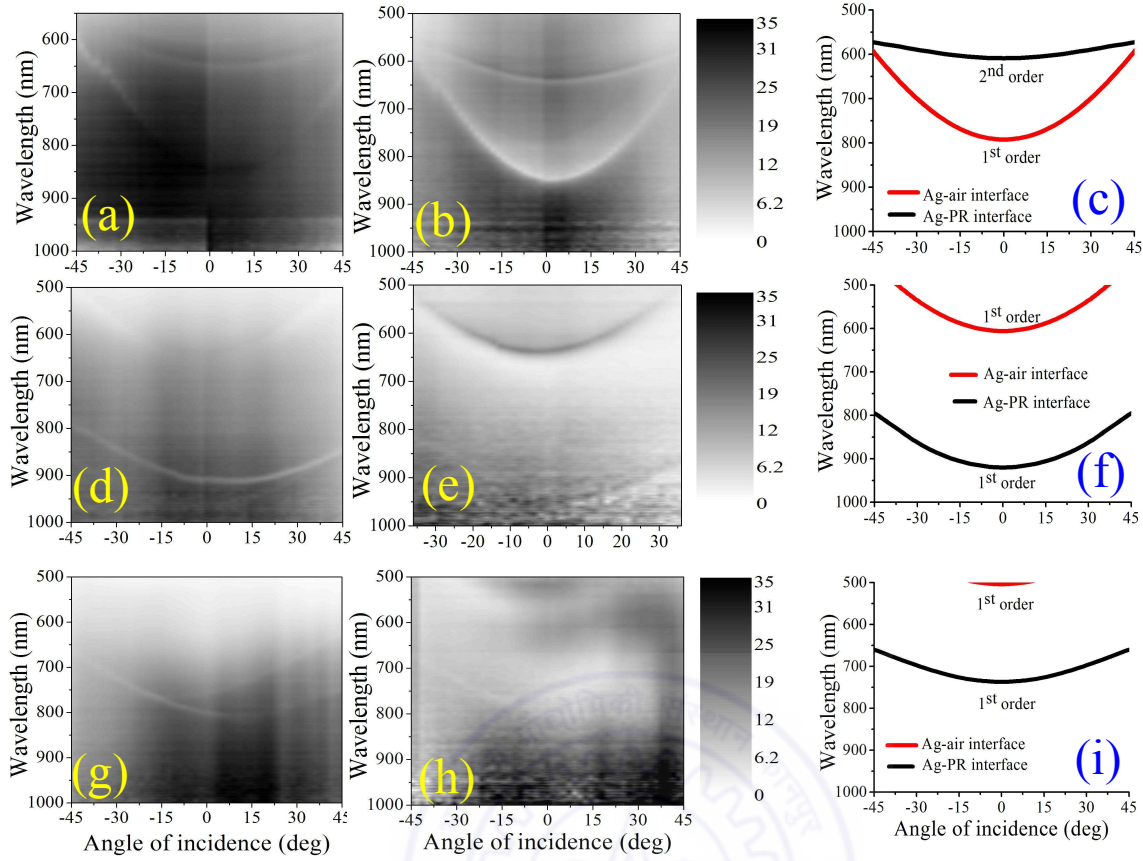


Figure 4.11: SPP dispersion plots when incident plane wave is orthogonal to the morphologically significant plane; when the incident light is p polarized and the period $d =$ (a) 770 nm, (d) 580 nm, and (g) 500 nm; angle-resolved transmittance spectra when the incident light is s polarized and the period $d =$ (b) 770 nm, (e) 580 nm, and (h) 500 nm; theoretical plots for the dispersion of SPP waves obtained using $\tilde{\epsilon}$ predicted by the Bruggeman model with ellipsoidal voids ($f_v = 0.88$, $\gamma_\tau^{(m)} = 7$, $\gamma_b^{(m)} = 1.2$, $\gamma_\tau^{(v)} = 10$, and $\gamma_b^{(v)} = 1$) when the period $d =$ (c) 770 nm, (g) 680 nm, (k) 580 nm, and (o) 500 nm; The theoretical predictions for the CTF/photoresist interface are black solid lines, while those for the CTF/air interface are red solid lines. The orders $n = \pm 1$ and ± 2 for Bragg scattering are indicated as 1st and 2nd order.

and $d = 770$ nm. The same quantity is presented in Fig. 4.11 (b), except that the incident light is s polarized.

In all these figures, there is a symmetry for the coupling of the SPP waves with the incident light coming from either side of the z axis in the $y - z$ plane; furthermore, the dispersion is quite parabolic for both linear-polarization states of the incident light. There is less symmetry in Fig. 4.11 (g), (h) with respect to θ than in Fig. 4.11 (d), (e) and 4.11 (a), (b), leading to the conjecture that there is a tendency towards complete symmetry for $\psi = 90^\circ$ as the period d increases.

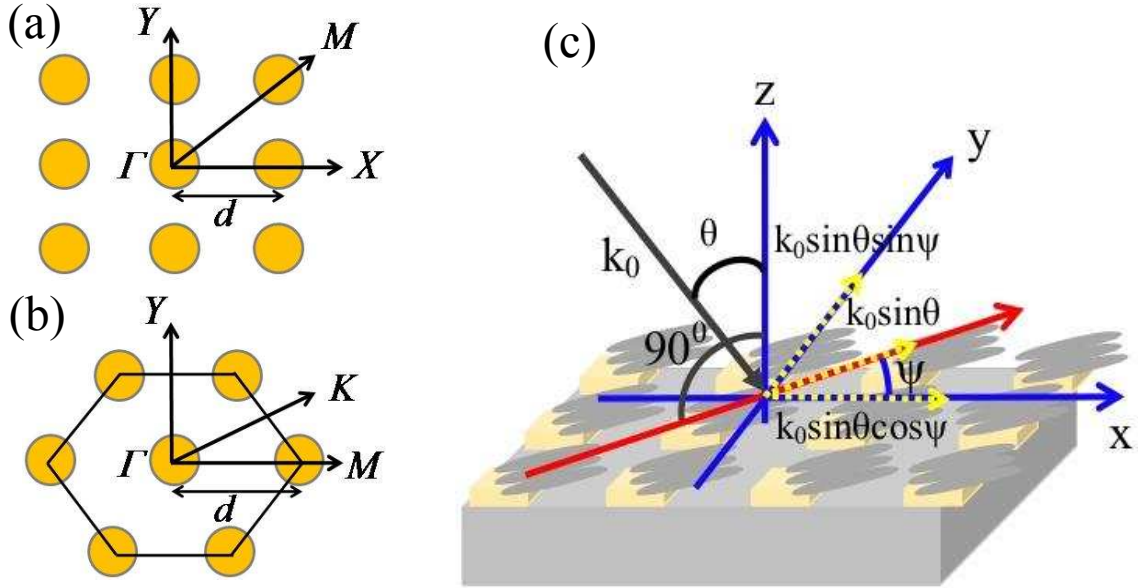


Figure 4.12: Schematics of (a) symmetry directions for 2D square and (b) hexagonal lattices in reciprocal space, which is important for the understanding of the in-plane momentum-matching condition for coupling of the incident light to an SPP wave. (c) Schematic of a periodically patterned CTF of silver with the xz plane as its morphologically significant plane [1, 136]. Also shown is the component $k_0 \sin \theta$ of the wave vector of the incident light in the xy plane, where θ is the angle of incidence with respect to the z axis. This in-plane component is split into components $k_0 \sin \theta \cos \psi$ along the x axis and $k_0 \sin \theta \sin \psi$ along the y axis.

We conclude from Figs. 4.11 that the asymmetry in the coupling of SPP waves with respect to the sense of the angle of incidence θ diminishes as $\psi \rightarrow 90^\circ$. This phenomenon can also be understood from studies of angular selective transmittance through CTFs comprising slanted metallic columns, it having been theoretically shown [107, 135] that angular selectivity is maximal when the plane of incidence coincides with a morphologically significant plane.

4.5 SPP dispersion on two dimensional (2-D) PPM-CTFs

As coupling of incident light to SPP waves is facilitated further when the 1D grating is replaced by a 2D grating [137], we grew slanted CTFs of silver by OAD on 2D gratings of different square and hexagonal lattices. Although the lattices are symmetric, the

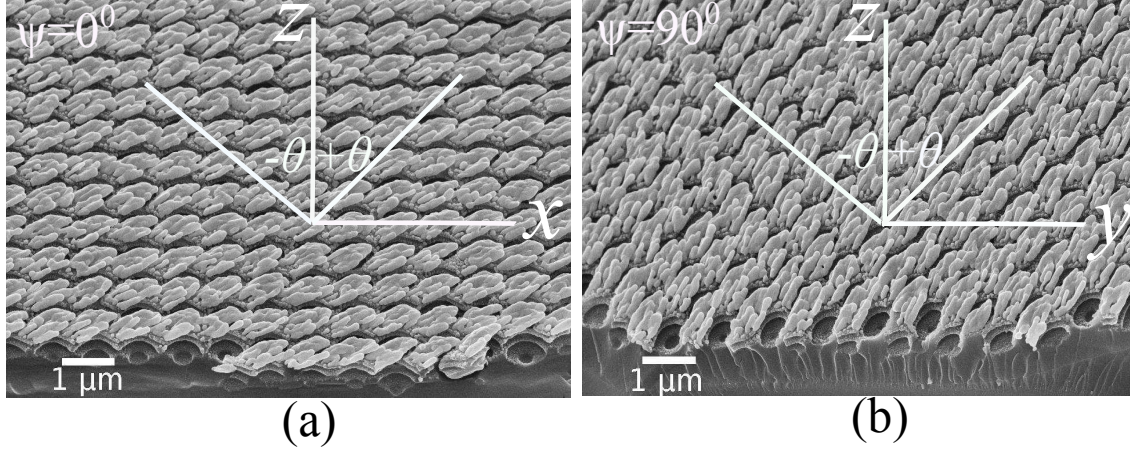


Figure 4.13: FESEM images of a PP-CTFs of silver on a square grating ($d = 580$ nm). The morphologically significant plane is the xz plane. Light is incident either (a) in the xz plane, i.e., $\psi = 0^\circ$, or (b) in the yz plane, i.e., $\psi = 90^\circ$. The positive and negative values of θ shown are needed to understand the asymmetry of the data in Figs. 4.15 and 4.16.

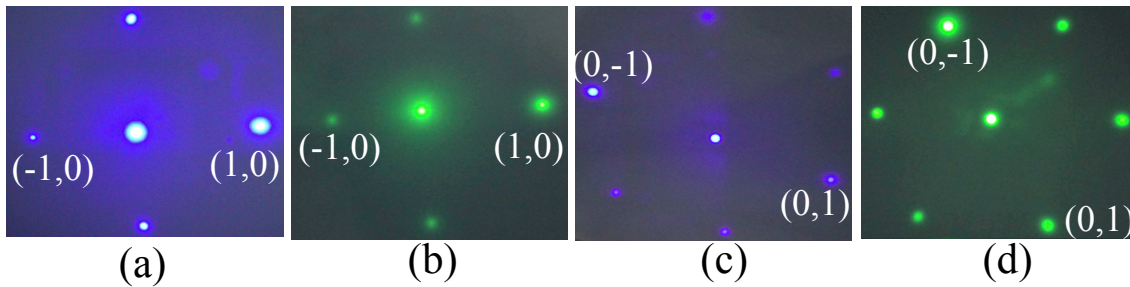


Figure 4.14: Photographs of asymmetric diffraction of normally incident p -polarized light by a CTF deposited on either (a,b) the square grating or (c,d) the hexagonal grating for either (a,c) $\lambda = 442$ nm or (b,d) $\lambda = 532$ nm.

overall structures have pronounced asymmetry due to the slant angle of the CTFs with respect to the interface plane. This asymmetry profoundly affects the nature of the coupling to SPP waves, which we studied via angle-resolved specular-transmittance measurements. The anisotropy of CTFs and the properties of blazing create conditions for unidirectional propagation of SPP waves when the grating has 2D periodicity.

The anisotropic plasmonic grating structure studied here is schematically shown in Fig. 4.12, where the photoresist grating, the nanocolumns of the silver CTF, and the propagation direction of the incident light are indicated. Figure 4.13(a) shows the FESEM image of a periodically patterned CTF comprising 500-nm-long and 90-nm-diameter nanocolumns of silver deposited on a square photoresist grating ($d = 580$ nm). This image shows that the silver nanocolumns were deposited only on the grating top and constitute an asymmetric structure in the morphologically significant plane of the CTF. Figure 4.13(b) shows the same structure rotated by 90° about the z axis. The plane of light incidence is the xz plane (i.e., $\psi = 0^\circ$) in Fig. 4.13(a), and the yz plane (i.e., $\psi = 90^\circ$) in Fig. 4.13(b).

Figure 4.14 shows optical images of the transmission diffraction patterns in the far-zone taken by a camera for normally incident (i.e., $\theta = 0^\circ$) p -polarized light ($\mathbf{E}_{inc} \parallel \hat{x}$) of $\lambda \in \{442, 532\}$ nm. The silver CTF was deposited on either the square or the hexagonal photoresist grating for this figure. The asymmetric diffraction evident in the figure is due to the slanting of the silver nanocolumns at an angle $\chi < 90^\circ$ with respect to the xy plane [136].

The loci of the specular-transmittance minima can be correlated with the excitation of SPP waves, when a plane wave is incident on the CTF-coated photoresist grating. Figures 4.15(a), (b), and (c) show plots of the measured specular transmittance as a function of both λ and θ for the structure comprising the silver CTF deposited on the square grating for: $\psi = 0^\circ$, $\psi = 45^\circ$, and $\psi = 90^\circ$, respectively, when the incident light is p polarized. The corresponding directions are marked as Γ -X, Γ -M, and Γ -Y in Fig. 4.12(a). Analogous plots for the silver CTF deposited on the hexagonal grating are shown in Figs. 4.16(a), (b), and (c), respectively for $\psi = 0^\circ$ (Γ -M in Fig. 4.12(b)),

$\psi = 30^\circ$ (Γ -K), and $\psi = 90^\circ$ (Γ -Y).

The loci of the specular-transmittance minima in Fig. 4.15 reveal that the coupling of the incident p -polarized light to an SPP wave is stronger for incidence from one side ($\theta \gtrless 0^\circ$) than from the other side ($\theta \lesseqgtr 0^\circ$). This asymmetry is evident from unequal specular transmittances. We can clearly see that the asymmetry is the most for $\psi = 0^\circ$ and the least for $\psi = 90^\circ$. Clearly, the slant of the silver nanocolumns in the xz plane has

- the greatest effect when $\psi = 0^\circ$ and \mathbf{E}_{inc} lies wholly in the morphologically significant plane, and
- the least effect when $\psi = 90^\circ$ and \mathbf{E}_{inc} is wholly perpendicular to the morphologically significant plane.

Another reason for the variation of asymmetry with ψ may be because the projection of the relative permittivity dyadic $\tilde{\epsilon}$ of the CTF (when assumed to be a homogeneous material [136]) on the nanocolumnar axis is very different from the projection of $\tilde{\epsilon}$ in any direction to which the nanocolumnar axis is orthogonal. Similar variations in asymmetry (with respect to θ) with ψ arise in Fig. 4.16 for the structure with the hexagonal grating.

4.6 Analysis of the SPP dispersion on 2-D PPM-CTFs

For analytical purposes, we assumed an $\exp(-i\omega t)$ dependence on time t , with $i = \sqrt{-1}$; $\omega = 2\pi/(\lambda\sqrt{\epsilon_0\mu_0})$ as the angular frequency; and ϵ_0 and μ_0 as, respectively, the permittivity and permeability of free space. The electric field phasor of the incident

plane wave was taken as

$$\begin{aligned} \mathbf{E}_{inc} = & \{[(\hat{x} \cos \psi + \hat{y} \sin \psi) \cos \theta + \hat{z} \sin \theta] \cos \delta \\ & + (-\hat{x} \sin \psi + \hat{y} \cos \psi) \sin \delta\} \exp [ik_0 (x \cos \psi + y \sin \psi) \sin \theta] \\ & \times \exp (-ik_0 z \cos \theta) , \end{aligned} \quad (4.17)$$

where \hat{x} , \hat{y} , and \hat{z} are the Cartesian unit vectors; the angles $\theta[-90^\circ, 90^\circ]$, $\psi \in [0^\circ, 180^\circ]$, and $\delta \in [0^\circ, 90^\circ]$; and $k_0 = 2\pi/\lambda$ is the free-space wavenumber. The incident plane wave is p polarized when $\delta = 0^\circ$, but s polarized when $\delta = 90^\circ$.

In the fabricated structures, the metal nanocolumns of the CTF have their axes oriented at an angle $\chi = 15^\circ \pm 2^\circ$ with respect to the x axis in the xz plane. As the diameters of the nanocolumns are in the range of 80-90 nm and the lengths are in the range of 500-600 nm, each nanocolumn can be modeled as a string of highly elongated ellipsoids [1]. The relative permittivity dyadic $\tilde{\epsilon}$ of the CTF (when viewed as a homogeneous material) depends on the slant angle χ , both shape factors of the ellipsoids, and the porosity of the CTF. The three eigenvalues $\epsilon_{a,b,c}$ of $\tilde{\epsilon}$ can be estimated using the Bruggeman homogenization formalism [1]. We have shown elsewhere [136] that $\text{Re}(\epsilon_a) > 0$, $\text{Re}(\epsilon_b) < 0$, and $\text{Re}(\epsilon_c) > 0$ for the silver CTFs. Whereas ϵ_b is the projection of $\tilde{\epsilon}$ on the nanocolumnar axis (i.e., parallel to the unit vector $\hat{\tau} = \hat{x} \cos \chi + \hat{z} \sin \chi$), ϵ_a and ϵ_c are the respective projections of $\tilde{\epsilon}$ on the unit vectors $\hat{n} = -\hat{x} \sin \chi + \hat{z} \cos \chi$ and \hat{y} . So, the CTF shows metallic behaviour for $\mathbf{E} \parallel \hat{\tau}$ but dielectric behaviour for $\mathbf{E} \perp \hat{\tau}$.

As the CTF was deposited on a 2D grating, Floquet analysis yields the in-plane momentum-matching condition between the SPP wave and a Floquet mode of order (m, n) as follows [89, p. 154]:

- square grating

$$\begin{aligned} \text{Re} [k_{spp}(\bar{\psi})] (\hat{x} \cos \bar{\psi} + \hat{y} \sin \bar{\psi}) &= k_0 \sin \theta (\hat{x} \cos \psi + \hat{y} \sin \psi) \\ &+ \frac{2\pi}{d} (m\hat{x} + n\hat{y}) , \quad m \in \mathbb{Z}, \quad n \in \mathbb{Z} , \end{aligned} \quad (4.18)$$

- hexagonal grating

$$\begin{aligned} \operatorname{Re} [k_{spp}(\bar{\psi})] (\hat{x} \cos \bar{\psi} + \hat{y} \sin \bar{\psi}) &= k_0 \sin \theta (\hat{x} \cos \psi + \hat{y} \sin \psi) \\ &+ \frac{2\pi}{d} \left[m \left(\hat{x} - \frac{1}{\sqrt{3}} \hat{y} \right) + n \frac{2}{\sqrt{3}} \hat{y} \right], \quad m \in \mathbb{Z}, \quad n \in \mathbb{Z}. \end{aligned} \quad (4.19)$$

The excited SPP wave propagates parallel to the unit vector $\hat{x} \cos \bar{\psi} + \hat{y} \sin \bar{\psi}$ in the xy plane, $k_0 = 2\pi/\lambda$ is the free-space wavenumber, and $\mathbb{Z} = \{0, \pm 1, \pm 2, \dots\}$. The angle $\bar{\psi}$ can be determined from Eq. (4.18) or (4.19) as a function of θ , ψ , $k_0 d$, m , and n as follows:

- square grating

$$\bar{\psi} = \tan^{-1} \left(\frac{k_0 d \sin \theta \sin \psi + 2n\pi}{k_0 d \sin \theta \cos \psi + 2m\pi} \right), \quad (4.20)$$

- hexagonal grating

$$\bar{\psi} = \tan^{-1} \left(\frac{k_0 d \sin \theta \sin \psi + 2(2n - m)\pi/\sqrt{3}}{k_0 d \sin \theta \cos \psi + 2m\pi} \right). \quad (4.21)$$

The complex-valued SPP wavenumber k_{spp} can be calculated as a function of $\bar{\psi}$ for the planar CTF/air and CTF/photoresist interfaces separately, as detailed in Appendix A. The loci of the specular-transmittance minima in Figs. 4.15(a-c) and 4.16(a-c) were fitted to Eqs. (4.18) and (4.19), respectively, following a procedure detailed for 1D gratings in the predecessor paper [136]. Note that the loci of the specular transmittance minima no longer trace out the dispersions of a unique SPP propagating on the interface between the isotropic dielectric and anisotropic metal. Rather due to the anisotropic nature, light incident from different directions (θ) couples to SPPs propagating in distinctly different directions in the plane.

As discussed previously in this section, the CTF was viewed as a composite material comprising highly elongated ellipsoids of air and silver. All ellipsoids of air were taken to be identical in shape and all ellipsoids of silver were similarly identical. The longest axes of all ellipsoids was set parallel to the unit vector $\hat{\tau}$. The volume

fraction of air is the porosity $f_v \in [0, 1]$, while the volume fraction of silver equals $1 - f_v$. This collection of ellipsoids was homogenized into a biaxial dielectric material of relative permittivity dyadic $\tilde{\varepsilon}$, using the Bruggeman formalism [1]. We used the Drude model for the relative permittivity of silver as $\varepsilon_m(\omega) = 5.7 - \omega_p^2/[\omega(\omega + i\gamma_p)]$, where the angular frequency ω is in units of eV, $\omega_p = 9.2$ eV, and $\gamma_p = 0.021$ eV [138]. The following parameters were found to be adequate to determine $\tilde{\varepsilon}$: CTF porosity $f_v = 0.7$, shape factors of silver ellipsoids $\gamma_\tau^{(m)} = 15$ and $\gamma_b^{(m)} = 1.5$, and shape factors of air ellipsoids $\gamma_\tau^{(v)} = 1$ and $\gamma_b^{(v)} = 1$. The Bruggeman equation solved to determine $\varepsilon_{a,b,c}$ is provided in Appendix B.

Once $\tilde{\varepsilon}$ had been estimated, values of $k_{spp}(\bar{\psi})$ for the planar CTF/air and CTF/photoresist interfaces were found (see Appendix A) and fitted to Eqs. (4.18) and (4.19), as appropriate. We set the relative permittivity of the photoresist material as $\varepsilon_p = 2.5$ for these calculations. Figures 4.15(d), (e), and (f) show the calculated solutions of Eq. (4.18) for the silver CTF deposited on the square grating for $\psi = 0^\circ$ (Γ -X), $\psi = 45^\circ$ (Γ -M), and $\psi = 90^\circ$ (Γ -Y), respectively. Let us note that the slanting of the nanocolumns in the xz plane breaks the fourfold rotational symmetry about the z axis, so that Γ -X and Γ -Y are not equivalent directions. Figures 4.16(d), (e), and (f) show the calculated solutions of Eq. (4.19) for the silver CTF deposited on the hexagonal grating for $\psi = 0^\circ$ (Γ -M), $\psi = 30^\circ$ (Γ -K), and $\psi = 90^\circ$ (Γ -Y), respectively. Again, let us note that the sixfold rotational symmetry about the z axis is broken by the slanting of the nanocolumns in the xz plane.

Plots of the measured specular transmittance in Figs. 4.15(a-c) and 4.16(a-c) show the excitation of SPP waves via diffraction due to the periodicity of the 2D grating. The coupling of the incident light to the SPP waves can be clearly understood from the theoretical curves in Figs. 4.15(d-f) and 4.16(d-f) for the corresponding symmetry directions. In Figs. 4.15(d-f) and 4.16(d-f), each curve is identified as either $(m, n)_a$ or $(m, n)_p$, where (m, n) is the index pair in Eqs. (4.18) and (4.19), the subscript ‘a’ indicates that the SPP wave is bound tightly to the CTF/air interface, and the subscript ‘p’ indicates that the SPP wave is bound tightly to the CTF/photoresist

interface.

Let us now discuss the coupling to SPP waves for propagation along various directions separately.

4.6.1 Square grating, $\psi = 0^\circ$ (Γ -X)

From Figs. 4.15(a) and (d), we conclude that the $(1, 0)_a$ Floquet mode is very strong and of narrow bandwidth, while the $(-1, 0)_a$ Floquet mode is much weaker in comparison. Also, the $(1, 0)_p$ mode is strong while the $(-1, 0)_p$ mode is weak, but the former has a broader bandwidth. The $(-2, 0)_p$ mode is weakly coupled, while the $(2, 0)_p$ mode is not even discernible in Fig. 4.15(a) implying no coupling. All of the foregoing Floquet modes show linear dispersion in accordance with the relation

$$\pm \operatorname{Re} [k_{spp}(0^\circ)] = k_0 \sin \theta + m \frac{2\pi}{d}, \quad (4.22)$$

but the $(0, 1)_p$ and $(0, -1)_p$ Floquet modes show quadratic dispersion according to the relation

$$\left. \begin{aligned} \pm \operatorname{Re} [k_{spp}(\bar{\psi})] &= \sqrt{k_0^2 \sin^2 \theta + \left(n \frac{2\pi}{d}\right)^2} \\ \bar{\psi} &= \tan^{-1} \left(n \frac{2\pi}{k_0 d \sin \theta} \right) \end{aligned} \right\}. \quad (4.23)$$

Both of these dispersions emerge from Eq. (4.18).

Clearly, in any pair of Floquet modes of either the type $(\pm|m|, 0)$ or the type $(0, \pm|n|)$, one of the two is more strongly coupled than the other to an SPP wave; the one with the larger transmittance couples more strongly to the SPP wave than the one with smaller transmittance. As discussed previously, this asymmetry arises from the slanting of the silver nanocolumns at an angle $\chi < 90^\circ$ with respect to the x axis in the morphologically significant plane. This asymmetry is also evident in Figs. 4.14(a) and (b) for $\lambda = 442$ nm and $\lambda = 532$ nm, respectively, wherein the $(1, 0)$ -order diffraction has higher intensity than the $(-1, 0)$ -order diffraction. The asymmetry of angular-selective transmittance through a slanted metal CTF can be well understood

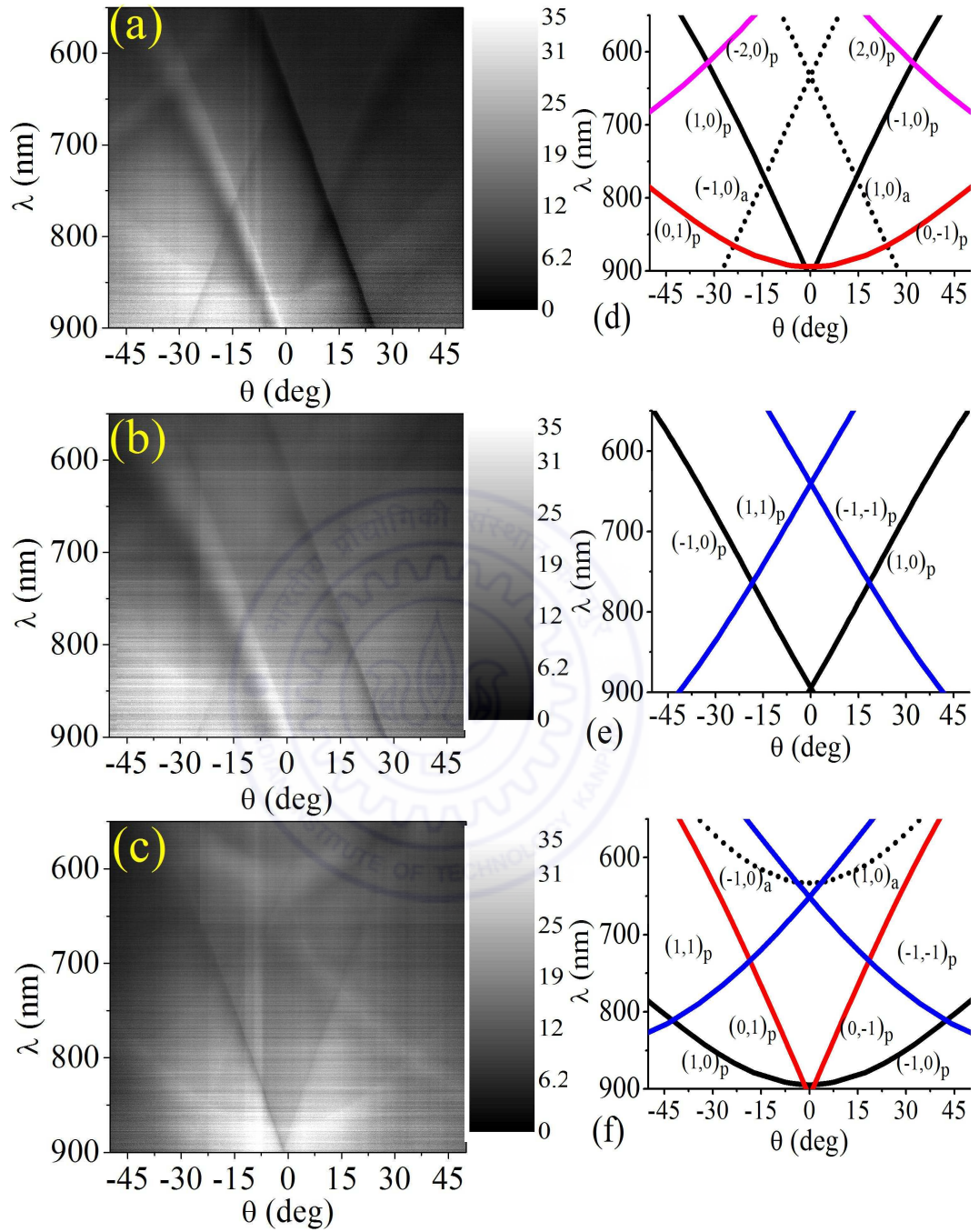


Figure 4.15: Measured specular transmittance of the silver CTF deposited on the square grating for (a) $\psi = 0^\circ$ (Γ -X), (b) $\psi = 45^\circ$ (Γ -M), and (c) $\psi = 90^\circ$ (Γ -Y), when the incident light is p polarized. Corresponding solutions of Eq. (4.18) for (d) $\psi = 0^\circ$ (Γ -X), (e) $\psi = 45^\circ$ (Γ -M), and (f) $\psi = 90^\circ$ (Γ -Y), with dotted curves representing the SPP waves bound tightly to the CTF/air interface and solid curves representing the SPP waves bound tightly to the CTF/photoresist interface.

from extant theoretical results [107, 135], the angular selectivity being maximal when the propagation vector of the incident plane wave lies wholly in the morphologically significant plane (i.e., when $\sin \psi = 0$).

4.6.2 Square grating, $\psi = 45^\circ$ (Γ -M)

From Fig. 4.15(e), we conclude that coupling with any SPP wave bound tightly to the CTF/air interface does not occur for $\psi = 45^\circ$. Furthermore, the $(1, 1)_p$, $(-1, -1)_p$, and $(\pm 1, 0)_p$ Floquet modes obeying the dispersion relation

$$\left. \begin{aligned} \pm \text{Re} [k_{spp}(\bar{\psi})] &= \sqrt{\left[\frac{k_0 \sin \theta}{\sqrt{2}} + m \left(\frac{2\pi}{d} \right) \right]^2 + \left[\frac{k_0 \sin \theta}{\sqrt{2}} + n \left(\frac{2\pi}{d} \right) \right]^2} \\ \bar{\psi} &= \tan^{-1} \left(\frac{k_0 d \sin \theta + 2\sqrt{2}n\pi}{k_0 d \sin \theta + 2\sqrt{2}m\pi} \right) \end{aligned} \right\} \quad (4.24)$$

are observed.

The couplings of the Floquet modes to SPP waves and their bandwidths in Fig 4.15(b) are similar to those in Fig 4.15(a), except that the asymmetry in the former is weaker than in the latter. The lessening of asymmetry and the decrease in angular selectivity is because the propagation vector of the incident plane wave casts the same projections on the xz and yz planes, the silver nanocolumns being slanted in the former plane but upright in the latter plane.

4.6.3 Square grating, $\psi = 90^\circ$ (Γ -Y)

According to Eq. (4.18), coupling of a Floquet mode to an SPP wave is predicted by the relation

$$\left. \begin{aligned} \pm \text{Re} [k_{spp}(\bar{\psi})] &= \sqrt{m^2 \left(\frac{2\pi}{d} \right)^2 + \left[k_0 \sin \theta + n \left(\frac{2\pi}{d} \right) \right]^2} \\ \bar{\psi} &= \tan^{-1} \left(\frac{k_0 d \sin \theta + 2n\pi}{2m\pi} \right) \end{aligned} \right\} \quad (4.25)$$

for $\psi = 90^\circ$. As the propagation vector is normal to the morphologically significant plane for light incident along the Γ -Y direction, the curves in Fig. 4.15(c) appear significantly different from those in Fig. 4.15(a). First, the $(1, 1)_p$ and $(-1, -1)_p$ Floquet modes couple to SPP waves for $\psi = 90^\circ$, but not for $\psi = 0^\circ$. Second, the couplings of the $(1, 0)_a$, $(-1, 0)_a$, $(1, 0)_p$, and $(-1, 0)_p$ Floquet modes to SPP waves show quadratic dispersion for $\psi = 90^\circ$, but linear for $\psi = 0^\circ$. Third, the couplings of the $(0, 1)_p$ and $(0, -1)_p$ Floquet modes to SPP waves show linear dispersion for $\psi = 90^\circ$, but quadratic for $\psi = 0^\circ$.

So, by changing the azimuthal orientation angle ψ of the propagation vector of the incident plane wave with respect to the morphologically significant plane of the CTF, one can exploit the anisotropy of the CTF to tune the dispersion characteristics of SPP waves. This is in contrast to a normal isotropic plasmonic thin-film grating for which the dispersion characteristics would be identical for $\psi = 0^\circ$ and $\psi = 90^\circ$. The anisotropy of the CTF is thus a tool for inducing changes in dispersion.

4.6.4 Hexagonal grating, $\psi = 0^\circ$ (Γ -M)

The measured specular-transmittance data are presented in Fig. 4.16(a) for $\psi = 0^\circ$, and the corresponding predictions from Eq. (4.19) are shown in Fig. 4.16(d). According to Eq. (4.19), the coupling of a Floquet mode to an SPP wave is predicted by the relations

$$\left. \begin{aligned} \pm \text{Re} [k_{spp}(\bar{\psi})] &= \sqrt{[k_0 \sin \theta + m \left(\frac{2\pi}{d}\right)]^2 + \left[(2n - m) \left(\frac{2\pi}{d\sqrt{3}}\right)\right]^2} \\ \bar{\psi} &= \tan^{-1} \left(\frac{2(2n-m)\pi/\sqrt{3}}{k_0 d \sin \theta + 2m\pi} \right) \end{aligned} \right\}. \quad (4.26)$$

In Fig. 4.16(a), the $(0, -1)_a$ Floquet mode appears to be very strongly coupled to an SPP wave, while the $(0, 1)_a$ mode is weakly coupled (if at all). The couplings of the $(1, 1)_p$, $(-1, -1)_p$, $(1, 1)_a$, $(-1, -1)_a$, and $(1, 2)_p$ modes are very weak, and the $(-1, -2)_p$ mode is not coupled to an SPP wave. Asymmetric coupling is evident Fig. 4.16(a), for the same reason as discussed in Sec. 4.6.1. The same asymmetry for the hexagonal

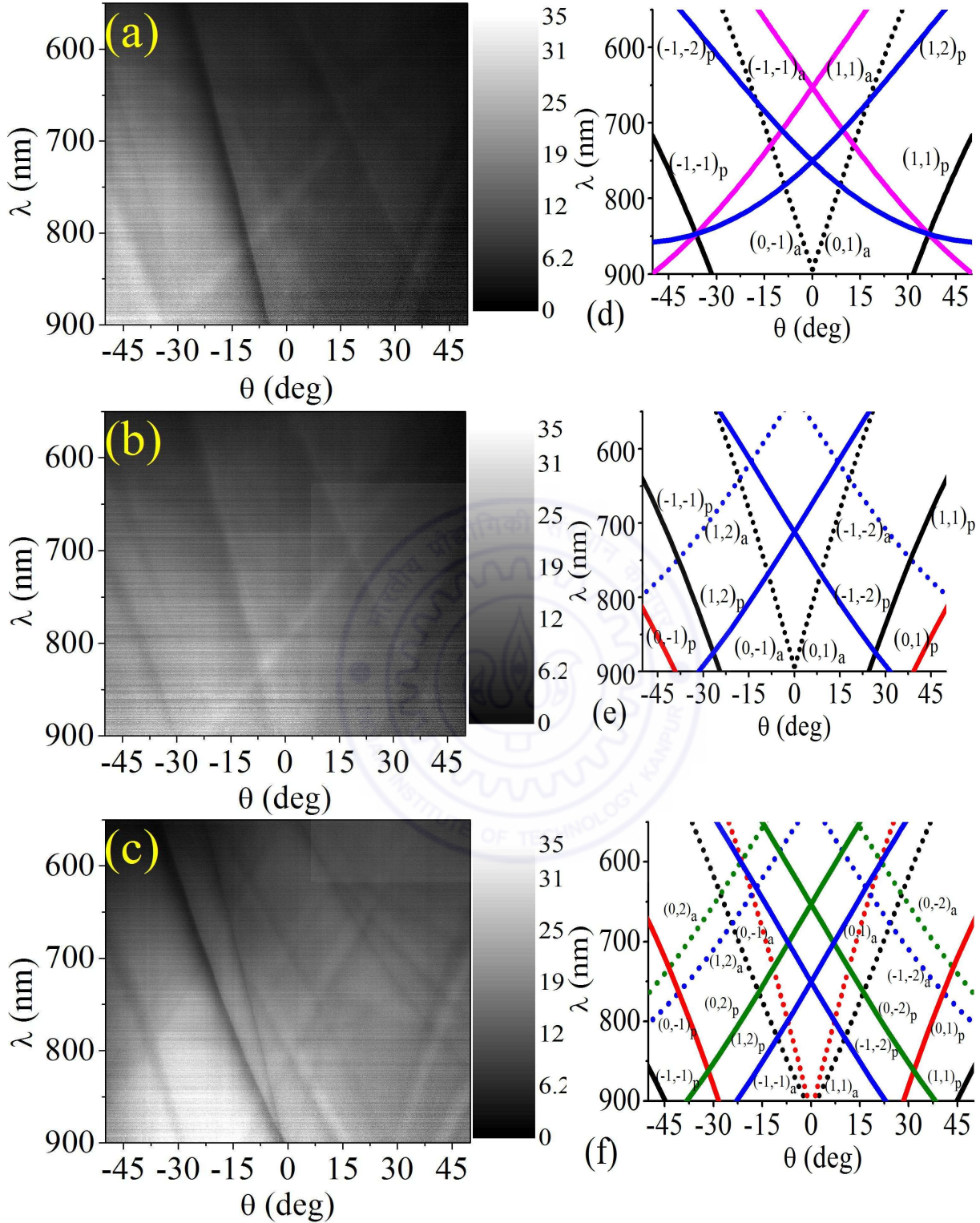


Figure 4.16: Measured specular transmittance of the silver CTF deposited on the hexagonal grating for (a) $\psi = 0^\circ$ (Γ -M), (b) $\psi = 30^\circ$ (Γ -K), and (c) $\psi = 90^\circ$ (Γ -Y), when the incident light is p polarized. Corresponding solutions of Eq. (4.19) for (d) $\psi = 0^\circ$ (Γ -M), (e) $\psi = 30^\circ$ (Γ -K), and (f) $\psi = 90^\circ$ (Γ -Y), with dotted curves representing the SPP waves bound tightly to the CTF/air interface and solid curves representing the SPP waves bound tightly to the CTF/photoresist interface.

lattice is evident in Fig. 4.14(c,d) for illumination by normally incident laser beams.

4.6.5 Hexagonal grating, $\psi = 30^\circ$ (Γ -K)

The measured specular-transmittance data are presented in Fig. 4.16(b) and the corresponding predictions from Eq. (4.19) are shown in Fig. 4.16(e) for $\psi = 30^\circ$. For light incident along the Γ -K symmetry direction, couplings of the $(1, 2)_a$, $(-1, -2)_a$, $(0, 1)_p$, and $(0, -1)_p$ Floquet modes to SPP waves are clearly evident, these couplings being absent for $\psi = 0^\circ$. Couplings of the other Floquet modes to SPP waves are the same as for $\psi = 0^\circ$. The only difference is that the asymmetry is poorer in Fig. 4.16(b) than in Fig. 4.16(a), which is due to the smaller projection of the propagation vector of the incident plane wave on the morphologically significant plane.

4.6.6 Hexagonal grating, $\psi = 90^\circ$ (Γ -Y)

Figure 4.16(c) presents the measured specular-transmittance data and Fig. 4.16(f) the corresponding predictions from Eq. (4.19) for $\psi = 90^\circ$. More Floquet modes appear to be coupled to SPP waves for $\psi = 90^\circ$ than for $\psi = 0^\circ$ and $\psi = 30^\circ$. As examples, the $(0, \pm 2)_p$ and $(0, \pm 2)_a$ Floquet modes are coupled to SPP waves for $\psi = 90^\circ$ but not for $\psi = 0^\circ$ and $\psi = 30^\circ$.

A major difference between the square and the hexagonal lattices is that the curves in Figs. 4.15(d-f) are both linear and quadratic, but most curves in Figs. 4.16(d-f) are linear.

4.7 Conclusions

The investigation of the FESEM images of anisotropic plasmonic structures on 1-D gratings, reveal that the deposition of silver nanocolumnar arrays took place only on the ridges of the gratings and formed an asymmetric structure with a well defined

morphologically significant plane. The highly oriented nanocolumns are distinct and well separated by a few nanometers and almost from an array on the ridges of the grating. These structures show strongly asymmetric diffraction with highly unequal positive and negative orders and provide asymmetric coupling to SPP waves on the anisotropic metal grating when the incident plane lies in the morphologically significant plane, which can be useful in many optical devices. Angle resolved transmittance measurements through a corrugated silver grating structure and such asymmetric silver grating structures are compared. From the dispersion plots it is clear that the coupling to SPP is symmetric with respect to the plane of incidence in case of a corrugated grating structure with linear dispersion for several branches. Whereas for an asymmetric silver grating structure, the coupling to SPP is asymmetric with respect to the plane of incidence with linear dispersion for several modes. The asymmetry in these gratings results in preferential coupling to SPP propagating only along one direction. The asymmetry is maximal when the plane of incidence coincides with the morphologically significant plane of the PP-CTF, and diminishes when the two planes are mutually orthogonal. The maximal asymmetric coupling occurs with quasilinear dispersion, while almost symmetric coupling occurs, when the asymmetric grating structure is rotated by an angle of 90° with quasiparabolic dispersion. Coupling to SPP occurs for both p and s polarizations in the case of a nanostructured grating in contrast to excitation of SPP only through p polarization in case of a corrugated grating structure.

In the case of an anisotropic plasmonic structure on a 2-D grating, for oblique illumination, highly asymmetric coupling to SPP waves occurs when the propagation vector of an incident p -polarized plane wave lies wholly in the morphologically significant plane. When the structure is rotated about the thickness direction (i.e., the z axis) while the direction of the propagation vector of the incident plane wave is held fixed, the asymmetry wanes. Thus, this rotation can be used to tune the dispersion characteristics of the SPP waves. Gratings with square and hexagonal lattices show different dispersion characteristics, thereby affording another way to tune the frequency-dependences of the SPP waves excited. The phase speeds and the attenua-

tion rates of SPP waves propagating in different directions guided by the interface of a silver CTF and an isotropic, homogeneous, dielectric material propagate are different. This feature is responsible for the asymmetric couplings observed. If the silver CTF were to be replaced by a dense layer of silver, which would be anisotropic, SPP waves would propagate along different directions with the same phase speed and attenuation rate, and the asymmetric coupling would vanish.

The Bruggeman formalism was used to homogenize the silver CTFs into homogeneous hyperbolic biaxial materials. The predicted dispersions of the SPP waves matched the measured dispersions of the SPPs in such PPCTFs very well. The nano-level porosity can be controlled easily by changing the direction of the metal-vapor flux during fabrication and is a critical parameter for controlling the dispersions. Our fabrication technique represents a cost-effective solution for making blazed gratings, which are traditionally fabricated by expensive electron-beam lithography. Furthermore, the pre-patterned gratings can be made by alternative rapid production methods such as nanoimprint technology [139] which are immediately applicable to large-area fabrication. The extremely anisotropic background offered by the CTF grating is novel and is of immense interest for wave mixing and plasmonic applications. We are exploring some of these aspects presently. Both the nano-columnar tilt angle and length need to be optimized for obtaining the desired blaze action and coupling strengths at the desired frequencies through full-wave 3-D photonic structure calculations. Some attempt at this is presently in Chapter 5.

Chapter 5

Reconfiguring PPCTFs by Ion Beam Irradiation

5.1 Introduction

Gratings with slanted plasmonic nanocolumns of silver (Ag) on top, fabricated by physical vapor deposition at large oblique angles on predefined gratings, show unique plasmonic properties. The slant angle of the nanocolumns in the PP-CTFs arises during the deposition process due to a self shadowing effect and is controlled by the angle of the collimated vapor flux. The slant angle in a given sample is thus, a quantity fixed during fabrication. The slant angle is a very critical parameter that determines the photonic properties like the diffraction and coupling efficiencies. Hence the ability to dynamically reorient the slant angle with fine control is highly desirable. In many cases, manipulation and modification of these nanocolumns is required to realize their full potential. We show here that these aligned nanocolumns with high aspect ratios can be uniformly re-oriented to any desired angle of slant by ion beam irradiation.

Several methods have been developed in literature to reorient or actuate nanocolumns. For example, elastic deformations caused by electrostatic forces [140], where four-turn Si nanosprings were grown by OAD technique with substrate rotation and on the top of that 10 nm Co layer is deposited to make it conductive by chemical vapor deposi-

tion. The electromechanical actuation of Si nanosprings was carried out by passing a dc current through it using a conductive Pt coated AFM tip. The electromagnetic force gives rise to spring compression, which is measured by the same AFM tip. Mechanical forces are used for permanent plastic deformation of metallic cantilevers and single carbon nanotubes by ion beam irradiation [141, 142]. CTFs of oriented nanocolumns of magnetic materials have been elastically reoriented by magnetostatic fields [143]. In this case, slanted nanorods of Fe, fabricated by OAD technique on a silicon substrate exhibited easy magnetization along their growth axis. By using a strong magnetic field, the slanted Fe nanorods could be reoriented towards the substrate surface normal and after re-orientation, the Fe nanorods retained the easy magnetization axis along their growth axis. Metal deposition at oblique angles on normally oriented polymer nanopillars can also re-orient the nanopillars because of differential stresses [144]. In this method, metal is deposited at an oblique angle to only one face of the polymer nanopillar, as a result, one face of the pillar is metalized and the other side is only polymer. The direction of bending is determined by the type of metal chosen. For example the pillars bent toward the metal face in the case of gold (Au) but toward the polymer face in the case of aluminum (Al). Compared to other processes, ion beam irradiation is faster, can result in large plastic reorientation, and gives complete control and flexibility over the process. The nanocolumns can be reoriented back to the original configuration simply changing the direction of the incident ion beam flux.

We explore the use of ion beam irradiation for uniformly reorienting entire gratings of slanted metallic nanocolumns. These gratings give rise to highly asymmetric diffraction and surface plasmon coupling due to blazing effects as shown in the earlier chapters, which can be flexibly controlled by reorienting the slanted metallic nanocolumns uniformly over large areas. Electromagnetic numerical simulations are performed to show that the photonic properties can be changed qualitatively by reorienting the slant angle. This demonstrates the possibility of using collimated ion-beams on macroscale for in-situ manipulation of nanocolumnar arrays or gratings. The reorientation can be uniformly carried over large areas of 0.2 mm^2 with the FIB and

the diffraction patterns from the reoriented grating show large scale changes in the diffraction efficiencies.

5.2 Bending of slanted Ag nanocolumnar arrays

The nanocolumns have one end free in space while the other end is tethered on a substrate as shown schematically in Fig. 5.1. The entire set of nanocolumns placed on the grating can be set into motion by ion-beam irradiation. The actuation of the nanocolumns resulted in a reorientation of the columns from a slanted configuration to becoming perpendicular (upright) to the substrate in a continuous manner, as a function of the irradiation time. Ga ions from the FIB at 30 keV energy and a current of 0.3 nA were made incident on the CTF such that the ion beam was almost normal to the substrate. It can be seen that the nanocolumns only in the region that is irradiated by the ion beam are re-oriented. Fig. 5.2 and 5.3 display a series of FESEM images of as grown and irradiated metallic nanocolumns using 30 KeV Ga ions with a flux of 7.5×10^7 ions $\mu\text{m}^{-2}\text{s}^{-1}$. Fig. 5.2 (a) shows 520nm long slanted Ag nanocolumn deposited on 500 nm periodicity 1D grating making an angle of 80° with the substrate normal. The total area of $5 \mu\text{m} \times 5 \mu\text{m}$ was exposed for 10 seconds which is shown in Fig. 5.2 (b) and for 20 seconds as shown in Fig. 5.2 (c). It is clearly observable that the bending of columns occurs forwards the direction of the ion-beam incidence.

Video clips for the bending of metallic nanocolumnar rods were obtained from the FESEM (see video clip multimedia material, in Ref. [145]) and also given in the CD with the thesis, which reveal more details showing the gradual bending of nanocolumns that rise up to an angle that is almost directly proportional to the time of irradiation until they are oriented in a direction parallel to the ion beam direction. Initially the rate of bending was slow and then increased gradually and the slant angle reached a maximum angle of 90° , which was the direction from which the ion beam was incident. On further irradiation there was no change in the column direction. Further exposure to the ion beam only caused slow etching of the material due to ion beam milling (as shown in the

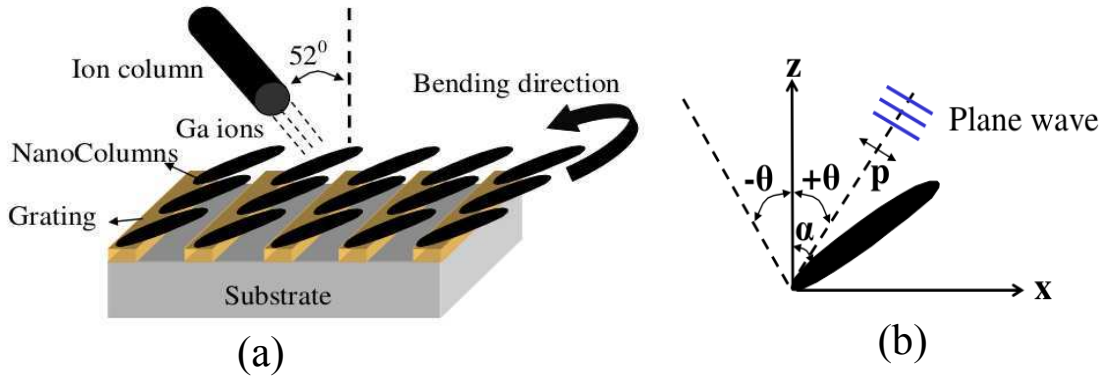


Figure 5.1: Schematic diagram showing (a) the direction of the ion beam at an angle of 52° and the bending direction of nanocolumns with respect to the substrate normal. (b) incident plane wave direction : $+\theta$ is the angle when the incident wave vector is mostly along the nanocolumnar axis and $-\theta$ is the angle when the incident wave vector has large perpendicular component to the columnar axis, α is the slant angle/orientation angle that Ag nanocolumn makes with z axis (substrate normal) and polarization of the incident plane wave is shown when direction E field is in the morphologically significant (xz) plane.

video clip). The irradiation time and dose have to be carefully controlled to minimize the etching. One important feature we observe in both the Fig. 5.2 and 5.3 is that all the columns within the irradiated area reorient to an angle by an equal amount in a reasonably uniform manner. Further, the nanocolumn reorientation that is obtained is a permanent deformation and does not relax back in time even after several weeks time.

The reoriented rods can be put back into their initial configuration by irradiating with the ion beam from the opposite direction as the nanocolumns deflect towards the ion beam. Because of etching of the material due to the ion beam, there is a limitation upto how many times this process can be repeated. So, we have estimated the thickness of the silver structure that is etched away by using the estimated sputtering rates for the given experimental conditions. The ion column is making an angle of 52° with the substrate normal and the nanocolumns are making an angle of 10° with the substrate plane. Angle between the direction of the ion beam and the normal to the nanocolumnar array is 42° . The sputtering yield due to the incoming Ga ions on Ag, is calculated using Monte Carlo simulation (SRIM program) [146] and is found to be

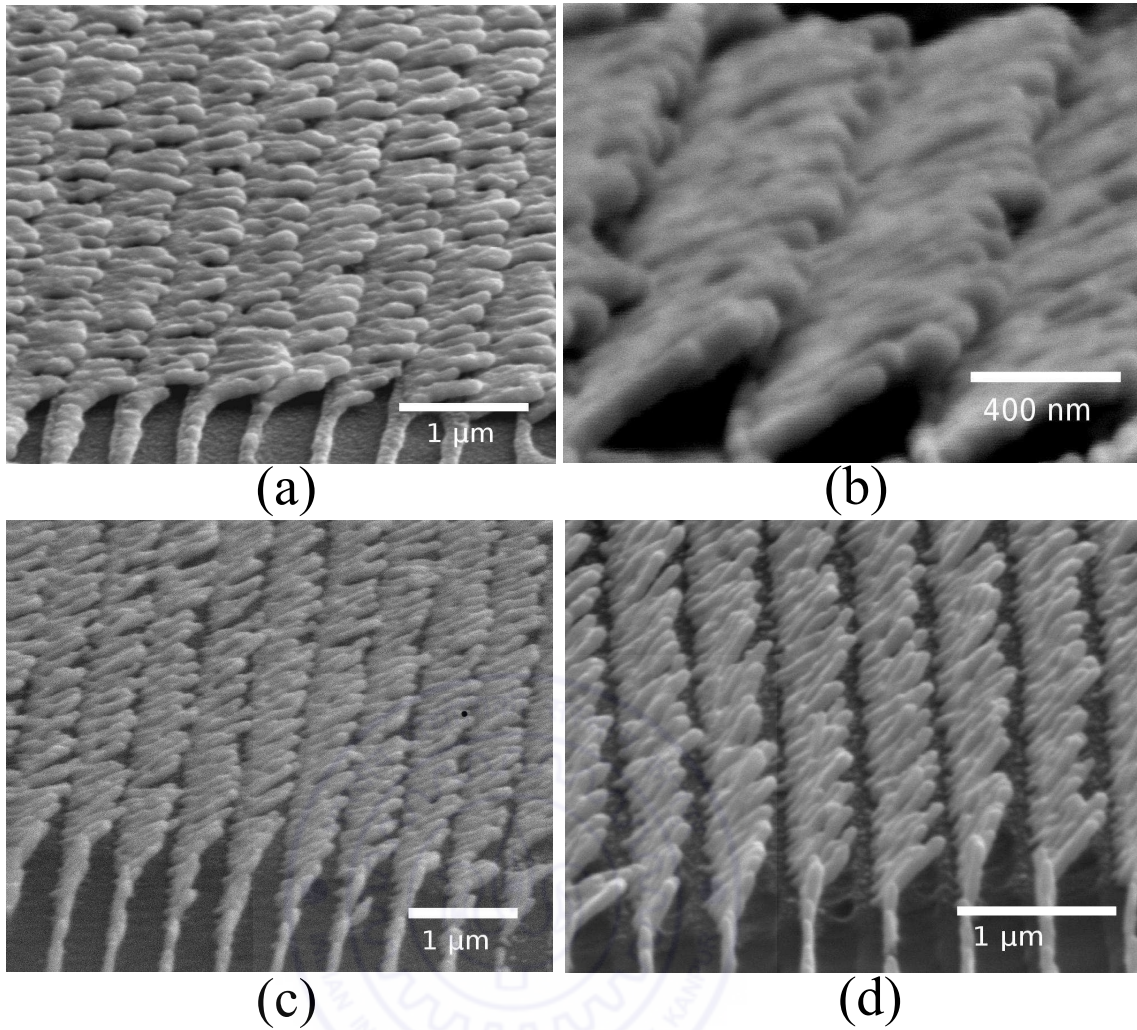


Figure 5.2: (a) Top view and (b) cross-sectional view of FESEM images showing periodically patterned array (periodicity = 500 nm) of Ag nanocolumns, nanocolumn dimensions are 520nm (length) \times 80nm (diameter) with orientation angle of 80° with respect to the substrate normal. (c) ion beam irradiation on an area of $5 \mu\text{m} \times 5 \mu\text{m}$ for exposure time of 10 s (d) for 20 s by 30 keV Ga ion beam and 0.3 nA beam current.

about 20 Ag atoms per Ga ion. For Ag nanocolumnar structure with 30 keV Ga ion, 0.3 nA current, irradiation time 10 sec and irradiating on square scanning pattern area of $25 \times 25 \mu\text{m}^2$, the etching thickness is estimated to be $\approx 10\text{nm}$. Since the diameter of the silver nanocolumns from the FESEM images are approximately 80 to 100 nm, so the columns can be bent back and forth from-to their original configuration about 4 to 5 times.

Fig. 5.3 (a) displays the FESEM image of the same sample before irradiation on smaller area. Fig. 5.3 (b), (c) show similar bending effect when we irradiated on a smaller area while keeping irradiation conditions the same as above. We can clearly

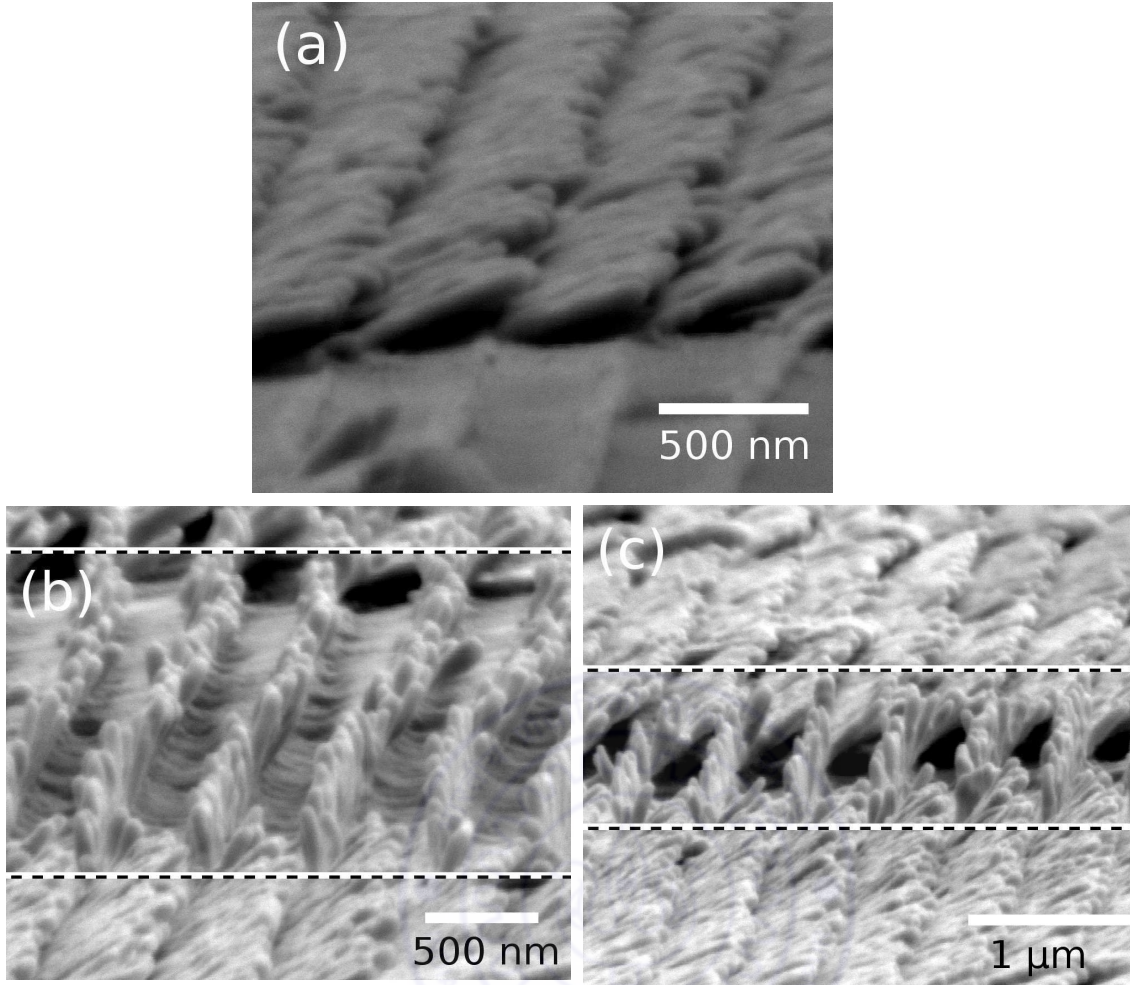


Figure 5.3: FESEM images showing (a) the same structure as mentioned above imaged with higher magnification. (b) ion beam irradiation on an area of $3 \mu\text{m} \times 3 \mu\text{m}$ for exposure time of 10 s (c) for 20 s by 30 keV Ga ion beam and 0.3 nA beam current. Dotted thin lines delineate the irradiated area.

see that only the nanocolumns within the irradiated area get reoriented while the remaining area is unmodulated. Compared to Fig. 5.2, the bending is more in Fig. 5.3 under the same irradiation conditions [see the area marked in Fig. 5.3 (b) and (c)]. This is because the irradiation was carried out with beam focussed on a smaller area, thereby effectively increasing the ion current density, which in turn leads to larger bending angles. These nanocolumns can be bent to the other side by appropriately changing the incident ion beam direction. In the video clips, the ion beam exposure time ranges from one second to about fifteen seconds in Ref. [145].

5.2.1 Mechanism of bending

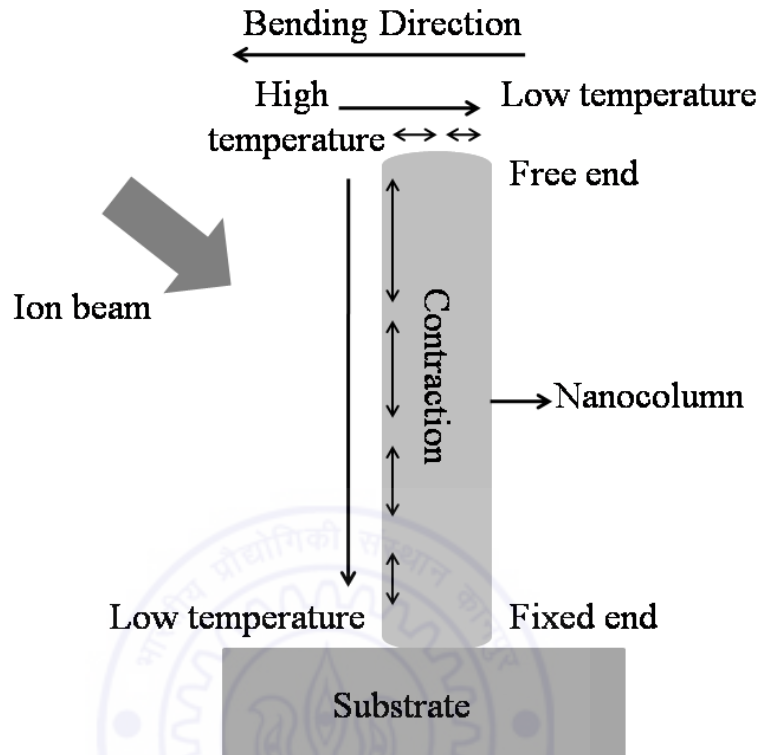


Figure 5.4: Schematic representation of the temperature gradient and thermal stress developed in the nanocolumn leading to its bending.

Several possible bending mechanisms can be found in the literature, for example, mechanisms based on defect formation [147, 148], or due to stresses produced by thermal gradients [149, 150]. According to the first model, due to the ion beam irradiation, defects such as interstitials and vacancies are produced and simultaneously tensile and compressive stresses are generated. These stresses cause the bending of the nanocolumns. When these stresses are relaxed by ion beam induced nucleation of dislocations and motion of dislocation, then the deformation of the nanocolumns becomes permanent. When an energetic ions fall on the surface of a solid material, they knock out some of the atoms from their equilibrium positions. Removal of the atoms result in defects in the surface layers and sputtering of material from the surface. Such changes in the structure produces stresses and as a result curvature occurs on the surface. The second model proposes that thermal gradients produce non-uniform stresses along the cross section of nanostructures, which are responsible for the bending. Based

on various explanations from literature, the bending mechanism can be understood as shown in Fig. 5.4. When ion beams impinge on the nanocolumn, inevitably some of the energy from the ion beam is converted into heat, thereby raising the temperature along the length and width of the nanocolumn and resulting in a non-uniform thermal gradient. The heating due to the ion beam spot and cooling due to radiation gives rise to large thermal gradients along the length and breadth of the nanocolumn. The bending can occur towards direction of ion beam if the material possesses a negative coefficient of thermal expansion. As the upper free end of the nanocolumn faces more heat compared to the bottom fixed end, the upper portion is brought to more contraction due to the interaction with the ion beam. Furthermore, the side wall which faces the ion beam will experience more heat and as a result of that more contraction. The temperature gradient creates non-uniform thermal stresses and hence the bending occurs towards the direction of the ion beam. As the ion beam is incident at an angle on the Ag nanocolumns, thereby only one side of the nanocolumns is exposed to the ion flux. This causes an asymmetry and the nanocolumns bend to one side. We are able to demonstrate that ion beam irradiation offers the possibility of simultaneous re-configuration of large periodic arrays of nanocolumns in a uniform manner. The time scale of forming defects and their annealing are of the order of picosecond [151].

5.3 Photonic Properties of the Ag CTF for different Slant Angles

Fig. 5.5 (a) shows the FESEM image of slanted Ag nanocolumns on a grating with 600 nm periodicity having 520nm long and 80 nm diameter. Fig. 5.5 (b) and (c) are photographs of the diffraction pattern transmitted through the sample of PPCTF of silver made on a glass substrate. Fig. 5.5 (d) shows the corresponding measured diffraction efficiencies and it is clearly observed that the +1 order is much larger than the -1 order. A similar asymmetry is present in the reflected orders as well.

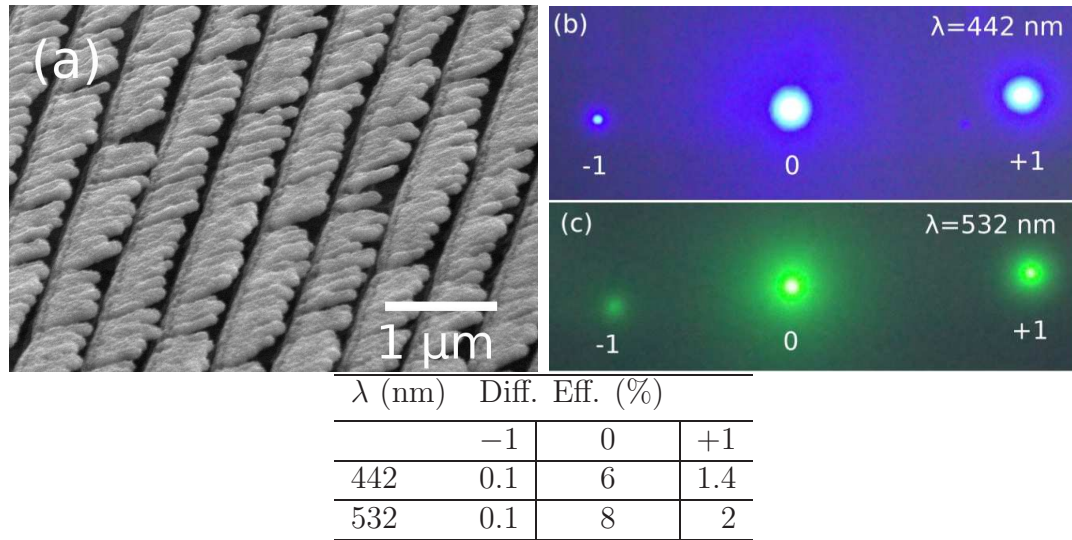


Figure 5.5: (a) FESEM image of periodically patterned array (periodicity = 600 nm) of Ag nanocolumns, nanocolumn dimensions are 520 nm (length) \times 80 nm (diameter) with orientation angle of (a) 80° with respect to the substrate normal, (b) and (c) are optical images of transmitted diffraction spots showing asymmetric diffraction at $\lambda = 442$ nm and at $\lambda = 532$ nm respectively, 0, +1 and -1 diffraction orders are mentioned below. The table shows the measured diffraction efficiencies in the transmission mode for the sample on fused silica substrate (a) at $\lambda \in \{442, 532\}$ nm for incident p -polarized light.

Fig. 5.6 (a) shows for reference, the scanning ion microscopy (SIM) image of a grating of 500 nm periodicity having slanted Ag nanocolumns having 520nm long and 80 nm diameter on a silicon substrate before ion beam irradiation. Fig. 5.6 (b) shows the SIM image of the same area after ion beam irradiation by raster scanning with the Ga ion beam at 30 KeV energy, beam current of 0.3 nA and a dwell time of 5 μ s. The image clearly shows that the nanocolumns now are vertically upright on the grating (slant angle = 0°) after the irradiation due to the ion beam induced reorientation. The reorientation could be carried out uniformly over areas of $400 \mu\text{m} \times 400 \mu\text{m}$, which is sufficiently large to probe easily with a laser beam. Photographs of the fraunhofer diffraction pattern reflected from this sample for p -polarized laser light at $\lambda=442$ nm from areas on the grating having the original slanted nanocolumns and the irradiated areas with upright nanocolumns are shown in Fig. 5.6 (c) and 5.6 (d) respectively. It is clearly observed from Fig. 5.6 (c) that the diffraction orders are extremely asymmetric for slanted nanorods where the -1 order is much larger than the +1 order, whereas in Fig. 5.6 (d) for upright nanorods, the diffraction orders are almost equal on both sides.

Thus, we demonstrate the possibility of uniformly reconfiguring the slant angle/ blaze angle for the grating over large macroscopic areas that can be probed by free space laser beam by this method of ion beam irradiation.

It is well known that the blaze angle and modulation height determines the efficiencies of a blazed diffraction grating for a specified pitch and wavelength [101, 120]. Here we have demonstrated a flexible manner to change the slant angle of our nanocolumnar gratings. Hence it is important to understand the extent of changes/modulation possible in the diffraction efficiencies with change in the slant angle. Since it is time consuming on a FIB to obtain reorientation over the large length scales that are needed for free space experiments with laser beams, we investigated the effect of slant angle through numerical simulations.

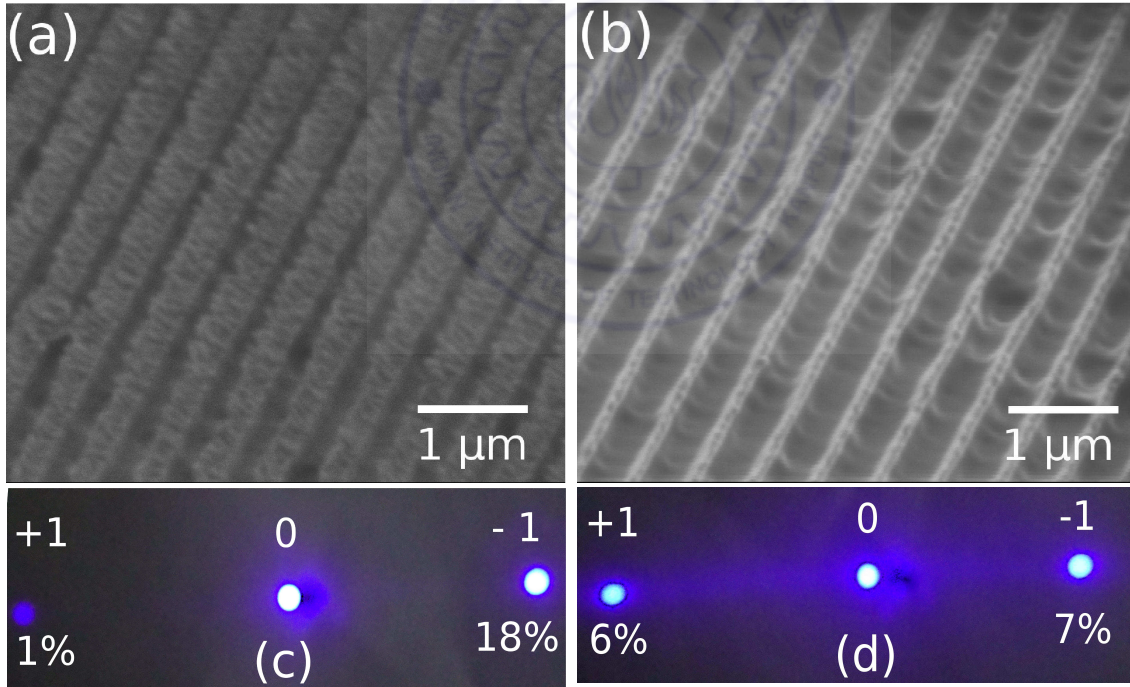


Figure 5.6: (a) Scanning ion microscopy images of periodically patterned array (periodicity = 500 nm) of Ag nanocolumns, nanocolumn dimensions are 520 nm (length) \times 80 nm (diameter) with orientation angle of (a) 80° and (b) 0° with respect to the substrate normal, (c) optical images of diffraction spots showing asymmetric diffraction at $\lambda = 442$ nm before irradiation, (d) symmetric diffraction after irradiation for the region shown in (b), 0, +1 and -1 diffraction orders with measured diffraction efficiencies in the reflection mode for the sample for incident p -polarized light.

5.4 Electromagnetic simulations of slanted nanocolumn gratings

The dielectric slanted grating with prismatic air cavities could be approximately considered as a phase grating [130], by which the diffraction efficiencies as function of the wavelength at any angle could be calculated. For metallic slanted nanocolumns, however, both the phase and the amplitude changes due to scattering become very appreciable and the PP-CTF can no longer be treated as a phase grating. Hence we performed full 3D simulations of the electromagnetic fields, to understand the interaction of light with the grating of the Ag slanted nanocolumns. A periodic array of Ag nanocolumns with diameters of 80 nm and lengths of 520 nm on a dielectric film ($n=1.65$) of thickness 100nm were assumed to be placed on a glass substrate. We confirmed that for a thin photoresist film of the thickness of 100 nm used in the experiments, the asymmetric waveguide formed by the photo-resist will be below cutoff for all wavelengths above 262 nm and there is no possibility of coupling to guided or quasi-guided waveguides. The dielectric permittivity of Ag is defined by the Lorentz-Drude model with plasma frequency, $\omega_p = 2180$ THz and damping $\gamma = 4.353$ THz [152]. Floquet periodic boundary conditions are applied along both the x and y directions. Periodic ports are used to compute the transmitted and the reflected diffraction orders as a function of incident angles and wavelength. The unit cell size has a period of 600 nm and sides $90 \text{ nm} \times 1300 \text{ nm}$. The distance between the two Ag nanocolumns along y direction is assumed to be 10 nm and the periodicity along x direction is 600 nm as seen in the SEM images. The slanted elliptical nanocolumns break the structural symmetry with respect to the direction of propagation of the incident EM wave. As a result there is an asymmetric transmittance with respect to the normal of the slanted aluminium CTFs [107], chromium CTFs [135] and silver CTFs (Chapter 4) The amount of asymmetric transmittance is also tunable as a function of the slant angle of periodically patterned nanocolumnar array, which is demonstrated by our results. Fig. 5.7 shows the angle dependent transmittance and reflectance spectra for the zeroth

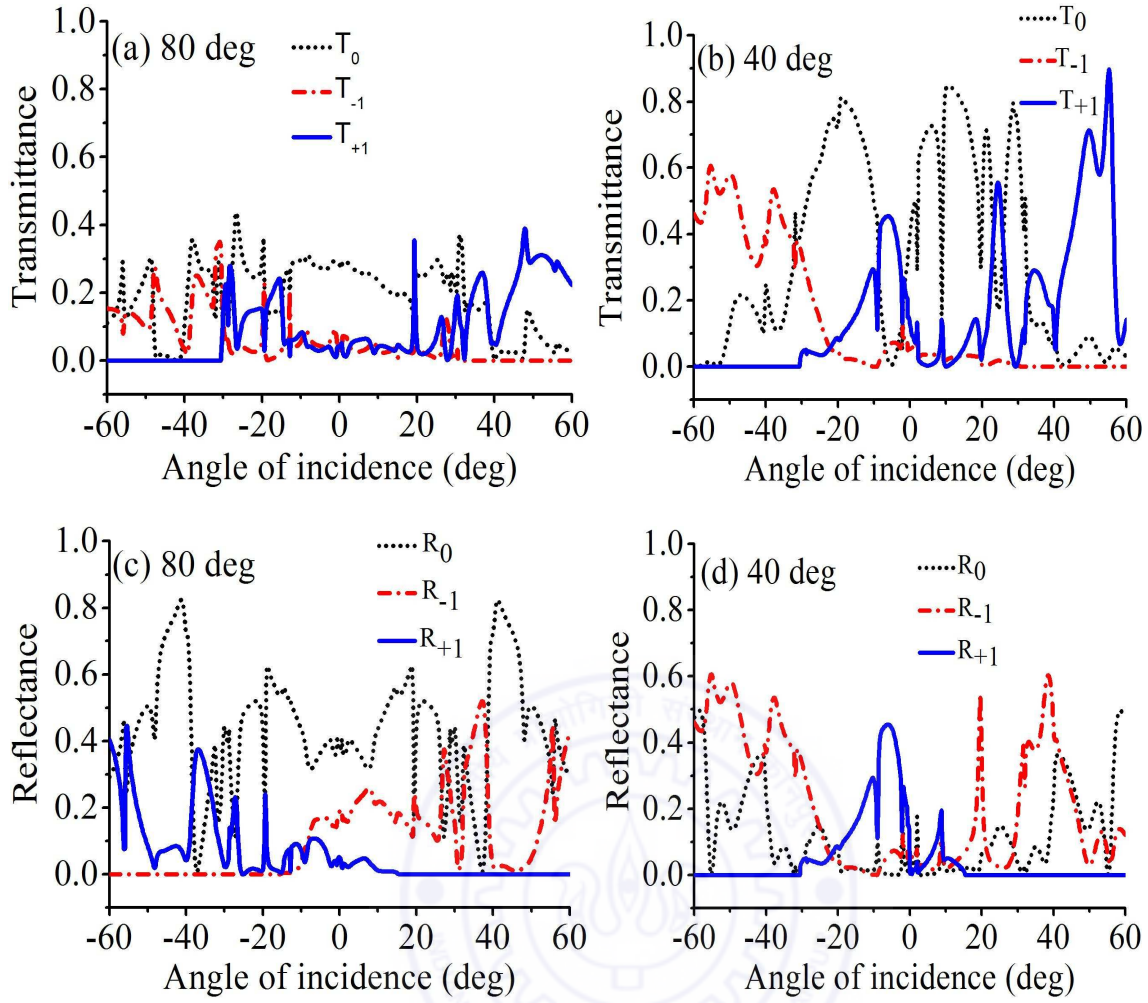


Figure 5.7: Calculated transmission and reflection from gratings of slanted nanocolumns: (a), (b) Angle dependent transmittance for 0, T_{-1} and T_{+1} diffraction order for the nanocolumn orientation angle of 80° and 40° and (c), (d) Angle dependent reflectance for 0, T_{-1} and T_{+1} diffraction order for the nanocolumn orientation angle of 80° and 40° . Wavelength of the incidence light is 442 nm

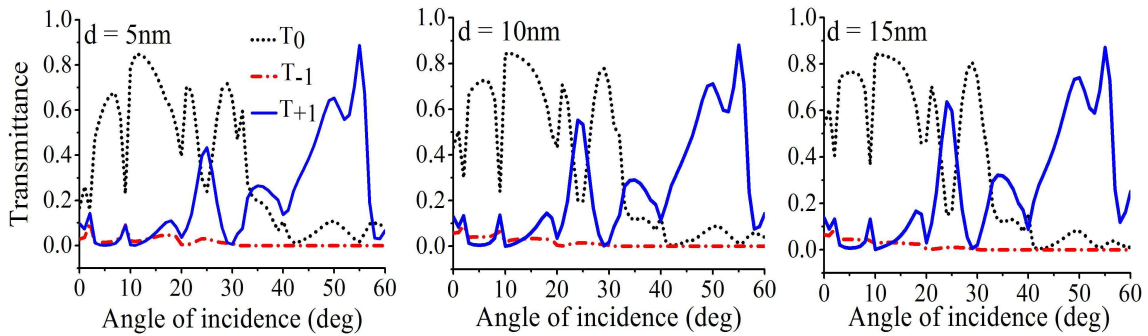


Figure 5.8: Transmittance spectra as a function of angle of incidence with slant angle of 40° and periodicity 600 nm with three different intercolumn separation such as (a) 5 nm, (b) 10 nm and (c) 15 nm along y direction.

order and ± 1 diffraction order for an incident wave with wavelength of 442 nm and a grating of period 600nm. The light is assumed to be incident in the morphologically

significant xz plane (Fig. 5.1 b) with the electric field in this plane (p -polarization). The angle of incidence (θ) is taken to be positive when the incident wave vector is mostly along the nanocolumnar axis. Here T_0 and R_0 are the 0^{th} order transmittance and reflectance respectively, T_{-1} and R_{+1} are the transmitted and reflected diffracted beams whose magnitudes are almost zero for all the angles greater than 15° . The T_{+1} and R_{-1} diffraction orders are highly prominent and become larger than the 0^{th} order over certain angular ranges.

Note that the sum of all the transmitted and reflected diffraction orders is less than 1. This arises due to the ohmic loss in the silver nanocolumns which are dissipative. Similar studies of dominance of one sided diffracted orders in transmission by varying the angle of incidence are reported by Serebryannikov and Ozbay [153] for non-symmetric grating containing metallic layers. The transmittance asymmetry is absent for the cases of upright nanocolumns (slant angle of 0°) and flat nanocolumns (slant angle of 90°). The asymmetry in the transmittance becomes very pronounced for certain angular ranges of the incidence. For example, the transmittance for $+1$ diffraction order at 55° angle of incidence becomes larger than 90% for 40° slant angle whereas for 80° slant angle it is merely 50% at 48° angle of incidence. Thus, a large change in the diffracted transmitted beams can be obtained by merely changing the slant angle of the nanocolumns. We observe that in Fig. 5.9 (c) for 80° , the field enhancements appear mostly in the open air cavity formed by the metallic nanocolumn with the substrate surface, but with increase in slant angle in Fig. 5.9 (f) effects of an air cavity disappears and the maximum field localization occurs entirely on the surface of the Ag nanocolumn. To see the possible effects of the inter-column interactions, three different inter-column separation “ d ” along y direction are taken as 5nm, 10nm and 15nm, while keeping the slant angle and periodicity fixed in the simulation parameters. From the transmittance spectra shown in Fig. 5.8 for three different values of d , we can conclude that the maximum transmittance at a particular slant angle is independent of the inter-column separation. However there is a slight difference in the transmission intensity at lower angles of incidence. We also note that the maximum

transmitted intensity at large angles is almost the same in all the three cases. This is obvious because the wavelength of the incident light is 442 nm, which is much larger than the separation d . So, the incident light will experience the nanocolumnar array along y direction as homogeneous.

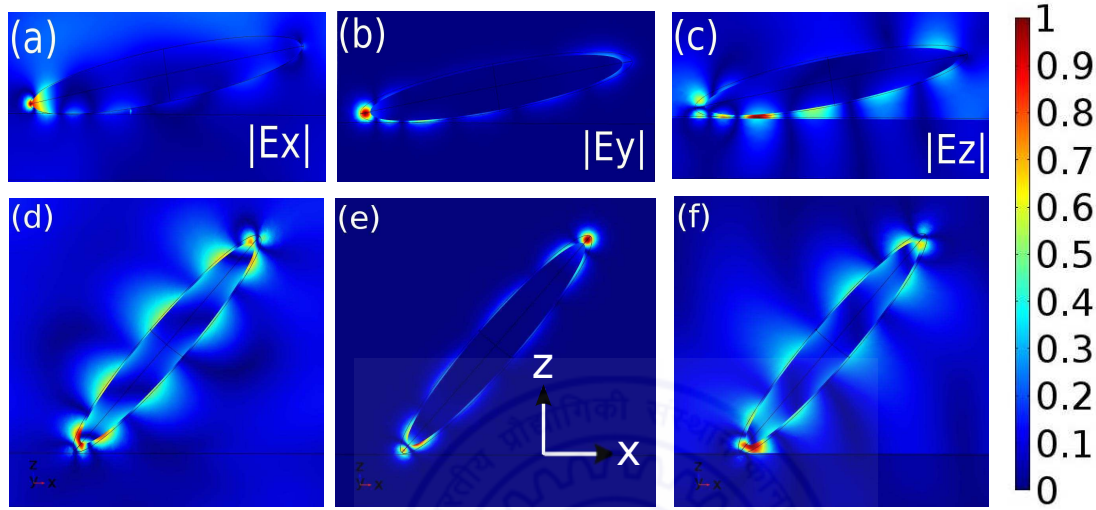


Figure 5.9: FEM simulations of electric fields $|E_x|$, $|E_y|$, $|E_z|$ distributions of standing waves pattern modes or Fabry perot modes in Ag nanocolumns array illuminated by p-polarized light of free-space wavelength 442 nm incident at $\theta = 0^\circ$ with period $d = 600$ nm when the nanocolumns makes an angle of (a), (b), (c) 80° (d), (e), (f) 40° with the substrate normal. Lengths of major and two minor axes of the ellipsoid are 520 nm and 80 nm respectively.

When an electromagnetic wave is illuminating with electric field polarized along the columnar axis, a surface plasmon resonance is excited in the nanocolumn. The electromagnetic field distributions on the slanted nanocolumns reveal very interesting physics about the plasmonic excitations of the system. Fig. 5.9 shows the calculated electric field components for two inclinations (slant angle) of the nanocolumns with respect to the substrate normal. The excitation of definite cavity modes of SPP supported by the length of the silver nanorod can be clearly seen. Cavity is formed by the two end walls of the nanocolumn, where SPP waves bounce back and forth inside the nanocolumn, where it causes the nanocolumn to sustain Fabry-Perot like resonances at specific wavelengths for a fixed geometry [154]. In these nanocolumns a resonance is supported whenever a surface plasmon per round-trip experiences a phase accumulation of a multiple of 2π . Such cavity modes were reported for isolated nanorods by others

recently [154, 155]. The $m=4$ mode can be clearly discerned in our simulations for the nanocolumns of length 520 nm and diameter 80 nm when excited by the incident plane wave with an electric field component along the columnar axis. The interaction with the dielectric substrate leads to interesting changes from that of an isolated nanocolumn. The polarization charges induced on the dielectric surface reasonably quench the E_y fields and remarkably enhance and localize the E_z (normal component) of the field for small slant angles. E_z component is the most dominating one. In a sense, the role of dielectric film appears similar to a metallic ground plane. For larger slant angle of the nanocolumn (for example in 5.9), there is a much larger coupling to the radiative fields and a weakening of the localized normal fields. Thus, by just changing the slant angle of the nanocolumn an enormous qualitative change from a localized regime to highly radiative regime can be obtained. Large qualitative changes in the optical near field are obtained by changing the slant angle. This change in the coupling results in the large transmittance for the +1 order and large reflectance for the -1 order diffraction in the case of both 40° and 80° slant angle.

5.5 Potential applications

Here we will dwell upon some potential applications of the technique that we have developed. Principally our results show that it is possible to uniformly reorient entire arrays of nanocolumns. While the slant angle of nanocolumns in a OAD process is principally determined by the angle of deposition [1], the nanoporosity/column thickness that results becomes different for different angles of deposition. Ion irradiation now enables us to decouple the nanoporosity/ column thickness as well as the column spacing from the slant angles of the columns. Recently there has been a tremendous surge of activity in using upright nanopillars of various materials such as Si, GaN, ZnO, CdS and SiO₂ on the front surface of solar cells and detectors for efficient index matching. (see for example, [156–158] etc.). Nanopillars deposited by OAD has also been explored for index matching applications. However, deposition of upright nanocolumns by OAD with

continuous substrate rotation [1] creates nanopillars with large diameters (> 150 nm) and also does not allow any flexibility on the nanostructure density. Ion beam irradiation gives a nice flexible option of reorienting the much thinner nanocolumns with different densities that become possible at various deposition angles with directional OAD.

Slanted columnar gratings (with metallic or dielectric nanocolumns) have been shown to have a high degree of blazed diffraction [130]. The ion beam irradiation gives rise to the possibility of reconfigurable blazed gratings, thereby maximizing the diffraction efficiencies for different wavelength bands by changing the blazing (angle) condition. This possibility is presently unachievable by any other technique. The blazing properties of such gratings also enables them to act as efficient unidirectional SPP couplers [136] analogous to other unidirectional surface plasmon grating couplers [121] and unidirectional SPP sources [124]. This enables reconfiguration of expensive large area gratings for spectroscopic purposes. Essentially the slanted nanocolumnar grating consist of a plurality of nanoantennas [159]. These arrays of nanoantennas can now be flexibly built and optimized for directional coupling to other plasmonic nanostructures.

We note other applications like angularly selective transmittance structure for the proposed control of sunlight and daylighting applications [160]. Coatings of thin film on windows which have different transmissive properties at equal angles on the two sides of the surface normal are very interesting for energy efficient windows. But this angular selectivity can not be attained with uniform films, whereas an inclined columnar feature is an effective solution for this. Angular selectivity in the optical behaviour can be utilized to realize energy efficiency, good daylighting and comfort in buildings with sloping windows, glass domes and glass blinds. It is possible to combine high luminous transmittance through a near-horizontal line of sight, so that good visual indoor-outdoor contact is maintained. Whereas a low solar transmittance occurs for near vertical incidence. These angularly selective gratings with different orientations over different areas can be extremely useful and can be made over large scale areas inexpensively with dielectric nanocolumns. Similar angle selective scattering

applications are desirable for solar thermal applications. Solar collectors trap the heat energy of the sun rays in the process of photothermal conversion by use of selective coating. These devices can be integrated on roofs, walls and even windows. The use of these plasmonic gratings for surface enhanced Raman spectroscopy (SERS) and surface enhanced fluorescence (SEF) could also be definitely advantageous. Localization of the electromagnetic fields within the nanocolumns, at the corners of the nanocolumns and within the air cavity formed by the slanted nanocolumns gives huge enhancements which help to produce large SERS and SEF responses and by infiltrating liquids (or biomolecules) inside the array, it can also be used for sensing purposes by SERS.

Other potential applications in data storage system suggest themselves. We have shown that both the far-field scattered radiation as well as the optical near fields depend critically on the orientation of the nanocolumns. The nanocolumn that is almost flat ($\sim 80^\circ$ slant angle) will give rise to very small scattering and near-fields compared to a nanocolumn at about 40° slant angle (optimized). Thus, it would enable a simple digital data storage system at the single nanocolumn level which can be written by a FIB and readout by a scattering scanning near-field optical microscope (s-SNOM) with great sensitivity. It is simple to create deposition conditions by which a single row of slanted nanocolumns get deposited on the grating ridges. Using a small grating pitch of 150 nm and a smaller nanocolumn density of one column per 100 nm (both of which are achievable by present day techniques), we end up with a data storage bit density of 129 Gbits/in². This exceeds the storage data in a single layer of a present day Blu-ray optical disc by more than ten times. Of course, the nanostructures here are more delicate and optimization would be required for such applications.

5.6 Conclusions

In summary, a method based on ion beam irradiation has been used to re-orient these Ag nanocolumns to any desired slant angle uniformly over large areas. The ion irradiation causes a plastic deformation in the nanocolumns by creating defects and

subsequent annealing. The directional ion irradiation from one side results in the reorientation of the nanocolumns as they bend towards the incident ion beam. The slanted nanocolumnar gratings are known to have a blazing effect and an asymmetric diffraction pattern, that depends on the slant angle. Video clips for the bending of metallic nanocolumnar rods in real time were obtained from the FESEM, which reveal more details showing the gradual bending of nanocolumns that rise up to an angle that is almost directly proportional to the time of irradiation until they are oriented in a direction parallel to the ion beam direction. The reorientation of the nanocolumns is shown to give rise to changed diffraction efficiencies and variable blaze action can now be obtained. Electromagnetic numerical simulations were carried out which clearly demonstrate a large change in the diffracted beam efficiencies for slant angles of 40° and 80° (taken as examples). The investigated large area reconfiguration of the silver nanocolumns on gratings by ion beam irradiation is very possibly the first demonstration of the method over large scale areas for optical applications.

Chapter 6

Fingerprint Visualization Enhancement

6.1 Introduction

The detection and visualization of latent fingerprints is a challenging subject, particularly when the marks are faint with small residue and the latent finger mark is on highly reflecting surfaces. The surface where the fingerprint is located may present many physical and optical constraints, such as large reflectivity and scattering due to roughness and high background fluorescence. A variety of physical and chemical treatments like powder dusting [161], vacuum metal vapor deposition [162,163], vacuum cyanoacrylate fuming [164], exposure to dyes [165] and nanoparticles [166–168] have been developed for the detection and visualization of fingerprints on various kinds of surfaces. Additionally, optical techniques like oblique angle illumination have been successfully used for visualization of fingermarks on smooth glass and mirror surfaces [169].

Advanced techniques like scanning Kelvin microprobe imaging that depends on the electrolytic salts present in the fingerprint residues have been successfully used [170] on metallic surfaces. Bond [171] studied the development of latent fingerprints through corrosion on brass surfaces, particularly after exposure to enhanced temperatures. The capability of visualizing latent prints on porous surfaces with 1,2-indanedione with

specifically binding to amino acids present is proven and documented in many papers [172–174], although it does not appear to work well on smooth surfaces. On white paper, fingerprints developed with 1,2-indanedione produce strongly fluorescent details under suitable blue-green light excitation [175]. Zinc chloride can be used as a post-treatment after 1,2-indanedione [175], and also as a combined formulation based on a catalytic process [176]. For surfaces characterized by strong luminescence, time resolved luminescence imaging [177–179], has been used in order to suppress the background fluorescence noise. Anti-Stokes phosphors were also used in the development of finger marks on strongly luminescent surfaces [180]. Photoluminescent semiconductor nanocrystals for latent fingermark detection, especially in concert with phase-resolved imaging for background fluorescence suppression, were used by Menzel et al. [181,182]. CdSe/ZnS nanocrystals [183] have given promising results on fingerprint enhancement. Fingerprints were developed on non-porous surfaces, using a petrol ether suspension of cadmium selenide/zinc sulphide nanoparticles stabilized by long chain amines. The nanoparticles adhere to the fingerprint by hydrophobic interactions.

The success of the possible use of nanostructured materials and fluorescent fingerprint reagents depends in many cases on the ability of the materials to react or adhere to the fingerprint residue. The techniques used also principally depend on the time history of the surface: for example, the aqueous and volatile substances constituting major portions of the debris evaporate away over several hours, or only the hydrophobic components would be left behind if the surface had been wetted, rendering chemical tracers that bind to hydrophilic amino-acids ineffective. Recently the deposition of vertical CTFs on sebaceous fingerprints by the conformally evaporated-film-by-rotation technique was successfully used to enhance the visibility of fingerprints [184,185]. This technique, originally developed for replicating biological surfaces over a variety of length scales [186], has been applied to fingermarks on a variety of smooth surfaces like duct tape, polished silicon and plastics. Two techniques for visualizing sebaceous fingermarks such as CTFs and the vacuum-metal-deposition (VMD) techniques are compared and it was observed that the CTF technique is superior for developing fin-

germarks on clear sandwich bags and partial bloody fingermarks on stainless steel [187].

CTFs [1] consist of clusters of high aspect ratio parallel straight nanowires with column diameters of about 10–40 nm. CTFs get created due to a self-shadowing mechanism (as explained in Chapter 2) that favors columnar growth for deposition by a collimated vapor flux at large oblique angles. If the vapor deposition were to be carried out on a modulated surface, several regions would additionally get shadowed out from the collimated vapor flux resulting in the CTF growth only on the upraised regions as schematically indicated in Fig. 6.1. The physical debris in a fingerprint act as a pre-deposited seed layer and the CTF growth can enhance the modulation in the fingerprints accurately. Applying this method to fingerprint enhancement depends only on the physical debris that can be minimal and not on the chemically reactive materials that can get removed from the fingerprint with time and environmental factors.

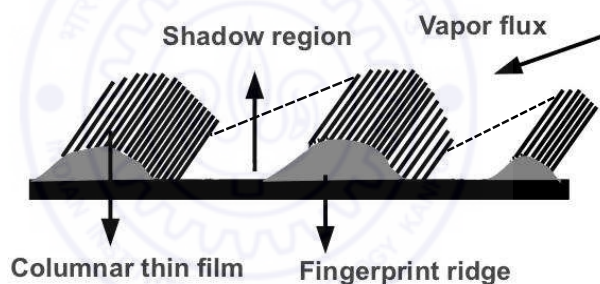


Figure 6.1: Schematic of CTF deposition on different regions of fingerprint ridges by oblique incident vapor flux.

In this Chapter, we report on a novel application of OAD deposition: the significant enhancement of latent fingerprints by the deposition of CTFs on two nonporous surfaces, namely, smooth glass slides and rough aluminum sheets, both of which are window and door materials, and likely to be touched in a crime scene. Further, it has been reported that fingerprint residues adhere strongly to smooth surfaces such as PVC window shutters and powder-coated aluminum window frames, and may last for a long time under harsh conditions [188]. The glass and aluminum surfaces are very different optically in that the rough aluminum surface is highly reflective as well as highly scattering, making even the detection of fingerprints on the surface very difficult in comparison to the glass surface. Calcium fluoride (CaF_2) and silica (SiO_2) were vapor

deposited at large oblique angles by electron beam vaporization. Only oblique angle deposition without rotation of the substrate was carried out and resulted in making both the presence and details of the fingerprint highly visible on both the surfaces. Subsequent treatment by fluorescent dyes (Rhodamine 6G) or the amino acid specific 1,2-indanedione–alanine, resulted in the fingerprints with CTF growth becoming highly visible under a fluorescence microscope. The reaction product of 1,2-indanedione with amino-acids such as alanine that are present in a fingerprint is fluorescent. In comparison, fingerprints without CTF deposited on them could hardly be detected on these surfaces even when treated with these fluorescent reagents. The CTFs appear to localize and entrench the dye within them by drawing the dye solutions into them by strong capillarity caused by their nanoporosity. The important issue that we explore is whether a high quantum yield fluorescent dye like Rhodamine 6G would be better or would a specific reactive agent like 1,2-indanedione be better in one scenario. The development and visual enhancement of fingerprints using CTF deposition followed by fluorescent reagents is an original development reported here that has immense potential for fingerprint development techniques.

6.2 CTFs deposition on Fingerprint and Fluorescent dye treatment

6.2.1 Sample preparation

Fingerprints were deposited on two non-porous surfaces (microscope glass slides and aluminum sheet), and also on a porous surface (white photocopier paper) for comparison purposes. White paper is a porous surface and 1,2-indanedione is a very good fingerprint reagent on it. The glass surfaces were cleaned by sequentially washing in acetone, trichloroethane, ethanol and de-ionized water to remove all greasy materials and chance fingerprints, while fresh windows frame aluminum were used. Both surfaces

were finally cleaned by blowing dry nitrogen to remove dust particles. In each case, the finger was washed with commercial handwash soap and dried just before depositing the fingerprint. Care was taken to just touch the surface without imposing much contact force so as to create fingerprints as if by chance contact. This was to prevent leaving behind large amounts of fingerprint residues in order to test the sensitivity of the methods. The samples were left at room temperature for two days to up to a week to allow them to dry. Before any physical or chemical treatment, the fingerprint substrates (glass, windows frame aluminum and paper) were then cut into two pieces (left and right). On one side, typically the left side, a CTF of CaF_2 or SiO_2 was deposited at large oblique angles at an angle 85° with the substrate normal by e-beam evaporation process. The deposition has been done at a nominal pressure of 5×10^{-6} mbar pressure for 15–20 min of typical total thickness of 500–600 nm as measured by a quartz crystal thickness monitor.

6.2.2 Post-treatment by Fluorescent dyes

For the dye solutions, 0.0292 g of 1,2-indanedione powder (indan-1,2-dione, 97%, Sigma-Aldrich Chemical Company) was dissolved in 50 ml of methanol (99.5%, Fisher Scientific) at room temperature to prepare a solution of 4×10^{-3} M. Methanol has the advantage of its high polarity and the possibility of dissolving some fingerprint residue such as amino acids. The solutions were divided into two parts: Solution A ($V_A = 25$ ml) and solution B ($V_B = 25$ ml). Solution B was reacted with an excess of alanine and solution A was left without any further reaction. The solutions were left at room temperature for one day and then were put in the refrigerator. The reaction in solution B needs some time to take place completely, because of the low solubility of alanine in methanol. Although heat may accelerate the reaction, no heating was used. Similarly, Rhodamine 6G was dissolved in chlorobenzene to form a 5.2×10^{-5} M solution. We should note here that 1,2-indanedione is not a fluorescent dye, but its reaction product with amino acid alanine fluoresces yellow under blue/green illumination. One set of

CTF coated fingerprint marks (left half) as well the corresponding control right half of the fingerprint mark with no deposition were treated with the dye solutions prepared as outlined before. The treatment consisted of spin coating the dye solutions onto the rapidly spinning substrates at 2500 rpm. The solvent in both the cases evaporates leaving behind the dye molecules on the samples. SiO_2 has the advantage of insolubility while CaF_2 is very mildly soluble in water for the post-treatment with dye solutions.

6.3 Optical Imaging Techniques

Optical imaging was performed by a Scientific CCD camera (Nano Tech Imaging (Seoul), MEM1300) using white light illumination at large oblique angles of 60° to highlight the scattering from the fingermarks while avoiding the direct reflection. Microscopic examination was carried out by an Olympus BX 51 microscope, typically by a $5\times$ objective which was the lowest available, while microstructure of the CTF and fingerprints were examined by $100\times$ objective. Fluorescence from the fluorescence dye imbedded CTFs and fingerprints were measured using a fluorescence attachment to the microscope, illuminated by a 100 W mercury vapour lamp. Blue band excitation ($\lambda = 488$ nm center-wavelength, FWHM = 23 nm) or green band excitation ($\lambda = 548$ nm center-wavelength, FWHM = 5 nm) could be used for the fluorescence excitation. The light from the fluorescence image was coupled by an optical fiber via the trinocular to an Ocean Optics HR 2000 spectrometer. For fluorescence images excited by a laser beam, a 532 nm diode pumped solid state laser (Dragon Lasers, China, Model no. MGL 50) was used to excite the fluorescence, which was imaged through a 532 nm notch filter (Newport optics, 17 nm bandwidth).

6.3.1 Observations under white light

The plain fingerprint marks made on glass slides were slightly visible to the plain eye, while the fingerprint marks on the reflecting aluminum sheets were barely visible to the

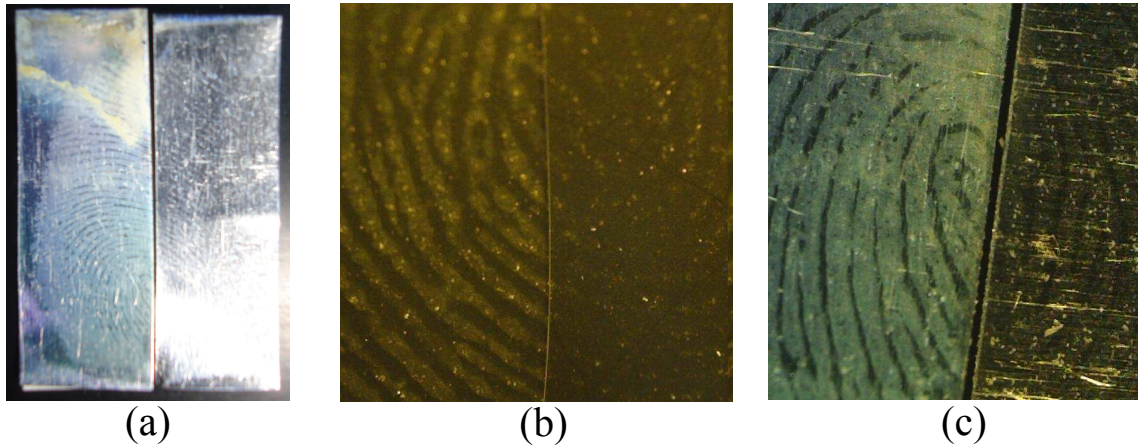


Figure 6.2: (a) Fingerprint on a highly reflecting aluminum sheet with (left side) and without (right side) CTF deposition, whitish marks on the substrate in the left side is clearly visible under room light conditions. (b) Fingerprint with deposited CTF (left side) and plain fingerprint (right side) on microscopic glass slide, observed under the white light, incident obliquely on the surfaces. (c) Fingerprint with deposited CTF (left side) and plain fingerprint (right side) on rough aluminum sheet, observed under the white light, incident obliquely on the surfaces.

unaided eye. It was observed that after deposition of the CaF_2 or SiO_2 CTFs, even the presence of the fingerprints became strongly visible as whitish marks on the substrates. See Fig. 6.2 (a) for a picture of a fingerprint on a reflecting aluminum sheet without and with CTF deposition. This is due to the porous deposited structure that strongly scatters light. Even the details of the fingerprints become discernible to the naked eye. For comparison, the plain fingerprints and the fingerprints with deposited CTFs were observed under white light incident obliquely on the surfaces. Only under oblique incidence could the plain fingerprint marks on the reflecting aluminum sheets become well resolved for photographing. For purposes of comparison, we properly positioned the left and right parts of the fingermark so as to simulate the uncut contiguous fingermark as closely as possible and images were taken simultaneously of both sides of the fingerprint mark, thereby ensuring identical conditions of lighting and camera gain for both sides.

Fig. 6.2 (b) and (c) shows the results we obtained with and without CTF deposition on fingerprints when viewed under obliquely incident white light illumination. While the fingerprint marks on the undeveloped right side are just visible, the enhancement of the fingerprint mark on the left side due to the CTF deposition is clearly

visible. Fig. 6.2 (b) shows the enhancement in the visibility of the fingerprint marks on a glass cover-slip the CTF deposition on the fingerprint features is clearly visible on the left, while fingerprint debris alone on the right can just about be traced out. There is almost no continuity to the lines formed by the debris alone on the right, while the lines on the left due to the deposited CTF are continuous. Similarly, in Fig. 6.2 (c), the fingerprint lines can just be discerned on the reflecting aluminum sheet on the right under oblique illumination which avoids the strong reflection from the aluminum sheet. The scratch marks on the sheet that also strongly scatter light are clearly visible on the right side. In comparison, the left side with the CTF deposition clearly shows the fingerprint mark with high clarity and detail. The enhancement in the visibility of the fingerprint marks with the CTF deposition cannot be contested, although the extent of the enhancement needs to be benchmarked against other techniques. While the features do get highly enhanced, it is also noted that at some places features may also be lost due to the overlapping and merging of the CTF ridges. This could be an effect of overdeposition of the CTF or it may also simply be due to small amounts of fingerprint debris leading to lowered levels of shadowing during the deposition. The exact thickness of the CTF deposition to maximize the visibility of the fingermarks needs to be optimized.

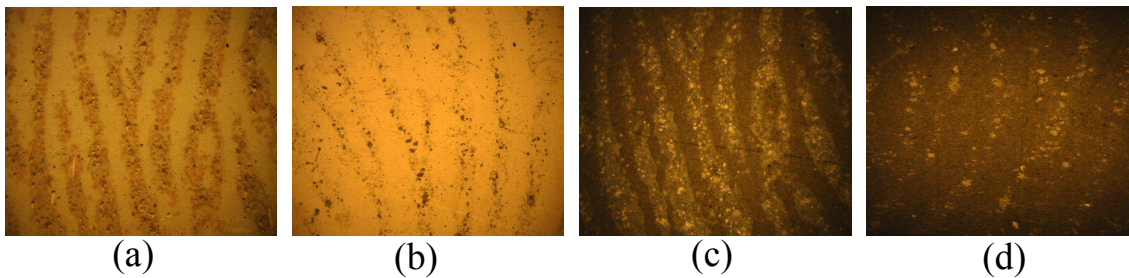


Figure 6.3: Fingerprint marks (a) with and (b) without the deposited CTF (evaporant material, SiO_2) on glass slide were viewed using optical microscope in reflection mode under bright field conditions with $5\times$ magnification. Fingerprint marks (c) with and (d) without the deposited CTF (evaporant material, SiO_2) on microscopic glass slide were viewed using optical microscope in reflection mode under dark field conditions with $5\times$ magnification.

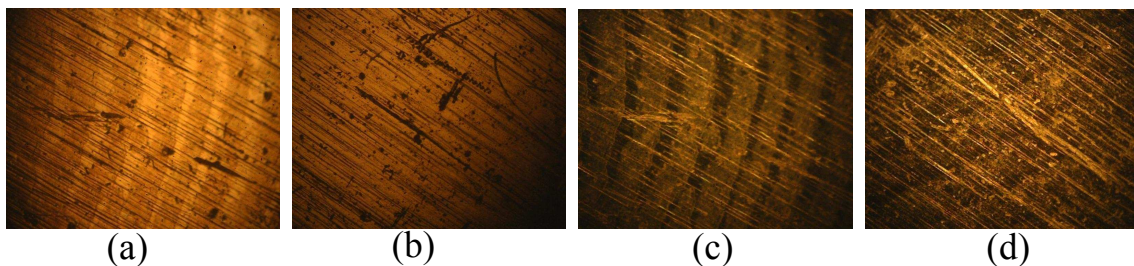


Figure 6.4: Fingerprint marks (a) with and (b) without the deposited CTF (evaporant material, SiO_2) on reflecting aluminum sheet were viewed using optical microscope in reflection mode under bright field conditions with $5\times$ magnification. Fingerprint marks (c) with and (d) without the deposited CTF (evaporant material, SiO_2) on reflecting aluminum sheet were viewed using optical microscope in reflection mode under dark field conditions with $5\times$ magnification.

6.3.2 Bright-field and Dark-field Microscopic Imaging

Microscopic imaging techniques were also tried to check the enhancement under different imaging conditions. Both the sides of the fingerprint mark with and without the deposited CTF were viewed using the optical microscope (Olympus BX 51) in reflection mode under both bright and dark fields modes under $5\times$ magnification. It should be noted that we can only see a small field of the fingermark under the microscope and it was attempted to find regions with the most visible marks, particularly for the plain fingermarks without CTF deposition. In Fig. 6.3, we show the microscopic images of the fingerprints on a glass slide: (a) and (b) are bright-field images while (c) and (d) are the dark-field images. The fingerprint debris on the glass slide can be discerned in the plain fingerprint marks (b and d), the CTF deposition in (a) and (c) clearly enhances the visibility of the fingerprints. The scattering nature of the CTF appears to make imaging using dark-field techniques which only images the scattered light most suitable for smooth substrates with minimal scattering. In Fig. 6.4, the microscopic images of the fingerprints on a reflecting aluminum sheet are shown: (a) and (b) are bright-field images while (c) and (d) are the dark-field images. In this case, the plain fingerprint marks can hardly be seen at all in the bright-field image due to the strong reflection from the aluminum sheet [Fig. 6.4 (b)], while the fingerprint debris can be resolved only slightly better in the dark-field image. This is due to the highly scat-

tering nature of the rough surface of the aluminum which masks the scattering from the fingerprint debris. But it can be seen that the CTF deposition on the fingerprint debris can be clearly discerned as continuous lines in both the bright-field and the dark-field images. The visibility of the fingerprint marks with the CTF deposition was comparable in the bright-field mode and the dark-field mode in this case of a highly reflecting and scattering substrate.

6.4 Fluorescence Spectra and Fluorescence Imaging of Fingerprints

The fluorescence spectra from the neat alanine + 1,2-indanedione solution and neat Rhodamine 6G in ethanol were measured using a spectrometer (Ocean-Optics, USB 4000+) and by exciting with 473 nm and 532 nm lasers. The obtained spectra are shown in Fig. 6.5. Alanine is required to combine with 1,2-indanedione to produce the fluorescence. The action of 1,2-indanedione was also tested by developing fingerprints on white paper (a porous surface where hydrophilic aminoacids also can adhere well). After 24 h of application of the dye, one could easily observe the fingerprint even under room light conditions while the fluorescence from the fingerprint was seen under a fluorescence microscope. Fluorescence spectra from the samples on paper show a peak at 559 nm under blue light excitation with a half width of 30 nm, and a peak at 600 nm under green light excitation with a half width of 26 nm. The fingermarks on aluminum and glass with the CaF_2 CTF deposited and post-treated with 1,2-indanedione solution shows broadband emission under blue and green excitations. The half width of the fluorescence peak is about 80 nm under either blue or green excitation. The broadening is likely to be due to the inhomogeneous environment of the CTF. Next the fluorescence from the dye applied on the CTF deposited fingermarks was imaged under the fluorescence microscope. The CTF ridges fluoresce more brightly than the regions with no CTF resulting in enhanced visualization of the finger print marks. This enhancement was obtained for both the Rhodamine 6G and alanine +

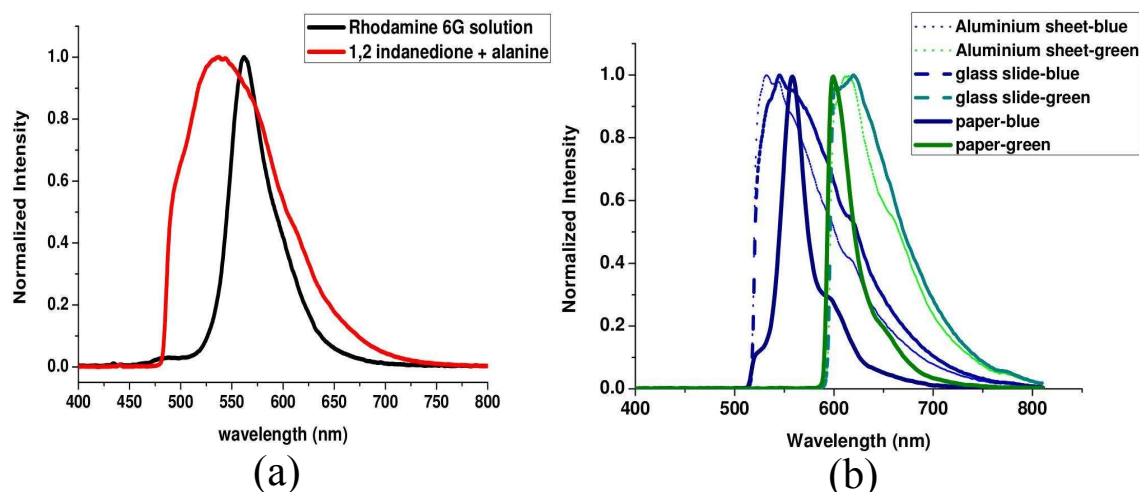


Figure 6.5: (a) Fluorescence spectra obtained from neat solutions of Rhodamine 6G and 1,2-indanedione + alanine when excited with 442 nm blue laser and a long pass filter with a cut off of 480 nm. (b) Spectra of fluorescence obtained from fingerprints on various surfaces and treated with 1,2-indanedione: paper (solid line), CaF_2 CTF deposited on aluminium sheet (... line) and glass slide (line). The blue excitation light had a peak wavelength of $\lambda = 488$ nm and green excitation had a peak wavelength of $\lambda = 542$ nm.

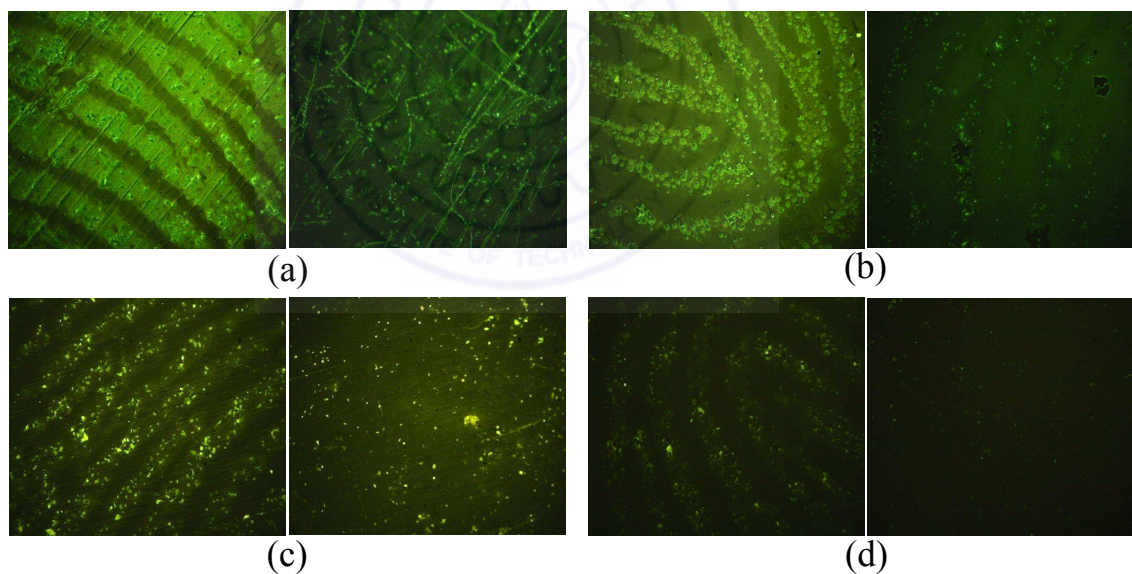


Figure 6.6: Fluorescence microscope images dye treated fingerprints and CTF deposited on fingerprint marks viewed under blue light excitation in a fluorescence microscope. Top row panels are for Rhodamine 6G treated fingerprint marks, while the bottom row panels are for alanine + 1,2-indanedione treated substrates. From left to right, the four panels in each row respectively correspond to CTF deposited fingerprint marks on aluminum substrate, plain fingerprint on rough aluminium substrate, CTF deposited finger mark on glass substrate and plain fingerprint on smooth glass substrate.

1,2-indanedione treated CTF deposited fingerprints. The CTF material was either SiO_2 or CaF_2 without any reduction in the visual enhancements. The fluorescence im-

ages are shown in Fig. 6.6 for both the CTF deposited and dye treated fingerprint marks, as well as the fingerprint marks on substrates with only dye treatment and no CTF deposition. The enhancement in the fluorescence images are extremely clear. In fact, due to its very high quantum efficiency, the improvement in the case of Rhodamine 6G treated CTF on fingerprint marks is better than the alanine + 1,2-indanedione. Further, due to the vacuum degradation as well as the deposition on the fingerprint mark, the 1,2-indanedione is probably not very effective to bind to the amino acids that may be present.

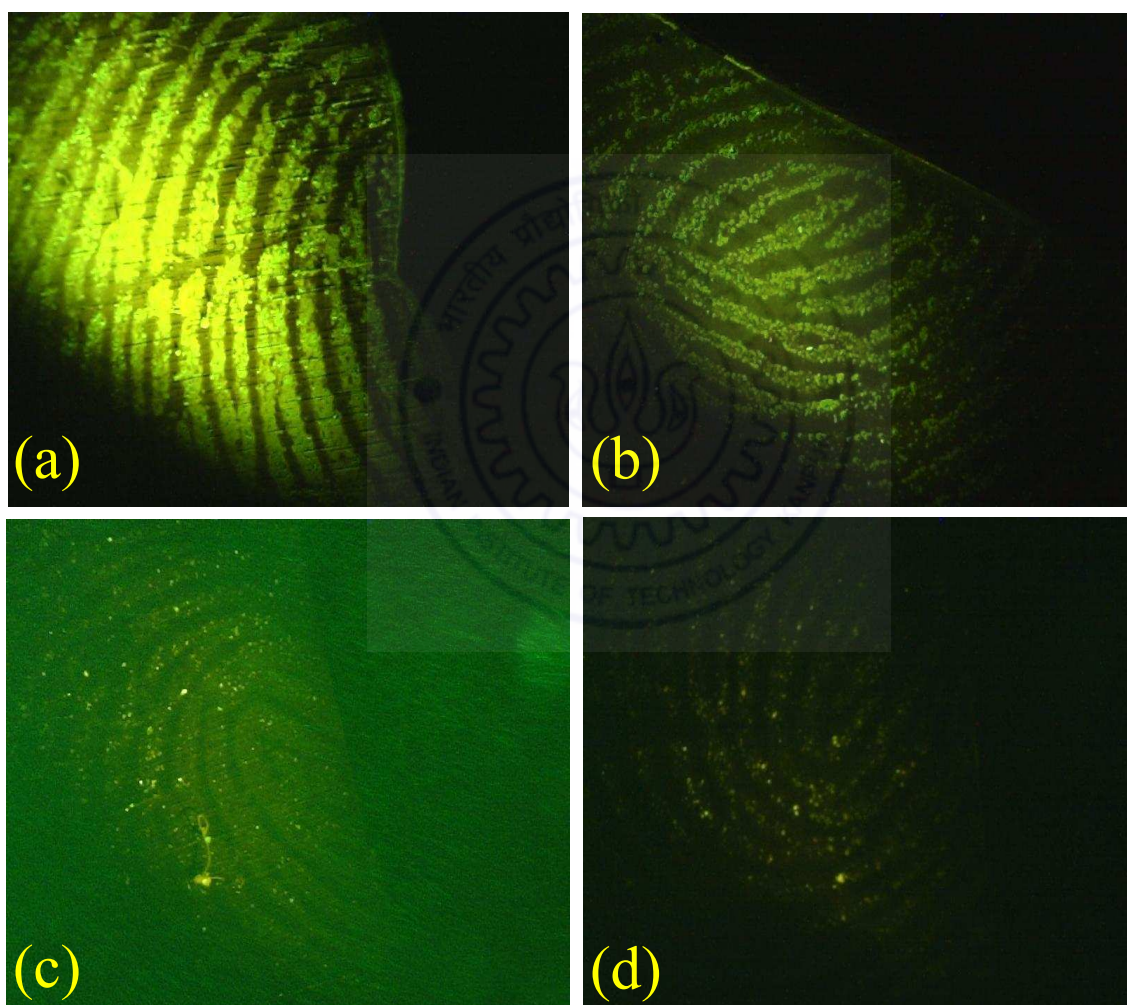


Figure 6.7: Fluorescence images of fingerprint marks detected by illuminating with a 532 nm laser and detecting the fluorescence through a 532 nm notch filter. Panels (a) and (b) are the fluorescence images fingerprint marks with SiO₂ CTF and Rhodamine 6G treatment on a rough aluminum sheet and a glass slide respectively. Panels (c) and (d) are the fluorescence images fingerprint marks with SiO₂ CTF and alanine + 1,2-indanedione treatment on a rough aluminium sheet and a glass slide respectively. The green background in panel (c) is due to the strong reflected laser light from the rough aluminium surface leaking through the notch filter, which is almost as bright as the fluorescence.

Without the CTF deposition, almost no fingerprint information can be obtained from the fluorescence imaging on the aluminum substrate while faint fingerprint impressions can be obtained from the glass substrates without deposited CTF by the dye treatment. The CTF structure on the fingermarks in glass viewed by fluorescence shows the presence of clumps of CTF. This could be due to the clumping of the fingerprint debris on the smooth glass surface which is less wettable by hydrophilic materials. Comparatively, the CTF growth on the fingerprints on aluminum substrates exhibits a more smooth nature and the enhancement of the visualization through fluorescence is very high in comparison to bright-field or dark-field microscopic techniques. Using a $100\times$ objective of the microscope we could measure fluorescence from small regions. These measurements of the fluorescence emanating from the CTF ridges and the empty regions in between showed that the fluorescence spectrum from both regions were almost the same except for the presence of only a small blue shift in the fluorescence from the CTF structures. The band widths of the fluorescence are almost the same with perhaps a slightly increased bandwidth for the fluorescence from the regions in between the ridges. Finally, we examined the possibility of detecting larger areas of the fingerprints by illuminating with 532 nm DPSS laser (100 mW) beam and imaging the fluorescence by a CCD camera through a 532 nm notch filter. The fluorescence from the Rhodamine 6G treated CTF deposited fingerprint marks stand out prominently on both the rough aluminum surfaces as well on the smooth glass surface (see Fig. 6.7). To prevent saturating the CCD camera the laser beam was attenuated to 5% for the Rhodamine 6G treated samples by using neutral density filters. The alanine + 1,2-indanedione samples show comparatively poor fluorescence and the laser intensity had to be enhanced by using a ND filter with 13.5% transmittance. In that case, the transmission through the notch filter of the strong scattered light from the rough aluminum surface was almost comparable to the fluorescence from the 1,2-indanedione (see Fig. 6.7) and in case of the glass slide also, the fluorescence was very weak. Hence we opine that for detection purposes, the Rhodamine 6G treatment on the CTF is much more efficient than the alanine + 1,2-indanedione case.

6.5 Conclusions

We have demonstrated the possibility of visualizing latent fingerprints on both rough aluminum (reflecting) surfaces and smooth glass surfaces by the deposition of nanostructured CTFs. The CTF when deposited at large oblique angles grow preferentially on the physical debris of the fingerprint, due to shadowing of the vapor flux by the debris already present on the surfaces. The deposited CTFs are highly scattering and result in an enhanced visibility of fingerprint. The fingerprints typically become visible even upon visual inspection when the CTF was deposited on the prints. Microscopic techniques such as dark-field imaging lead to enhanced visibility of the CTF treated fingerprints on the smooth surfaces of glass. For a rough aluminum surface, the dark-field images and bright-field images yield almost comparable visibility of the CTF ridges on the substrate due to large scattering from the roughness. The ability to detect and visualize the fingerprints is further enhanced by treatment of the CTF deposited fingerprint marks with fluorescent dyes. Both 1,2-indanedione-alanine and Rhodamine 6G molecules resulted in enhanced visualization through the fluorescence of the molecules, although the Rhodamine 6G molecules gave better visualization due to their higher quantum efficiency. These results may open new options in fingerprint visualization and detection using CTFs followed by fluorescent reagents. Our preliminary results show that this technique can be useful for latent fingerprints on nonporous surfaces. Further work is necessary to optimize the CTF deposition process (thickness, porosity, etc.) and the chemical post-treatment (kind of dye, solution concentration, temperature, humidity, etc.).

Chapter 7

Conclusions and Future Work

In the introduction to the thesis, I expressed the hope that the work carried out here could be a first step towards exploring new photonic applications of PP-CTFs. In this final chapter, I will conclude by describing the progress made towards this goal in terms of the different applications developed in the thesis. Although we may consider that considerable progress towards this goal of the thesis has been accomplished, but there are plenty of improvements that are possible as well as many new promising avenues in these lines of thought that I will touch upon in this chapter.

7.1 Conclusions

The essence of this research work is well encapsulated by the title of this work, namely, “Photonic and Plasmonic properties of Periodically Patterned Columnar Thin Films”. The broad research objectives successively attained by the work presented in the chapters within this thesis can be briefly listed as

- PP-CTFs are effectively and controllably fabricated by evaporating dielectric/metals and directing the resultant collimated vapor flux obliquely towards one and two dimensional micrometer/sub-micrometer gratings fabricated by LIL.
- Periodically patterned dielectric CTFs are shown to behave as blazed diffraction gratings and show highly asymmetric diffraction patterns. The blazed diffraction

in these gratings arises due to the presence of triangular air prismatic cavities within the PP-CTF and could be analysed within the Kirchhoff-Fresnel diffraction theory.

- Periodically patterned silver CTFs show asymmetric diffraction and can provide asymmetric coupling of incident radiation to SPP waves. The Bruggeman homogenization formalism was used to homogenize the silver CTFs and the silver CTF was treated to be a hyperbolic indefinite permittivity effective medium. The gratings of an hyperbolic medium may will be the first such manifestation studied and provide for unidirectional coupling to SPR.
- The slant angle of silver nanocolumns can be changed to any angle from as-grown to upright nanocolumns uniformly over large areas by irradiating the grating with ion beam irradiation, in particular a focused Ga ion beam was used by us. The measured diffraction from these two regions, could be changed from asymmetric to a completely symmetric diffraction pattern. Electromagnetic numerical simulations also reveal tuning of the photonic and plasmonic properties such as diffraction efficiencies and surface plasmon coupling for two different orientation of silver nanocolumns.
- A novel application of the process to visualization of fingerprints is explored. Visualization of latent fingerprints is shown to be enhanced by the deposition of nanostructured CTFs at large oblique angle on the fingerprint marks on non-porous surfaces such as smooth glass slides and highly reflecting rough aluminium sheets. The visualization can be further enhanced by treating the deposited CTFs with a fluorescent dye and fluorescence imaging.

In conclusions, various photonic properties such as blazed diffraction efficiencies and it's tunability, fluorescence and various plasmonic properties such as unidirectional coupling, local electric field enhancement have been well explored through the PP-CTFs.

7.2 Suggestions for Future Work

Here I discuss some of the possible open issues that deserve further research (some of which we are already working on) in extension of the present work carried out in this thesis. I will also suggest some future research directions that could provide the next steps towards practical device applicable systems.

- We demonstrated that the SPP dispersion plots for the PPMCTFs show asymmetric coupling for different periodicities of gratings, while keeping the length and slant angle of the columns fixed. However this work needs further optimization. The length and orientation of nanorods for given pitch of a grating for maximum anisotropic coupling at a given wavelength will require to be optimized. Such asymmetric coupling to unidirectional SPP waves is very important for efficiently coupling radiation to the SPP waves in plasmonic devices and circuits. We propose one possible design here for a SPP coupler as shown in Fig. 7.1. Since every SPP device needs a coupler and it can be in the form of a waveguide, a prism, or a grating. SPP waves have decay lengths of the order of about 20-30 micrometers. Long-range SPP waves may have decay lengths of several hundred micrometers. Just about 6 to 8 grating lines (over about 3-4 micrometers length scale) would be sufficient to create asymmetric coupling (as we have in our simulations). The large increase (by a factor of 2) in coupling more than justifies this small decay over this lengthscale. Further, due to the porosity and reduced amount of metal, the dissipation (imaginary part of the relative permittivity) can be smaller in our structure than in commonplace SPP devices using plain metal films and the decay lengths might be even larger than in commonplace SPP devices. The grating in our structure could be easily a part of an adiabatic coupler to an SPP waveguide as pictured by us as and shown schematically in Fig. 7.1. Such couplers could be expected to play a key role in future “plasmonic chips”.

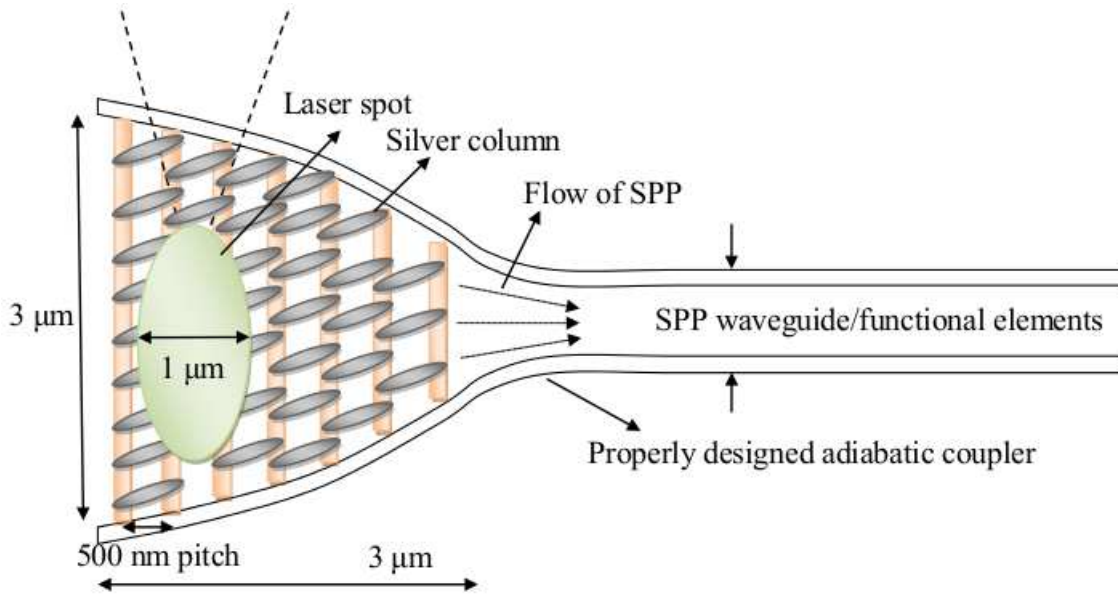


Figure 7.1: SPP Coupler

- We demonstrated experimentally the re-orientation of slanted plasmonic nanocolumns of silver grown on small period photoresist gratings by ion beam irradiation. A possible next step is to perform the tuning of the silver nanocolumnar array by other techniques, such as magnetostatically or by MEMS technologies. Such investigations would reveal the promise of these nanostructured materials in existing micro/nano devices and could further enhance the functionalities of such devices.
- We carried some work on Organic photovoltaic device (OPVD) to explore the use of ITO nanostructured columnar electrodes in collaboration with Arun D Rao and Praveen C Ramamurthy from the Indian Institute of Science, Bangalore, India. We obtained some preliminary results on the enhancement of photovoltaic performance. Fig. 7.2 (a) shows the cross-section FESEM image of as grown ITO columnar structure and Fig. 7.2 (b) shows the cross-section FESEM image of ITO columnar structure on which the P3HT : PCBM active layer is deposited. Fig. 7.2 (c) shows the J-V (current density-voltage) plot, where devices with aligned ITO columnar structure showed an almost three-fold increase in current density presumably due to the high surface area compared to the planar thin film of ITO. This work, however, needs to progress to increase this performance

further by properly optimizing the growth of ITO columnar structures and the deposition of the photovoltaic material.

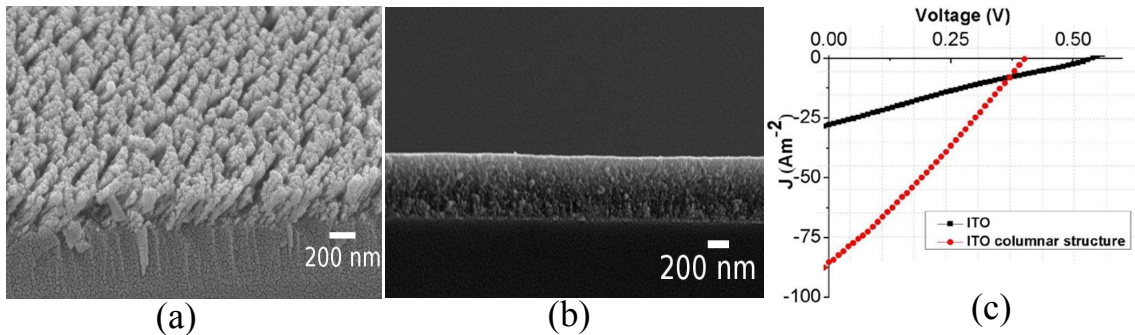


Figure 7.2: (a) Cross-sectional FESEM image of ITO columnar structure, (b) ITO columnar structure interpenetrated with P3HT : PCBM active layer and (c) J-V plot of OPVDs of ITO columnar structure and planar ITO substrate

- Apart from these, it would be extremely interesting to study the Surface Enhanced Fluorescence (SEF) and the Surface Enhanced Raman Spectroscopy (SERS) measurements from molecules deposited on such samples. Since the CTFs are known to be good SERS substrates, we believe that the periodically patterned columnar structure can give much further enhanced SEF and SERS properties by carefully optimizing the local field enhancements in these systems.

Finally, in terms of applications of the periodically patterned metallic and dielectric CTFs, there are a plethora of possible areas in which it can be applied: from integrated optical devices to chemical and biological sensors. This area of study appears to be very promising in the future.



Bibliography

- [1] A. Lakhtakia, Sculptured thin films: Nanoengineered morphology and optics (SPIE press, Bellingham, Washington 98227-0010 USA, 2005), Vol. 143.
- [2] I. J. Hodgkinson and Q. hong Wu, Birefringent thin films and polarizing elements (World Scientific, Singapore, 1997).
- [3] K. Robbie, M. Brett, and A. Lakhtakia, *Nature* **384**, 616 (1996).
- [4] P.-G. De Gennes and J. Prost, The physics of liquid crystals (Clarendon press Oxford, New York, 1993), Vol. 23.
- [5] Q. Wu, I. J. Hodgkinson, and A. Lakhtakia, *Optical Engineering* **39**, 1863 (2000).
- [6] J. Wang, J. Shao, and Z. Fan, *Optics Communications* **247**, 107 (2005).
- [7] W. Chang, *IEEE Transactions on Microwave Theory and Techniques* **21**, 775 (1973).
- [8] J. Nieuwenhuizen and H. Haanstra, *Philips Tech. Rev.* **27**, 87 (1966).
- [9] D. Schmidt, B. Booso, T. Hofmann, E. Schubert, A. Sarangan, and M. Schubert, *Applied Physics Letters* **94**, 011914 (2009).
- [10] D. Schmidt, B. Booso, T. Hofmann, E. Schubert, A. Sarangan, and M. Schubert, *Optics Letters* **34**, 992 (2009).
- [11] T. Motohiro and Y. Taga, *Applied Optics* **28**, 2466 (1989).
- [12] J. D. Driskell, S. Shanmukh, Y.-J. Liu, S. Hennigan, L. Jones, Y.-P. Zhao, R. A. Dluhy, D. C. Krause, and R. A. Tripp, *Sensors Journal, IEEE* **8**, 863 (2008).
- [13] S. A. Maier, Plasmonics: fundamentals and applications: fundamentals and applications (Springer Science & Business Media, New York, 2007).
- [14] H. Ohno, E. Mendez, J. Brum, J. Hong, F. Agulló-Rueda, L. Chang, and L. Esaki, *Physical Review Letters* **64**, 2555 (1990).
- [15] O. Takayama, L. Crasovan, D. Artigas, and L. Torner, *Physical Review Letters* **102**, 043903 (2009).
- [16] D. P. Pulsifer, M. Faryad, A. Lakhtakia, A. S. Hall, and L. Liu, *Optics Letters* **39**, 2125 (2014).
- [17] T. G. Mackay and A. Lakhtakia, *Photonics and Nanostructures-Fundamentals and Applications* **8**, 140 (2010).
- [18] S. R. Kennedy and M. J. Brett, *Applied Optics* **42**, 4573 (2003).

- [19] F. Yang, G. Bradberry, and J. Sambles, *Thin Solid Films* **196**, 35 (1991).
- [20] T. Hofmann, D. Schmidt, A. Boosalis, P. Kühne, R. Skomski, C. Herzinger, J. Woollam, M. Schubert, and E. Schubert, *Applied Physics Letters* **99**, 081903 (2011).
- [21] Y. Sun, X. Xiao, G. Xu, G. Dong, G. Chai, H. Zhang, P. Liu, H. Zhu, and Y. Zhan, *Scientific Reports* **3**, (2013).
- [22] Y. Liu, J. Fan, Y.-P. Zhao, S. Shanmukh, and R. A. Dluhy, *Applied Physics Letters* **89**, 173134 (2006).
- [23] I. Abdulhalim, A. Karabchevsky, C. Patzig, B. Rauschenbach, B. Fuhrmann, E. Eltzov, R. Marks, J. Xu, F. Zhang, and A. Lakhtakia, *Applied Physics Letters* **94**, 063106 (2009).
- [24] K. D. Harris, A. C. van Popta, J. C. Sit, D. J. Broer, and M. J. Brett, *Advanced Functional Materials* **18**, 2147 (2008).
- [25] J. W. Leem and J. S. Yu, *Optics Express* **19**, A258 (2011).
- [26] A. Jagdish, P. C. Ramamurthy, D. R. Mahapatra, and G. Hegde, *Journal of Applied Physics* **116**, 074504 (2014).
- [27] M. Born and E. Wolf, Principles of optics: electromagnetic theory of propagation, interference and diffraction of light (Cambridge university press, United Kingdom, 1999).
- [28] J. Peatross and M. Ware, Physics of light and optics (Brigham Young University, Department of Physics, 2011).
- [29] F. L. Pedrotti and L. S. Pedrotti, *Introduction to Optics* 2nd Edition by Frank L. Pedrotti, S.J, Leno S. Pedrotti New Jersey: Prentice Hall, 1993 **1**, (1993).
- [30] N. Lu, D. Kuang, and G. Mu, *Applied Optics* **47**, 3743 (2008).
- [31] G. A. Niklasson, C. Granqvist, and O. Hunderi, *Applied Optics* **20**, 26 (1981).
- [32] T. G. Mackay and A. Lakhtakia, *Journal of Nanophotonics* **6**, 069501 (2012).
- [33] W. S. Weiglhofer, A. Lakhtakia, and B. Michel, *Microwave and Optical Technology Letters* **15**, 263 (1997).
- [34] S. A. Ramakrishna and T. M. Grzegorzczuk, Physics and applications of negative refractive index materials (CRC press, Taylor & Francis Group, 2008).
- [35] J. B. Pendry, A. J. Holden, D. Robbins, and W. Stewart, *Microwave Theory and Techniques, IEEE Transactions on* **47**, 2075 (1999).
- [36] D. R. Smith, W. J. Padilla, D. Vier, S. C. Nemat-Nasser, and S. Schultz, *Physical Review Letters* **84**, 4184 (2000).
- [37] S. O'brien, D. McPeake, S. A. Ramakrishna, and J. Pendry, *Physical Review B* **69**, 241101 (2004).
- [38] J. Pendry, A. Holden, W. Stewart, and I. Youngs, *Physical Review Letters* **76**, 4773 (1996).
- [39] J. Pendry, A. Holden, D. Robbins, and W. Stewart, *Journal of Physics: Condensed Matter* **10**, 4785 (1998).

- [40] S. Chakrabarti, S. A. Ramakrishna, and H. Wanare, *Optics Letters* **34**, 3728 (2009).
- [41] N. Fang, H. Lee, C. Sun, and X. Zhang, *Science* **308**, 534 (2005).
- [42] S. A. Ramakrishna, *Reports on Progress in Physics* **68**, 449 (2005).
- [43] D. Schurig, J. Mock, B. Justice, S. A. Cummer, J. Pendry, A. Starr, and D. Smith, *Science* **314**, 977 (2006).
- [44] N. Landy, S. Sajuyigbe, J. Mock, D. Smith, and W. Padilla, *Physical Review Letters* **100**, 207402 (2008).
- [45] D. Smith and D. Schurig, *Physical Review Letters* **90**, 077405 (2003).
- [46] A. Poddubny, I. Iorsh, P. Belov, and Y. Kivshar, *Nature Photonics* **7**, 948 (2013).
- [47] S. A. Ramakrishna, J. Pendry, M. Wiltshire, and W. Stewart, *Journal of Modern Optics* **50**, 1419 (2003).
- [48] Z. Jacob, L. V. Alekseyev, and E. Narimanov, *Optics Express* **14**, 8247 (2006).
- [49] S. S. Kruk, D. A. Powell, A. Minovich, D. N. Neshev, and Y. S. Kivshar, *Optics Express* **20**, 15100 (2012).
- [50] B. Casse, W. Lu, Y. Huang, E. Gultepe, L. Menon, and S. Sridhar, *Applied Physics Letters* **96**, 023114 (2010).
- [51] J. B. Pendry, *Physical Review Letters* **85**, 3966 (2000).
- [52] J. Yao, Z. Liu, Y. Liu, Y. Wang, C. Sun, G. Bartal, A. M. Stacy, and X. Zhang, *Science* **321**, 930 (2008).
- [53] Z. Liu, H. Lee, Y. Xiong, C. Sun, and X. Zhang, *Science* **315**, 1686 (2007).
- [54] S. Ishii, A. V. Kildishev, E. Narimanov, V. M. Shalaev, and V. P. Drachev, *Laser & Photonics Reviews* **7**, 265 (2013).
- [55] D. R. Smith, D. Schurig, J. J. Mock, P. Kolinko, and P. Rye, *Applied Physics Letters* **84**, 2244 (2004).
- [56] P. Evans, W. Hendren, R. Atkinson, G. Wurtz, W. Dickson, A. Zayats, and R. Pollard, *Nanotechnology* **17**, 5746 (2006).
- [57] E. Yablonovitch, *Physical Review Letters* **58**, 2059 (1987).
- [58] C. Kittel, P. McEuen, and P. McEuen, Introduction to solid state physics (Wiley, New York, 1976), Vol. 8.
- [59] J. D. Joannopoulos, S. G. Johnson, J. N. Winn, and R. D. Meade, Photonic crystals: molding the flow of light (Princeton university press, Princeton AND Oxford, 2011).
- [60] K. Ho, C. Chan, and C. Soukoulis, *Physical Review Letters* **65**, 3152 (1990).
- [61] O. Toader and S. John, *Science* **292**, 1133 (2001).
- [62] O. Painter, R. Lee, A. Scherer, A. Yariv, J. O'Brien, P. Dapkus, and I. Kim, *Science* **284**, 1819 (1999).
- [63] T. W. Ebbesen, H. Lezec, H. Ghaemi, T. Thio, and P. Wolff, *Nature* **391**, 667 (1998).

- [64] S. Lal, S. Link, and N. J. Halas, *Nature Photonics* **1**, 641 (2007).
- [65] H. A. Atwater and A. Polman, *Nature Materials* **9**, 205 (2010).
- [66] M. Kauranen and A. V. Zayats, *Nature Photonics* **6**, 737 (2012).
- [67] M. L. Brongersma and V. M. Shalaev, (2010).
- [68] D. K. Gramotnev and S. I. Bozhevolnyi, *Nature Photonics* **4**, 83 (2010).
- [69] N. C. Lindquist, P. Nagpal, K. M. McPeak, D. J. Norris, and S.-H. Oh, *Reports on progress in physics. Physical Society (Great Britain)* **75**, 036501 (2012).
- [70] H. Raether, Surface plasmons on smooth surfaces (Springer, the University of Virginia, 1988).
- [71] S. Enoch and N. Bonod, Plasmonics: from basics to advanced topics (PUBLISHER, ADDRESS, YEAR), Vol. 167.
- [72] J. A. Polo and A. Lakhtakia, *Laser & Photonics Reviews* **5**, 234 (2011).
- [73] M. Dyakonov, *Zh. Eksp. Teor. Fiz* **94**, 119 (1988).
- [74] P. Yeh, A. Yariv, and C.-S. Hong, *Journal of the Optical Society of America* **67**, 423 (1977).
- [75] D. P. Pulsifer, M. Faryad, and A. Lakhtakia, *Physical Review Letters* **111**, 243902 (2013).
- [76] N. Meinzer, W. L. Barnes, and I. R. Hooper, *Nature Photonics* **8**, 889 (2014).
- [77] C. Escobedo, *Lab on a Chip* **13**, 2445 (2013).
- [78] M. M. Hawkeye and M. J. Brett, *Journal of Vacuum Science & Technology A* **25**, 1317 (2007).
- [79] M. Jensen and M. Brett, *Optics Express* **13**, 3348 (2005).
- [80] M. M. Hawkeye and M. J. Brett, *Journal of Applied Physics* **100**, 044322 (2006).
- [81] V. Fiumara, F. Chiadini, A. Scaglione, and A. Lakhtakia, *Optics Communications* **268**, 182 (2006).
- [82] K. Robbie and M. Brett, *Journal of Vacuum Science & Technology A* **15**, 1460 (1997).
- [83] L. Abelmann and C. Lodder, *Thin Solid Films* **305**, 1 (1997).
- [84] R. Tait, T. Smy, and M. Brett, *Thin Solid Films* **226**, 196 (1993).
- [85] J. J. Steele, A. C. van Popta, M. M. Hawkeye, J. C. Sit, and M. J. Brett, *Sensors and Actuators B: Chemical* **120**, 213 (2006).
- [86] S. Kesapragada, P. Victor, O. Nalamasu, and D. Gall, *Nano Letters* **6**, 854 (2006).
- [87] Y. J. Park, K. Sobahan, J. B. Kim, and C. K. Hwangbo, *Thin Solid Films* **519**, 1673 (2010).
- [88] C. Lu and R. Lipson, *Laser & Photonics Reviews* **4**, 568 (2010).
- [89] M. Maldovan and E. L. Thomas, Periodic Materials and Interference Lithography: For Photonics, Phononics and Mechanics (John Wiley & Sons, Weinheim, 2009).

- [90] D. Xia, Z. Ku, S. Lee, and S. Brueck, *Advanced Materials* **23**, 147 (2011).
- [91] K. Du, I. Wathuthanthri, W. Mao, W. Xu, and C.-H. Choi, *Nanotechnology* **22**, 285306 (2011).
- [92] M. O. Jensen and M. J. Brett, *Nanotechnology, IEEE Transactions on* **4**, 269 (2005).
- [93] M. W. Horn, M. D. Pickett, R. Messier, and A. Lakhtakia, *Nanotechnology* **15**, 303 (2004).
- [94] M. Malac, R. Egerton, M. Brett, and B. Dick, *Journal of Vacuum Science & Technology B* **17**, 2671 (1999).
- [95] B. Dick, M. Brett, and T. Smy, *Journal of Vacuum Science & Technology B* **21**, 23 (2003).
- [96] B. Dick, M. Brett, T. Smy, M. Freeman, M. Malac, and R. Egerton, *Journal of Vacuum Science & Technology A* **18**, 1838 (2000).
- [97] J. Jin, The finite element method in electromagnetics (John Wiley & Sons, Wiley-IEEE, 2014).
- [98] C. Hafner and J. Smajic, *Journal of Modern Optics* **58**, 467 (2011).
- [99] C.-H. Chang, Ph.D. thesis, Massachusetts Institute of Technology, 2004.
- [100] F. Lütolf, M. Stalder, and O. J. Martin, *Optics Letters* **39**, 6557 (2014).
- [101] B. Bai, X. Meng, J. Laukkanen, T. Sfez, L. Yu, W. Nakagawa, H. P. Herzig, L. Li, and J. Turunen, *Physical Review B* **80**, 035407 (2009).
- [102] P. Lalanne *et al.*, *Optics Letters* **23**, 1081 (1998).
- [103] S. Astilean, P. Lalanne, P. Chavel, E. Cambril, and H. Launois, *Optics Letters* **23**, 552 (1998).
- [104] E. Walsby, M. Arnold, Q.-h. Wu, I. Hodgkinson, and R. Blaikie, *Microelectronic Engineering* **78**, 436 (2005).
- [105] L. Ward, The optical constants of bulk materials and films (A. Hilger, Bristol, England ; Philadelphia, 1988).
- [106] S. Sinzinger and M. Testorf, *Applied Optics* **34**, 5970 (1995).
- [107] G. Smith, *Applied Optics* **29**, 3685 (1990).
- [108] T. Tamulevičius, R. Šeperys, M. Andrulevičius, and S. Tamulevičius, *Photonics and Nanostructures-Fundamentals and Applications* **9**, 140 (2011).
- [109] F. Chiadini and A. Lakhtakia, *Microwave and Optical Technology Letters* **42**, 72 (2004).
- [110] R. K. Heilmann, M. Ahn, and M. L. Schattenburg, in SPIE Astronomical Telescopes+ Instrumentation, International Society for Optics and Photonics (Proc. SPIE, Marseille, France, 2008), pp. 701106–701106.
- [111] M. Yeung, M. Zepf, M. Geissler, and B. Dromey, *Optics Letters* **36**, 2333 (2011).
- [112] M. Kreiter, S. Mittler, W. Knoll, and J. R. Sambles, *Physical Review B* **65**, 125415 (2002).

- [113] E. Ozbay, *Science* **311**, 189 (2006).
- [114] W. L. Barnes, A. Dereux, and T. W. Ebbesen, *Nature* **424**, 824 (2003).
- [115] T. W. Ebbesen, C. Genet, and S. I. Bozhevolnyi, *Physics Today* **61**, 44 (2008).
- [116] M. Faryad and A. Lakhtakia, *JOSA B* **27**, 2218 (2010).
- [117] S. E. Swiontek, D. P. Pulsifer, and A. Lakhtakia, *Scientific Reports* **3**, (2013).
- [118] J.-Y. Laluet, E. Devaux, C. Genet, T. W. Ebbesen, J.-C. Weeber, and A. Dereux, *Optics Express* **15**, 3488 (2007).
- [119] Z. Han and S. I. Bozhevolnyi, *Reports on Progress in Physics* **76**, 016402 (2013).
- [120] N. Bonod, E. Popov, L. Li, and B. Chernov, *Optics Express* **15**, 11427 (2007).
- [121] B. Wang, J. Jiang, and G. Nordin, *Optics Express* **12**, 3313 (2004).
- [122] F. López-Tejiera *et al.*, *Nature Physics* **3**, 324 (2007).
- [123] T. Liu, Y. Shen, W. Shin, Q. Zhu, S. Fan, and C. Jin, *Nano Letters* **14**, 3848 (2014).
- [124] L. Wang, T. Li, L. Li, W. Xia, X. Xu, and S. Zhu, *Optics Express* **20**, 8710 (2012).
- [125] M. Kadic, S. Guenneau, S. Enoch, and S. A. Ramakrishna, *ACS Nano* **5**, 6819 (2011).
- [126] A. Shalabney, A. Lakhtakia, I. Abdulhalim, A. Lahav, C. Patzig, I. Hazeq, A. Karabchevsky, B. Rauschenbach, F. Zhang, and J. Xu, *Photonics and Nanostructures-Fundamentals and Applications* **7**, 176 (2009).
- [127] D. Schmidt, E. Schubert, and M. Schubert, *Applied Physics Letters* **100**, 011912 (2012).
- [128] A. Shalabney, C. Khare, B. Rauschenbach, and I. Abdulhalim, *Sensors and Actuators B: Chemical* **159**, 201 (2011).
- [129] J. Dutta, S. A. Ramakrishna, and A. Lakhtakia, *Journal of Applied Physics* **117**, 013102 (2015).
- [130] J. Dutta, S. A. Ramakrishna, and A. Lakhtakia, *Applied Physics Letters* **102**, 161116 (2013).
- [131] C. Billaudeau, S. Collin, C. Sauvan, N. Bardou, F. Pardo, and J.-L. Pelouard, *Optics Letters* **33**, 165 (2008).
- [132] I. S. Nefedov, C. A. Valagiannopoulos, S. M. Hashemi, and E. I. Nefedov, *Scientific Reports* **3**, (2013).
- [133] T. G. Mackay and A. Lakhtakia, *Optics Communications* **234**, 35 (2004).
- [134] J. Sherwin, A. Lakhtakia, and I. Hodgkinson, *Optics Communications* **209**, 369 (2002).
- [135] G. Mbjise, D. Le Bellac, G. Niklasson, and C. Granqvist, *Journal of Physics D: Applied Physics* **30**, 2103 (1997).
- [136] J. Dutta, S. A. Ramakrishna, and A. , *Journal Of Applied Physics* **117**, 013102 (2015).

- [137] L. Liu, M. Faryad, A. S. Hall, G. D. Barber, S. Erten, T. E. Mallouk, A. Lakhtakia, and T. S. Mayer, *Journal of Nanophotonics* **9**, 093593 (2015).
- [138] W. Cai and V. M. Shalaev, *Optical metamaterials* (Springer, ADDRESS, 2010).
- [139] L. J. Guo, *Journal of Physics D: Applied Physics* **37**, R123 (2004).
- [140] J. Singh, D.-L. Liu, D.-X. Ye, R. Picu, T.-M. Lu, and G.-C. Wang, *Applied Physics Letters* **84**, 3657 (2004).
- [141] N. S. Rajput, A. Banerjee, and H. Verma, *Nanotechnology* **22**, 485302 (2011).
- [142] B. C. Park *et al.*, *Advanced Materials* **18**, 95 (2006).
- [143] Y. Hu, Z. Zhang, Q. Zhou, W. Liu, Z. Li, and D. Meng, *Nano Research* **3**, 438 (2010).
- [144] H. Yoon, H. Woo, M. K. Choi, K. Y. Suh, and K. Char, *Langmuir* **26**, 9198 (2010).
- [145] J. Dutta and S. A. Ramakrishna, *Nanotechnology* **26**, 205301 (2015).
- [146] J. F. Ziegler, *Nuclear Instruments and Methods in Physics Research Section B: Beam Interactions with Materials and Atoms* **219**, 1027 (2004).
- [147] C. Borschel, R. Niepelt, S. Geburt, C. Gutsche, I. Regolin, W. Prost, F.-J. Tegude, D. Stichtenoth, D. Schwen, and C. Ronning, *Small* **5**, 2576 (2009).
- [148] C. Borschel, S. Spindler, D. Leroose, A. Bochmann, S. H. Christiansen, S. Nietzsche, M. Oertel, and C. Ronning, *Nanotechnology* **22**, 185307 (2011).
- [149] N. Gour and S. Verma, *Soft Matter* **5**, 1789 (2009).
- [150] S. K. Tripathi, N. Shukla, S. Dhamodaran, and V. N. Kulkarni, *Nanotechnology* **19**, 205302 (2008).
- [151] N. S. Rajput, Z. Tong, and X. Luo, *Materials Research Express* **2**, 015002 (2015).
- [152] M. A. Ordal *et al.*, *Applied Optics* **24**, 4493 (1985).
- [153] A. Serebryannikov and E. Ozbay, *Optics Express* **17**, 13335 (2009).
- [154] J. Dorfmueller, R. Vogelgesang, R. T. Weitz, C. Rockstuhl, C. Etrich, T. Pertsch, F. Lederer, and K. Kern, *Nano Letters* **9**, 2372 (2009).
- [155] S. B. Hasan, C. Etrich, R. Filter, C. Rockstuhl, and F. Lederer, *Physical Review B* **88**, 205125 (2013).
- [156] K.-C. Park, H. J. Choi, C.-H. Chang, R. E. Cohen, G. H. McKinley, and G. Barbastathis, *ACS Nano* **6**, 3789 (2012).
- [157] H. W. Choi, K.-S. Lee, and T. Alford, *Applied Physics Letters* **101**, 153301 (2012).
- [158] Y.-R. Lin, K. Lai, H.-P. Wang, and J.-H. He, *Nanoscale* **2**, 2765 (2010).
- [159] P. Mühlischlegel, H.-J. Eisler, O. Martin, B. Hecht, and D. Pohl, *Science* **308**, 1607 (2005).
- [160] G. B. Smith and C.-G. S. Granqvist, *Green nanotechnology: solutions for sustainability and energy in the built environment* (CRC Press, Boca Raton, 2010).

- [161] H. C. Lee and R. Gaensslen, *Advances in Fingerprint Technology* **2**, 105 (2001).
- [162] G. Batey, J. Copeland, D. Donnelly, C. Hill, P. Laturnus, C. McDiarmid, K. Miller, A. Misner, and A. Tario, *J. Forensic Identification* **48**, 165 (1998).
- [163] A. Ramos and M. Vieira, *Forensic Science International* **217**, 196 (2012).
- [164] J. Watkin, D. Wilkinson, A. Misner, and A. Yamashita, *J. Forensic Identification* **44**, 545 (1994).
- [165] A. M. D.A. Wilkinson, *J. Forensic Identification* **44**, 387 (1994).
- [166] A. Bécue and A. A. Cantú, Fingermark detection using nanoparticles (CRC Press LLC, United States, 2012).
- [167] H. C. Lee, R. Ramotowski, and R. Gaensslen, Advances in fingerprint technology (CRC press, Boca Raton, FL, 2010).
- [168] J. Dilag, H. J Kobus, and A. V Ellis, *Current Nanoscience* **7**, 153 (2011).
- [169] L. S. Miller, N. Marin, and R. T. McEvoy Jr, Police Photography (Elsevier, Burlington, 2010).
- [170] G. Williams, H. N. McMurray, and D. A. Worsley, *Journal of Forensic Sciences* **46**, 1085 (2001).
- [171] J. W. Bond, *Journal of Forensic Sciences* **53**, 812 (2008).
- [172] O. Petrovskaia, B. M. Taylor, D. B. Hauze, P. J. Carroll, and M. M. Joullié, *The Journal of organic chemistry* **66**, 7666 (2001).
- [173] I. M. Alaoui, E. Menzel, M. Farag, K. Cheng, and R. Murdock, *Forensic Science International* **152**, 215 (2005).
- [174] S. Wiesner, E. Springer, Y. Sasson, and J. Almog, *Journal of Forensic Sciences* **46**, 1082 (2001).
- [175] I. M. Alaoui, T. Troxler, and M. Joullié, *Journal of Forensic Identification* **62**, 1 (2012).
- [176] X. Spindler, M. Stoilovic, C. Lennard, and A. Lennard, *Journal of Forensic Identification* **59**, 308 (2009).
- [177] K. E. Mitchell and E. Menzel, in Time-resolved luminescence imaging: application to latent fingerprint detection (Fluorescence Detection III, SPIE Proceedings, 1989), Vol. 1054, pp. 191–195.
- [178] E. R. Menzel, Fingerprint detection with lasers (M. Dekker, New York, 1999).
- [179] I. M. Alaoui, Imaging for Detection and Identification (Springer, Netherlands, 2007), pp. 243–248.
- [180] B. Drabarek, A. Siejca, J. Moszczynski, and B. Konior, *Journal of Forensic Identification* **62**, 28 (2012).
- [181] E. R. Menzel, S. M. Savoy, S. J. Ulvick, K. H. Cheng, R. H. Murdock, and M. R. Sudduth, *Journal of Forensic Sciences* **45**, 545 (2000).
- [182] E. Menzel, M. Takatsu, R. Murdock, K. Bouldin, and K. Cheng, *Journal of Forensic Sciences* **45**, 770 (2000).

- [183] M. Sametband, I. Shweky, U. Banin, D. Mandler, and J. Almog, *Chem. Commun.* 1142 (2007).
- [184] R. C. Shaler, A. Lakhtakia, J. W. Rogers, D. P. Pulsifer, and R. J. Martín-Palma, *Journal of Nanophotonics* **5**, 051509 (2011).
- [185] S. A. Muhlberger, D. P. Pulsifer, A. Lakhtakia, R. J. Martín-Palma, and R. C. Shaler, *Journal of forensic sciences* **59**, 94 (2014).
- [186] R. Martín-Palma, C. Pantano, and A. Lakhtakia, *Applied Physics Letters* **93**, 083901 (2008).
- [187] S. F. Williams, D. P. Pulsifer, R. C. Shaler, R. S. Ramotowski, S. Brazelle, and A. Lakhtakia, *Journal of forensic sciences* (2014).
- [188] Y. Cohen, E. Rozen, M. Azoury, D. Attias, B. Gavrielli, and M. Levin Elad, *J Forensic Identification* **62**, 47 (2012).
- [189] J. Polo, T. Mackay, and A. Lakhtakia, Electromagnetic Surface Waves: A Modern Perspective (Newnes, ADDRESS, 2013).



Appendix A

Suppose the half space $z < 0$ is occupied by the CTF and the half space $z > 0$ by the photoresist material of relative permittivity ε_p . We are interested in determining the wavenumber $k_{spp}(\bar{\psi})$ of the SPP wave which travels along the direction $\hat{x} \cos \bar{\psi} + \hat{y} \sin \bar{\psi}$ guided by the CTF/photoresist interface. The procedure to determine $k_{spp}(\bar{\psi})$ is explained in detailed elsewhere [189, Sec. 3.5].

Briefly, the four eigenvalues α_ℓ and the corresponding eigenvectors $[\tilde{t}_\ell]$, $\ell \in [1, 4]$, of the 4×4 matrix

$$[\tilde{P}_{CTF}] = \begin{bmatrix} 0 & 0 & 0 & \omega\mu_0 \\ 0 & 0 & -\omega\mu_0 & 0 \\ 0 & -\omega\varepsilon_0\varepsilon_c & 0 & 0 \\ \omega\varepsilon_0\varepsilon_d & 0 & 0 & 0 \end{bmatrix} + k_{spp} \frac{(\varepsilon_a - \varepsilon_b)\varepsilon_d}{\varepsilon_a\varepsilon_b} \sin\chi \cos\chi \begin{bmatrix} \cos\bar{\psi} & 0 & 0 & 0 \\ \sin\bar{\psi} & 0 & 0 & 0 \\ 0 & 0 & 0 & 0 \\ 0 & 0 & -\sin\bar{\psi} & \cos\bar{\psi} \end{bmatrix} \quad (1)$$

$$+ k_{spp}^2 \frac{\varepsilon_d}{\omega\varepsilon_0\varepsilon_a\varepsilon_b} \begin{bmatrix} 0 & 0 & \cos\bar{\psi} \sin\bar{\psi} & -\cos^2\bar{\psi} \\ 0 & 0 & \sin^2\bar{\psi} & -\cos\bar{\psi} \sin\bar{\psi} \\ 0 & 0 & 0 & 0 \\ 0 & 0 & 0 & 0 \end{bmatrix} \quad (2)$$

$$+ k_{spp}^2 \frac{1}{\omega\mu_0} \begin{bmatrix} 0 & 0 & 0 & 0 \\ 0 & 0 & 0 & 0 \\ -\cos\bar{\psi} \sin\bar{\psi} & \cos^2\bar{\psi} & 0 & 0 \\ -\sin^2\bar{\psi} & \cos\bar{\psi} \sin\bar{\psi} & 0 & 0 \end{bmatrix} \quad (3)$$

have to be determined for the CTF; here, $\varepsilon_d = \varepsilon_a\varepsilon_b/(\varepsilon_a \cos^2\chi + \varepsilon_b \sin^2\chi)$ is a shorthand notation. The eigenvalues (and the corresponding eigenvectors) are labeled such that $\text{Im}(\alpha_1) > 0$ and $\text{Im}(\alpha_2) > 0$; *ipso facto*, $\text{Im}(\alpha_3) < 0$ and $\text{Im}(\alpha_4) < 0$.

Likewise, the four eigenvalues β_ℓ and the corresponding eigenvectors $[\tilde{u}_\ell]$, $\ell \in$

[1, 4], of the 4×4 matrix

$$[\tilde{P}_p] = \begin{bmatrix} 0 & 0 & 0 & \omega\mu_0 \\ 0 & 0 & -\omega\mu_0 & 0 \\ 0 & -\omega\varepsilon_0\varepsilon_p & 0 & 0 \\ \omega\varepsilon_0\varepsilon_p & 0 & 0 & 0 \end{bmatrix} + k_{spp}^2 \frac{1}{\omega\varepsilon_0\varepsilon_p} \begin{bmatrix} 0 & 0 & \cos\bar{\psi}\sin\bar{\psi} & -\cos^2\bar{\psi} \\ 0 & 0 & \sin^2\bar{\psi} & -\cos\bar{\psi}\sin\bar{\psi} \\ 0 & 0 & 0 & 0 \\ 0 & 0 & 0 & 0 \end{bmatrix} \quad (4)$$

$$+ k_{spp}^2 \frac{1}{\omega\mu_0} \begin{bmatrix} 0 & 0 & 0 & 0 \\ 0 & 0 & 0 & 0 \\ -\cos\bar{\psi}\sin\bar{\psi} & \cos^2\bar{\psi} & 0 & 0 \\ -\sin^2\bar{\psi} & \cos\bar{\psi}\sin\bar{\psi} & 0 & 0 \end{bmatrix} \quad (5)$$

have to be determined for the photoresist material. The eigenvalues (and the corresponding eigenvectors) are labeled such that $\text{Im}(\beta_1) > 0$ and $\text{Im}(\beta_2) > 0$; *ipso facto*, $\text{Im}(\beta_3) < 0$ and $\text{Im}(\beta_4) < 0$.

Since the fields of the SPP wave must decay as $z \rightarrow \pm\infty$, the dispersion equation of the SPP wave is

$$\det [\tilde{t}_3; \tilde{t}_4; -\tilde{u}_1; -\tilde{u}_2] = 0. \quad (6)$$

Its solution provides k_{spp} as a function of $\bar{\psi}$.

For an SPP wave guided by the CTF/air interface, the foregoing procedure is repeated but with ε_p replaced by unity.

Appendix B

Determination of $\tilde{\varepsilon}$ for the CTF via the Bruggeman formalism requires the solution of the dyadic equation [1]

$$(1 - f_v) \left(\varepsilon_m \tilde{I} - \tilde{\varepsilon} \right) \cdot \left[\tilde{I} + i\omega\varepsilon_0 \tilde{D}^{(m)} \cdot \left(\varepsilon_m \tilde{I} - \tilde{\varepsilon} \right) \right]^{-1} + f_v \left(\varepsilon_v \tilde{I} - \tilde{\varepsilon} \right) \cdot \left[\tilde{I} + i\omega\varepsilon_0 \tilde{D}^{(v)} \cdot \left(\varepsilon_v \tilde{I} - \tilde{\varepsilon} \right) \right]^{-1} = \tilde{0}. \quad (7)$$

Here, ε_m and $\varepsilon_v = 1$ are the relative permittivity scalars of the metal and air, respectively; $\tilde{I} = \hat{\tau}\hat{\tau} + \hat{n}\hat{n} + \hat{b}\hat{b}$ is the identity dyadic, with $\hat{b} = -\hat{y}$; $\tilde{0}$ is the null dyadic; and the depolarization dyadics

$$\tilde{D}^{(m,v)} = \frac{2}{i\pi\omega\varepsilon_0} \int_{\varphi=0}^{\frac{\pi}{2}} \int_{\vartheta=0}^{\frac{\pi}{2}} \sin \vartheta \frac{(\sin \vartheta \cos \varphi)^2 \hat{n}\hat{n} + (\sin \vartheta \sin \varphi / \gamma_b^{(m,v)})^2 \hat{b}\hat{b} + (\cos \vartheta / \gamma_\tau^{(m,v)})^2 \hat{\tau}\hat{\tau}}{(\sin \vartheta \cos \varphi)^2 \varepsilon_a + (\sin \vartheta \sin \varphi / \gamma_b^{(m,v)})^2 \varepsilon_c + (\cos \vartheta / \gamma_\tau^{(m,v)})^2 \varepsilon_b} d\vartheta d\varphi. \quad (8)$$

The parameters $\gamma_{\tau,b}^{(m,v)}$ and f_v have to be chosen by comparing theoretical predictions of optical response characteristics against their experimental counterparts [136].

